Compressible Multi-Component and Multi-Phase Flows: Interfaces and Asymptotic Regimes

Lukas Ostrowski

University of Stuttgart
Germany

Compressible Multi-Component and Multi-Phase Flows: Interfaces and Asymptotic Regimes

Von der Fakultät Mathematik und Physik
und dem Stuttgart Center for Simulation Science der
Universität Stuttgart zur Erlangung der Würde eines Doktors der
Naturwissenschaften (Dr. rer. nat.) genehmigte Abhandlung

vorgelegt von

Lukas Christian Ostrowski

aus Stuttgart

Hauptberichter:	Prof. Dr. Christian Rohde
Mitberichter:	Prof. Dr. Francesco Bassi
	Prof. Dr. Miriam Schulte
	Prof. Dr. Claus-Dieter Munz

Tag der mündlichen Prüfung: 10.02.2021

Institut für Angewandte Analysis und Numerische Simulation,
Universität Stuttgart

2021


University of Stuttgart
Germany


ians


DROPIT


SimTech

For my family, for my friends.

Acknowledgements

This thesis greatly benefited from the input and support of many people. I am very grateful for all of them and want to thank some explicitly.
First of all I would like to express my sincere gratitude to my supervisor Prof. Dr. Christian Rohde for his guidance, support, and encouragement over the last years. Thank you for giving me the opportunity to be part of your research team.
I would like to thank Prof. Dr. Francesco Bassi, Prof. Dr. Miriam Schulte, and Prof. Dr. Claus-Dieter Munz for reviewing this thesis as referees.
Further, I want to thank my colleagues of DROPIT. I really enjoyed working with you in this interdisciplinary environment. I am especially grateful for the possibility to work three months at the Università degli Studi di Bergamo with the group of Prof. Bassi. I was welcomed warmly and profited a lot from joint discussions, especially with Carlo, whom I value both as a colleague and a person.
Moreover, I want to thank all my former and present colleagues from IANS. I will miss our coffee breaks which, more than once, turned into elaborate discussions about our work. I am especially grateful to Prof. Dr. Jan Giesselmann for providing valuable input in our fruitful discussions. In the past years I had the pleasure to work with many great people at the institute, some of whom I can gladly count among my friends. By name I would like to mention David, Elissa, Fabian, Iryna, Jan, Jim, Lars, Maria, Markus, and Samuel.
This work was financially supported by the Deutsche Forschungsgemeinschaft (DFG) in the frame of the International Research Training Group ”Droplet Interaction Technologies” (DROPIT), for which I am very grateful.
At this point I want to thank my friends and family. Their support carried me through the last years. It must have been difficult to be patient when I sometimes had a hard time freeing my mind and my calendar from mathematics. I am even more thankful that you managed to do so.
I especially thank Sarah and Samson. Thank you for your understanding and never-ending support.

Finally, I want to thank my sister Sarah, and my parents Ulrike and Bernd. They have enabled and encouraged me to pursue the things I am passionate about. Thank you.

Abstract

This thesis consists of three parts. In the first part we consider multi-component flows through porous media. We introduce a hyperbolic system of partial differential equations which describes such flows, prove the existence of solutions, the convergence in a long-time-large-friction regime to a parabolic limit system, and finally present a new numerical scheme to efficiently simulate flows in this regime.
In the second part we study two-phase flows where both phases are considered compressible. We introduce a Navier–Stokes–Allen–Cahn phase-field model and derive an energy-consistent discontinuous Galerkin scheme for this system. This scheme is used for the simulation of two complex examples, namely drop–wall interactions and multi-scale simulations of coupled porous-medium/free-flow scenarios including drop formation at the interface between the two domains.
In the third part we investigate two-phase flows where one phase is considered incompressible, while the other phase is assumed to be compressible. We introduce an incompressible–compressible Navier–Stokes–Cahn–Hilliard model to describe such flows. Further, we present some analytical results for this system, namely a computable expression for the effective surface tension in the system and a formal proof of the convergence to a (quasi-)incompressible system in the low Mach regime. As a first step towards a discontinuous Galerkin discretization of the system, which is based on Godunov fluxes, we introduce the concept of an artificial equation of state modification, which is examined for a basic single-phase incompressible setting.

Zusammenfassung

Diese Arbeit besteht aus drei Teilen. Der erste Teil befasst sich mit Mehrkomponentenströmungen durch poröse Medien. Wir führen ein System von hyperbolischen partiellen Differentialgleichungen ein, das diese Art von Strömungen beschreibt. Für dieses System beweisen wir die Existenz von Lösungen. Außerdem beweisen wir den Übergang zu einem parabolischen Grenzsystem in Strömungsregimen, die durch lange Zeiten und große Reibung charakterisiert sind. Zuletzt wird ein neues numerisches Verfahren vorgestellt, das eine effiziente numerische Simulation von Strömungen in diesem asymptotischen Regime erlaubt.
Im zweiten Teil untersuchen wir Zweiphasenströmungen, wobei beide Phasen als kompressibel betrachtet werden. Für deren Beschreibung führen ein Navier–Stokes–Allen–Cahn Phasenfeldmodell ein. Zur Diskretisierung des Modells leiten wir ein energiekonsistentes discontinuous Galerkin Verfahren her. Dieses Verfahren wird zur Simulation zweier komplexer Beispiele benutzt. Zum einen für Tropfen–Wand Interaktionen und zum anderen für Multiskalen Simulationen von gekoppelter Strömung in porösen Medien und freier Strömung. Dabei wird die Bildung von Tropfen an der Grenzfläche zwischen dem porösen Medien Gebiet und dem Gebiet der freien Strömung berücksichtigt.
Der dritte Teil beschäftigt sich mit Zweiphasenströmungen, bei denen eine Phase als kompressibel betrachtet wird, wohingegen die andere Phase als inkompressibel angenommen wird. Zur Beschreibung solcher Strömungen führen wir ein inkompressibles–kompressibles Navier–Stokes–Cahn–Hilliard Modell ein und präsentieren für dieses zwei analytische Resultate. Zum einen ein berechenbarer Ausdruck für die effektive Oberflächenspannung im System und zum anderen ein formaler Beweis der Konvergenz zu einem (quasi-)inkompressiblen Grenzsystem im Regime für kleine Machzahlen. Als ersten Schritt zu einem discontinuous Galerkin Verfahren, welches auf Godunov-Flüssen basiert, stellen wir ein Konzept vor, das auf einer künstlichen Zustandsgleichung basiert. Dieses Konzept wird dann für den einfacheren Fall einer inkompressiblen Einphasenströmung untersucht.

Contents

List of Abbreviations

AP	asymptotic preserving
CFL	Courant–Friedrichs–Lewy
CT	continuum thermodynamics
dG	discontinuous Galerkin
DI	diffuse-interface
DOF	degree(s) of freedom
EOS	equation of state
FF	free flow
FF/PM	free-flow/porous-medium-flow
FV	finite volume
GNCB	general Navier boundary conditions
ICNSCH	incompressible–compressible–Navier–Stokes–Cahn–Hilliard
ILES	implicit large eddy simulation
IMEX	implicit–explicit
INS	incompressible Navier–Stokes
IVP	initial value problem
LT	Lowengrub–Truskinovsky
MCL	moving contact line
MS	Maxwell–Stefan
NSAC	Navier–Stokes–Allen–Cahn
NSCH	Navier–Stokes–Cahn–Hilliard
NSK	Navier–Stokes–Kortweg
PDE	partial differential equation
PM	porous medium
SI	sharp-interface

Preface

This thesis deals with two peculiar features of fluid dynamics occurring in many real-world scenarios — multi-component and multi-phase flows. These are ubiquitous in our everyday life. For example even the air we breath is a mixture of several gases (mainly nitrogen and oxygen). A simple example to illustrate multi-phase flows is rain. In this case water in its liquid form moves through the multi-component gas mixture of air. An additional example are evaporation and condensation processes during the formation of fog. Of course there are considerably more examples in different fields, including technical, environmental, chemical, and biological applications.

In this thesis we focus on two main topics of multi-component and multi-phase flows, specifically on interfaces and asymptotic regimes. The thesis contains contributions to the modeling, the analysis, and the numerical discretization for such flows. These topics are investigated in three parts.

In the first part of this thesis, we study *compressible multi-component flow in porous media*, e.g. in soil. We derive a hyperbolic system of partial differential equations which is capable to describe such kind of flows. Further, we consider a specific asymptotic regime of the flow, namely for large times and high friction. Extending results for single-component flow in porous media, using entropy techniques of [32, 33, 38], we show rigorously that smooth solutions of the hyperbolic system converge to a nonlinear parabolic limit system. Concerning the numerical discretization, the limit regime is challenging. In order to simulate flows in this asymptotic regime, we present a new numerical scheme which preserves the asymptotic behavior of the system.

In the second part, we examine multi-phase flow, precisely *compressible–compressible liquid–vapor flow*, i.e. both phases are compressible. In this case the description of the dividing interface of the two phases is of crucial importance. We use a diffuse-interface description by employing a Navier–Stokes–Allen–Cahn phase-field model. We are able to develop a novel energy-consistent numerical scheme based on discontinuous Galerkin techniques. For two scenarios we show that the scheme is able to deal with complex flow situations. The first example is droplet–

wall interaction. There, the contact line, i.e. the interface between the solid wall, the liquid, and the vapor poses the major challenge. We develop a numerical treatment that allows to include different contact angles. The second example is a multi-scale framework to simulate the growth and detachment of drops at the interface between a porous medium and the free flow. We show that with help of the phase-field model, our multi-scale approach is capable to describe drop-related processes at the interface between the porous-medium and the free-flow domain.
Finally, in the third part we consider a similar situation as in the second part, however for the specific, but important flow regimes, where the liquid phase is considered as incompressible fluid, i.e. *incompressible–compressible liquid–vapor flows*. Consequently, we use a different phase-field model in this part. For this model we formally show in an asymptotic regime, particularly a low Mach regime, the convergence to a model where both phases are incompressible. Moreover, in order to discretize the corresponding system, we present an idea towards a discontinuous Galerkin scheme, based on Godunov fluxes. The main issue to define these Godunov fluxes is the solution of Riemann problems at the interfaces between elements of the underlying computational mesh.
The content of this work lead to several publications. Most of the content of Chapters 2–4 in Part I has been published in [89]. In Part II, Chapter 5 lead to the joint publication [4]. The remaining chapters have been partially published in [86, 88]. In all the above mentioned publications I provided the main contributions. Finally, Part III lead to joint work [78, 87], where both authors contributed equally.

Part I
Compressible Multi-Component Flow in Porous Media with Maxwell–Stefan Diffusion

1 Introduction

Multi-component fluid flows in porous media appear in various fields of applications such as fuel cells, oxygen sensors, and respiratory airways [18, 22, 53, 109]. To demonstrate the modeling challenge we elaborate the last example.

As stated in [22], following the model of Weibel [104], the bronchial tree can be divided into two parts. The upper conducting zone and the lower respiratory zone. In the lower part, the velocity of the air is very small. Therefore, mainly diffusive effects determine the dynamics of the gas mixture in this region of the bronchial tree. For the treatment of certain diseases of the lung, the gas mixture Heliox (20% O_2, 80% He) is used to improve the patient's well-being [9]. In order to achieve the greatest benefit for the patient, analysis based on mathematical models can be performed.

For modeling the afore-mentioned situation, the classical Fickian diffusion law [46] is too simplistic to capture important diffusive effects in the lower respiratory zone. Important phenomena, for instance uphill diffusion [70, 105], cannot be described by this approach. Uphill diffusion means flux of a mixture constituent from regions of low concentrations to ones with high concentration, see [23] and references therein. This phenomenon can occur in mixtures with at least three constituents. Duncan & Toor have given an experimental example of a three-component gas mixture in [41], which clearly demonstrates the uphill diffusion effect even in a simple configuration.

A generalization of the Fickian approach roots in the classical works of Maxwell [80] and Stefan [99]. It led to the concept which is nowadays called Maxwell–Stefan (MS) diffusion. A main difference to Fick's diffusion model is the use of chemical potential gradients as driving forces, in contrast to concentration gradients. The MS concept employs binary interactions between different constituents of the mixture. It captures more complex diffusive effects, but leads to a coupled nonlinear system of partial differential equations (PDE) and is therefore mathematically more challenging.

In this part of the thesis we provide a mathematical model for compressible multi-component flow in fully saturated porous media on the Darcy-scale. This model takes the form of a nonlinear hyperbolic balance law. Therefore, global classical solutions might not exist [34]. However, we show that dissipative effects of the Maxwell–Stefan diffusion and porous media friction suffice to ensure the classical well-posedness for initial data close to equilibrium. Note that we account for the effect of the solid skeleton in the porous medium (PM) similar to dusty gas models from [77, 105]. The PM is treated as an additional component of the mixture with vanishing velocity and constant density. In contrast to dusty gas models, which rely on the kinetic theory of gases, we utilize the continuum thermodynamics (CT) framework as developed in [20].

The solutions to the resulting system satisfy an entropy condition. This implies the validity of the second law of thermodynamics. If we drop the MS coupling terms, we obtain a system of uncoupled equations each of which correspond to the compressible Euler equations with friction. This hyperbolic model describes single-component flow through porous media. It has been shown in [44, 58, 59, 71, 75] that the solutions to this system tend, in a long-time limit, to the solution to a parabolic porous-media equation. We establish a corresponding result for the multi-component case that yields a parabolic system of porous-media equations in the limit. This parabolic system is similar to the multi-component system of [65].

The numerical discretization of hyperbolic systems in such a long-time-large-friction asymptotic regime, characterized by $\varepsilon > 0$, is challenging. This stems from the fact that the type of the limiting system is different from the type for finite values of ε. Chapter 5 of this part is dedicated to derive an *asymptotic preserving* (AP) [63] numerical scheme. That means a scheme which preserves the asymptotic limit from the hyperbolic system to the parabolic system at the discrete level. For fixed mesh size and time step size the AP scheme transforms into a stable discretization of the limiting system as ε tends to zero.

This part is organized as follows. In Chapter 2 we derive the governing equations for compressible multi-component flow in porous media within the CT framework. We start with multiple Euler equations with friction, which are coupled by a right hand side using Maxwell–Stefan cross-diffusion terms. In the subsequent Chapter 3 we prove the existence of smooth solutions to this system. To this end, we show that the dissipative effects due to MS diffusion and friction fit into the well-posedness theory [108] for general hyperbolic balance laws (see Theorem 3.2).

The second major result, namely the existence of a parabolic limit system is established in Chapter 4. We utilize a relative entropy framework to prove our main Theorem 4.3. For this purpose we adapt techniques from [71], where the convergence of the compressible Euler system with friction to the porous media equation has been proven.

In Chapter 5 we derive an AP scheme which preserves the asymptotic limit on a discrete level. Equipped with this scheme we conduct some numerical experiments where we illustrate the phenomenon of uphill diffusion and verify the asymptotic convergence rate from Theorem 4.3 numerically.
We finally conclude in Chapter 6.

Compressible Flow in Porous Media

2

First, in Section 2.1 we review a single-component model and show available analytical results. In the remainder of this part we will generalize them to the multi-component case. In Section 2.2 the multi-component model is derived using fundamental thermodynamical principles. It follows the presentation in [20] for free flow problems and extends the classical Fickian diffusion modeling to a Maxwell–Stefan approach.

2.1 Single-Component Flow

Compressible single-component flow with friction, induced by the resistance of the solid skeleton in a porous medium, can be described on a macroscopic averaged scale by the Euler–Darcy model, see [76] and references therein. We consider an isothermal situation. For $t \in (0, T)$, $T > 0$ and $\boldsymbol{x} \in \mathbb{R}^d$, $d \in \mathbb{N}$, the unknowns mass density $\rho = \rho(\boldsymbol{x}, t) > 0$ and momentum $\boldsymbol{m} = \rho \boldsymbol{v} \in \mathbb{R}^d$ with velocity $\boldsymbol{v} = \boldsymbol{v}(\boldsymbol{x}, t) \in \mathbb{R}^d$ satisfy the system

$$\begin{aligned} \partial_t \rho + \operatorname{div}(\boldsymbol{m}) &= 0, \\ \partial_t \boldsymbol{m} + \operatorname{div}\left(\frac{\boldsymbol{m} \otimes \boldsymbol{m}}{\rho} + p(\rho) \boldsymbol{I}_d \right) &= -M \boldsymbol{m}. \end{aligned} \qquad \text{in } \mathbb{R}^d \times (0, T) \tag{2.1}$$

Here $p = p(\rho)$ is the smooth pressure function, $M > 0$ is the mobility constant, and $\boldsymbol{I}_d$ is the d-dimensional identity tensor. Note that we use in (2.1) the same notation for the divergence operator applied to vector- or matrix-valued functions, see Appendix A.

It is well-known that (2.1) is a hyperbolic system of nonlinear balance laws as long as the pressure is monotonically increasing. Hence, shock-type singularities might evolve in finite time, independent of the initial data's regularity. The system (2.1) is endowed with an entropy–entropy flux pair (see (2.2) below), which can be used to ensure an appropriate form of the second law of thermodynamics for classical

as well as weak solutions. Precisely, solutions to (2.1) are required to satisfy the entropy inequality

$$\partial_t \eta(\rho, \boldsymbol{m}) + \operatorname{div}(\boldsymbol{q}(\rho, \boldsymbol{m})) \leq 0 \quad \text{in } \mathcal{D}'(\mathbb{R}^d \times (0, T)).$$

The entropy–entropy flux pair $(\eta, \boldsymbol{q})$ is given by

$$\eta(\rho, \boldsymbol{m}) = \frac{1}{2}\frac{|\boldsymbol{m}|^2}{\rho} + \rho\psi(\rho), \qquad \boldsymbol{q}(\rho, \boldsymbol{m}) = \frac{1}{2}\boldsymbol{m}\frac{|\boldsymbol{m}|^2}{\rho^2} + \boldsymbol{m}(\psi(\rho) + \rho\psi'(\rho)). \tag{2.2}$$

Here, given a smooth pressure function $p = p(\rho)$ as equation of state (EOS), the Helmholtz free energy density $\rho\psi$ is determined from the Gibbs–Duhem relation

$$\rho\psi(\rho) = \rho(\rho\psi)'(\rho) - p(\rho). \tag{2.3}$$

The nonlinear flux in (2.1) can generate shock waves. However, the dissipative effect of the friction term, i.e. the right hand side, might suffice to counteract the destabilizing effect of the flux. Indeed, depending on the initial data and the size of the mobility constant M, the initial value problem (IVP) for (2.1) can have global smooth solutions (see e.g. [44]). We will show that a similar result holds for the multi-component case. Furthermore, the dissipative friction effect leads to certain limit regimes such that the system (2.1) changes its characteristic type in the limit. We consider a long-time and large-mobility regime in (2.1), i.e., the time t is scaled by a small parameter $\varepsilon > 0$ and the mobility M by ε^{-1}. After rescaling (2.1) and renaming the variables in an obvious way, (2.1) is recasted in the form

$$\begin{aligned} \varepsilon\partial_t \rho^\varepsilon + \operatorname{div}(\boldsymbol{m}^\varepsilon) &= 0, \\ \varepsilon\partial_t \boldsymbol{m}^\varepsilon + \operatorname{div}\left(\frac{\boldsymbol{m}^\varepsilon \otimes \boldsymbol{m}^\varepsilon}{\rho^\varepsilon} + p(\rho^\varepsilon)\boldsymbol{I}_d\right) &= -\frac{1}{\varepsilon} M \boldsymbol{m}^\varepsilon \end{aligned} \qquad \text{in } \mathbb{R}^d \times (0, T). \tag{2.4}$$

The sequence $\{\rho^\varepsilon\}_{\varepsilon>0}$ of densities $\rho^\varepsilon > 0$, solving the initial value problems for (2.4), converge for $\varepsilon \longrightarrow 0$ towards a solution $\bar{\rho}$ of the IVP for the porous-medium equation

$$\partial_t \bar{\rho} - M^{-1} \operatorname{div}(\nabla p(\bar{\rho})) = 0 \text{ in } \mathbb{R}^d \times (0, T). \tag{2.5}$$

This is shown in [71] (see also [59]). In other words, the hyperbolic balance laws turn into a parabolic evolution with much more regular solution behavior. In the following, we derive a corresponding result for the multi-component case.

2.2 Multi-Component Flow

While single-component flow in a porous medium is well understood, much less is known for multi-component flow. As long as bulk viscosity is neglected, standard model approaches take the form of the Euler equations with a damping term in the momentum equations, like (2.1). However, for flow of multi-component gaseous mixtures in porous media, inter-component viscosity effects become important. They do not occur in the single-component case. The classical Fick's law for diffusion does not suffice to describe these phenomena. As a possible remedy we follow a Maxwell–Stefan ansatz. In order to derive governing equations in a thermodynamically consistent way, we follow the work of Bothe & Dreyer [20]. They establish governing equations for multi-component free flow, i.e. without a porous medium.

2.2.1 Multi-Component Flow and Maxwell–Stefan Diffusion

Let a fluid mixture consist of $n \in \mathbb{N}$ components $A_1, ..., A_n$ with corresponding mass densities $\rho_i = \rho_i(\boldsymbol{x}, t) > 0$ and velocities $\boldsymbol{v}_i = \boldsymbol{v}_i(\boldsymbol{x}, t) \in \mathbb{R}^d$, $i = 1, ..., n$. We define the total mass density ρ and the barycentric velocity $\boldsymbol{v}$ (not to be interchanged with the single-component case in Section 2.1) as

$$\rho := \sum_{i=1}^{n} \rho_i, \qquad \boldsymbol{v} := \frac{1}{\rho} \sum_{i=1}^{n} \rho_i \boldsymbol{v}_i.$$

Further, we define the diffusion velocities

$$\boldsymbol{u}_i := \boldsymbol{v}_i - \boldsymbol{v} \in \mathbb{R}^d.$$

We ignore mass exchange as well as exterior forces. Restricting ourselves to the case of a simple mixture, the component pressures p_i depend on ρ_i only, i.e. they satisfy $p_i = p_i(\rho_i)$. For $i = 1, \dots, n$ we start from the partial balances of mass and momentum given by

$$\partial_t \rho_i + \operatorname{div}(\rho_i \boldsymbol{v}_i) = 0, \tag{2.6a}$$

$$\partial_t (\rho_i \boldsymbol{v}_i) + \operatorname{div}(\rho_i \boldsymbol{v}_i \otimes \boldsymbol{v}_i + p_i(\rho_i) \boldsymbol{I}_d) = \boldsymbol{f}_i. \tag{2.6b}$$

Here $\boldsymbol{f}_i \in \mathbb{R}^d$ states the momentum production due to diffusive mixing, later specified with the Maxwell–Stefan ansatz. As a natural requirement the conservation law for total momentum has to hold, which implies the condition

$$\sum_{i=1}^{n} \boldsymbol{f}_i = \boldsymbol{0}. \tag{2.7}$$

The crux is to find an expression for $\boldsymbol{f}_i$ such that, with the (physical) entropy production ζ (see (2.9) below), the second law of thermodynamics holds true.
We introduce for each component A_i a strictly convex free energy density $h_i(\rho_i) = \rho_i \psi_i(\rho_i)$ that relates to the partial pressure $p_i(\rho_i)$ via the Gibbs–Duhem equations (see (2.3) for the single-component velocity)

$$h_i(\rho_i) + p_i(\rho_i) = \rho_i h_i'(\rho_i).$$

Thus, the strict convexity of $\rho_i \psi_i$ implies

$$p_i'(\rho_i) > 0.$$

Moreover, the function

$$h(\rho_1, \dots, \rho_n) \coloneqq \sum_{i=1}^{n} h_i(\rho_i) \tag{2.8}$$

is a mixture free energy density for simple mixtures.
For the special case of simple isothermal, inviscid fluid mixtures without chemical reactions, the entropy production ζ of some solution $(\rho_1, \dots, \rho_n, \boldsymbol{m}_1^\top, \dots, \boldsymbol{m}_n^\top)$ of (2.6a), (2.6b) is derived in [20] and reads as

$$\zeta = -\sum_{i=1}^{n} \boldsymbol{u}_i \cdot \boldsymbol{f}_i. \tag{2.9}$$

According to the second law of thermodynamics, the entropy production ζ is not allowed to be negative. Using (2.7), we infer the condition

$$\zeta = -\sum_{i=1}^{n-1} (\boldsymbol{u}_i - \boldsymbol{u}_n) \cdot \boldsymbol{f}_i \geq 0. \tag{2.10}$$

In the following we take the Maxwell–Stefan ansatz for $\boldsymbol{f}_i$ to guarantee that (2.10) holds true. Let

$$\tilde{\mathcal{T}} \coloneqq (\tau_{ij})_{i,j=1}^{n-1} \succ 0, \text{ with } \tau_{ij} = \tau_{ij}(\rho_i, \rho_j) \tag{2.11}$$

be a positive-definite matrix. With (2.11) we set

$$\boldsymbol{f}_i \coloneqq -\sum_{j=1}^{n-1} \tau_{ij}(\boldsymbol{u}_j - \boldsymbol{u}_n), \quad i = 1, ..., n-1. \tag{2.12}$$

In order to make the right hand side in (2.12) symmetric with respect to the components, we extend $\tilde{\mathcal{T}} \in \mathbb{R}^{(n-1)\times(n-1)}$ to the *Maxwell–Stefan matrix* [100] $\mathcal{T} \coloneqq (\tau_{ij})_{i,j=1}^{n} \in \mathbb{R}^{n\times n}$ by

$$\tau_{nj} \coloneqq -\sum_{i=1}^{n-1} \tau_{ij}, \quad j = 1, ..., n-1, \qquad \tau_{in} \coloneqq -\sum_{j=1}^{n-1} \tau_{ij}, \quad i = 1, ..., n. \tag{2.13}$$

Additionally let

$$\tau_{ij} \leq 0 \text{ for all } i \neq j. \tag{2.14}$$

In the case of binary interactions, the matrix $\mathcal{T}$ is symmetric. Furthermore, provided (2.11), it can be proven to be positive semi-definite, see [20].
The following ansatz for the components of $\tilde{\mathcal{T}}$ is made to match the requirements (2.13) and (2.14). We define

$$\lambda_{ij}(\rho_i, \rho_j) \coloneqq -\frac{\tau_{ij}(\rho_i, \rho_j)}{\rho_i \rho_j} \qquad (i \neq j) \tag{2.15}$$

and λ_{ii} through (2.13), i.e.

$$\lambda_{ii} \coloneqq -\sum_{j=1, j\neq i}^{n} \lambda_{ij} \frac{\rho_j}{\rho_i}.$$

With $\boldsymbol{r} \coloneqq (\rho_1, \dots, \rho_n)^\top$, we introduce the negative semi-definite matrix

$$\Lambda = \Lambda(\boldsymbol{r}) = \Big(\lambda_{ij}(\rho_i, \rho_j)\Big)_{i,j=1}^{n} \in \mathbb{R}^{n\times n}. \tag{2.16}$$

With the definitions (2.13), we infer from (2.12)

$$\boldsymbol{f}_i = -\sum_{j=1}^{n} \tau_{ij}(\boldsymbol{u}_j - \boldsymbol{u}_n), \quad i = 1, ..., n, \tag{2.17a}$$

$$\sum_{j=1}^{n} \tau_{ij} = 0, \qquad i = 1, ..., n. \tag{2.17b}$$

Thus, by replacing $\boldsymbol{u}_n$ with $\boldsymbol{u}_i$ in (2.17a), we obtain a symmetrical version of (2.12), namely

$$\boldsymbol{f}_i = \sum_{j=1}^{n} \tau_{ij}(\boldsymbol{u}_i - \boldsymbol{u}_j), \quad i = 1, ..., n. \tag{2.18}$$

With (2.18) and the symmetry of $\mathcal{T}$, the entropy production (2.9) can be written as

$$\zeta = -\sum_{i=1}^{n} \boldsymbol{u}_i \cdot \boldsymbol{f}_i = -\frac{1}{2}\sum_{i,j=1}^{n} \tau_{ij}|\boldsymbol{u}_i - \boldsymbol{u}_j|^2.$$

Obviously, condition (2.14) is necessary to achieve $\zeta \geq 0$. Due to (2.15) the entropy production reads as

$$\zeta = \frac{1}{2}\sum_{i,j=1}^{n} \lambda_{ij}(\rho_i, \rho_j)\rho_i\rho_j|\boldsymbol{v}_i - \boldsymbol{v}_j|^2. \tag{2.19}$$

Finally, with the Maxwell–Stefan ansatz the constitutive law for the momentum production $\boldsymbol{f}_i$ results from (2.15) and (2.18) as

$$\boldsymbol{f}_i = -\sum_{j=1}^{n} \lambda_{ij}(\rho_i, \rho_j)\rho_i\rho_j(\boldsymbol{v}_i - \boldsymbol{v}_j). \tag{2.20}$$

Note that in (2.20) the diffusion velocities are replaced by the velocities of the corresponding component.
With this result the partial momentum balances (2.6b) become

$$\partial_t(\rho_i\boldsymbol{v}_i) + \operatorname{div}(\rho_i\boldsymbol{v}_i \otimes \boldsymbol{v}_i + p_i(\rho_i)\boldsymbol{I}_d) = -\sum_{j=1}^{n} \lambda_{ij}(\rho_i, \rho_j)\rho_i\rho_j(\boldsymbol{v}_i - \boldsymbol{v}_j).$$

2.2.2 Compressible Multi-Component Flow in Porous Media

In the previous section we considered a free flow problem. In this section we include the porous medium in our model.
We realize the porous medium matrix as a static component A_{pm} of the mixture with velocity $\boldsymbol{v}_{\mathrm{pm}} = 0$ and density $\rho_{\mathrm{pm}} = \mathrm{const}$.
The component A_{pm} needs no equations for the mass and momentum balance. However, we have to account for the effects on the other components. Hence, the sum from (2.20) extends to

$$-\sum_{j=1}^{n} \lambda_{ij}(\rho_i, \rho_j)\rho_i\rho_j(\boldsymbol{v}_i - \boldsymbol{v}_j) - \lambda_{i,\mathrm{pm}}(\rho_i, \rho_{\mathrm{pm}})\rho_{\mathrm{pm}}\rho_i(\boldsymbol{v}_i - \boldsymbol{v}_{\mathrm{pm}}).$$

In the sequel we ignore the explicit dependence of $\lambda_{i,\mathrm{pm}}$ on the component densities ρ_i and proceed with the mobility constants

$$M_i = M_i(\rho_{\mathrm{pm}}) \coloneqq \lambda_{i,\mathrm{pm}}(\rho_{\mathrm{pm}})\rho_{\mathrm{pm}}.$$

Then we arrive at our final *Euler–Darcy–MS* system which reduces in the single-component case to (2.1).
Define with $\boldsymbol{m}_i = \rho_i\boldsymbol{v}_i$ for $i = 1, \dots, n$, the momentum vector $\boldsymbol{m} = (\boldsymbol{m}_1^\top, \dots, \boldsymbol{m}_n^\top)^\top$. We search for the function $U = (\boldsymbol{r}^\top, \boldsymbol{m}^\top)^\top$ with values in the state space

$$G = \mathbb{R}_+^n \times \mathbb{R}^{nd}, \tag{2.21}$$

that satisfies the multi-component Euler–Darcy system with Maxwell–Stefan type diffusion

$$\begin{aligned} &\partial_t\rho_i + \operatorname{div}(\boldsymbol{m}_i) = 0, \\ &\partial_t\boldsymbol{m}_i + \operatorname{div}\left(\frac{\boldsymbol{m}_i \otimes \boldsymbol{m}_i}{\rho_i} + p_i(\rho_i)\boldsymbol{I}_d\right) \\ &\qquad = -M_i\boldsymbol{m}_i - \sum_{j=1}^{n} \lambda_{ij}(\rho_i, \rho_j)(\rho_j\boldsymbol{m}_i - \rho_i\boldsymbol{m}_j) \end{aligned} \qquad \text{in } \mathbb{R}^d \times (0, T), \tag{2.22}$$

subject to the initial condition

$$U(\cdot, 0) = U_0 \coloneqq (\boldsymbol{r}_0^\top, \boldsymbol{m}_0^\top)^\top = (\rho_{1,0}, \dots, \rho_{n,0}, \boldsymbol{m}_{1,0}^\top, \dots, \boldsymbol{m}_{n,0}^\top)^\top \text{ in } \mathbb{R}^d. \tag{2.23}$$

Due to the arguments from Section 2.2.1 we note that the second law of thermodynamics is automatically satisfied along smooth solution trajectories of (2.22)–(2.23).

Remark 2.1: *1. By including the porous medium, the condition* (2.17b) *contains the summand of the porous-medium part as well. We neglect this fact. That means precisely that we neglect the effect of the porous medium on the conservation of momentum* (2.20)*. This is in accordance with the single-component case. The effect of the porous medium has the character of a body force.*

2. It turns out in experiments that the λ_{ij} are only weakly dependent on the mixture. Often affine functions suffice to describe this dependence, see [100].

3. The structure of the porous medium is only captured in the scalar parameter M_i. If the porous medium is not homogeneous and isotropic, one should allow for matrix-valued parameters with spatial dependence.

4. The terms M_i scale with the density of the porous medium, which is significantly larger than the densities of a gaseous mixture. Hence, typically it holds $M_i \gg \lambda_{ij}$.

Similar to Section 2.1, we consider a long-time/large-mobility/large-diffusion regime for (2.22). To be precise, let $\bar{x}$, $\bar{t}$, $\bar{\rho} > 0$, $\bar{v}$, $\bar{p}$, $\bar{M}$, and $\bar{\lambda}$ be the characteristic scales of the corresponding quantities. The long-time/large-mobility/large-diffusion regime is characterized by

$$\frac{\bar{x}}{\bar{v}\bar{t}} = O(\varepsilon), \quad \frac{\bar{p}}{\bar{v}^2\bar{\rho}} = O(1), \quad \frac{\bar{M}\bar{x}}{\bar{v}} = O(\varepsilon^{-1}) \quad \text{and} \quad \frac{\bar{\lambda}\bar{\rho}\bar{x}}{\bar{v}} = O(\varepsilon^{-1}),$$

using a small parameter $\varepsilon > 0$. After rescaling the system (2.22) and renaming the unknown as $U^\varepsilon = (\boldsymbol{r}^{\varepsilon\top} = (\rho_1^\varepsilon, \dots, \rho_n^\varepsilon), \boldsymbol{m}^{\varepsilon\top} = (\boldsymbol{m}_1^{\varepsilon\top}, \dots, \boldsymbol{m}_n^{\varepsilon\top}))^\top$ it reads in this regime as

$$\begin{aligned}
&\varepsilon\partial_t\rho_i^\varepsilon + \operatorname{div}(\boldsymbol{m}_i^\varepsilon) = 0,\\
&\varepsilon\partial_t\boldsymbol{m}_i^\varepsilon + \operatorname{div}\left(\frac{\boldsymbol{m}_i^\varepsilon \otimes \boldsymbol{m}_i^\varepsilon}{\rho_i^\varepsilon} + p_i(\rho_i^\varepsilon)\boldsymbol{I}_d\right)\\
&\qquad = -\frac{1}{\varepsilon}M_i\boldsymbol{m}_i^\varepsilon - \frac{1}{\varepsilon}\sum_{j=1}^n \lambda_{ij}(\rho_j^\varepsilon\boldsymbol{m}_i^\varepsilon - \rho_i^\varepsilon\boldsymbol{m}_j^\varepsilon),
\end{aligned} \qquad \text{in } \mathbb{R}^d \times (0,T) \quad (2.24)$$

with the (ε-dependent) initial conditions

$$U^\varepsilon(\cdot,0) = U_0^\varepsilon := (\boldsymbol{r}_0^{\varepsilon\top}, \boldsymbol{m}_0^{\varepsilon\top})^\top = (\rho_{1,0}^\varepsilon, \dots, \rho_{n,0}^\varepsilon, \boldsymbol{m}_{1,0}^{\varepsilon\top}, \dots, \boldsymbol{m}_{n,0}^{\varepsilon\top})^\top \qquad \text{in } \mathbb{R}^d. \quad (2.25)$$

As for the single-component case we will show that the multi-component case admits global smooth solutions exploiting the dissipative effect due to friction as well as due to the Maxwell–Stefan diffusion.

The other major goal is to prove that the density component sequence $\{\boldsymbol{r}^\varepsilon\}_{\varepsilon>0}$ of solutions to the IVP (2.24)–(2.25) converges for $\varepsilon \longrightarrow 0$ to the vector-valued density field $\bar{\boldsymbol{r}} = (\bar{\rho}_1, ..., \bar{\rho}_n)^\top$ solving the system of porous medium equations

$$\partial_t \bar{\boldsymbol{r}} - \operatorname{div}\left((\mathcal{B}(\bar{\boldsymbol{r}}))^{-1} \nabla \boldsymbol{p}(\bar{\boldsymbol{r}})\right) = \boldsymbol{0} \qquad \text{in } \mathbb{R}^d \times (0, T), \tag{2.26}$$

subject to the initial conditions

$$\bar{\boldsymbol{r}}(\cdot, 0) = \bar{\boldsymbol{r}}_0 \qquad \text{in } \mathbb{R}^d. \tag{2.27}$$

In (2.26) we used the vector-valued pressure

$$\boldsymbol{p}(\bar{\boldsymbol{r}}) = (p_1(\bar{\rho}_1), ..., p_n(\bar{\rho}_n))^\top,$$

and the matrices

$$\begin{aligned} \mathcal{B}(\bar{\boldsymbol{r}}) &= \tilde{\mathcal{B}}(\bar{\boldsymbol{r}}) \otimes \boldsymbol{I}_d \in \mathbb{R}^{nd \times nd}, \\ \tilde{\mathcal{B}}(\bar{\boldsymbol{r}}) &= \operatorname{diag}(M_i) - \operatorname{diag}(\bar{\rho}_i)\Lambda \in \mathbb{R}^{n \times n}. \end{aligned} \tag{2.28}$$

The matrix Λ from (2.16) is negative semi-definite. This implies that $\tilde{\mathcal{B}}$ is positive definite due to $M_i > 0$ and the positivity of the densities $\bar{\rho}_i > 0$. In particular $\mathcal{B}$ is positive definite as the Kronecker product of two positive definite matrices. For the definition of the generalized gradient/divergence operators in the system (2.26) and the Kronecker matrix product $\otimes$ in (2.28) we refer to Appendix A.

Remark 2.2: *1. For the single component case $n = 1$ the system* (2.26) *reduces to the porous-media equation* (2.5).

2. If no porous medium is present, i.e. $M_i = 0$, the system (2.26) *in this framework corresponds for perfect gas laws to the following version of the Maxwell–Stefan equations formulated for the molar concentrations c_i often seen in the literature, e.g. in [65]:*

$$\begin{aligned} \partial_t c_i + \operatorname{div} \boldsymbol{J}_i &= 0, \\ \nabla c_i &= -\sum_{j=1, j\neq i}^{n} \frac{c_j \boldsymbol{J}_i - c_i \boldsymbol{J}_j}{D_{ij}}. \end{aligned} \tag{2.29}$$

Here $D_{ij} = \dfrac{R}{c\mathcal{M}_i\mathcal{M}_j\lambda_{ij}}$, with the ideal gas constant R, total molar concentration $c = \sum_{i=1}^n c_i$ and molar masses $\mathcal{M}_i$.

3. *Without a porous medium contribution, a different (high friction) scaling for multi-component flow is considered in [60]. For the limit* $\varepsilon \longrightarrow 0$ *the authors show the convergence to a hyperbolic zeroth-order system with a parabolic first order correction system which is of Maxwell–Stefan type similar to* (2.29).

Existence of Smooth Solutions in Multiple Space Dimensions

3

The main result in this chapter is Theorem 3.2 on the classical well-posedness of the IVP for system (2.22). To this end, we propose an entropy concept for (2.22) and adapt a result of Yong [108] on hyperbolic balance laws, see Appendix B. It exploits dissipative effects of the balance terms that counteract the development of singularities driven by the hyperbolic flux [34]. To state and prove our main result Theorem 3.2, we summarize below all assumptions on the system (2.22) according to the notations from Chapter 2.

Assumption 3.1: *We make the following assumptions:*

1. *The functions* $\lambda_{ij} \in C^\infty((0,\infty)^2, \mathbb{R})$, $i, j = 1, \dots, n$, *satisfy* (2.15) *and* (2.17b).
2. *The symmetric matrix* $\Lambda(\boldsymbol{r}) = \left(\lambda_{ij}(\rho_i, \rho_j)\right)_{i,j=1}^{n}$ *is negative semi-definite for all* $\boldsymbol{r} \in (0,\infty)^n$.
3. *The free energy densities* $h_i = \rho_i \psi_i \in C^3((0,\infty))$ *are strictly convex for* $i = 1, \dots, n$.
4. *The mobility constants* M_i *are positive for* $i = 1, \dots, n$.

Theorem B.1 applies to general hyperbolic balance laws.
With $U = (\rho_1, \dots, \rho_n, (\boldsymbol{m}_1^\top, \dots, \boldsymbol{m}_n^\top))^\top$ we can rewrite (2.22) in this form, that is

$$\partial_t U + \sum_{\alpha=1}^{d} \partial_{x_\alpha} F_\alpha(U) = S(U) = \begin{pmatrix} \mathbf{0} \\ \boldsymbol{s}(\boldsymbol{r}, \boldsymbol{m}) \end{pmatrix}. \tag{3.1}$$

The fluxes $F_\alpha(U) \in \mathbb{R}^{(d+1)n}$ and the source $\boldsymbol{s}(\boldsymbol{r}, \boldsymbol{m}) \in \mathbb{R}^{nd}$ are given by

$$F_\alpha(U) = \left(m_1^{(\alpha)}, \dots, m_n^{(\alpha)}, \frac{m_1^{(\alpha)}}{\rho_1} \boldsymbol{m}_1^\top + p_1(\rho_1) \boldsymbol{e}_\alpha^\top, \dots, \frac{m_n^{(\alpha)}}{\rho_n} \boldsymbol{m}_n^\top + p_n(\rho_n) \boldsymbol{e}_\alpha^\top \right)^\top \tag{3.2}$$

$$\boldsymbol{s}(\boldsymbol{r}, \boldsymbol{m}) = \begin{pmatrix} -M_1 \boldsymbol{m}_1 - \sum_{j=1}^n \lambda_{1j}(\rho_j \boldsymbol{m}_1 - \rho_1 \boldsymbol{m}_j) \\ -M_2 \boldsymbol{m}_2 - \sum_{j=1}^n \lambda_{2j}(\rho_j \boldsymbol{m}_2 - \rho_2 \boldsymbol{m}_j) \\ \vdots \\ -M_n \boldsymbol{m}_n - \sum_{j=1}^n \lambda_{nj}(\rho_j \boldsymbol{m}_n - \rho_n \boldsymbol{m}_j) \end{pmatrix}.$$

Here we used $\boldsymbol{m}_i = (m_i^{(1)}, \dots, m_i^{(d)})^\top$ and $\boldsymbol{e}_\alpha \in \mathbb{R}^d$ denotes the α-th unit vector. Furthermore, we require an entropy–entropy flux pair $(\eta, \boldsymbol{q}) \in C^2(G)$ for (3.1) on the state space G from (2.21). Following [34], the tuple $(\eta, \boldsymbol{q})$ is called an entropy–entropy flux pair to the system (2.22) provided $\mathrm{D}^2\, \eta(U)$ is positive-definite and the compatibility conditions

$$\mathrm{D}\, \eta(U)\, \mathrm{D}\, F_\alpha(U) = \mathrm{D}\, q_\alpha(U), \qquad \alpha = 1, \dots, d, \tag{3.3}$$

are satisfied for all $U \in G$. Motivated by the considerations in Chapter 2 we suggest for (2.22) the functions

$$\eta(U) = \frac{1}{2} \sum_{i=1}^n \frac{|\boldsymbol{m}_i|^2}{\rho_i} + \sum_{i=1}^n h_i(\rho_i), \qquad \boldsymbol{q}(U) = \frac{1}{2} \sum_{i=1}^n \boldsymbol{m}_i \frac{|\boldsymbol{m}_i|^2}{\rho_i^2} + \boldsymbol{m}_i h_i(\rho_i)'. \tag{3.4}$$

Note that η in (3.4) is obviously strictly convex, by Assumption 3.1 (iii).
Equipped with the assumptions and definitions above, we state our main Theorem.

Theorem 3.2 (Global classical well-posedness of the IVP for (2.22))**:**
Let $s \geq \lfloor d/2 \rfloor + 2$ and let Assumption 3.1 hold. Consider a static equilibrium solution $\hat{U} \in G$ to (2.22) *of the form*

$$\hat{U} = (\hat{\rho}_1, ..., \hat{\rho}_n, \boldsymbol{0}, ..., \boldsymbol{0})^\top, \qquad \hat{\rho}_i > 0, \qquad i = 1, ..., n. \tag{3.5}$$

Then there exists a constant $c_1 > 0$, such that for all $U_0 \in H^s(\mathbb{R}^d)$ with

$$\|U_0 - \hat{U}\|_{H^s} \leq c_1$$

and all $T > 0$ the IVP (2.22)–(2.23) *has an unique solution $U \in C([0, T), H^s(\mathbb{R}^d))$ taking values in the state space G.*

Additionally, the solution U satisfies the entropy inequality

$$\partial_t \eta(U) + \operatorname{div} \boldsymbol{q}(U) \leq -\zeta - \sum_{i=1}^{n} M_i \frac{|\boldsymbol{m}_i|^2}{\rho_i}, \tag{3.6}$$

with $\zeta = \sum_{i,j=1}^{n} \frac{\lambda_{ij}(\rho_i,\rho_j)}{2\rho_i\rho_j} |\rho_j \boldsymbol{m}_i - \rho_i \boldsymbol{m}_j|^2$ *(see* (2.19)*).*

Proof. For better readability we omit the argument (ρ_i, ρ_j) of the functions λ_{ij}. With (3.1) we match the setting (6.3) to apply Theorem B.1. We compute the Jacobian for the equilibrium state $\hat{U}$ from (3.5)

$$\mathrm{D}_{\boldsymbol{m}} \boldsymbol{s}(\hat{U}) = \begin{pmatrix} -M_1 - \sum\limits_{j=1, j\neq 1}^{n} \hat{\rho}_j \lambda_{1j} & \hat{\rho}_1 \lambda_{12}, & \cdots & \hat{\rho}_1 \lambda_{1n} \\ \hat{\rho}_2 \lambda_{21} & \ddots & & \vdots \\ \vdots & & \ddots & \hat{\rho}_{n-1} \lambda_{n-1n-1} \\ \hat{\rho}_n \lambda_{n1} & \cdots & \hat{\rho}_n \lambda_{nn-1} & -M_n - \sum\limits_{j=1, j\neq n}^{n} \hat{\rho}_j \lambda_{nj} \end{pmatrix} \otimes \boldsymbol{I}_d.$$

From Assumption 3.1 (i) we have $\hat{\rho}_i \lambda_{ii} = -\sum_{j=1, j\neq i}^{n} \hat{\rho}_j \lambda_{ij}$ which implies

$$\mathrm{D}_{\boldsymbol{m}} \boldsymbol{s}(\hat{U}) = (-\mathcal{M} + \mathcal{R}\Lambda) \otimes \boldsymbol{I}_d,$$

with $\mathcal{M} = \operatorname{diag}(M_i) \in \mathbb{R}^{n\times n}$, $\mathcal{R} = \operatorname{diag}(\hat{\rho}_i) \in \mathbb{R}^{n\times n}$ being positive-definite. The Jacobian $\mathrm{D}_{\boldsymbol{m}} \boldsymbol{s}(\hat{U}) \prec 0$ is in particular a regular matrix which implies the first condition in Theorem B.1.

For the entropy η from (3.4) and any open set $\hat{\mathcal{G}} \subset G$ containing $\hat{U}$ we have $\mathrm{D}\,\eta(U) \in \mathbb{R}^{n(d+1)}, \mathrm{D}^2\,\eta \in \mathbb{R}^{n(d+1)\times n(d+1)}$, $U \in \hat{\mathcal{G}}$. The derivatives of η read with (2.8) as

$$\mathrm{D}\,\eta(U) = \left(\frac{\partial(\rho_1\psi_1)}{\partial\rho_1}(\rho_1) - \frac{|\boldsymbol{m}_1|^2}{2\rho_1^2}, \dots, \frac{\partial(\rho_n\psi_n)}{\partial\rho_n}(\rho_n) - \frac{|\boldsymbol{m}_n|^2}{2\rho_n^2}, \frac{\boldsymbol{m}_1^\top}{\rho_1}, \dots, \frac{\boldsymbol{m}_n^\top}{\rho_n} \right)^\top,$$

$$\mathrm{D}\,\eta(\hat{U}) = \left(\frac{\partial(\rho_1\psi_1)}{\partial\rho_1}(\hat{\rho}_1), \dots, \frac{\partial(\rho_n\psi_n)}{\partial\rho_n}(\hat{\rho}_n), \boldsymbol{0}^\top, \dots, \boldsymbol{0}^\top \right)^\top,$$

$$\mathrm{D}^2\,\eta(U) = \begin{pmatrix} \operatorname{diag}\left(\frac{1}{\rho_i} p_i'(\rho_i) + \frac{|\boldsymbol{m}_i|^2}{\rho_i^3} \right) & \operatorname{blockdiag}\left(-\frac{\boldsymbol{m}_i}{\rho_i^2} \right)^\top \\ \operatorname{blockdiag}\left(-\frac{\boldsymbol{m}_i}{\rho_i^2} \right) & \operatorname{diag}\left(\frac{1}{\rho_i} \otimes 1_d \right) \end{pmatrix}.$$

For the definition of the operator blockdiag, the Kronecker product $\otimes$ and the entry-wise product $\odot$ we refer to the Appendix A. From the definition of the fluxes F_α in (3.2) we compute

$$\mathrm{D}\,F_\alpha(U) = \begin{pmatrix} \mathbf{0}_{n\times n} & I_n \otimes \boldsymbol{e}_\alpha^\top \\ \operatorname{blockdiag}\left(-\frac{\boldsymbol{m}_i m_i^{(\alpha)}}{\rho_i^2} + p_i'(\rho_i)\boldsymbol{e}_\alpha\right) & \operatorname{diag}\left(\frac{m_i^{(\alpha)}}{\rho_i} 1_d\right) + \operatorname{blockdiag}\left(\boldsymbol{e}_\alpha \odot \frac{\boldsymbol{m}_i}{\rho_i}\right) \end{pmatrix},$$

where $\boldsymbol{e}_\alpha$ denotes the α-th unit vector and $1_d := (1,\dots,1)^\top \in \mathbb{R}^d$. We see that the matrix

$$\mathrm{D}^2\,\eta(U)\,\mathrm{D}\,F_\alpha(U) = \begin{pmatrix} \operatorname{diag}\left(\frac{|\boldsymbol{m}_i|^2 m_i^{(\alpha)}}{\rho_i^4} - \frac{p_i'(\rho_i) m_i^{(\alpha)}}{\rho_i^2}\right) & \operatorname{blockdiag}\left(\frac{p_i'(\rho_i)}{\rho_i}\boldsymbol{e}_\alpha - \frac{\boldsymbol{m}_i m_i^{(\alpha)}}{\rho_i^3}\right)^\top \\ \operatorname{blockdiag}\left(\frac{p_i'(\rho_i)}{\rho_i}\boldsymbol{e}_\alpha - \frac{\boldsymbol{m}_i m_i^{(\alpha)}}{\rho_i^3}\right) & \operatorname{diag}\left(\frac{m_i^{(\alpha)}}{\rho_i^2} 1_d, \dots, \frac{m_n^{(\alpha)}}{\rho_n^2} 1_d\right) \end{pmatrix}$$

is symmetric. Altogether we have verified the second condition in Theorem B.1, up to now for any open set $\hat{\mathcal{G}}$ that contains the equilibrium state $\hat{U}$.
To check the third condition in Theorem B.1 let $U, \hat{U} \in \hat{\mathcal{G}}$. We use the symmetry of Λ and (2.19) to obtain

$$\begin{aligned} -(\mathrm{D}\,\eta(U) - \mathrm{D}\,\eta(\hat{U}))\cdot S(U) &= \sum_{i=1}^n M_i \frac{|\boldsymbol{m}_i|^2}{\rho_i} + \sum_{j=1}^n \lambda_{ij}\left(\frac{\rho_j}{\rho_i}|\boldsymbol{m}_i|^2 - \boldsymbol{m}_i\cdot\boldsymbol{m}_j\right) \\ &= \sum_{i=1}^n M_i \frac{|\boldsymbol{m}_i|^2}{\rho_i} + \frac{1}{2}\sum_{i,j=1}^n \lambda_{ij}\rho_i\rho_j\left|\frac{\boldsymbol{m}_i}{\rho_i} - \frac{\boldsymbol{m}_j}{\rho_j}\right|^2 \\ &= \sum_{i=1}^n M_i \frac{|\boldsymbol{m}_i|^2}{\rho_i} + \zeta. \end{aligned} \tag{3.7}$$

Furthermore, we now choose $\mathcal{G}$ as a compact, convex subset of $\hat{\mathcal{G}}$ such that we have for all $U \in \mathcal{G}$ the estimate

$$\begin{aligned} |S(U)|^2 &= \sum_{i=1}^n \left|M_i\boldsymbol{m}_i + \sum_{j=1}^n \lambda_{ij}(\rho_j\boldsymbol{m}_i - \rho_i\boldsymbol{m}_j)\right|^2 \\ &\le \sum_{i=1}^n 2M_i^2|\boldsymbol{m}_i|^2 + 2\left|\sum_{j=1}^n \lambda_{ij}(\rho_j\boldsymbol{m}_i - \rho_i\boldsymbol{m}_j)\right|^2 \end{aligned}$$

$$\leq \sum_{i=1}^{n} 2M_i^2 |\boldsymbol{m}_i|^2 + 2n^2 \sum_{i,j=1}^{n} \lambda_{ij}^2 |\rho_j \boldsymbol{m}_i - \rho_i \boldsymbol{m}_j|^2$$

$$\leq 2\hat{c}_{\mathcal{G}} \sum_{i=1}^{n} M_i \frac{|\boldsymbol{m}_i|^2}{\rho_i} + 2\tilde{c}_{\mathcal{G}} \sum_{i,j=1}^{n} \lambda_{ij} \rho_i \rho_j \left| \frac{\boldsymbol{m}_i}{\rho_i} - \frac{\boldsymbol{m}_j}{\rho_j} \right|^2,$$

with

$$\hat{c}_{\mathcal{G}} = \left(\max_{i=1,\dots,n} M_i \right) \cdot \left(\max_{i=1,\dots,n} \max_{\rho_i \in \mathcal{G}} \rho_i \right),$$

$$\tilde{c}_{\mathcal{G}} = n^2 \left(\max_{i,j=1,\dots,n} \max_{\rho_i,\rho_j \in \mathcal{G}} \lambda_{ij}(\rho_i, \rho_j) \right) \cdot \left(\max_{i=1,\dots,n} \max_{\rho_i \in \mathcal{G}} \rho_i \right)^2.$$

Hence, we get from (3.7) with $c_{\mathcal{G}}^{-1} = 2 \max\{\hat{c}_{\mathcal{G}}, \tilde{c}_{\mathcal{G}}\}$ the inequality

$$-c_{\mathcal{G}} |S(U)|^2 \geq (\mathrm{D}\,\eta(U) - \mathrm{D}\,\eta(\hat{U}))S(U) \quad \text{in } \mathcal{G},$$

which implies the third condition.
Finally,

$$\mathrm{D}\,S(U) = \begin{pmatrix} \mathbf{0}_{n\times n} & \mathbf{0}_{n\times nd} \\ \mathcal{A}(U) & \mathrm{D}_{\boldsymbol{m}}\,\boldsymbol{s}(U) \end{pmatrix},$$

with $\mathcal{A}(\hat{U}) = \mathbf{0}_{nd\times n}$. Evaluating at $\hat{U}$ yields

$$\mathrm{D}\,S(\hat{U}) = \begin{pmatrix} \mathbf{0}_{n\times n} & \mathbf{0}_{n\times nd} \\ \mathbf{0}_{nd\times n} & \mathrm{D}_{\boldsymbol{m}}\,\boldsymbol{s}(\hat{U}) \end{pmatrix}.$$

The lower right block of this matrix is invertible as shown above. Consequently,

$$\ker(\mathrm{D}\,S(\hat{U})) = \mathrm{span}\{\boldsymbol{e}_1, \dots, \boldsymbol{e}_n\} \subset \mathbb{R}^{n(d+1)}.$$

Due to the zero block in $\mathrm{D}\,F_j(\hat{U})$, the corresponding eigenvectors must have non-zero entries at the $n+1$-th to $n(d+1)$-th position. Therefore, the last condition of Theorem B.1 holds.
We verified all the conditions of Theorem B.1. Hence, the system (2.22) with U_0 as initial value has an unique solution $U = U(\boldsymbol{x}, t) \in C([0, T), H^s(\mathbb{R}^d))$, $s \geq \lfloor d/2 \rfloor + 2$. The entropy inequality (3.6) is a consequence of (3.3), (3.7), and $\mathrm{D}\,\eta(\hat{U})S(U) = 0$. ∎

Remark 3.3: *1. Note that due to $s \geq \lfloor d/2 \rfloor + 2$ we have with the Sobolev embedding theorem even $U \in C^1(\mathbb{R}^d \times (0, T))$.*

2. *The symmetry of* $\mathrm{D}^2\,\eta(U)\,\mathrm{D}\,F_j(U)$ *follows directly from the compatibility condition* (3.3) *of the entropy–entropy flux pair and the strict convexity of* η*. However, since the matrices are needed in the proof, we checked this property by hand.*

Convergence to the Parabolic Limit System

4

The goal of this chapter is to prove the convergence of solutions to (2.24)–(2.25) to solutions to an IVP for the parabolic limit system (2.26), as ε tends to zero. Due to Theorem 3.2, there exists for each $\varepsilon > 0$ an unique global solution $U^\varepsilon = (\boldsymbol{r}^{\varepsilon\top}, \boldsymbol{m}^{\varepsilon\top})^\top$ to the IVP for the ε-scaled system (2.24). However, the convex set $\mathcal{G}$ might depend on ε such that the set of admissible initial conditions could shrink to the equilibrium for $\varepsilon \longrightarrow 0$. Nevertheless, the techniques of [90] allow to show that there exists a time interval, independent of ε, where solutions U^ε exist. Hence, we assume that there is a time $T > 0$ and a compact, convex set $\mathcal{G}$ such that for all $\varepsilon > 0$ the solutions U^ε exist on the interval $(0, T)$ and are contained in $\mathcal{G}$.
Our convergence proof relies on the relative entropy method which traces back to [32, 33], and [38]. This technique only requires one solution to be a strong (in fact Lipschitz continuous) solution, whereas the other can be a discontinuous entropy solution. We regard the solutions to (2.24) as weak solutions and the solution to the limit system as strong solution. We rely on the technical framework that has been established in [71]. First, we prove a dissipation relation (Proposition 4.1) for so-called relative entropies in Section 4.1 and finally, we conclude the convergence estimate with the main result in Theorem 4.3 of Section 4.2.
In the following, we omit the arguments of λ_{ij}. With a slight misuse of notation we use the expression $(\boldsymbol{r}^\varepsilon, \boldsymbol{m}^\varepsilon)$ for the solution U^ε.

4.1 The Relative Entropy Estimate

Let us consider (2.24)–(2.25) for $\varepsilon > 0$. To obtain a convergence estimate for the solutions $(\boldsymbol{r}^\varepsilon, \boldsymbol{m}^\varepsilon)$ to (2.24)–(2.25), we fix well-prepared functions for the initial conditions in (2.25) and (2.27) in $\mathbb{R}^d$.
Let $R_0 > 0$ and $\hat{\boldsymbol{r}} \in (0, \infty)^n$ be given. We restrict the initial data $(\boldsymbol{r}_0^\varepsilon, \boldsymbol{m}_0^\varepsilon) \in L^\infty(\mathbb{R}^d)$ in (2.25) to take values in $\mathcal{G}$ and to satisfy

$$(\boldsymbol{r}_0^\varepsilon(\boldsymbol{x}), \boldsymbol{m}_0^\varepsilon(\boldsymbol{x})) = (\hat{\boldsymbol{r}}, 0) \text{ for } |\boldsymbol{x}| > R_0. \tag{4.1}$$

For the initial data $\bar{\boldsymbol{r}}_0 \in C^3(\mathbb{R}^d)$ of the limit equation (2.26), we impose the analogous condition

$$\bar{\boldsymbol{r}}_0(\boldsymbol{x}) = \hat{\boldsymbol{r}}, \quad \text{for } |\boldsymbol{x}| > R_0. \tag{4.2}$$

Using the entropy–entropy flux pair $(\eta, \boldsymbol{q})$ from (3.4), we define an *entropy solution* $(\boldsymbol{r}^\varepsilon, \boldsymbol{m}^\varepsilon) \in L^\infty(\mathbb{R}^d \times (0,T))$ to (2.24)–(2.25) as a weak solution to (2.24)–(2.25) that takes values in $\mathcal{G}$ and satisfies

$$\begin{aligned}\partial_t \eta(\boldsymbol{r}^\varepsilon, \boldsymbol{m}^\varepsilon) + \frac{1}{\varepsilon} \operatorname{div} \boldsymbol{q}(\boldsymbol{r}^\varepsilon, \boldsymbol{m}^\varepsilon) \\ + \frac{1}{\varepsilon^2}\left(\sum_{i=1}^n M_i \frac{|\boldsymbol{m}_i^\varepsilon|^2}{\rho_i^\varepsilon} + \frac{1}{2}\sum_{i,j=1}^n \lambda_{ij}\rho_i^\varepsilon \rho_j^\varepsilon \left|\frac{\boldsymbol{m}_i^\varepsilon}{\rho_i^\varepsilon} - \frac{\boldsymbol{m}_j^\varepsilon}{\rho_j^\varepsilon}\right|^2\right) \le 0\end{aligned} \tag{4.3}$$

in $\mathcal{D}'(\mathbb{R}^d \times [0,T))$. Note that entropy flux scales with ε^{-1} according to the flux scaling in (2.24).
Further, let $\bar{\boldsymbol{r}} \in C^{3,1}(\mathbb{R}^d \times (0,T)) := \{\boldsymbol{g} \mid \boldsymbol{g}(\cdot,t) \in C^3(\mathbb{R}^d), t \in (0,T),\ \boldsymbol{g}(\boldsymbol{x},\cdot) \in C^1((0,T)), \boldsymbol{x} \in \mathbb{R}^d\}$, with $\bar{\boldsymbol{r}} \in (0,\infty)^n$, be a smooth solution to (2.26)–(2.27). We observe that $\bar{\boldsymbol{r}}$ satisfies for all $\varepsilon > 0$ the expanded, but equivalent system

$$\begin{aligned}\partial_t \bar{\boldsymbol{r}} + \frac{1}{\varepsilon}\operatorname{div}(\bar{\boldsymbol{m}}) = 0, \\ \bar{\boldsymbol{m}} = -\varepsilon(\mathcal{B}(\bar{\boldsymbol{r}}))^{-1}\nabla \boldsymbol{p}(\bar{\boldsymbol{r}}).\end{aligned} \tag{4.4}$$

Recall that the matrix $\mathcal{B}$ has been defined in (2.28). The regularity of $\bar{\boldsymbol{r}}$ implies $\bar{\boldsymbol{m}} \in C^{2,1}(\mathbb{R}^d \times (0,T))$. Note that $\bar{\boldsymbol{m}}$ depends on ε which is suppressed in the notation. Through evaluation of $\bar{\boldsymbol{m}}$ at initial time, the equivalent formulation (4.4) of system (2.26) causes with (4.2) the compatibility condition

$$\bar{\boldsymbol{m}}(\boldsymbol{x},0) = -\varepsilon\mathcal{B}(\bar{\boldsymbol{r}}_0(\boldsymbol{x}))^{-1}\nabla \boldsymbol{p}(\bar{\boldsymbol{r}}_0(\boldsymbol{x})) = 0 \text{ for } |\boldsymbol{x}| > R_0. \tag{4.5}$$

For this choice of $\bar{\boldsymbol{m}}$ we define now the relative entropy expression

$$\begin{aligned}\eta(\boldsymbol{r}^\varepsilon, \boldsymbol{m}^\varepsilon | \bar{\boldsymbol{r}}, \bar{\boldsymbol{m}}) &:= \eta(\boldsymbol{r}^\varepsilon, \boldsymbol{m}^\varepsilon) - \eta(\bar{\boldsymbol{r}}, \bar{\boldsymbol{m}}) \\ &\quad - \mathrm{D}_{\boldsymbol{r}}\,\eta(\bar{\boldsymbol{r}}, \bar{\boldsymbol{m}}) \cdot (\boldsymbol{r}^\varepsilon - \bar{\boldsymbol{r}}) - \mathrm{D}_{\boldsymbol{m}}\,\eta(\bar{\boldsymbol{r}}, \bar{\boldsymbol{m}}) \cdot (\boldsymbol{m}^\varepsilon - \bar{\boldsymbol{m}}) \\ &= \frac{1}{2}\sum_{i=1}^n \rho_i^\varepsilon \left|\frac{\boldsymbol{m}_i^\varepsilon}{\rho_i^\varepsilon} - \frac{\bar{\boldsymbol{m}}_i}{\bar{\rho}_i}\right|^2 + \sum_{i=1}^n h_i(\rho_i^\varepsilon | \bar{\rho}_i),\end{aligned} \tag{4.6}$$

with

$$h_i(\rho_i^\varepsilon | \bar{\rho}_i) := h_i(\rho_i^\varepsilon) - h_i(\bar{\rho}_i) - h_i'(\bar{\rho}_i)(\rho_i^\varepsilon - \bar{\rho}_i).$$

The relative entropy flux is defined by

$$\begin{aligned}\boldsymbol{q}(\boldsymbol{r}^\varepsilon, \boldsymbol{m}^\varepsilon|\bar{\boldsymbol{r}}, \bar{\boldsymbol{m}}) &:= \boldsymbol{q}(\boldsymbol{r}^\varepsilon, \boldsymbol{m}^\varepsilon) - \boldsymbol{q}(\bar{\boldsymbol{r}}, \bar{\boldsymbol{m}}) - (\mathrm{D}_{\boldsymbol{r}}\,\eta(\bar{\boldsymbol{r}}, \bar{\boldsymbol{m}})^\top \otimes \boldsymbol{I}_d)(\boldsymbol{m}^\varepsilon - \bar{\boldsymbol{m}}) \\ &\quad - (\boldsymbol{I}_d \otimes \mathrm{D}_{\boldsymbol{m}_1}\,\eta(\bar{\boldsymbol{r}}, \bar{\boldsymbol{m}})^\top, \dots, \boldsymbol{I}_d \otimes \mathrm{D}_{\boldsymbol{m}_n}\,\eta(\bar{\boldsymbol{r}}, \bar{\boldsymbol{m}})^\top)(F(\boldsymbol{r}^\varepsilon, \boldsymbol{m}^\varepsilon) - F(\bar{\boldsymbol{r}}, \bar{\boldsymbol{m}})) \\ &= \sum_{i=1}^n \left(\frac{1}{2}\boldsymbol{m}_i^\varepsilon \left| \frac{\boldsymbol{m}_i^\varepsilon}{\rho_i^\varepsilon} - \frac{\bar{\boldsymbol{m}}_i}{\bar{\rho}_i} \right|^2 + \rho_i(h_i'(\rho_i^\varepsilon) - h_i'(\bar{\rho}_i)) \left(\frac{\boldsymbol{m}_i^\varepsilon}{\rho_i^\varepsilon} - \frac{\bar{\boldsymbol{m}}_i}{\bar{\rho}_i} \right) \right. \\ &\quad \left. + \frac{\bar{\boldsymbol{m}}_i}{\bar{\rho}_i} h_i(\rho_i^\varepsilon|\bar{\rho}_i) \right), \end{aligned} \tag{4.7}$$

with F being a vectorial collection of the momentum fluxes given by

$$F(\boldsymbol{r}, \boldsymbol{m}) = \left[\left(\frac{\boldsymbol{m}_i \otimes \boldsymbol{m}_i}{\rho_i} + p_i(\rho_i)(\boldsymbol{e}_1^\top, \boldsymbol{e}_2^\top, \dots, \boldsymbol{e}_d^\top)^\top \right) \right]_{i=1}^n \in \mathbb{R}^{nd^2}. \tag{4.8}$$

In the last formula we used the notation

$$[\boldsymbol{u}_i]_{i=1}^n := (\boldsymbol{u}_1^\top, \dots, \boldsymbol{u}_n^\top)^\top \in \mathbb{R}^{nm}, \quad \boldsymbol{u}_i \in \mathbb{R}^m,\ i = 1, \dots, n,$$

which appears frequently in the sequel. Additionally, Theorem A.1 will be used often.

After artificially expanding the system (2.26) to obtain (4.12), we are able to compare the solutions $(\boldsymbol{r}^\varepsilon, \boldsymbol{m}^\varepsilon)$ and $(\bar{\boldsymbol{r}}, \bar{\boldsymbol{m}})$ to (2.24) and (4.12), respectively.

Proposition 4.1: *Let Assumption 3.1 hold, let the pressure p_i satisfy* (4.17)*, and let the initial functions $(\boldsymbol{r}_0^\varepsilon, \boldsymbol{m}_0^\varepsilon) \in L^\infty(\mathbb{R}^d)$ and $\bar{\boldsymbol{r}}_0 \in C^3(\mathbb{R}^d)$ satisfy* (4.1)–(4.2)*.*
Consider for $\varepsilon > 0$ an entropy solution $(\boldsymbol{r}^\varepsilon, \boldsymbol{m}^\varepsilon) \in L^\infty(\mathbb{R}^d \times (0, T))$ to (2.24), (2.25) *and a smooth solution $(\bar{\boldsymbol{r}}, \bar{\boldsymbol{m}}) \in C^{3,1}(\mathbb{R}^d \times [0, T)) \times C^{2,1}(\mathbb{R}^d \times [0, T))$ to* (2.26)–(2.27)*, supposed to take values in a convex, compact set $\mathcal{G} \subset G$.*
Then, with $\psi \in C_0^\infty(\mathbb{R}^d \times [0, T), (0, \infty))$ we have the estimate

$$\begin{aligned}&\int_0^T \int_{\mathbb{R}^d} \eta(\boldsymbol{r}^\varepsilon, \boldsymbol{m}^\varepsilon|\bar{\boldsymbol{r}}, \bar{\boldsymbol{m}})\partial_t\psi + \frac{1}{\varepsilon}\boldsymbol{q}(\boldsymbol{r}^\varepsilon, \boldsymbol{m}^\varepsilon|\bar{\boldsymbol{r}}, \bar{\boldsymbol{m}}) \cdot \nabla\psi \ \mathrm{d}\boldsymbol{x}\ \mathrm{d}t \\ &\quad \geq -\int_{\mathbb{R}^d} \eta(\boldsymbol{r}_0^\varepsilon, \boldsymbol{m}_0^\varepsilon|\bar{\boldsymbol{r}}_0, \bar{\boldsymbol{m}}(\cdot, 0))\psi(\cdot, 0) \ \mathrm{d}\boldsymbol{x} \\ &\qquad + \int_0^T \int_{\mathbb{R}^d} \left(\frac{1}{\varepsilon^2} R_\varepsilon(\boldsymbol{r}^\varepsilon, \boldsymbol{m}^\varepsilon, \bar{\boldsymbol{r}}, \bar{\boldsymbol{m}}) + Q_\varepsilon + E_\varepsilon \right)\psi \ \mathrm{d}\boldsymbol{x}\ \mathrm{d}t, \end{aligned} \tag{4.9}$$

with

$$
\begin{aligned}
R_\varepsilon(\boldsymbol{r}^\varepsilon, \boldsymbol{m}^\varepsilon, \bar{\boldsymbol{r}}, \bar{\boldsymbol{m}}) &= R_{1,\varepsilon}(\boldsymbol{r}^\varepsilon, \boldsymbol{m}^\varepsilon, \bar{\boldsymbol{r}}, \bar{\boldsymbol{m}}) + R_{2,\varepsilon}(\boldsymbol{r}^\varepsilon, \boldsymbol{m}^\varepsilon, \bar{\boldsymbol{r}}, \bar{\boldsymbol{m}}),\\
R_{1,\varepsilon}(\boldsymbol{r}^\varepsilon, \boldsymbol{m}^\varepsilon, \bar{\boldsymbol{r}}, \bar{\boldsymbol{m}}) &= \sum_{i=1}^{n} M_i \rho_i^\varepsilon \left| \frac{\boldsymbol{m}_i^\varepsilon}{\rho_i^\varepsilon} - \frac{\bar{\boldsymbol{m}}_i}{\bar{\rho}_i} \right|^2,\\
R_{2,\varepsilon}(\boldsymbol{r}^\varepsilon, \boldsymbol{m}^\varepsilon, \bar{\boldsymbol{r}}, \bar{\boldsymbol{m}}) &= \frac{1}{2} \sum_{i,j=1}^{n} \lambda_{ij} \Bigg[\rho_i^\varepsilon \rho_j^\varepsilon \left| \left(\frac{\boldsymbol{m}_i^\varepsilon}{\rho_i^\varepsilon} - \frac{\boldsymbol{m}_j^\varepsilon}{\rho_j^\varepsilon} \right) - \left(\frac{\bar{\boldsymbol{m}}_i}{\bar{\rho}_i} - \frac{\bar{\boldsymbol{m}}_j}{\bar{\rho}_j} \right) \right|^2 \\
&\qquad + \rho_i^\varepsilon \left(\frac{\bar{\boldsymbol{m}}_i}{\bar{\rho}_i} - \frac{\bar{\boldsymbol{m}}_j}{\bar{\rho}_j} \right) \cdot \left(\frac{\boldsymbol{m}_i^\varepsilon}{\rho_i^\varepsilon} - \frac{\bar{\boldsymbol{m}}_i}{\bar{\rho}_i} \right) (\rho_j^\varepsilon - \bar{\rho}_j) \\
&\qquad - \rho_j^\varepsilon \left(\frac{\bar{\boldsymbol{m}}_i}{\bar{\rho}_i} - \frac{\bar{\boldsymbol{m}}_j}{\bar{\rho}_j} \right) \cdot \left(\frac{\boldsymbol{m}_j^\varepsilon}{\rho_j^\varepsilon} - \frac{\bar{\boldsymbol{m}}_j}{\bar{\rho}_j} \right) (\rho_i^\varepsilon - \bar{\rho}_i) \Bigg], \qquad (4.10)\\
Q_\varepsilon(\boldsymbol{r}^\varepsilon, \boldsymbol{m}^\varepsilon, \bar{\boldsymbol{r}}, \bar{\boldsymbol{m}}) &= \frac{1}{\varepsilon} (\mathrm{D}^2\, \eta(\bar{\boldsymbol{r}}, \bar{\boldsymbol{m}}) \otimes \boldsymbol{I}_d) \nabla \begin{pmatrix} \bar{\boldsymbol{r}} \\ \bar{\boldsymbol{m}} \end{pmatrix} \cdot \begin{pmatrix} \boldsymbol{0} \\ F(\boldsymbol{r}^\varepsilon, \boldsymbol{m}^\varepsilon | \bar{\boldsymbol{r}}, \bar{\boldsymbol{m}}) \end{pmatrix},\\
E_\varepsilon(\boldsymbol{r}^\varepsilon, \boldsymbol{m}^\varepsilon, \bar{\boldsymbol{r}}, \bar{\boldsymbol{m}}) &= \bar{\boldsymbol{e}}_\varepsilon \cdot \left[\frac{\rho_i^\varepsilon}{\bar{\rho}_i} \left(\frac{\boldsymbol{m}_i^\varepsilon}{\rho_i^\varepsilon} - \frac{\bar{\boldsymbol{m}}_i}{\bar{\rho}_i} \right) \right]_{i=1}^{n},\\
\bar{\boldsymbol{e}}_\varepsilon = \bar{\boldsymbol{e}}_\varepsilon(\bar{\boldsymbol{r}}, \bar{\boldsymbol{m}}) &= \frac{1}{\varepsilon} \left[\operatorname{div} \left(\frac{\bar{\boldsymbol{m}}_i \otimes \bar{\boldsymbol{m}}_i}{\bar{\rho}_i} \right) \right]_{i=1}^{n} - \varepsilon \partial_t (\mathcal{B}(\bar{\boldsymbol{r}})^{-1} \nabla \boldsymbol{p}(\bar{\boldsymbol{r}})).
\end{aligned}
$$

Before we present the proof of Proposition 4.1, we summarize two remarks on the scaling of the remainder terms Q_ε and E_ε with respect to ε. These remarks are needed in Section 4.2.

Remark 4.2: *1. The first factor of Q_ε depends only on $(\bar{\boldsymbol{r}}, \bar{\boldsymbol{m}})$. Although $\bar{\boldsymbol{m}}$ involves ε, the factor is independent of ε, i.e.,*

$$
\begin{aligned}
&\frac{1}{\varepsilon} \left((\mathrm{D}^2_{\boldsymbol{r},\boldsymbol{m}}\, \eta(\bar{\boldsymbol{r}}, \bar{\boldsymbol{m}}) \otimes \boldsymbol{I}_d) \nabla \bar{\boldsymbol{r}} + (\mathrm{D}^2_{\boldsymbol{m},\boldsymbol{m}}\, \eta(\bar{\boldsymbol{r}}, \bar{\boldsymbol{m}}) \otimes \boldsymbol{I}_d) \nabla \bar{\boldsymbol{m}} \right)\\
&\qquad = \frac{1}{\varepsilon} \left[\nabla \left(\frac{\bar{\boldsymbol{m}}_i}{\bar{\rho}_i} \right) \right]_{i=1}^{n} = -\nabla \left(\operatorname{diag} \left(\frac{1}{\bar{\rho}_i \otimes 1_d} \right) \mathcal{B}(\bar{\boldsymbol{r}})^{-1} \nabla \boldsymbol{p}(\bar{\boldsymbol{r}}) \right) = O(1).
\end{aligned}
$$

2. Recalling the definition of $\mathcal{B}$ from (2.28)*, the smoothness of $\bar{\boldsymbol{r}}$ and $\boldsymbol{p}$ implies*

$$
\begin{aligned}
\bar{\boldsymbol{e}}_\varepsilon &= \frac{1}{\varepsilon} \left[\operatorname{div} \left(\frac{\bar{\boldsymbol{m}}_i \otimes \bar{\boldsymbol{m}}_i}{\bar{\rho}_i} \right) \right]_{i=1}^{n} - \varepsilon \partial_t (\mathcal{B}(\bar{\boldsymbol{r}})^{-1} \nabla \boldsymbol{p}(\bar{\boldsymbol{r}}))\\
&= \frac{1}{\varepsilon} \left[\operatorname{div} \left(\operatorname{diag} \left(\frac{1}{\bar{\rho}_i \otimes 1_d} \right) [\bar{\boldsymbol{m}}_i \otimes \bar{\boldsymbol{m}}_i]_{i=1}^{n} \right) \right] - \varepsilon \partial_t (\mathcal{B}(\bar{\boldsymbol{r}})^{-1} \nabla \boldsymbol{p}(\bar{\boldsymbol{r}}))
\end{aligned}
$$

$$
\begin{aligned}
&= \varepsilon \left[\operatorname{div} \left(\operatorname{diag} \left(\frac{1}{\bar{\rho}_i \otimes 1_d} \right) \left[\tilde{\mathcal{B}}(\bar{\boldsymbol{r}})^{-1} \nabla p_i(\bar{\rho}_i) \left(\tilde{\mathcal{B}}(\bar{\boldsymbol{r}})^{-1} \nabla p_i(\bar{\rho}_i) \right)^{\top} \right]_{i=1}^{n} \right) \right] \\
&\quad - \varepsilon \partial_t (\mathcal{B}(\bar{\boldsymbol{r}})^{-1} \nabla \boldsymbol{p}(\bar{\boldsymbol{r}})) \\
&= O(\varepsilon). \qquad (4.11)
\end{aligned}
$$

Hence the vector $\bar{\boldsymbol{e}}_\varepsilon = O(\varepsilon)$ in E_ε is of order $O(\varepsilon)$.

Proof of Proposition 4.1. To simplify the notation we may omit the index ε and write $(\boldsymbol{r}, \boldsymbol{m}) = (\boldsymbol{r}^\varepsilon, \boldsymbol{m}^\varepsilon)$. The entropy solution $(\boldsymbol{r}, \boldsymbol{m})$ to the IVP for (2.24) satisfies the inequality (4.3).
In order to derive a similar expression for the solution $\bar{\boldsymbol{r}}$ of the IVP for (2.26), we further rewrite the equivalent system (4.4) for $(\bar{\boldsymbol{r}}, \bar{\boldsymbol{m}})$.
With $\lambda_{ii} r_i = -\sum_{i \neq j} \lambda_{ij} r_j$, (2.15), and (2.17b), it is easy to see that the solution $(\bar{\boldsymbol{r}}, \bar{\boldsymbol{m}})$ of (4.4) also satisfies

$$
\begin{aligned}
\partial_t \bar{\boldsymbol{r}} + \frac{1}{\varepsilon} \operatorname{div}(\bar{\boldsymbol{m}}) &= 0, \\
\partial_t \bar{\boldsymbol{m}} + \frac{1}{\varepsilon} \operatorname{div}(F(\bar{\boldsymbol{r}}, \bar{\boldsymbol{m}})) &= \left[-\frac{1}{\varepsilon^2} M_i \bar{\boldsymbol{m}}_i - \frac{1}{\varepsilon^2} \sum_{j=1}^{n} \lambda_{ij} (\bar{\rho}_j \bar{\boldsymbol{m}}_i - \bar{\rho}_i \bar{\boldsymbol{m}}_j) \right]_{i=1}^{n} + \bar{\boldsymbol{e}}_\varepsilon(\bar{\boldsymbol{r}}, \bar{\boldsymbol{m}}),
\end{aligned} \qquad (4.12)
$$

with $\bar{\boldsymbol{e}}_\varepsilon$ from (4.10) and F from (4.8).
With (4.12) and (3.4) we see that $(\bar{\boldsymbol{r}}, \bar{\boldsymbol{m}})$ satisfies in the sense of distributions

$$
\begin{aligned}
\partial_t \eta(\bar{\boldsymbol{r}}, \bar{\boldsymbol{m}}) + \frac{1}{\varepsilon} \operatorname{div} \boldsymbol{q}(\bar{\boldsymbol{r}}, \bar{\boldsymbol{m}}) = &- \frac{1}{\varepsilon^2} \left(\sum_{i=1}^{n} M_i \frac{|\bar{\boldsymbol{m}}_i|^2}{\bar{\rho}_i} + \frac{1}{2} \sum_{i,j=1}^{n} \lambda_{ij} \bar{\rho}_i \bar{\rho}_j \left| \frac{\bar{\boldsymbol{m}}_i}{\bar{\rho}_i} - \frac{\bar{\boldsymbol{m}}_j}{\bar{\rho}_j} \right|^2 \right) \\
&+ \mathrm{D}_{\boldsymbol{m}} \eta(\bar{\boldsymbol{r}}, \bar{\boldsymbol{m}}) \cdot \bar{\boldsymbol{e}}_\varepsilon. \qquad (4.13)
\end{aligned}
$$

Before we use the entropy relations (4.3) and (4.13), we return to the weak formulations: We subtract the weak formulations of (4.12) from the weak formulation for (2.24) and obtain for the mass balance equations

$$
\begin{aligned}
&- \int_0^T \int_{\mathbb{R}^d} \partial_t \boldsymbol{\phi} \cdot (\boldsymbol{r} - \bar{\boldsymbol{r}}) + \frac{1}{\varepsilon} \nabla \boldsymbol{\phi} \cdot (\boldsymbol{m} - \bar{\boldsymbol{m}}) \, \mathrm{d}\boldsymbol{x} \, \mathrm{d}\tau \\
&\qquad - \int_{\mathbb{R}^d} \boldsymbol{\phi}(\boldsymbol{x}, 0) \cdot (\boldsymbol{r}_0 - \bar{\boldsymbol{r}}_0) \, \mathrm{d}\boldsymbol{x} = 0. \qquad (4.14)
\end{aligned}
$$

Using the definition of $\bar{\boldsymbol{e}}_\varepsilon$ in (4.10) yields for the momentum components

$$
- \int_0^T \int_{\mathbb{R}^d} \partial_t \boldsymbol{\theta} \cdot (\boldsymbol{m} - \bar{\boldsymbol{m}}) + \frac{1}{\varepsilon} \nabla \boldsymbol{\theta} \cdot (F(\boldsymbol{r}, \boldsymbol{m}) - F(\bar{\boldsymbol{r}}, \bar{\boldsymbol{m}})) \, \mathrm{d}\boldsymbol{x} \, \mathrm{d}\tau
$$

$$
\begin{aligned}
&-\int_{\mathbb{R}^d} \boldsymbol{\theta}(\boldsymbol{x},0)\cdot(\boldsymbol{m}_0-\bar{\boldsymbol{m}}(\cdot,0))\ \mathrm{d}\boldsymbol{x}\\
&=\int_0^T\int_{\mathbb{R}^d}\boldsymbol{\theta}\cdot\Bigg(-\frac{1}{\varepsilon^2}\Big[M_i(\boldsymbol{m}_i-\bar{\boldsymbol{m}}_i)\Big]_{i=1}^n\\
&\qquad\qquad+\Big[\sum_{j=1}^n\lambda_{ij}(\rho_j\boldsymbol{m}_i-\rho_i\boldsymbol{m}_j+\bar{\rho}_j\bar{\boldsymbol{m}}_i-\bar{\rho}_i\bar{\boldsymbol{m}}_j)\Big]_{i=1}^n-\bar{\boldsymbol{e}}_\varepsilon\Bigg)\ \mathrm{d}\boldsymbol{x}\ \mathrm{d}\tau. \quad (4.15)
\end{aligned}
$$

Here, $\boldsymbol{\phi}$ and $\boldsymbol{\theta}$ are vector-valued test functions with compact support in $\mathbb{R}^d\times[0,T)$. With some function $\psi\in C_0^\infty(\mathbb{R}^d\times[0,T),(0,\infty))$ we make the specific choices

$$
\begin{aligned}
\boldsymbol{\phi}(\boldsymbol{x},\tau)&=\psi(\boldsymbol{x},\tau)\,\mathrm{D}_{\boldsymbol{r}}\,\eta(\bar{\boldsymbol{r}}(\boldsymbol{x},\tau),\bar{\boldsymbol{m}}(\boldsymbol{x},\tau)),\\
\boldsymbol{\theta}(\boldsymbol{x},\tau)&=\psi(\boldsymbol{x},\tau)\,\mathrm{D}_{\boldsymbol{m}}\,\eta(\bar{\boldsymbol{r}}(\boldsymbol{x},\tau),\bar{\boldsymbol{m}}(\boldsymbol{x},\tau)),
\end{aligned}
$$

which lead in (4.14) and (4.15) to

$$
\begin{aligned}
&\int_0^T\int_{\mathbb{R}^d}\big(\mathrm{D}_{\boldsymbol{r}}\,\eta(\bar{\boldsymbol{r}},\bar{\boldsymbol{m}})\cdot(\boldsymbol{r}-\bar{\boldsymbol{r}})+\mathrm{D}_{\boldsymbol{m}}\,\eta(\bar{\boldsymbol{r}},\bar{\boldsymbol{m}})\cdot(\boldsymbol{m}-\bar{\boldsymbol{m}})\big)\,\psi_t\ \mathrm{d}\boldsymbol{x}\ \mathrm{d}t\\
&\quad+\int_0^T\int_{\mathbb{R}^d}\frac{1}{\varepsilon^2}\Big((\mathrm{D}_{\boldsymbol{r}}\,\eta(\bar{\boldsymbol{r}},\bar{\boldsymbol{m}})\otimes\nabla\psi)\cdot(\boldsymbol{m}-\bar{\boldsymbol{m}})\\
&\qquad\qquad+(\mathrm{D}_{\boldsymbol{m}}\,\eta(\bar{\boldsymbol{r}},\bar{\boldsymbol{m}})\otimes\nabla\psi)\cdot(F(\boldsymbol{r},\boldsymbol{m})-F(\bar{\boldsymbol{r}},\bar{\boldsymbol{m}}))\Big)\ \mathrm{d}\boldsymbol{x}\ \mathrm{d}t\\
&=-\int_{\mathbb{R}^d}\Big(\mathrm{D}_{\boldsymbol{r}}\,\eta(\bar{\boldsymbol{r}}_0,\bar{\boldsymbol{m}}_0)\cdot(\boldsymbol{r}_0-\bar{\boldsymbol{r}}_0)\\
&\qquad\qquad+\mathrm{D}_{\boldsymbol{m}}\,\eta(\bar{\boldsymbol{r}}_0,\bar{\boldsymbol{m}}(\cdot,0))\cdot(\boldsymbol{m}_0-\bar{\boldsymbol{m}}(\cdot,0))\Big)\psi(\cdot,0)\ \mathrm{d}\boldsymbol{x}\\
&\quad-\int_0^T\int_{\mathbb{R}^d}J_\varepsilon\psi\ \mathrm{d}\boldsymbol{x}\ \mathrm{d}t. \qquad (4.16)
\end{aligned}
$$

The term J_ε in (4.16) is defined as

$$
\begin{aligned}
J_\varepsilon&:=\mathrm{D}_{\boldsymbol{m}}\,\eta(\bar{\boldsymbol{r}},\bar{\boldsymbol{m}})\\
&\quad\cdot\left(-\frac{1}{\varepsilon^2}\left[M_i(\boldsymbol{m}_i-\bar{\boldsymbol{m}}_i)+\sum_{j=1}^n\lambda_{ij}(\rho_j\boldsymbol{m}_i-\rho_i\boldsymbol{m}_j-\bar{\rho}_j\bar{\boldsymbol{m}}_i+\bar{\rho}_i\bar{\boldsymbol{m}}_j)\right]_{i=1}^n-\bar{\boldsymbol{e}}_\varepsilon\right)\\
&\quad+\partial_t\big[\mathrm{D}_{\boldsymbol{r}}\,\eta(\bar{\boldsymbol{r}},\bar{\boldsymbol{m}})\big]\cdot(\boldsymbol{r}-\bar{\boldsymbol{r}})+\partial_t\big[\mathrm{D}_{\boldsymbol{m}}\,\eta(\bar{\boldsymbol{r}},\bar{\boldsymbol{m}})\big]\cdot(\boldsymbol{m}-\bar{\boldsymbol{m}})\\
&\quad+\frac{1}{\varepsilon}\nabla(\mathrm{D}_{\boldsymbol{r}}\,\eta(\boldsymbol{r},\boldsymbol{m}))\cdot(\boldsymbol{m}-\bar{\boldsymbol{m}})+\frac{1}{\varepsilon}\nabla(\mathrm{D}_{\boldsymbol{m}}\,\eta(\bar{\boldsymbol{r}},\bar{\boldsymbol{m}}))\cdot(F(\boldsymbol{r},\boldsymbol{m})-F(\bar{\boldsymbol{r}},\bar{\boldsymbol{m}})).
\end{aligned}
$$

Combining the entropy inequality (4.3) for $(\boldsymbol{r}^\varepsilon, \boldsymbol{m}^\varepsilon)$, the entropy equation (4.13) for $(\bar{\boldsymbol{r}}, \bar{\boldsymbol{m}})$, and the relation (4.16), the definition of the relative entropy–entropy flux pair in (4.6)–(4.7) implies that the following inequality holds in the weak sense:

$$\begin{aligned}
&\partial_t \eta(\boldsymbol{r}, \boldsymbol{m}|\bar{\boldsymbol{r}}, \bar{\boldsymbol{m}}) + \frac{1}{\varepsilon} \operatorname{div} \boldsymbol{q}(\boldsymbol{r}, \boldsymbol{m}|\bar{\boldsymbol{r}}, \bar{\boldsymbol{m}}) \\
&\quad \leq -\frac{1}{\varepsilon^2} \left(\mathrm{D}_{\boldsymbol{m}} \eta(\boldsymbol{r}, \boldsymbol{m}) \cdot \left[M_i \boldsymbol{m}_i + \sum_{j=1}^n \lambda_{ij} (\rho_j \boldsymbol{m}_i - \rho_i \boldsymbol{m}_j) \right]_{i=1}^n \right) \\
&\qquad + \frac{1}{\varepsilon^2} \left(\mathrm{D}_{\boldsymbol{m}} \eta(\bar{\boldsymbol{r}}, \bar{\boldsymbol{m}}) \cdot \left[M_i \bar{\boldsymbol{m}}_i + \sum_{j=1}^n \lambda_{ij} (\bar{\rho}_j \bar{\boldsymbol{m}}_i - \bar{\rho}_i \bar{\boldsymbol{m}}_j) \right]_{i=1}^n \right) \\
&\qquad - \mathrm{D}_{\boldsymbol{m}} \eta(\bar{\boldsymbol{r}}, \bar{\boldsymbol{m}}) \cdot \bar{\boldsymbol{e}}_\varepsilon - J_\varepsilon.
\end{aligned}$$

In the term J_ε we use (4.13) and Theorem A.1 to compute the time derivative of $\nabla_{\boldsymbol{m}} \eta(\bar{\boldsymbol{r}}, \bar{\boldsymbol{m}})$ by the chain rule. This leads to

$$\begin{aligned}
J_\varepsilon &= -\frac{1}{\varepsilon^2} \mathrm{D}_{\boldsymbol{m}} \eta(\bar{\boldsymbol{r}}, \bar{\boldsymbol{m}}) \cdot \left[M_i (\boldsymbol{m}_i - \bar{\boldsymbol{m}}_i) + \sum_{j=1}^n \lambda_{ij} (\rho_j \boldsymbol{m}_i - \rho_i \boldsymbol{m}_j - \bar{\rho}_j \bar{\boldsymbol{m}}_i + \bar{\rho}_i \bar{\boldsymbol{m}}_j) \right]_{i=1}^n \\
&\quad - \mathrm{D}_{\boldsymbol{m}} \eta(\bar{\boldsymbol{r}}, \bar{\boldsymbol{m}}) \cdot \bar{\boldsymbol{e}}_\varepsilon \\
&\quad + \mathrm{D}^2 \eta(\bar{\boldsymbol{r}}, \bar{\boldsymbol{m}}) \partial_t \begin{pmatrix} \bar{\boldsymbol{r}} \\ \bar{\boldsymbol{m}} \end{pmatrix} \cdot \begin{pmatrix} \boldsymbol{r} - \bar{\boldsymbol{r}} \\ \boldsymbol{m} - \bar{\boldsymbol{m}} \end{pmatrix} \\
&\quad + \frac{1}{\varepsilon} (\mathrm{D}^2 \eta(\bar{\boldsymbol{r}}, \bar{\boldsymbol{m}}) \otimes \boldsymbol{I}_d) \nabla \begin{pmatrix} \bar{\boldsymbol{r}} \\ \bar{\boldsymbol{m}} \end{pmatrix} \cdot \begin{pmatrix} \boldsymbol{m} - \bar{\boldsymbol{m}} \\ F(\boldsymbol{r}, \boldsymbol{m}) - F(\bar{\boldsymbol{r}}, \bar{\boldsymbol{m}}) \end{pmatrix} \\
&= -\frac{1}{\varepsilon^2} \mathrm{D}_{\boldsymbol{m}} \eta(\bar{\boldsymbol{r}}, \bar{\boldsymbol{m}}) \cdot \left[M_i (\boldsymbol{m}_i - \bar{\boldsymbol{m}}_i) + \sum_{j=1}^n \lambda_{ij} (\rho_j \boldsymbol{m}_i - \rho_i \boldsymbol{m}_j - \bar{\rho}_j \bar{\boldsymbol{m}}_i + \bar{\rho}_i \bar{\boldsymbol{m}}_j) \right]_{i=1}^n \\
&\quad - \mathrm{D}_{\boldsymbol{m}} \eta(\bar{\boldsymbol{r}}, \bar{\boldsymbol{m}}) \cdot \bar{\boldsymbol{e}}_\varepsilon \\
&\quad + \mathrm{D}^2 \eta(\bar{\boldsymbol{r}}, \bar{\boldsymbol{m}}) \begin{pmatrix} \boldsymbol{0} \\ \left[-\frac{1}{\varepsilon^2} M_i \bar{\boldsymbol{m}}_i - \frac{1}{\varepsilon^2} \sum_{j=1}^n \lambda_{ij} (\bar{\rho}_j \bar{\boldsymbol{m}}_i - \bar{\rho}_i \bar{\boldsymbol{m}}_j) \right]_{i=1}^n + \bar{\boldsymbol{e}}_\varepsilon \end{pmatrix} \cdot \begin{pmatrix} \boldsymbol{r} - \bar{\boldsymbol{r}} \\ \boldsymbol{m} - \bar{\boldsymbol{m}} \end{pmatrix} \\
&\quad + \frac{1}{\varepsilon} (\mathrm{D}^2 \eta(\bar{\boldsymbol{r}}, \bar{\boldsymbol{m}}) \otimes \boldsymbol{I}_d) \nabla \begin{pmatrix} \bar{\boldsymbol{r}} \\ \bar{\boldsymbol{m}} \end{pmatrix} \cdot \begin{pmatrix} \boldsymbol{0} \\ F(\boldsymbol{r}, \boldsymbol{m}|\bar{\boldsymbol{r}}, \bar{\boldsymbol{m}}) \end{pmatrix}.
\end{aligned}$$

Finally, we proceed with this expression for J_ϵ and deduce

$$
\begin{aligned}
&\partial_t \eta(\boldsymbol{r}, \boldsymbol{m}|\bar{\boldsymbol{r}}, \bar{\boldsymbol{m}}) + \frac{1}{\varepsilon} \operatorname{div} \boldsymbol{q}(\boldsymbol{r}, \boldsymbol{m}|\bar{\boldsymbol{r}}, \bar{\boldsymbol{m}}) \\
&\quad = -\frac{1}{\varepsilon^2} \left(\mathrm{D}_{\boldsymbol{m}} \eta(\boldsymbol{r}, \boldsymbol{m}) \cdot \left[M_i \boldsymbol{m}_i + \sum_{j=1}^n \lambda_{ij} (\rho_j \boldsymbol{m}_i - \rho_i \boldsymbol{m}_j) \right]_{i=1}^n \right) \\
&\qquad + \frac{1}{\varepsilon^2} \left(\mathrm{D}_{\boldsymbol{m}} \eta(\bar{\boldsymbol{r}}, \bar{\boldsymbol{m}}) \cdot \left[M_i \bar{\boldsymbol{m}}_i + \sum_{j=1}^n \lambda_{ij} (\bar{\rho}_j \bar{\boldsymbol{m}}_i - \bar{\rho}_i \bar{\boldsymbol{m}}_j) \right]_{i=1}^n \right) \\
&\qquad + \frac{1}{\varepsilon^2} \mathrm{D}_{\boldsymbol{m}} \eta(\bar{\boldsymbol{r}}, \bar{\boldsymbol{m}}) \cdot \left[M_i (\boldsymbol{m}_i - \bar{\boldsymbol{m}}_i) + \sum_{j=1}^n \lambda_{ij} (\rho_j \boldsymbol{m}_i - \rho_i \boldsymbol{m}_j + \bar{\rho}_i \bar{\boldsymbol{m}}_j - \bar{\rho}_j \bar{\boldsymbol{m}}_i) \right]_{i=1}^n \\
&\qquad - \mathrm{D}^2 \eta(\bar{\boldsymbol{r}}, \bar{\boldsymbol{m}}) \begin{pmatrix} \boldsymbol{0} \\ -\frac{1}{\varepsilon^2} \left[M_i \bar{\boldsymbol{m}}_i + \sum_{j=1}^n \lambda_{ij} (\bar{\rho}_j \bar{\boldsymbol{m}}_i - \bar{\rho}_i \bar{\boldsymbol{m}}_j) \right]_{i=1}^n \end{pmatrix} \cdot \begin{pmatrix} \boldsymbol{r} - \bar{\boldsymbol{r}} \\ \boldsymbol{m} - \bar{\boldsymbol{m}} \end{pmatrix} \\
&\qquad - \mathrm{D}^2 \eta(\bar{\boldsymbol{r}}, \bar{\boldsymbol{m}}) \begin{pmatrix} \boldsymbol{0} \\ \bar{\boldsymbol{e}} \end{pmatrix} \cdot \begin{pmatrix} \boldsymbol{r} - \bar{\boldsymbol{r}} \\ \boldsymbol{m} - \bar{\boldsymbol{m}} \end{pmatrix} - \frac{1}{\varepsilon} (\mathrm{D}^2 \eta(\bar{\boldsymbol{r}}, \bar{\boldsymbol{m}}) \otimes \boldsymbol{I}_d) \nabla \begin{pmatrix} \bar{\boldsymbol{r}} \\ \bar{\boldsymbol{m}} \end{pmatrix} \cdot \begin{pmatrix} \boldsymbol{0} \\ F(\boldsymbol{r}, \boldsymbol{m}|\bar{\boldsymbol{r}}, \bar{\boldsymbol{m}}) \end{pmatrix} \\
&\quad = -\frac{1}{\varepsilon^2} R_\varepsilon - Q_\varepsilon - E_\varepsilon.
\end{aligned}
$$

The last line follows from the definitions in (4.10) and concludes the proof. ■

4.2 The Convergence Estimate

In this section we make an additional assumption on the pressure.
Let there exist constants $a_i > 0$, $i = 1, \dots, n$ such that

$$
p_i''(r) \le a_i \frac{p_i'(r)}{r} \quad \text{for all } r > 0, \text{ and } i = 1, \dots, n. \tag{4.17}
$$

The condition (4.17) is satisfied for instance for the isentropic pressure laws $p_i(r) = k_i r^{\gamma_i}$ ($\gamma_i \ge 1$, $k_i > 0$) with $a_i \ge \gamma_i - 1$, if $\gamma_i > 1$ and any $a_i > 0$, if $\gamma_i = 1$.
Due to (4.17) we have

$$
\frac{1}{a_i} p_i''(r) \le h_i''(r) = \frac{p_i'(r)}{r}. \tag{4.18}
$$

Note that

$$
p_i(\rho_i|\bar{\rho}_i) = p_i(\rho_i) - p_i(\bar{\rho}_i) - p_i'(\bar{\rho}_i)(\rho_i - \bar{\rho}_i)
$$

$$= (\rho_i - \bar{\rho}_i)^2 \int_0^1 \int_0^\tau p''(s\rho_i + (1-s)\bar{\rho}_i)\ \mathrm{d}s\ \mathrm{d}\tau.$$

Hence, with

$$|F(\boldsymbol{r}^\varepsilon, \boldsymbol{m}^\varepsilon|\bar{\boldsymbol{r}}, \bar{\boldsymbol{m}})| = \eta(\boldsymbol{r}^\varepsilon, \boldsymbol{m}^\varepsilon|\bar{\boldsymbol{r}}, \bar{\boldsymbol{m}}) + \sum_{i=1}^n p_i(\rho_i|\bar{\rho}_i) - h_i(\rho_i|\bar{\rho}_i),$$

the inequality (4.18) implies with some $c > 0$

$$|F(\boldsymbol{r}^\varepsilon, \boldsymbol{m}^\varepsilon|\bar{\boldsymbol{r}}, \bar{\boldsymbol{m}})| \le c\eta(\boldsymbol{r}^\varepsilon, \boldsymbol{m}^\varepsilon|\bar{\boldsymbol{r}}, \bar{\boldsymbol{m}}). \tag{4.19}$$

Here, $F(\boldsymbol{r}, \boldsymbol{m}|\bar{\boldsymbol{r}}, \bar{\boldsymbol{m}}) = F(\boldsymbol{r}, \boldsymbol{m}) - F(\bar{\boldsymbol{r}}, \bar{\boldsymbol{m}}) - \mathrm{D}\,F(\bar{\boldsymbol{r}}, \bar{\boldsymbol{m}})(\boldsymbol{r} - \bar{\boldsymbol{r}}, \boldsymbol{m} - \bar{\boldsymbol{m}})$.
We need to introduce a slightly different entropy–entropy flux pair to obtain a convergence estimate that corresponds to convergence in standard Lebesgue spaces. Subtracting the constant $\eta(\hat{\boldsymbol{r}}, \boldsymbol{0}) = \sum_{i=1}^n h_i(\hat{\rho}_i)$ from the entropy η, we obtain a modified entropy–entropy flux pair $(\tilde{\eta}, \tilde{\boldsymbol{q}})$ with the property $\tilde{\eta}(\hat{\boldsymbol{r}}, 0) = 0$ by setting

$$\tilde{\eta}(\boldsymbol{r}, \boldsymbol{m}) = \eta(\boldsymbol{r}, \boldsymbol{m}) - \eta(\hat{\boldsymbol{r}}, \boldsymbol{0}), \quad \tilde{\boldsymbol{q}}(\boldsymbol{r}, \boldsymbol{m}) = \boldsymbol{q}(\boldsymbol{r}, \boldsymbol{m}).$$

Since (2.24) is a hyperbolic balance law, due to (4.1) and the uniform bound in $\mathcal{G}$, the functions $(\boldsymbol{r}^\varepsilon - \hat{\boldsymbol{r}}, \boldsymbol{m}^\varepsilon)$ have uniform compact support. Again, the uniform boundedness implies that there are constants $K_1, K_2 > 0$ such that for any $\varepsilon > 0$ the entropy solution $(\boldsymbol{r}^\varepsilon, \boldsymbol{m}^\varepsilon)$ to (2.24)–(2.25) satisfies

$$\begin{aligned} \max_{i=1,\dots,n} \sup_{t\in[0,T]} \left\{ \int_{\mathbb{R}^d} |\rho_i^\varepsilon(\boldsymbol{x}, t) - \hat{\rho}_i(\boldsymbol{x}, t)|\ \mathrm{d}\boldsymbol{x} \right\} &\le K_1, \\ \sup_{t\in[0,T]} \left\{ \int_{\mathbb{R}^d} \tilde{\eta}(\boldsymbol{r}^\varepsilon(\boldsymbol{x}, t), \boldsymbol{m}^\varepsilon(\boldsymbol{x}, t))\ \mathrm{d}\boldsymbol{x} \right\} &\le K_2. \end{aligned} \tag{4.20}$$

As discussed in the introduction to Chapter 4 we will consider a classical solution $\bar{\boldsymbol{r}}$ to (2.26). Let $(\bar{\boldsymbol{r}}, \bar{\boldsymbol{m}}) \in C^{3,1}(\mathbb{R}^d \times [0, T)) \times C^{2,1}\mathbb{R}^d \times [0, T))$ be a classical solution to (2.26) (respectively the equivalent system (4.4)), (2.27) with initial data satisfying (4.2). Since (2.26) is a regular parabolic system we can assume under corresponding conditions on $\bar{\boldsymbol{r}}_0$,that $(\bar{\boldsymbol{r}}, \bar{\boldsymbol{m}})$ is also contained in $\mathcal{G}$. With the relative entropy $\tilde{\eta}(\boldsymbol{r}^\varepsilon, \boldsymbol{m}^\varepsilon|\bar{\boldsymbol{r}}, \bar{\boldsymbol{m}}) = \eta(\boldsymbol{r}^\varepsilon, \boldsymbol{m}^\varepsilon|\bar{\boldsymbol{r}}, \bar{\boldsymbol{m}}) - \sum_{i=1}^n h_i(\hat{\rho}_i)$, we measure the distance between the solutions $(\boldsymbol{r}^\varepsilon, \boldsymbol{m}^\varepsilon)$ and $(\bar{\boldsymbol{r}}, \bar{\boldsymbol{m}})$ via the expression

$$\varphi_\varepsilon(t) := \int_{\mathbb{R}^d} \tilde{\eta}(\boldsymbol{r}^\varepsilon(\boldsymbol{x}, t), \boldsymbol{m}^\varepsilon(\boldsymbol{x}, t)|\bar{\boldsymbol{r}}(\boldsymbol{x}, t), \bar{\boldsymbol{m}}(\boldsymbol{x}, t))\ \mathrm{d}\boldsymbol{x}. \tag{4.21}$$

Note that the conditions (4.1), (4.2), and (4.5) show that $\varphi_\varepsilon(0)$ is finite. Due to the strict convexity of $\tilde{\eta}$ there are some constants $c, C > 0$ (which depend on $\mathcal{G}$) such that

$$c|(\boldsymbol{s}, \boldsymbol{n}) - (\bar{\boldsymbol{s}}, \bar{\boldsymbol{n}})|^2 \le \tilde{\eta}(\boldsymbol{s}, \boldsymbol{n}|\bar{\boldsymbol{s}}, \bar{\boldsymbol{n}}) \le C|(\boldsymbol{s}, \boldsymbol{n}) - (\bar{\boldsymbol{s}}, \bar{\boldsymbol{n}})|^2, \tag{4.22}$$

holds for all vectors $(\boldsymbol{s}, \boldsymbol{n}), (\bar{\boldsymbol{s}}, \bar{\boldsymbol{n}}) \in \mathcal{G}$. The relation (4.22) relies on a Taylor expansion of $\tilde{\eta}$. The constants c and C depend on the expansion point of this expansion. If $\mathcal{G}$ approaches the boundary of the state space G (2.21), i.e. $\rho_i \longrightarrow 0$ for some $i \in \{1, \dots, n\}$, the constants c , C degenerate in the limit. These constants also depend on the pressure laws $p_i(r)$, $i = 1, \dots, n$. For the example of isentropic pressure laws they depend on the adiabatic exponent γ_i. For typical physical applications with $\gamma_i \in [1, 2]$ the relation (4.22) holds.
As a consequence, since the solutions $(\boldsymbol{r}^\varepsilon, \boldsymbol{m}^\varepsilon)$ and $(\bar{\boldsymbol{r}}, \bar{\boldsymbol{m}})$ take values in $\mathcal{G}$, expression (4.21) is compatible with the L^2-difference of the solutions. We can now state the final theorem.

Theorem 4.3 (Asymptotic behavior for (2.24))**:** *Let Assumption 3.1 hold, let the pressure p_i satisfy* (4.17)*, and let the initial functions $(\boldsymbol{r}_0^\varepsilon, \boldsymbol{m}_0^\varepsilon) \in L^\infty(\mathbb{R}^d)$ and $\bar{\boldsymbol{r}}_0 \in C^3(\mathbb{R}^d)$ satisfy* (4.1), (4.2).
Consider for $\varepsilon > 0$ an entropy solution $(\boldsymbol{r}^\varepsilon, \boldsymbol{m}^\varepsilon) \in L^\infty(\mathbb{R}^d \times (0, T))$ to (2.24), (2.25) *and a smooth solution $(\bar{\boldsymbol{r}}, \bar{\boldsymbol{m}}) \in C^{3,1}(\mathbb{R}^d \times [0, T)) \times C^{2,1}\mathbb{R}^d \times [0, T))$ to* (2.26), (2.27)*, supposed to take values in a convex, compact set $\mathcal{G} \subset G$.*
Then there exist constants $c_i > 0$, $i = 1, \dots, n$ such that for

$$M_i \ge c_i \max_{j=1,\dots,n} \max_{(r_i, r_j) \in \mathcal{G} \times \mathcal{G}} \left\{ |\lambda_{ij}(r_i, r_j)| \right\} \tag{4.23}$$

we have the estimate

$$\varphi_\varepsilon(t) \le K(\varphi_\varepsilon(0) + \varepsilon^4) \qquad (t \in (0, T]). \tag{4.24}$$

Here $K > 0$ is a constant that depends only on T, $\mathcal{G}$, and $\bar{\boldsymbol{r}}$ but not on ε.

Remark 4.4: *1. If the initial data $(\boldsymbol{r}_0^\varepsilon, \boldsymbol{m}_0^\varepsilon)$ converge for $\varepsilon \longrightarrow 0$ to $(\bar{\boldsymbol{r}}_0, \bar{\boldsymbol{m}}(\cdot, 0))$ in $L^2_{\mathrm{loc}}(\mathbb{R}^d)$, the estimate* (4.24) *implies*

$$\|(\boldsymbol{r}^\varepsilon, \boldsymbol{m}^\varepsilon)(\cdot, t) - (\bar{\boldsymbol{r}}, \bar{\boldsymbol{m}})(\cdot, t)\|_{L^2(\mathbb{R}^d)} \longrightarrow 0,$$

due to the compatibility relation (4.22).

2. The condition (4.23) *holds especially for $\lambda_{ij} = 0$, $i, j = 1, \dots, n$ what corresponds exactly to [71]. In gaseous mixtures* (4.23) *is expected to hold, see Remark 2.1.*

Proof (of Theorem 4.3). For the proof we write again $(\boldsymbol{r}, \boldsymbol{m}) = (\boldsymbol{r}^\varepsilon, \boldsymbol{m}^\varepsilon)$.
We consider the relative entropy statement from (4.9) in Proposition 4.1 which holds also for the entropy pair $(\tilde{\eta}, \tilde{\boldsymbol{q}})$. As test function ψ we make the choice $\psi(\boldsymbol{x}, t) = \theta_\kappa(\tau)\omega_R(\boldsymbol{x})$ with θ_κ given for $\kappa > 0$ by

$$\theta_\kappa(\tau) \coloneqq \begin{cases} 1, & 0 \le \tau < t, \\ \frac{t-\tau}{\kappa} + 1, & t \le \tau < t + \kappa, \\ 0, & \tau \ge t + \kappa, \end{cases}$$

and with ω_R given for $R, \delta > 0$ by

$$\omega_R(\boldsymbol{x}) = \begin{cases} 1, & |\boldsymbol{x}| < R, \\ 1 + \frac{R-|\boldsymbol{x}|}{\delta}, & R < |\boldsymbol{x}| < R + \delta, \\ 0, & \text{else.} \end{cases}$$

By taking the limit $R \longrightarrow \infty$, using the asymptotic properties (4.1)–(4.2) of $(\boldsymbol{r}, \boldsymbol{m})$ and $(\bar{\boldsymbol{r}}, \bar{\boldsymbol{m}})$, and finally sending $\kappa \longrightarrow 0$, we obtain using the definition of ϕ_ε from (4.21) the inequality

$$\begin{aligned} \varphi_\varepsilon(t) + \frac{1}{\varepsilon^2} \int_0^t \int_{\mathbb{R}^d} R_\varepsilon(\boldsymbol{r}, \boldsymbol{m}, \bar{\boldsymbol{r}}, \bar{\boldsymbol{m}}) \, \mathrm{d}\boldsymbol{x} \, \mathrm{d}\tau \\ \le \varphi_\varepsilon(0) + \int_0^t \int_{\mathbb{R}^d} \left(|Q_\varepsilon| + |E_\varepsilon| \right) \, \mathrm{d}\boldsymbol{x} \, \mathrm{d}\tau, \end{aligned} \tag{4.25}$$

with $Q_\varepsilon, E_\varepsilon$, and R_ε from (4.10) in Proposition 4.1.
Due to Remark 4.2 and (4.19) it holds

$$\int_0^t \int_{\mathbb{R}^d} |Q_\varepsilon| \, \mathrm{d}\boldsymbol{x} \, \mathrm{d}\tau \le C_1 \int_0^t \varphi_\varepsilon(\tau) \, \mathrm{d}\tau,$$

where $C_1 > 0$ depends on the L^∞-norm of $\nabla \bar{\boldsymbol{r}}$ but not on ε. The error term E_ε can be estimated for any number $C_2 > 0$ with Young's inequality by

$$\begin{aligned} \int_0^t \int_{\mathbb{R}^d} |E_\varepsilon| \, \mathrm{d}\boldsymbol{x} \, \mathrm{d}\tau \le \frac{C_2 \varepsilon^2}{2} \int_0^t \int_{\mathbb{R}^d} \sum_{i=1}^n \left| \frac{\bar{\boldsymbol{e}}_{\varepsilon,i}}{\bar{\rho}_i} \right|^2 \rho_i \, \mathrm{d}\boldsymbol{x} \, \mathrm{d}\tau \\ + \frac{1}{2C_2\varepsilon^2} \int_0^t \int_{\mathbb{R}^d} \sum_{i=1}^n M_i \rho_i \left| \frac{\boldsymbol{m}_i}{\rho_i} - \frac{\bar{\boldsymbol{m}}_i}{\bar{\rho}_i} \right|^2 \mathrm{d}\boldsymbol{x} \, \mathrm{d}\tau. \end{aligned}$$

Additionally, we have from (4.11) with $\bar{\boldsymbol{e}}_\varepsilon = O(\varepsilon)$ (see Remark 4.2) the inequality

$$\begin{aligned}\int_0^t \int_{\mathbb{R}^d} \sum_{i=1}^n \left| \frac{\bar{\boldsymbol{e}}_{\varepsilon,i}}{\bar{\rho}_i} \right|^2 \rho_i \, \mathrm{d}\boldsymbol{x} \, \mathrm{d}\tau \le \sum_{i=1}^n \Bigg(\left\| \frac{\bar{\boldsymbol{e}}_{\varepsilon,i}}{\bar{\rho}_i} \right\|_{L^\infty}^2 \int_0^t \int_{\mathbb{R}^d} \left| \rho_i - \hat{\rho}_i \right| \, \mathrm{d}\boldsymbol{x} \, \mathrm{d}\tau \\ + |\hat{\rho}_i| \int_0^t \int_{\mathbb{R}^d} \left| \frac{\bar{\boldsymbol{e}}_{\varepsilon,i}}{\bar{\rho}_i} \right|^2 \, \mathrm{d}\boldsymbol{x} \, \mathrm{d}\tau \Bigg) \\ \le C_3 \varepsilon^2 t,\end{aligned}$$

where the constant $C_3 > 0$ depends on T, K_1 from (4.20), $\mathcal{G}$, and also on $\bar{\boldsymbol{r}}$ through (4.11).
Plugging these estimates into (4.25) leads to

$$\begin{aligned}\varphi_\varepsilon(t) + \frac{1}{\varepsilon^2} \int_0^t \int_{\mathbb{R}^d} R_\varepsilon(\boldsymbol{r}, \boldsymbol{m}, \bar{\boldsymbol{r}}, \bar{\boldsymbol{m}}) - \frac{1}{2C_2} R_{1,\varepsilon}(\boldsymbol{r}, \boldsymbol{m}, \bar{\boldsymbol{r}}, \bar{\boldsymbol{m}}) \, \mathrm{d}\boldsymbol{x} \, \mathrm{d}\tau \\ \le \varphi_\varepsilon(0) + C_1 \int_0^t \varphi_\varepsilon(\tau) \, \mathrm{d}\tau + C_3 \varepsilon^4 t.\end{aligned}$$

We need the integral on the left hand side of the last estimate to be positive. The integrand reads as

$$R_\varepsilon(\boldsymbol{r}, \boldsymbol{m}, \bar{\boldsymbol{r}}, \bar{\boldsymbol{m}}) - \frac{1}{2C_2} R_{1,\varepsilon}(\boldsymbol{r}, \boldsymbol{m}, \bar{\boldsymbol{r}}, \bar{\boldsymbol{m}}) = \left(1 - \frac{1}{2C_2}\right) R_{1,\varepsilon} + R_{2,\varepsilon}.$$

The term $R_{1,\varepsilon}$ is positive and scales with the mobilities M_i, whereas the term $R_{2,\varepsilon}$ can have arbitrary sign and scales with the diffusion coefficients λ_{ij}.
Hence, if the first term dominates, we can assure positivity of the integral. This follows with (4.10), (4.23), and choosing C_2 sufficiently large. Then, Gronwall's inequality yields a constant $K > 0$ such that

$$\varphi_\varepsilon(t) \le K(\varphi_\varepsilon(0) + \varepsilon^4), \quad t \in (0, T].$$

■

Asymptotic Preserving Numerical Scheme

5

In Chapter 2 we derived the Euler–Darcy–MS model which describes compressible multi-component porous-media flow. This model has the type of a system of hyperbolic balance laws. However, in certain regimes, characterized by a small parameter $\varepsilon > 0$, the solution to this system converges to the solution to a parabolic limit system for $\varepsilon \longrightarrow 0$. This is proven in Chapter 4. In the present chapter we introduce a numerical scheme for simulations of the system in the asymptotic regime. The scheme is designed to be asymptotic preserving. This means that the asymptotic limit of the system is preserved on the discrete level. To be precise, for fixed mesh size Δx and time step width Δt, for $\varepsilon \longrightarrow 0$ the scheme yields a consistent discretization of the limit system. AP schemes go back to [63]. For a review on AP schemes we refer to [64].
The idea of AP schemes is illustrated in Figure 5.1. We consider the hyperbolic

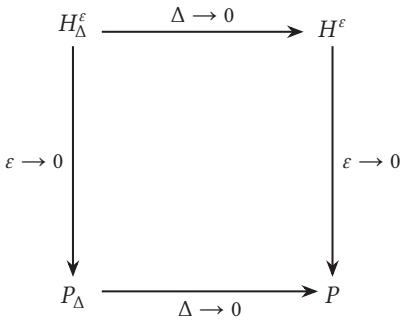

Figure 5.1: Illustration of asymptotic preserving schemes.

model H^ε with the corresponding numerical discretization H^ε_Δ. This discretization is consistent, i.e. for discretization parameter $\Delta \longrightarrow 0$ (mesh size or time step), we recover the model H^ε. The hyperbolic model H^ε tends for $\varepsilon \longrightarrow 0$ to the parabolic

limit system P, which is independent of ε. If a limit discretization P_Δ of H^ε_Δ for $\varepsilon \longrightarrow 0$ with fixed Δ exists and is a consistent discretization of P, we call the scheme H^ε_Δ asymptotic preserving.
We derive an AP scheme for the Euler–Darcy–MS system in Section 5.1. Next, in Section 5.2, we present numerical experiments which illustrate the concept of uphill diffusion. Further, we numerically check the convergence rate (4.24) with respect to ε. To this end we use a discrete version of the relative entropy and compare the numerical solution to the ε system with a reference solution to the parabolic limit system.

5.1 AP Scheme for the Euler–Darcy–MS Model

Consider the system (2.24)–(2.25) in one space dimension, i.e. $d = 1$. This system serves as model H^ϵ, see Figure 5.1.
For $i = 1, \dots, n$ the system reads as:

$$\begin{aligned} &\varepsilon \partial_t \rho_i^\varepsilon + \partial_x m_i^\varepsilon = 0, \\ &\varepsilon \partial_t m_i^\varepsilon + \partial_x \left(\frac{m_i^{\varepsilon 2}}{\rho_i^\varepsilon} + p_i(\rho_i^\varepsilon) \right) \\ &\qquad = -\frac{1}{\varepsilon} M_i m_i^\varepsilon - \frac{1}{\varepsilon} \sum_{j=1}^n \lambda_{ij} (\rho_j^\varepsilon m_i^\varepsilon - \rho_i^\varepsilon m_j^\varepsilon) \end{aligned} \qquad \text{in } \mathbb{R} \times (0, T), \quad (5.1)$$

with initial conditions

$$U^\varepsilon(\cdot, 0) = U_0^\varepsilon := (\boldsymbol{r}_0^{\varepsilon\top}, \boldsymbol{m}_0^{\varepsilon\top})^\top = (\rho_{1,0}^\varepsilon, \dots, \rho_{n,0}^\varepsilon, m_{1,0}^\varepsilon, \dots, m_{n,0}^\varepsilon)^\top \qquad \text{in } \mathbb{R}. \quad (5.2)$$

In this chapter we want Theorem 4.3 to hold. Hence, we make the same assumptions on the data as in the previous chapters, namely Assumption 3.1. Additionally, let the pressure functions p_i satisfy (4.17).
We consider entropy solutions to (5.1)–(5.2). To this end recall the entropy–entropy flux pair (3.4) and entropy inequality (4.3):

$$\partial_t \eta(\boldsymbol{r}^\varepsilon, \boldsymbol{m}^\varepsilon) + \frac{1}{\varepsilon} \partial_x q(\boldsymbol{r}^\varepsilon, \boldsymbol{m}^\varepsilon) + \frac{1}{\varepsilon^2} \left(\sum_{i=1}^n M_i \frac{m_i^{\varepsilon 2}}{\rho_i^\varepsilon} + \frac{1}{2} \sum_{i,j=1}^n \lambda_{ij} \rho_i^\varepsilon \rho_j^\varepsilon \left(\frac{m_i^\varepsilon}{\rho_i^\varepsilon} - \frac{m_j^\varepsilon}{\rho_j^\varepsilon} \right)^2 \right) \leq 0,$$

with

$$\eta(U) = \frac{1}{2} \sum_{i=1}^n \frac{m_i^2}{\rho_i} + \sum_{i=1}^n h_i(\rho_i), \qquad q(U) = \frac{1}{2} \sum_{i=1}^n m_i \frac{m_i^2}{\rho_i^2} + m_i h_i(\rho_i)'.$$

We recap the convergence of solutions to (5.1)–(5.2) to solutions to (2.26)–(2.27) as proven in Chapter 4. In one space dimension the limit system reads

$$\partial_t \bar{\boldsymbol{r}} - \partial_x\big((\mathcal{B}(\bar{\boldsymbol{r}}))^{-1}\partial_x \boldsymbol{p}(\bar{\boldsymbol{r}})\big) = 0 \text{ in } \mathbb{R}\times(0,T), \tag{5.3}$$

with initial conditions

$$\bar{\boldsymbol{r}}(\cdot,0) = \bar{\boldsymbol{r}}_0 \text{ in } \mathbb{R},$$

where

$$\mathcal{B}(\bar{\boldsymbol{r}}) = \operatorname{diag}(M_i) - \operatorname{diag}(\bar{\rho}_i)\Lambda \in \mathbb{R}^{n\times n}. \tag{5.4}$$

This limit system corresponds to model P in Figure 5.1. The relative entropy $\eta(\boldsymbol{r}^\varepsilon, \boldsymbol{m}^\varepsilon|\bar{\boldsymbol{r}}, \bar{\boldsymbol{m}})$ (4.6) served as yardstick to measure the convergence. In Theorem 4.3, we established the convergence estimate (4.24):

$$\varphi_\varepsilon(t) \le K(\varphi_\varepsilon(0) + \varepsilon^4) \qquad (t\in(0,T]),$$

with (4.21)

$$\varphi_\varepsilon(t) = \int_{\mathbb{R}} \eta(\boldsymbol{r}^\varepsilon(x,t), \boldsymbol{m}^\varepsilon(x,t)|\bar{\boldsymbol{r}}(x,t), \bar{\boldsymbol{m}}(x,t))\ \mathrm{d}x. \tag{5.5}$$

Our goal is to verify this analytical result numerically. That means we aim to recover the convergence rate of ε^4 for the approximate solutions U^ε and $\bar{U}$ obtained by appropriate numerical schemes.
For this purpose, first we note that the momentum solutions m_i^ε in (5.1) scale with ε, i.e. $m_i^\varepsilon = \varepsilon\tilde{m}_i^\varepsilon$. Hence, we drop the tilde notation and investigate the following system in one space dimension

$$\begin{aligned}
\partial_t \rho_i^\varepsilon + \partial_x m_i^\varepsilon &= 0,\\
\partial_t m_i^\varepsilon + \partial_x\left(\frac{m_i^{\varepsilon 2}}{\rho_i^\varepsilon}\right) + \frac{1}{\varepsilon^2}\partial_x p_i(\rho_i^\varepsilon) &= -\frac{1}{\varepsilon^2}\left(M_i m_i^\varepsilon + \sum_{j=1}^n \lambda_{ij}(\rho_j^\varepsilon m_i^\varepsilon - \rho_i^\varepsilon m_j^\varepsilon)\right).
\end{aligned} \tag{5.6}$$

The corresponding entropy inequality and entropy–entropy flux pair read

$$\partial_t \eta(\boldsymbol{r}^\varepsilon, \boldsymbol{m}^\varepsilon) + \frac{1}{\varepsilon}\partial_x q(\boldsymbol{r}^\varepsilon, \boldsymbol{m}^\varepsilon) + \frac{1}{\varepsilon^2}\left(\sum_{i=1}^n M_i \frac{m_i^{\varepsilon 2}}{\rho_i^\varepsilon} + \frac{1}{2}\sum_{i,j=1}^n \lambda_{ij}\rho_i^\varepsilon\rho_j^\varepsilon\left(\frac{m_i^\varepsilon}{\rho_i^\varepsilon} - \frac{m_j^\varepsilon}{\rho_j^\varepsilon}\right)^2\right) \le 0,$$

with

$$\eta(U) = \frac{1}{2}\varepsilon^2 \sum_{i=1}^{n} \frac{m_i^2}{\rho_i} + \sum_{i=1}^{n} h_i(\rho_i), \qquad q(U) = \frac{1}{2} \sum_{i=1}^{n} \varepsilon^3 m_i \frac{m_i^2}{\rho_i^2} + \varepsilon m_i h_i(\rho_i)'. \tag{5.7}$$

5.1.1 IMEX Splitting

We derive an AP scheme based on ideas from [17] and [35].
Recall the rescaled system (5.6). According to [35] we split the scheme in two parts. One is treated explicitly and the other one implicitly. Methods of this type are called *Implicit–Explicit* (IMEX) *Methods* . The entire stiff source term is handled implicitly and the pressure term is split into an explicit and an implicit part. For this purpose we introduce a parameter $\alpha \in (0, 1/\varepsilon^2]$ which dictates how much of the pressure term is handled explicitly and implicitly. Consequently, we rewrite (5.6) as

$$\begin{aligned} \partial_t \rho_i + \partial_x m_i &= 0, \\ \partial_t m_i + \partial_x \left(\frac{m_i^2}{\rho_i} + \alpha p_i(\rho_i) \right) &= -\frac{1}{\varepsilon^2} \left(M_i m_i + \sum_{j=1}^{n} \lambda_{ij} (\rho_j m_i - \rho_i m_j) \right. \\ &\qquad \left. + (1 - \alpha\varepsilon^2) \partial_x p_i(\rho_i) \right). \end{aligned} \tag{5.8}$$

Then, we solve the system (5.8) as proposed in [17] by using a splitting method. First, we solve

$$\begin{aligned} \partial_t \rho_i + \partial_x m_i &= 0, \\ \partial_t m_i + \partial_x \left(\frac{m_i^2}{\rho_i} + \alpha p_i(\rho_i) \right) &= 0 \end{aligned} \tag{5.9}$$

with the Finite Volume (FV) method employing the standard Lax–Friedrichs numerical flux [101].
Afterwards we solve in a second step

$$\begin{aligned} \partial_t \rho_i &= 0, \\ \partial_t m_i &= -\frac{1}{\varepsilon^2} \left(M_i m_i + \sum_{j=1}^{n} \lambda_{ij} (\rho_j m_i - \rho_i m_j) + (1 - \alpha\varepsilon^2) \partial_x p_i(\rho_i) \right) \end{aligned} \tag{5.10}$$

with the implicit Euler method.

Consider an uniform mesh with cells $(x_{k-1/2}, x_{k+1/2})_{k\in\mathbb{Z}}$ with $x_{k+1/2} := k + 1/2\Delta x$ and uniform cell size Δx. Further, let $0 = t_0 < t_1 < \ldots < t_N = T$ be a time mesh. Additionally, let $\Delta t_n := t_{n+1} - t_n > 0$. In the following, the subscripts i, j denote the corresponding constituents of the fluid mixture, while k denotes the k-th cell midpoint of the spatial discretization. The piecewise constant solution at time t_n in cell k is denoted by $U_k^n := (\boldsymbol{r}_k^n, \boldsymbol{m}_k^n)^\top$.
In the first step, utilizing a FV scheme, we have to ensure the Courant–Friedrichs–Lewy (CFL) condition [30]

$$\lambda_{\max}^n \frac{\Delta t_n}{\Delta x} \le \frac{1}{2}, \tag{5.11}$$

where

$$\lambda_{\max}^n := \max_{i,k} \left\{ \left| m_{i,k}^n/\rho_{i,k}^n \pm \sqrt{\alpha p_i'(\rho_{i,k}^n)} \right| \right\} \tag{5.12}$$

denotes the largest absolute Eigenvalue of the Jacobian D $F(U^n)$ of the flux $F(U^n)$. Note that if the pressure term is handled fully explicit, i.e. $\alpha = \varepsilon^{-2}$, the time step width Δt_n scales with ε^{-1}. This renders the scheme unfeasible for small values of ε. However, this is not the case if α is chosen smaller. On the other hand, we cannot set $\alpha = 0$ because we lose strict hyperbolicity of (5.9) in this case. In practice, the choice of α depends on the problem at hand. We comment on this issue in Section 5.2. We describe the scheme in the following:

Algorithm 5.1 (AP scheme for Euler–Darcy–MS): *Starting from t_n we obtain from the first step the intermediate discrete solution $\left(\rho_{i,k}^\star, m_{i,k}^\star\right)$ as*

$$\begin{pmatrix} \boldsymbol{r} \\ \boldsymbol{m} \end{pmatrix}_k^\star = \begin{pmatrix} \boldsymbol{r} \\ \boldsymbol{m} \end{pmatrix}_k^n - \frac{\Delta t}{\Delta x}(\hat{F}_{k+1/2}^n - \hat{F}_{k-1/2}^n),$$

with

$$\hat{F}_{k+1/2}^n := \frac{1}{2}(F(U_{k+1}^n) + F(U_k^n)) - \frac{\lambda}{2}(U_{k+1}^n - U_k^n).$$

Here, we choose

$$\lambda \ge \sup_{0\le n\le N} \lambda_{\max}^n,$$

with $\lambda_{\max}^n$ from (5.12)*. For this step we prescribe the CFL condition* (5.11)*.*
In the second step (see (5.10)*) we then solve*

$$\frac{\rho_{i,k}^{n+1} - \rho_{i,k}^\star}{\Delta t} = 0, \tag{5.13a}$$

$$\frac{m_{i,k}^{n+1} - m_{i,k}^{\star}}{\Delta t} = -\frac{1}{\varepsilon^2}\left(M_i m_{i,k}^{n+1} + \sum_{j=1}^{n} \lambda_{ij}\left(\rho_{j,k}^{n+1} m_{i,k}^{n+1} - \rho_{i,k}^{n+1} m_{j,k}^{n+1}\right) + (1-\alpha\varepsilon^2)\frac{p_{i,k+1/2}^{n+1} - p_{i,k-1/2}^{n+1}}{\Delta x}\right), \tag{5.13b}$$

with

$$p_{i,k+1/2}^{n+1} = \frac{1}{2}\left(p_i(\rho_{i,k}^{n+1}) + p_i(\rho_{i,k+1}^{n+1})\right).$$

From (5.13a) follows $\rho_{i,k}^{n+1} = \rho_{i,k}^{\star}$, hence from now on we only consider (5.13b). With

$$A_k^n(\varepsilon) := \frac{1}{\Delta t}\boldsymbol{I}_N + \frac{1}{\varepsilon^2}\operatorname{diag}(M_i) - \frac{1}{\varepsilon^2}\operatorname{diag}(\rho_{i,k}^{\star})\Lambda,$$

equation (5.13b) is equivalent to

$$A_k^n(\varepsilon)\left(m_{1,k}^{n+1}, \dots, m_{n,k}^{n+1}\right)^{\top} = \frac{1}{\Delta t}\left(m_{1,k}^{\star}, \dots, m_{n,k}^{\star}\right)^{\top} - \frac{(1-\alpha\varepsilon^2)}{\varepsilon^2}\frac{p_{i,k+1/2}^{n+1} - p_{i,k-1/2}^{n+1}}{\Delta x}.$$

Remark 5.2: *1. As mentioned in [35] the choice of the parameter α is difficult because it depends in a complex way on ε and the required accuracy. In [17] they choose $\alpha = 1$.*

2. The hyperbolic CFL condition in Algorithm 5.1 does not lead to a stable discretization for small values of ε. For the limit system even a parabolic CFL condition is needed. Hence, in our numerical experiments in Section 5.2.2 we choose a parabolic CFL condition to assure stability.

5.1.2 The AP Property of Algorithm 5.1

In the following we prove the AP property of the Algorithm 5.1. For the sake of readability we consider the case of two components, i.e. $k = 2$. However, this generalizes straightforwardly to the case of arbitrary many components.

Theorem 5.3: *The discrete numerical scheme prescribed through Algorithm 5.1 is asymptotic preserving in the limit $\varepsilon \longrightarrow 0$. It transforms into a consistent discretization of* (5.3) *as $\varepsilon \longrightarrow 0$.*

Proof. Without loss of generality consider the case of two components, $k = 2$. The explicit part (5.9) reads as

$$\begin{aligned}
\begin{pmatrix}\rho_1\\ \rho_2\end{pmatrix}_k^{\star} &= \begin{pmatrix}\rho_1\\ \rho_2\end{pmatrix}_k^{n} - \frac{\Delta t_n}{\Delta x}\left(\frac{1}{2}\left(\begin{pmatrix}m_1\\ m_2\end{pmatrix}_{k+1}^{n} - \begin{pmatrix}m_1\\ m_2\end{pmatrix}_{k-1}^{n}\right)\right.\\
&\qquad \left. -\frac{\lambda}{2}\left(\begin{pmatrix}\rho_1\\ \rho_2\end{pmatrix}_{k+1}^{n} - 2\begin{pmatrix}\rho_1\\ \rho_2\end{pmatrix}_{k}^{n} + \begin{pmatrix}\rho_1\\ \rho_2\end{pmatrix}_{k-1}^{n}\right)\right)\\
\begin{pmatrix}m_1\\ m_2\end{pmatrix}_k^{\star} &= \begin{pmatrix}m_1\\ m_2\end{pmatrix}_k^{n} - \frac{\Delta t_n}{\Delta x}\left[\frac{1}{2}\left(\begin{pmatrix}\frac{m_1^2}{\rho_1} + \alpha p_1(\rho_1)\\ \frac{m_2^2}{\rho_2} + \alpha p_2(\rho_2)\end{pmatrix}_{k+1}^{n} - \begin{pmatrix}\frac{m_1^2}{\rho_1} + \alpha p_1(\rho_1)\\ \frac{m_2^2}{\rho_2} + \alpha p_2(\rho_2)\end{pmatrix}_{k-1}^{n}\right)\right.\\
&\qquad \left. -\frac{\lambda}{2}\left(\begin{pmatrix}m_1\\ m_2\end{pmatrix}_{k+1}^{n} - 2\begin{pmatrix}m_1\\ m_2\end{pmatrix}_{k}^{n} + \begin{pmatrix}m_1\\ m_2\end{pmatrix}_{k-1}^{n}\right)\right]
\end{aligned} \tag{5.14}$$

and the implicit part (5.13) as

$$\begin{aligned}
\begin{pmatrix}\rho_1\\ \rho_2\end{pmatrix}_k^{n+1} &= \begin{pmatrix}\rho_1\\ \rho_2\end{pmatrix}_k^{\star},\\
\begin{pmatrix}m_1\\ m_2\end{pmatrix}_k^{n+1} &= \left(A_k^n(\varepsilon)\right)^{-1}\left[\frac{1}{\Delta t_n}\begin{pmatrix}m_1\\ m_2\end{pmatrix}_k^{\star} - \frac{(1-\alpha\varepsilon^2)}{\varepsilon^2}\frac{p_{k+1/2}^{n+1} - p_{k-1/2}^{n+1}}{\Delta x}\right].
\end{aligned} \tag{5.15}$$

Now, we combine (5.14) and (5.15) to obtain

$$\begin{aligned}
\begin{pmatrix}\rho_1\\ \rho_2\end{pmatrix}_k^{n+1} &= \begin{pmatrix}\rho_1\\ \rho_2\end{pmatrix}_k^{n} - \frac{\Delta t_n}{\Delta x}\left(\frac{1}{2}\left(\begin{pmatrix}m_1\\ m_2\end{pmatrix}_{k+1}^{n} - \begin{pmatrix}m_1\\ m_2\end{pmatrix}_{k-1}^{n}\right)\right.\\
&\qquad \left. -\frac{\lambda}{2}\left(\begin{pmatrix}\rho_1\\ \rho_2\end{pmatrix}_{k+1}^{n} - 2\begin{pmatrix}\rho_1\\ \rho_2\end{pmatrix}_{k}^{n} + \begin{pmatrix}\rho_1\\ \rho_2\end{pmatrix}_{k-1}^{n}\right)\right),\\
\begin{pmatrix}m_1\\ m_2\end{pmatrix}_k^{n+1} &= \left(A_k^n(\varepsilon)\right)^{-1}\left[\frac{1}{\Delta t_n}\begin{pmatrix}m_1\\ m_2\end{pmatrix}_k^{n}\right.\\
&\qquad -\frac{1}{\Delta x}\left(\frac{1}{2}\left(\begin{pmatrix}\frac{m_1^2}{\rho_1} + \alpha p_1(\rho_1)\\ \frac{m_2^2}{\rho_2} + \alpha p_2(\rho_2)\end{pmatrix}_{k+1}^{n} - \begin{pmatrix}\frac{m_1^2}{\rho_1} + \alpha p_1(\rho_1)\\ \frac{m_2^2}{\rho_2} + \alpha p_2(\rho_2)\end{pmatrix}_{k-1}^{n}\right)\right.\\
&\qquad \left.\left. -\frac{\lambda}{2}\left(\begin{pmatrix}m_1\\ m_2\end{pmatrix}_{k+1}^{n} - 2\begin{pmatrix}m_1\\ m_2\end{pmatrix}_{k}^{n} + \begin{pmatrix}m_1\\ m_2\end{pmatrix}_{k-1}^{n}\right)\right)\right]
\end{aligned} \tag{5.16}$$

$$-\frac{(1-\alpha\varepsilon^2)}{\varepsilon^2}\frac{p_{k+1/2}^{n+1}-p_{k-1/2}^{n+1}}{\Delta x}\Bigg], \tag{5.17}$$

with

$$\begin{aligned}A_k^n(\varepsilon)^{-1} =&\Delta t_n\varepsilon^2\left(\varepsilon^4+\varepsilon^2\Delta t_n(M_1+M_2+\lambda_{12}(\rho_{1,k}^n+\rho_{2,k}^n))\right.\\ &\left.+\Delta t_n^2(M_1M_2+\lambda_{12}(M_1\rho_{1,k}^n+M_2\rho_{2,k}^n))\right)^{-1}\\ &\begin{pmatrix}\varepsilon^2+\Delta t_n(M_2+\lambda_{12}\rho_{1,k}^n) & \Delta t_n\lambda_{12}\rho_{1,k}^n\\ \Delta t_n\lambda_{12}\rho_{2,k}^n & \varepsilon^2+\Delta t_n(M_1+\lambda_{12}\rho_{2,k}^n)\end{pmatrix}.\end{aligned}$$

Now we investigate the scheme in the limit for $\varepsilon\longrightarrow 0$. We infer for (5.17)

$$\begin{aligned}\begin{pmatrix}m_1\\ m_2\end{pmatrix}_k^{n+1} &= -\frac{1}{M_1M_2+\lambda_{12}(M_1\rho_{1,k}^n+M_2\rho_{2,k}^n)}\frac{p_{k+1/2}^{n+1}-p_{k-1/2}^{n+1}}{\Delta x}\\ &\quad\begin{pmatrix}M_2+\lambda_{12}\rho_{1,k}^n & \lambda_{12}\rho_{1,k}^n\\ \lambda_{12}\rho_{2,k}^n & M_1+\lambda_{12}\rho_{2,k}^n\end{pmatrix}\\ &= -\left(\begin{pmatrix}M_1 & 0\\ 0 & M_2\end{pmatrix}+\lambda_{12}\begin{pmatrix}\rho_{2,k}^n & -\rho_{1,k}^n\\ -\rho_{2,k}^n & \rho_{1,k}^n\end{pmatrix}\right)^{-1}\frac{p_{k+1/2}^{n+1}-p_{k-1/2}^{n+1}}{\Delta x}.\end{aligned} \tag{5.18}$$

This is a consistent discretization of

$$\boldsymbol{m} = -\mathcal{B}^{-1}\partial_x\boldsymbol{p},$$

cf. (5.4).
Hence, with (5.18) we obtain for (5.16) in the limit $\varepsilon\longrightarrow 0$,

$$\begin{aligned}\begin{pmatrix}\rho_1\\ \rho_2\end{pmatrix}_k^{n+1} &= \begin{pmatrix}\rho_1\\ \rho_2\end{pmatrix}_k^{n}-\frac{\Delta t_n}{2\Delta x^2}\left((-\mathcal{B}_k^n)^{-1}(p_{k+1/2}^{n+1}-p_{k-1/2}^{n+1})+(\mathcal{B}_{k-1}^n)^{-1}(p_{k-1/2}^{n+1}-p_{k-3/2}^{n+1})\right)\\ &\quad+\frac{\lambda\Delta t_n}{2\Delta x}\left(\begin{pmatrix}\rho_1\\ \rho_2\end{pmatrix}_{k+1}^{n}-2\begin{pmatrix}\rho_1\\ \rho_2\end{pmatrix}_k^{n}+\begin{pmatrix}\rho_1\\ \rho_2\end{pmatrix}_{k-1}^{n}\right).\end{aligned} \tag{5.19}$$

Since $\boldsymbol{r}_{k+1}^n-2\boldsymbol{r}_k^n+\boldsymbol{r}_{k-1}^n=O(\Delta x^2)$ corresponds to numerical viscosity, this is a consistent discretization for the limit system (5.3) independent of ε. Therefore the scheme (5.14)–(5.15) is asymptotic preserving. ■

5.2 Numerical Experiments

In this section we perform numerical experiments in one space dimension. We stress that the chosen initial values or parameters might not be realistic but help to illustrate important characteristics of the systems (2.22) and (2.24).
In the following we distinguish the cases $\varepsilon = 1$ and $\varepsilon \ll 1$.

5.2.1 Uphill Diffusion

In order to illustrate the concept of uphill diffusion [70], we set $\varepsilon = 1$ and consider the free flow of a three component gas mixture, i.e. $M_i = 0, i = 1, \dots, 3$.
In the Duncan–Toor experiment [41] they consider two bulbs filled with a mixture of H_2, N_2 and CO_2. The bulbs are connected by a capillary. The initial compositions in the left and right bulb are

$H_2 = 0$	$H_2 = 0.501$
$N_2 = 0.501$	$N_2 = 0.499$
$CO_2 = 0.499$	$CO_2 = 0.$

They found that the diffusion behavior of H_2 and CO_2 is similar to Fickian diffusion. However, the second component, i.e. N_2, shows the uphill diffusion behavior. The composition in both bulbs is initially nearly the same. Nevertheless, diffusion takes place, decreasing the composition in the left bulb while the composition in the right bulb increases.
The idea is to simulate a similar situation as in Duncan and Toor's experiment. However, we use artificial values for densities and parameters to simplify computations.
The space domain throughout all simulations is

$$\Omega \coloneqq (-1, 1).$$

As EOS, we use the perfect gas law

$$p_i(\rho_i) = c_i \rho_i, \quad c_i > 0, \quad i = 1, ..., N,$$

with $c_1 = 10$, $c_2 = 5$, and $c_3 = 3$.
For the Maxwell–Stefan coefficients we use

$$\lambda_{12} = 30, \lambda_{13} = 20, \lambda_{23} = 10.$$

The spatial discretization consists of 400 cells, the time step width Δt_n is computed in every time step according to the CFL condition (5.11). We run the simulation up to time $T = 0.25$. Neumann boundary conditions are prescribed.

As initial conditions we use

$$\begin{pmatrix}\rho_{1,0}\\ \rho_{2,0}\\ \rho_{3,0}\end{pmatrix} = \begin{cases}\begin{pmatrix}10^{-5} & 8 & 12\end{pmatrix}^\top, & x < 0\\ \begin{pmatrix}1 & 7.9 & 10^{-5}\end{pmatrix}^\top, & x \geq 0,\end{cases} \qquad \begin{pmatrix}m_{1,0}\\ m_{2,0}\\ m_{3,0}\end{pmatrix} = \mathbf{0}. \tag{5.20}$$

In Figure 5.2 we depict the density part of the solution.

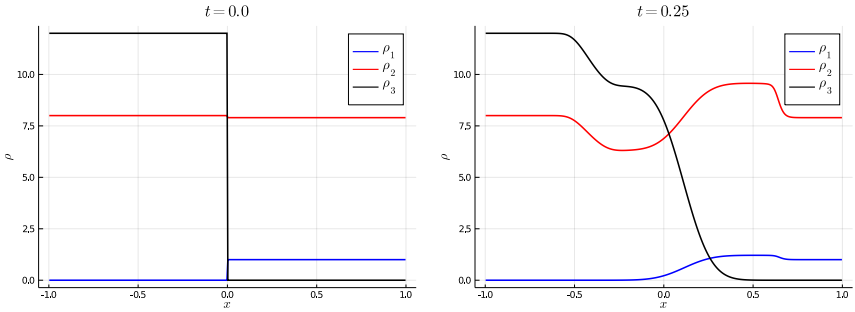

Figure 5.2: Illustration of the uphill diffusion phenomenon. Densities of the solution. Left: Initial data for $t = 0$, Right: Solution with Maxwell–Stefan diffusion at time $t = 0.25$.

The initial conditions (5.20) are shown in the left part in Figure 5.2. Uphill diffusion can be observed in the second component (right). The second component in our example corresponds to N_2 in the Duncan–Toor experiment. As in the experiment, although the density of the second component is nearly the same in the left and right part of the domain, the density in the left part decreases over time, while it increases in the right part. This is similar to the behavior observed experimentally [41].
In summary this numerical experiment demonstrates that indeed the Euler–MS model is capable of capturing effects like uphill diffusion.

5.2.2 Relative Entropy Convergence Rate

In this section we investigate the behavior of our Algorithm 5.1 for the system (5.1) with decreasing ε. The goal is to verify the convergence rate from Theorem 4.3 numerically. For this purpose we compare the solution to (5.6) obtained with our Algorithm 5.1 to the solution to the limit system (5.3) obtained through (5.19). With the scaled entropy (5.7) we introduce the discrete version of the relative entropy

(5.5), namely

$$\phi_\varepsilon^n := \sum_{k\in\mathbb{Z}} \Delta x \eta_k^{\varepsilon,n}, \tag{5.21}$$

with the discrete relative entropy

$$\begin{aligned}\eta_k^{\varepsilon,n} &:= \eta(\boldsymbol{r}_k^{\varepsilon,n}, \boldsymbol{m}_k^{\varepsilon,n} \mid \bar{\boldsymbol{r}}_k^n, \bar{\boldsymbol{m}}_k^n)\\ &= \frac{1}{2}\varepsilon^2 \sum_{i=1}^n \rho_{i,k}^{\varepsilon,n} \left| \frac{\boldsymbol{m}_{i,k}^{\varepsilon,n}}{\rho_{i,k}^{\varepsilon,n}} - \frac{\bar{\boldsymbol{m}}_{i,k}^n}{\bar{\rho}_{i,k}^n} \right|^2 + \sum_{i=1}^n h_i(\rho_{i,k}^{\varepsilon,n} \mid \bar{\rho}_{i,k}^n).\end{aligned}$$

We consider two examples with three components and different initial data. We apply Neumann boundary conditions for all simulations. For both test cases we use $\alpha = 1$.
Since we solve the parabolic limit system in an explicit fashion, it is natural that we need a parabolic time step restriction. In [25] the discrete version of the relative entropy estimate under a parabolic time step restriction for the p–system with damping is proven.
Hence, we prescribe

$$\lambda \frac{\Delta t_n}{\Delta x^2} \le \frac{1}{2}$$

also for the case $\varepsilon > 0$.
We compute approximate solutions for $\varepsilon \in \{1.0, 0.5, 0.3, 0.1, 0.03, 0.01, 0.001, 0.0001\}$ and vary the numbers of cells $N_{\text{cells}} \in \{50, 100, 200, 500\}$.
For both test cases we employ the perfect gas EOS:

$$\begin{aligned}p_1(\rho_1) &= \rho_1,\\ p_2(\rho_2) &= 1.2\rho_2,\\ p_3(\rho_3) &= 0.8\rho_3.\end{aligned}$$

For the first test case we choose the parameter:

$$\begin{aligned}M_1 &= M_2 = M_3 = 1,\\ \lambda_{12} &= 0.1,\\ \lambda_{23} &= \lambda_{13} = 0.\end{aligned}$$

The initial conditions are

$$\begin{pmatrix}\rho_{1,0}\\ \rho_{2,0}\\ \rho_{3,0}\end{pmatrix} = \begin{cases}\begin{pmatrix}2 & 1 & 3\end{pmatrix}^\top, & x \le 0\\ \begin{pmatrix}1 & 0.5 & 2\end{pmatrix}\top, & x \ge 0,\end{cases} \quad \begin{pmatrix}m_{1,0}\\ m_{2,0}\\ m_{3,0}\end{pmatrix} = \mathbf{0}.$$

For the second test case we choose:

$$\begin{aligned} M_1 &= M_2 = M_3 = 1,\\ \lambda_{12} &= 0.1,\\ \lambda_{23} &= \lambda_{13} = 0.2. \end{aligned}$$

The initial conditions are

$$\begin{pmatrix}\rho_{1,0}\\ \rho_{2,0}\\ \rho_{3,0}\end{pmatrix} = \begin{pmatrix}1.5 + 0.75\cos(\pi x)\\ 1.2 + 0.75\cos(\pi x)\\ 1.35 + 0.375\cos(\pi x)\end{pmatrix}, \quad \begin{pmatrix}m_{1,0}\\ m_{2,0}\\ m_{3,0}\end{pmatrix} = -\mathcal{B}(\boldsymbol{r}_0)^{-1}\partial_x \boldsymbol{p}(\boldsymbol{r}_0).$$

Here, we use compatible initial condition, i.e. the momenta fulfill the analog version of (5.18) for three components.
We present in Figure 5.3 the results for both test cases. The discrete (space) integral Φ_ε (5.21) of the relative entropy is plotted at final time $T = 0.5$. We can see that the convergence rate of ε^4 is recovered for both test cases. This agrees with the analytical result of Theorem 4.3.

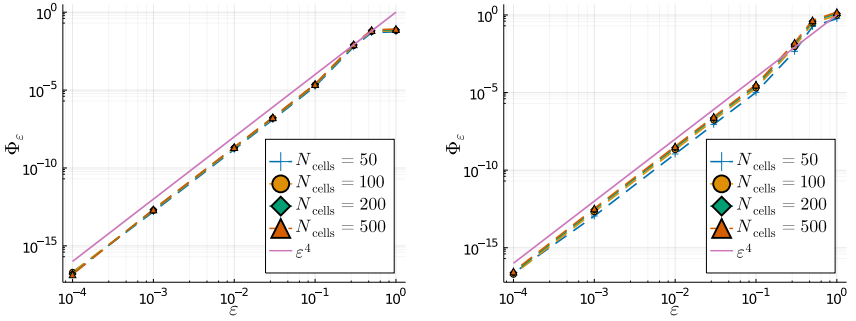

(a) Discontinuous initial data. *(b) Smooth initial data.*

Figure 5.3: Log–log plot of space integral Φ_ε^n (5.21) of the relative entropy over ε at time $T = 0.5$. Solution for different number N_{cells} of cells and initial data. Left: discontinuous initial data, Right: smooth initial data.

6 Conclusion

In this first part we examined compressible multi-component flow in porous media. We have presented how to derive the Euler–Darcy–MS system (2.22) in such a way that it automatically satisfies an entropy inequality and hence fulfills the second law of thermodynamics. We utilized the CT framework of [20] for this purpose. There exist smooth solutions globally in time to this system if the smooth initial data are close enough to an equilibrium. This was proven in Chapter 3. Further, in an asymptotic long-time-large-friction regime we proved the convergence to a parabolic limit system generalizing results on the single-component case. Here, we used a relative entropy framework. A numerical discretization for the Euler–Darcy–MS system in afore-mentioned asymptotic regime is not straightforward since the system changes its characteristic type from hyperbolic to parabolic in the limit. To overcome this issue we introduced an AP scheme which turns into a consistent discretization of the parabolic limit system in the limit. Equipped with this scheme we illustrated the uphill diffusion phenomenon and verified the convergence rate in the relative entropy in the discrete setting.

Appendix

A Operators and Matrix Algebra

We collect some definitions from vector analysis and matrix algebra which are frequently used in Chapter 2–Chapter 4.
For some vector $\boldsymbol{u}(\boldsymbol{x}) = (u_1(\boldsymbol{x}), \dots, u_n(\boldsymbol{x}))^\top \in \mathbb{R}^n$ the (generalized) gradient is defined as

$$\nabla \boldsymbol{u}(\boldsymbol{x}) \coloneqq (\nabla u_1(\boldsymbol{x}), \dots \nabla u_n(\boldsymbol{x}))^\top \in \mathbb{R}^{nd}, \tag{6.1}$$

and for $\boldsymbol{v}(\boldsymbol{x}) = (\boldsymbol{v}_1^\top(\boldsymbol{x}), \dots, \boldsymbol{v}_n^\top(\boldsymbol{x}))^\top \in \mathbb{R}^{nd}$ the (generalized) divergence is given by

$$\operatorname{div}(\boldsymbol{v}(\boldsymbol{x})) \coloneqq \sum_{i=1}^{n} \operatorname{div}(\boldsymbol{v}_i(\boldsymbol{x})).$$

By $\otimes$ we denote the Kronecker product of two matrices, i.e., with $\boldsymbol{A} \in \mathbb{R}^{m\times n}, \boldsymbol{B} \in \mathbb{R}^{p\times q}$

$$\boldsymbol{A} \otimes \boldsymbol{B} \coloneqq \begin{pmatrix} a_{11}\boldsymbol{B} & \dots & a_{1n}\boldsymbol{B} \\ \vdots & \ddots & \vdots \\ a_{m1}\boldsymbol{B} & \cdots & a_{mn}\boldsymbol{B} \end{pmatrix} \in \mathbb{R}^{mp\times nq},$$

and by $\odot$ the entry-wise product for matrices of identical dimensions. We define $\operatorname{blockdiag}(\boldsymbol{x}_i)$, with $\boldsymbol{x}_i \in \mathbb{R}^d$, $i = 1, \dots, n$, as

$$\operatorname{blockdiag}(\boldsymbol{x}_i) \coloneqq \begin{pmatrix} \boldsymbol{x}_1 & \boldsymbol{0}_{d\times 1} & \cdots & \cdots & \boldsymbol{0}_{d\times 1} \\ \boldsymbol{0}_{d\times 1} & \boldsymbol{x}_2 & \boldsymbol{0}_{d\times 1} & \cdots & \boldsymbol{0}_{d\times 1} \\ \vdots & \ddots & \ddots & \ddots & \vdots \\ \vdots & \ddots & \ddots & \ddots & \boldsymbol{0}_{d\times 1} \\ \boldsymbol{0}_{d\times 1} & \cdots & \cdots & \boldsymbol{0}_{d\times 1} & \boldsymbol{x}_n \end{pmatrix} \in \mathbb{R}^{nd\times n}.$$

In addition, with matrices $\boldsymbol{A}_i \in \mathbb{R}^{d\times d}$, $i = 1, \dots, n$, let

$$\operatorname{blockdiag}(\boldsymbol{A}_i) = \begin{pmatrix} \boldsymbol{A}_1 & \boldsymbol{0}_{d\times d} & \cdots & \boldsymbol{0}_{d\times d} \\ \boldsymbol{0}_{d\times d} & \ddots & \ddots & \vdots \\ \vdots & \ddots & \ddots & \boldsymbol{0}_{d\times d} \\ \boldsymbol{0}_{d\times d} & \cdots & \boldsymbol{0}_{d\times d} & \boldsymbol{A}_n \end{pmatrix} \in \mathbb{R}^{nd\times nd}.$$

We conclude with the following rules for the generalized gradient defined in (6.1).

Lemma A.1: *For smooth functions $\alpha : \mathbb{R}^d \longrightarrow \mathbb{R}$, $\boldsymbol{a} : \mathbb{R}^d \longrightarrow \mathbb{R}^n$, $\boldsymbol{b} : \mathbb{R}^d \longrightarrow \mathbb{R}^n$, and $\boldsymbol{c} : \mathbb{R}^n \longrightarrow \mathbb{R}^n$ it holds*

$$\begin{aligned} \nabla(\alpha(\boldsymbol{x})\boldsymbol{a}(\boldsymbol{x})) &= \boldsymbol{a}(\boldsymbol{x}) \otimes \nabla\alpha(\boldsymbol{x}) + \alpha(\boldsymbol{x})\nabla\boldsymbol{a}(\boldsymbol{x}), \\ \nabla(\boldsymbol{c}(\boldsymbol{b}(\boldsymbol{x})) &= (\mathrm{D}_{\boldsymbol{b}}\, \boldsymbol{c}(\boldsymbol{b}(\boldsymbol{x})) \otimes \boldsymbol{I}_d)\nabla\boldsymbol{b}(\boldsymbol{x}). \end{aligned}$$

Proof. We have

$$\nabla(\alpha(\boldsymbol{x})\boldsymbol{a}(\boldsymbol{x})) = \begin{pmatrix} \nabla(\alpha(\boldsymbol{x})a_1(\boldsymbol{x})) \\ \vdots \\ \nabla(\alpha(\boldsymbol{x})a_n(\boldsymbol{x})) \end{pmatrix} = \begin{pmatrix} \nabla(\alpha(\boldsymbol{x}))a_1(\boldsymbol{x}) + \alpha(\boldsymbol{x})\nabla a_1(\boldsymbol{x}) \\ \vdots \\ \nabla(\alpha(\boldsymbol{x}))a_n(\boldsymbol{x}) + \alpha(\boldsymbol{x})\nabla a_n(\boldsymbol{x}) \end{pmatrix}$$

$$= \boldsymbol{a} \otimes \nabla\alpha(\boldsymbol{x}) + \alpha(\boldsymbol{x})\nabla\boldsymbol{a}(\boldsymbol{x})$$

and

$$\nabla(\boldsymbol{c}(\boldsymbol{b}(\boldsymbol{x})) = \begin{pmatrix} \nabla c_1(\boldsymbol{b}(\boldsymbol{x})) \\ \vdots \\ \nabla c_n(\boldsymbol{b}(\boldsymbol{x})) \end{pmatrix} = \begin{pmatrix} \sum_{i=1}^n \mathrm{D}_{b_i}\, c_1(\boldsymbol{b}(\boldsymbol{x}))\nabla b_i(\boldsymbol{x}) \\ \vdots \\ \sum_{i=1}^n \mathrm{D}_{b_i}\, c_n(\boldsymbol{b}(\boldsymbol{x}))\nabla b_i(\boldsymbol{x}) \end{pmatrix}$$

$$= \begin{pmatrix} D_{b_1} c_1(\boldsymbol{b}(\boldsymbol{x}))\boldsymbol{I}_d & \dots & D_{b_n} c_1(\boldsymbol{b}(\boldsymbol{x}))\boldsymbol{I}_d \\ \vdots & & \vdots \\ D_{b_1} c_n(\boldsymbol{b}(\boldsymbol{x}))\boldsymbol{I}_d & \dots & D_{b_n} c_n(\boldsymbol{b}(\boldsymbol{x}))\boldsymbol{I}_d \end{pmatrix} \nabla\boldsymbol{b}(\boldsymbol{x})$$

$$= (D_{\boldsymbol{b}}\boldsymbol{c}(\boldsymbol{b}(\boldsymbol{x})) \otimes \boldsymbol{I}_d)\nabla\boldsymbol{b}(\boldsymbol{x}).$$

■

B Global Classical Well-Posedness of IVPs for Hyperbolic Balance Laws

Let the state space $G \subset \mathbb{R}^{n(d+1)}$ be open and denote by $U : \mathbb{R}^d \times [0, T) \longrightarrow G$ the function that satisfies for some $T > 0$ the IVP for the nonlinear system of balance laws given by

$$\partial_t U + \sum_{\alpha=1}^{d} \partial_{x_\alpha} F_\alpha(U) = S(U) \text{ in } \mathbb{R}^d \times (0, T). \tag{6.2}$$

Here, $S : G \longrightarrow \mathbb{R}^{n(d+1)}$ and $F_\alpha : G \longrightarrow \mathbb{R}^{n(d+1)}$, $\alpha = 1, \dots, d$ are smooth functions with

$$S(U) = \begin{pmatrix} \mathbf{0} \\ \boldsymbol{s}(U) \end{pmatrix}.$$

From now on we assume that U can be split according to $U = (\boldsymbol{r}^\top, \boldsymbol{m}^\top)^\top$, with $\boldsymbol{r} \in \mathbb{R}^n$, $\boldsymbol{m} \in \mathbb{R}^{nd}$. The system (6.2) can then be written as

$$\partial_t \begin{pmatrix} \boldsymbol{r} \\ \boldsymbol{m} \end{pmatrix} + \sum_{\alpha=1}^{d} \partial_{x_\alpha} F_\alpha(\boldsymbol{r}, \boldsymbol{m}) = \begin{pmatrix} \mathbf{0} \\ \boldsymbol{s}(\boldsymbol{r}, \boldsymbol{m}) \end{pmatrix}. \tag{6.3}$$

Theorem B.1 ([108]): *Let $s \geq s_0 + 1 = \lfloor d/2 \rfloor + 2$ be an integer and $\hat{U} \in G$ be a constant equilibrium state such that the following conditions hold:*

1. *The Jacobian $\mathrm{D}_{\boldsymbol{m}} \boldsymbol{s}(\hat{U}) \in \mathbb{R}^{nd \times nd}$ is invertible.*
2. *There exists a strictly convex smooth entropy function $\eta : \mathcal{G} \longrightarrow \mathbb{R}$, defined in a convex, compact neighborhood $\mathcal{G} \subset G$ of $\hat{U}$ such that $\mathrm{D}^2 \eta(U)\, \mathrm{D} F_\alpha(U)$ is symmetric for all $U \in \mathcal{G}$ and all $\alpha = 1, \dots, d$.*
3. *There is a positive constant $c_{\mathcal{G}}$ such that for all $U \in \mathcal{G}$,*

$$[\mathrm{D}\, \eta(U) - \mathrm{D}\, \eta(\hat{U})] S(U) \leq -c_{\mathcal{G}} |S(U)|^2,$$

   where $|\cdot|$ denotes the Euclidean norm of a vector.
4. *The kernel $\ker(\mathrm{D}\, S(\hat{U}))$ of the Jacobian $\mathrm{D}\, S(\hat{U})$ contains no eigenvector of the matrix*
   $\sum_{\alpha=1}^{d} \omega_\alpha \mathrm{D}\, F_\alpha(\hat{U})$, for any $\omega = (\omega_1, \dots, \omega_d) \in \mathbb{S}^{d-1}$.

Then there is a constant $c_1 > 0$ such that for $U_0 \in H^s(\mathbb{R}^d)$ with

$$\|U_0 - \hat{U}\|_s \leq c_1$$

the system of balance laws (6.3) *with* U_0 *as its initial value has an unique global solution* $U = U(\boldsymbol{x}, t) \in C([0, T); H^s(\mathbb{R}^d))$ *satisfying*

$$\|U(\cdot, T) - \hat{U}\|_s^2 + \int_0^T \|S(U)(\cdot, t)\|_s^2 \, \mathrm{d}t + \int_0^T \|\nabla U(\cdot, t)\|_{s-1}^2 \, \mathrm{d}t \leq c_2 \|U_0 - \hat{U}\|_s^2$$

for any $T > 0$ *and some* $c_2 > 0$.

Part II
Compressible Phase-Field Flow

1 Introduction

In this part we study a fluid in two phases, namely liquid–vapor flow. Phase-field models are widely used to simulate interfacial phenomena. They form a special class of diffuse-interface (DI) models. In contrast to sharp-interface (SI) models, the interface has a (small) finite thickness γ. In the interfacial region the different phases are allowed to mix, see Figure 1.1.

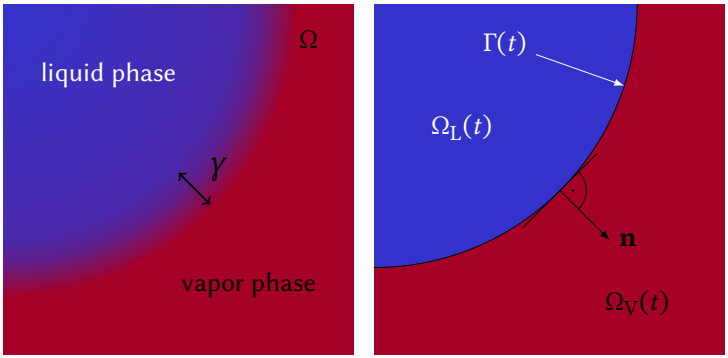

(a) Diffuse interface *(b) Sharp interface*

Figure 1.1: Illustration of diffuse and sharp interfaces.

An additional variable, the *phase-field*, is introduced which allows to distinguish the different phases. Since interface dynamics are determined on a molecular scale and there indeed, to some extent, a mixture exists, this approach is reasonable. However, the thickness of the interface is in practice artificially enlarged to the macro-scale. It is important that diffuse-interface models are consistent with sharp-interface models where the physical basis is simpler. Having this in mind another point of view is that DI models are smeared out versions of the corresponding sharp interface limit models.

The DI model concept has the advantage that only one system of PDE on the entire considered domain needs to be solved, whereas for sharp-interface models bulk systems need to be solved, which are coupled across the interface by possibly complex conditions. On the other hand the correct combination of the flow equations with the phase-field dynamics is far from being obvious.
Based on energy principles, phase-field models can be derived in a thermodynamic framework, see [5, 48] for an overview. They fulfill the second law of thermodynamics, meaning that the Clausius–Duhem inequality [102] is satisfied. In the case of isothermal models this is equivalent to an energy inequality. In addition, surface tension is included in the system by means of energy principles and a resulting capillary stress tensor contribution.
There are several (quasi-)incompressible [2, 74], compressible [19, 39, 106] and recently even incompressible–compressible phase-field models [87, 96]. Hence, phase-field models are a large class of models for different regimes. Depending on the application, it is feasible to neglect the compressibility of one or two phases. This is often the case for the liquid phase, namely in low Mach regimes.
In this part we consider a phase-field model, where both phases are assumed to be compressible. This system can be regarded as a special case for one component of the system [39]. However, it differs in the scaling of the double-well potential W, which yields the correct surface tension, namely the expression (2.18). Additionally, in our version the viscosity parameter are different for each phase. This is not the case in [39], where both phases share the same viscosity parameter. The resulting system is of mixed hyperbolic–parabolic type. This renders its numerical discretization non-straightforward. In Chapter 3 we develop an energy-consistent discontinuous Galerkin scheme for our model. This is a high order scheme which additionally enjoys the property of energy consistency, i.e. it satisfies an energy inequality on the discrete level. Especially, in contrast to similar approaches [69], we achieve second order of accuracy in time.
There are very little numerical examples using compressible phase-field models in the literature. In [69] a simulation shows the evolution of static bubble ensembles without gravity. However, with our scheme we are able to use the compressible phase field model in complex numerical simulations. To illustrate the flexibility of this phase-field model we provide two examples. The first one is related to droplet–wall interactions. In this case especially the contact line dynamic is important. We demonstrate how the phase-field model can be used in such scenarios. The second example is the coupling of porous-medium and free flows. In this example we want to include processes which are related to drops forming at the interface between a porous medium and the free flow (FF) . There are different approaches, however in all macro-scale approaches micro-scale information is lost. For that reason we embed the phase-field model into a multi-scale framework and resolve single drops directly.

This part is structured as follows. In the following Chapter 2 we introduce the isothermal compressible Navier–Stokes–Allen–Cahn (NSAC) phase-field model. Further, we investigate some important properties. The energy inequality, which renders the system thermodynamically consistent, the sharp-interface limit, and the effective surface tension inside the model. In the subsequent Chapter 3 we derive the energy-consistent discontinuous Galerkin (dG) scheme. To utilize the model and numerical scheme, in Chapter 4 we give an example of droplet–wall interaction and in Chapter 5 we present the example of the multi-scale framework for coupled porous-medium and free flow. Finally, we conclude in Chapter 6.

2 A Compressible Navier–Stokes–Allen–Cahn Model

In this chapter we introduce a compressible Navier–Stokes–Allen–Cahn model. We consider a viscous fluid at constant temperature. The fluid is assumed to exist in two phases, a liquid phase denoted by subscript L and a vapor phase denoted by subscript V. In each phase the fluid is thermodynamically described by the corresponding Helmholtz free energy density $\rho f_{\mathrm{L/V}}(\rho)$. The fluid occupies a domain $\Omega \subset \mathbb{R}^d$, $d \in \mathbb{N}$. Let $\rho > 0$ be the density of the fluid, $\boldsymbol{v} \in \mathbb{R}^d$ the velocity and $\varphi \in [0,1]$ the phase-field. Following [39] we assume that the dynamics of the fluid is described by the isothermal compressible Navier–Stokes–Allen–Cahn system. With the parameter $\gamma > 0$, which relates to surface tension, the Helmholtz free energy density reads as

$$\rho f(\rho, \varphi, \nabla\varphi) = h(\varphi)\rho f_{\mathrm{L}}(\rho) + (1 - h(\varphi))\rho f_{\mathrm{V}}(\rho) + \frac{1}{\gamma} W(\varphi) + \frac{\gamma}{2}|\nabla\varphi|^2. \tag{2.1}$$

It consists of the interpolated free energy densities $\rho f_{\mathrm{L/V}}$ of the pure liquid and vapor phases with the nonlinear interpolation function

$$h(\varphi) = 3\varphi^2 - 2\varphi^3, \tag{2.2}$$

and a mixing energy [26] using the double well potential $W(\varphi) = \varphi^2(1-\varphi)^2$. We assume that the free energy densities $\rho f_{\mathrm{L/V}}(\rho)$ are convex functions. Let us define the energy densities

$$\rho\psi(\varphi, \rho) \coloneqq h(\varphi)\rho f_{\mathrm{L}}(\rho) + (1 - h(\varphi))\rho f_{\mathrm{V}}(\rho) \quad \text{and}$$
$$\rho\tilde{f}(\varphi, \rho) \coloneqq \rho\psi(\varphi, \rho) + \frac{1}{\gamma} W(\varphi).$$

Then we can rewrite (2.1) as

$$\rho f(\rho, \varphi, \nabla\varphi) = \rho\psi(\varphi, \rho) + \frac{1}{\gamma} W(\varphi) + \frac{\gamma}{2}|\nabla\varphi|^2$$

$$= \rho \tilde{f}(\varphi, \rho) + \frac{\gamma}{2}|\nabla\varphi|^2.$$

The hydrodynamic pressure p is determined through the Helmholtz free energy ρf by the thermodynamic relation

$$p = p(\rho, \varphi, \nabla\varphi) = -\rho f(\rho, \varphi, \nabla\varphi) + \rho \frac{\partial(\rho f)}{\partial \rho}(\rho, \varphi, \nabla\varphi). \tag{2.3}$$

We define the generalized chemical potential

$$\mu = \frac{1}{\gamma} W'(\varphi) + \frac{\partial(\rho\psi)}{\partial\varphi} - \gamma\Delta\varphi,$$

which steers the phase-field variable into equilibrium. Additionally, we denote by $\eta > 0$ the (artificial) mobility.
The isothermal compressible NSAC system reads then as

$$\partial_t \rho + \operatorname{div}(\rho \boldsymbol{v}) = 0, \tag{2.4}$$

$$\partial_t(\rho \boldsymbol{v}) + \operatorname{div}(\rho \boldsymbol{v} \otimes \boldsymbol{v} + p\boldsymbol{I}) = \operatorname{div}(\boldsymbol{S}) - \gamma \operatorname{div}(\nabla\varphi \otimes \nabla\varphi) \quad \text{in } \Omega \times (0, T), \tag{2.5}$$

$$\rho\partial_t\varphi + \rho\nabla\varphi \cdot \boldsymbol{v} = -\eta\mu. \tag{2.6}$$

Here, the dissipative viscous part of the stress tensor is

$$\boldsymbol{S} = \boldsymbol{S}(\varphi, \nabla\boldsymbol{v}) = \nu(\varphi)(\nabla\boldsymbol{v} + \nabla\boldsymbol{v}^\top - \operatorname{div}(\boldsymbol{v})\boldsymbol{I}),$$

with an interpolation of the viscosities $\mu_{\mathrm{L/V}}$ of the pure phases

$$\nu(\varphi) = h(\varphi)\mu_{\mathrm{L}} + (1 - h(\varphi))\mu_{\mathrm{V}} > 0. \tag{2.7}$$

As long as wall effects are neglected, the energy of the system (2.4)–(2.6) at time t is defined as

$$\begin{aligned} E(t) &\coloneqq E_{\mathrm{free}}(t) + E_{\mathrm{kin}}(t) \\ &= \int_\Omega \rho(\boldsymbol{x}, t) f(\rho(\boldsymbol{x}, t), \varphi(\boldsymbol{x}, t), \nabla\varphi(\boldsymbol{x}, t)) + \frac{1}{2}\rho(\boldsymbol{x}, t)|\boldsymbol{v}(\boldsymbol{x}, t)|^2 \, \mathrm{d}\boldsymbol{x}. \end{aligned} \tag{2.8}$$

Remark 2.1: *1. The phase-field φ is in general an artificial variable, however in this case it can be viewed as a mass fraction $\varphi = \frac{m_{\mathrm{V}}}{m}$, with the mass m_{V} of the vapor constituent and the total mass m of the fluid.*

2. *The special form of the nonlinear interpolation function h with $h'(0) = h'(1) \neq 0$ guarantees that* (2.4)–(2.6) *allows for physical meaningful equilibria. This can be easily seen by considering a static single-phase equilibrium $\boldsymbol{v} = \mathbf{0}$, $\varphi \equiv 0$. If $h'(0) \neq 0$ then the right hand side of the phase-field equation* (2.6) *does not vanish.*

Assuming an impermeable no-slip wall and 90° static contact angle, we have the boundary conditions

$$\boldsymbol{v} = \mathbf{0}, \qquad \text{on } \partial\Omega. \tag{2.9}$$

$$\nabla\varphi \cdot \boldsymbol{n} = 0 \tag{2.10}$$

Additionally, the system is endowed with initial conditions

$$\rho = \rho_0, \quad \boldsymbol{v} = \boldsymbol{v}_0, \quad \varphi = \varphi_0 \quad \text{on } \Omega \times \{0\},$$

using suitable functions $(\rho_0, \boldsymbol{v}_0, \varphi_0) : \Omega \longrightarrow \mathbb{R}^+ \times \mathbb{R}^d \times [0, 1]$.

Remark 2.2 (Existence of solutions)**:** *There are results on existence of solutions to similar systems than* (2.4)–(2.6)*. These systems mainly differ in the scaling of the second order operators. The scalings are needed in order to ensure the boundedness of the phase-field variable. In [45] the existence of global-in-time weak solutions without any restriction on the size of the initial data is proven. Further, in [67] the authors prove the existence and uniqueness of local strong solutions for arbitrary initial data. Our notion of weak solutions differs from [45]. We introduce a notion of weak solutions in Definition 3.3 for a mixed-formulation of* (2.4)–(2.6)*. This is the basis for the derivation of our dG scheme Algorithm 3.11. However, there is no existence result for Definition 3.3, hence we assume the existence of weak solutions.*

2.1 Properties of the NSAC System

In this section we prove some important properties of the NSAC system.

In the next section we provide an energy inequality, which renders the NSAC system (2.4)–(2.6) thermodynamically consistent.

Diffuse-interface models need to have a meaningful limit, if we let the interface width tend to zero. In Section 2.1.2 we briefly comment on this so-called *sharp-interface limit*.

In the subsequent Section 2.1.3, we investigate the surface tension in the system.

The Navier–Stokes–Kortweg (NSK) model is a different diffuse-interface model, where the density acts like a phase-field. For the NSK model it is known that,

for most scalings, the surface tension vanishes in the sharp-interface limit [40]. However, we show that for the NSAC system this is not the case and the SI limit system still has a surface tension contribution.

2.1.1 Energy Inequality

For isothermal models thermodynamical consistency means to verify that solutions of the problem at hand admit an energy inequality.
The energy introduced in (2.8) consists of the bulk free energies and the kinetic energy. To describe the total energy the entropic part is missing. That means the entropy production of the system (2.4)–(2.6) is exactly $-\frac{\mathrm{d}}{\mathrm{d}t}E(t)$. Hence, by assuring that the energy E decreases over time, we show increasing entropy and therefore thermodynamical consistency.
For the system (2.4)–(2.6) we have the following result.

Theorem 2.3 (Energy inequality): *Let $(\rho, \boldsymbol{v}, \varphi)$ with values in $(0,\infty)\times\mathbb{R}^d\times[0,1]$ be a classical solution to (2.4)–(2.6) in $(0,T)\times\Omega$ satisfying the boundary conditions (2.9)–(2.10) on $\partial\Omega\times(0,T)$. Then for all $t\in(0,T)$ the following energy inequality holds:*

$$\begin{aligned}\frac{\mathrm{d}}{\mathrm{d}t}E(t) &= \frac{\mathrm{d}}{\mathrm{d}t}\left(E_{\text{free}}(t)+E_{\text{kin}}(t)\right)\\ &= \frac{\mathrm{d}}{\mathrm{d}t}\left(\int_\Omega \rho f(\rho,\varphi,\nabla\varphi)+\frac{1}{2}\rho|\boldsymbol{v}|^2\ \mathrm{d}\boldsymbol{x}\right)\\ &= -\int_\Omega \frac{\eta}{\rho}\mu^2\ \mathrm{d}\boldsymbol{x}-\int_\Omega \boldsymbol{S}:\nabla\boldsymbol{v}\ \mathrm{d}\boldsymbol{x}\le 0. \end{aligned} \tag{2.11}$$

As expected, we have entropy production due to phase transition and viscosity.

Proof. In a straightforward way we compute:

$$\begin{aligned}\frac{\mathrm{d}}{\mathrm{d}t}E(t) =& \frac{\mathrm{d}}{\mathrm{d}t}\left(\int_\Omega \rho f(\rho,\varphi,\nabla\varphi)+\frac{1}{2}\rho|\boldsymbol{v}|^2\ \mathrm{d}\boldsymbol{x}\right)\\ =& \frac{\mathrm{d}}{\mathrm{d}t}\left(\int_\Omega \frac{1}{\gamma}W(\varphi)+\rho\psi(\rho,\varphi)+\frac{\gamma}{2}|\nabla\varphi|^2+\frac{1}{2}\rho|\boldsymbol{v}|^2\ \mathrm{d}\boldsymbol{x}\right)\\ =& \int_\Omega \varphi_t\left(\frac{1}{\gamma}W'(\varphi)+\frac{\partial(\rho\psi)}{\partial\varphi}-\gamma\Delta\varphi\right)+\rho_t\left(\frac{\partial(\rho\psi)}{\partial\rho}-\frac{1}{2}|\boldsymbol{v}|^2\right)+(\rho\boldsymbol{v})_t\cdot\boldsymbol{v}\ \mathrm{d}\boldsymbol{x}\\ &+\int_{\partial\Omega}\varphi_t(\gamma\nabla\varphi\cdot\boldsymbol{n})\ \mathrm{d}s.\end{aligned}$$

Now we use (2.4)–(2.6) to replace the time derivatives in the volume integrals. Using (2.3) we obtain after basic algebraic manipulations

$$\frac{\mathrm{d}}{\mathrm{d}t}E(t) = -\int_\Omega \operatorname{div}(\rho\boldsymbol{v})\left(\frac{\partial(\rho\psi)}{\partial\rho} - \frac{1}{2}|\boldsymbol{v}|^2\right) + \operatorname{div}(\rho\boldsymbol{v}\otimes\boldsymbol{v})\cdot\boldsymbol{v}\ \mathrm{d}\boldsymbol{x} - \int_\Omega \frac{\eta}{\rho}\mu^2\ \mathrm{d}\boldsymbol{x}$$
$$-\int_\Omega \boldsymbol{v}\cdot\rho\nabla\left(\frac{\partial(\rho\psi)}{\partial\rho}\right) - \operatorname{div}(\boldsymbol{S})\cdot\boldsymbol{v}\ \mathrm{d}\boldsymbol{x} + \int_{\partial\Omega}\varphi_t(\gamma\nabla\varphi\cdot\boldsymbol{n})\ \mathrm{d}s.$$

We integrate by parts and have

$$\frac{\mathrm{d}}{\mathrm{d}t}E(t) = -\int_\Omega \frac{\eta}{\rho}\mu^2\ \mathrm{d}\boldsymbol{x} - \int_\Omega \boldsymbol{S} : \nabla\boldsymbol{v}\ \mathrm{d}\boldsymbol{x}$$
$$+\int_{\partial\Omega}\boldsymbol{S}\boldsymbol{v}\cdot\boldsymbol{n} - \rho\boldsymbol{v}\left(\frac{\partial(\rho\psi)}{\partial\rho} + \frac{1}{2}|\boldsymbol{v}|^2\right)\cdot\boldsymbol{n}\ \mathrm{d}s + \int_{\partial\Omega}\varphi_t(\gamma\nabla\varphi\cdot\boldsymbol{n})\ \mathrm{d}s.$$

With the boundary conditions (2.9)–(2.10) we finally obtain

$$\frac{\mathrm{d}}{\mathrm{d}t}E(t) = -\int_\Omega \frac{\eta}{\rho}\mu^2\ \mathrm{d}\boldsymbol{x} - \int_\Omega \boldsymbol{S} : \nabla\boldsymbol{v}\ \mathrm{d}\boldsymbol{x}.$$

This concludes the proof. ■

2.1.2 Sharp Interface Limit

From a physical point of view, basically no interface in the real world is completely sharp. At least on the molecular-scale there is diffusive mixing. With this view, diffuse-interface models approximate the interfaces by lifting the interfacial layer from the molecular- to the macro-scale. On the other hand, from a more mathematical point of view, DI models are an approximation to sharp-interface models. In any case, DI models should recover physical admissible SI limits in order to give accurate descriptions of flow dynamics.

The SI limit is investigated for NSAC models with slightly different scaling than (2.4)–(2.6) in [39, 106, 107].

We briefly comment on the SI limits. The resulting SI limit systems depend on the scaling. With a nondimensionalization, the system (2.4)–(2.6) essentially turns into

$$\begin{aligned}
\partial_t\rho + \operatorname{div}(\rho\boldsymbol{v}) &= 0,\\
\partial_t(\rho\boldsymbol{v}) + \operatorname{div}(\rho\boldsymbol{v}\otimes\boldsymbol{v} + p\boldsymbol{I}) &= \frac{1}{\mathrm{Re}}\operatorname{div}(\boldsymbol{S}) - \varepsilon\operatorname{div}(\nabla\varphi\otimes\nabla\varphi) \quad \text{in } \Omega\times(0,T),\\
\rho\partial_t\varphi + \rho\nabla\varphi\cdot\boldsymbol{v} &= -\eta^c\eta\mu,
\end{aligned}$$

with

$$\mu = \frac{1}{\varepsilon} W'(\varphi) + \frac{\partial(\rho\psi)}{\partial\varphi} - \varepsilon\Delta\varphi.$$

Here we omit the dimensionless quantities which are chosen to be $O(1)$. They do not affect the resulting SI limit system. Therefore we restrict ourselves to the dimensionless quantities Re, ε, and η^c. Here, Re denotes the Reynolds number, ε is related to the interface thickness, and η^c to the mobility. The sharp-interface limit is characterized by taking $\varepsilon \longrightarrow 0$.
In [39] they show that $\mathrm{Re} = O(1)$ is needed in order to obtain a two-phase Navier–Stokes system in the limit. However, this either rules out mass fluxes across the interface, i.e. no phase transition, or jumps in the density. This is the situation in [106]. However, in [39] they choose $\mathrm{Re} = O(\varepsilon^{-2})$. This case leads to a two-phase Euler system in the SI limit. Then, η^c is chosen either as ε^{-2} or ε^{-3}, where the former choice leads to a dissipative regime and the latter to a non-dissipative regime. At the interface they obtain classical conditions like the Young–Laplace law and Rankine–Hugoniot conditions.
In [107] a Navier–Stokes SI limit system with phase transition is obtained. However, for that purpose the double-well potential needs to have its minima at different heights. This means that the energy cannot be controlled in the sharp interface limit, only for positive fixed interface width.
In summary there are meaningful SI limits for our system (2.4)–(2.6), where depending on the considered regime phase transition can occur.

2.1.3 Surface Tension

There are different interpretations of surface tension. It can be either viewed as a force acting in tangential direction of the interface or as an excess energy stored in the interface [61]. In line with our energy-based derivation in Section 2.1.1, we consider a planar equilibrium profile and integrate the excess free energy density over this profile. We assume that static equilibrium conditions hold, i.e. $\boldsymbol{v} = \mathbf{0}$. The planar profile is assumed to be parallel to the x_1-axis and density, velocity and phase-field are independent from t and the other space dimensions x_i, $i \neq 1$. For readability in the following we omit the subscript in x_1. Then, the equilibrium is governed by the solution of the following boundary value problem on the real line. Find $\rho = \rho(x)$, $\varphi = \varphi(x)$ such that

$$\left(-\rho\psi - \frac{1}{\gamma} W(\varphi) - \frac{\gamma}{2}\varphi_x^2 + \rho\frac{\partial(\rho\psi)}{\partial\rho}\right)_x = -\gamma(\varphi_x^2)_x, \tag{2.12}$$

$$\frac{1}{\gamma} W'(\varphi) + \frac{\partial(\rho\psi)}{\partial\varphi} - \gamma\varphi_{xx} = 0, \tag{2.13}$$

and

$$\rho(\pm\infty) = \rho_{\mathrm{V/L}}, \quad \varphi(-\infty) = 0, \quad \varphi(\infty) = 1, \quad \varphi_x(\pm\infty) = 0. \tag{2.14}$$

We assume that there exists a solution to (2.12)–(2.14). Multiplying (2.13) with φ_x and subtracting from (2.12) yields

$$\frac{\partial(\rho\psi)}{\partial\rho} = \text{const.} \tag{2.15}$$

Multiplying (2.13) with φ_x, integrating from $-\infty$ to some $x \in \mathbb{R}$ using (2.12) and (2.14) leads to

$$\frac{1}{\gamma} W(\varphi(x)) + \rho(x)\psi(\rho(x), \varphi(x)) - \rho_{\mathrm{V}}(x)\psi(\rho_{\mathrm{V}}(x), 0) = \frac{\gamma}{2}\varphi_x^2(x). \tag{2.16}$$

From (2.16) we obtain for $x \longrightarrow \infty$

$$\rho_{\mathrm{L}}\psi(\rho_{\mathrm{L}}, 1) = \rho_{\mathrm{V}}\psi(\rho_{\mathrm{V}}, 0) =: \overline{\rho\psi}. \tag{2.17}$$

As mentioned before, surface tension can be defined by means of excess free energy. Roughly speaking an excess quantity is the difference of the quantity in the considered system and in a (sharp-interface) reference system where the bulk values are maintained up to a dividing interface. We specify the interface position x_0 by vanishing excess density, i.e. the balance of mass of the two phases.
In summary, we define surface tension σ via the relationship

$$\begin{aligned}\sigma = &\int_{-\infty}^{x_0} \rho f(\rho, \varphi, \varphi_x) - \rho_{\mathrm{V}}\psi(\rho_{\mathrm{V}}, 0)\ \mathrm{d}x \\ &+ \int_{x_0}^{\infty} \rho f(\rho, \varphi, \varphi_x) - \rho_{\mathrm{L}}\psi(\rho_{\mathrm{L}}, 1)\ \mathrm{d}x,\end{aligned}$$

where (ρ, φ) is a solution of (2.12)–(2.14). Using (2.16) we have

$$\sigma = \int_{-\infty}^{x_0} \gamma\varphi_x^2\ \mathrm{d}x + \int_{x_0}^{\infty} \gamma\varphi_x^2 + (\rho_{\mathrm{V}}\psi(\rho_{\mathrm{V}}, 0) - \rho_{\mathrm{L}}\psi(\rho_{\mathrm{L}}, 1))\ \mathrm{d}x.$$

With (2.17) it follows

$$\sigma = \int_{-\infty}^{\infty} \gamma\varphi_x^2\ \mathrm{d}x,$$

and finally, with the substitution $\phi = \varphi(x)$ and (2.16), we obtain

$$\sigma = \sqrt{2} \int_{\varphi_V}^{\varphi_L} \sqrt{W(\phi) + \gamma(\rho\psi(\hat{\rho}(\phi), \phi) - \overline{\rho\psi})} \, \mathrm{d}\phi. \tag{2.18}$$

In the last step we used the transformation from x to ϕ integration. The free energies $\rho f_{L/V}$ are assumed to be convex (see (2.1) above). Hence, the function $\rho\psi$ is also convex in ρ. Due to (2.15) and the implicit function theorem there exists a function $\hat{\rho}$ such that $\rho\psi(\rho, \varphi) = \rho\psi(\hat{\rho}(\varphi), \varphi)$.
One can see that the surface tension is mainly dictated by the double well potential $W(\varphi)$. Additionally, there is a contribution due to the EOS of the different phases. However, in the sharp-interface limit, i.e. $\gamma \longrightarrow 0$, this contribution vanishes. This is a difference to (quasi-)incompressible models like in [74]. There is no contribution due to the EOS and the surface tension is purely determined by the double well potential. Of course surface tension is a material parameter and given by physics depending on the considered fluids and walls. Therefore, in simulations the double well should be scaled accordingly to yield the correct surface tension. However, this can lead to numerical difficulties. To match typical surface tension values, W has to be scaled with very small parameters. This in turn demands an even smaller γ and therefore a high spatial resolution of the computational mesh. For that reason, we use a moderate scaling in our numerical experiments in Chapters 4 and 5.

An Energy-Consistent Discontinuous Galerkin Scheme for NSAC

3

Phase-field modeling is based on a variational principle. Our model (2.4)–(2.6) is thermodynamically consistent and follows the energy dissipation law (2.11). Numerical schemes with artificial dissipation for stabilization can lead to problems like increase of energy or parasitic currents [37, 61]. Hence, it is desirable that the numerical scheme fulfills the energy dissipation inequality (2.11) on a discrete level without artificial numerical dissipation. Additionally, as common for all diffuse-interface models, we need to resolve steep gradients in the interfacial area. This motivates the use of *energy-consistent discontinuous Galerkin schemes* to solve phase-field systems [51, 69, 96].

The derivation of our scheme to solve the system (2.4)–(2.6) is based on [50]. In contrast to [69], where an energy-consistent dG scheme for a similar model has been derived, we obtain a numerical scheme with second order accuracy in time, instead of order one. The resulting scheme is by construction energy-consistent and mass conservative.

The derivation consists of multiple parts. First, in the following Section 3.1, we derive a mixed non-conservative formulation, which is needed to prove the energy consistency of the scheme. Then, in Section 3.2, we derive the spatial semi-discretization and in Section 3.3 the temporal semi-discretization. These are combined in Section 3.4 to obtain the fully discrete Scheme, described in Algorithm 3.11.

3.1 Mixed Non-Conservative Formulation

In order to prove a discrete version of Theorem 2.3, we need to use the velocity $\boldsymbol{v}$ and the variation of the energy E with respect to the density ρ and the phase-field φ as test functions. Since they depend nonlinearly on $\rho, \rho\boldsymbol{v}$, and φ, we rely on a mixed non-conservative form, which is derived in the following.

Recall the free energy density ρf, and the notations $\rho\tilde{f}$ and $\rho\psi$ from (2.1). First, we introduce auxiliary variables

$$\boldsymbol{\sigma} = \nabla\varphi,$$

$$\mu = \frac{\partial(\rho\tilde{f})}{\partial\varphi} - \operatorname{div}(\gamma\boldsymbol{\sigma}),$$
$$\tau = \frac{\partial(\rho\tilde{f})}{\partial\rho} + \frac{1}{2}|\boldsymbol{v}|^2.$$

With these, we rewrite the system (2.4)–(2.6) into a non-conservative mixed formulation

$$\partial_t\rho + \operatorname{div}(\rho\boldsymbol{v}) = 0, \tag{3.1}$$
$$\rho\partial_t\boldsymbol{v} + \operatorname{div}(\rho\boldsymbol{v}\otimes\boldsymbol{v}) - \operatorname{div}(\rho\boldsymbol{v})\boldsymbol{v} - \frac{1}{2}\rho\nabla|\boldsymbol{v}|^2 + \rho\nabla\tau = \operatorname{div}(\boldsymbol{S}) + \mu\nabla\varphi, \tag{3.2}$$
$$\partial_t\varphi + \nabla\varphi\cdot\boldsymbol{v} = -\eta\frac{\mu}{\rho}, \tag{3.3}$$
$$\mu = \frac{\partial(\rho\tilde{f})}{\partial\varphi} - \gamma\operatorname{div}(\boldsymbol{\sigma}), \tag{3.4}$$
$$\tau = \frac{\partial(\rho\tilde{f})}{\partial\rho} + \frac{1}{2}|\boldsymbol{v}|^2, \tag{3.5}$$
$$\boldsymbol{\sigma} = \nabla\varphi, \tag{3.6}$$

with the boundary conditions

$$\boldsymbol{v} = \boldsymbol{0}, \quad \boldsymbol{\sigma}\cdot\boldsymbol{n} = 0 \text{ on } \partial\Omega. \tag{3.7}$$

We define weak solutions for this mixed system. This is the basis for our following spatial dG semi-discretization.
We include the boundary conditions in the function spaces by defining

$$H_0^1(\Omega) \coloneqq \{\phi \in H^1(\Omega) : \ \phi|_{\partial\Omega} = 0\},$$
$$H_{\boldsymbol{n}}^1(\Omega) \coloneqq \{\boldsymbol{\phi} \in \left(H^1(\Omega)\right)^d \ : \ \boldsymbol{\phi}|_{\partial\Omega}\cdot\boldsymbol{n} = 0\}.$$

Let us introduce some notation in order to derive a spatial semi-discretization of (3.1)–(3.6). Let $\mathcal{T}$ be a conforming shape regular triangulation of Ω. That means $\mathcal{T} = \{T\}$ is a finite family of sets T such that

1. $T \in \mathcal{T}$ implies T is an open simplex,
2. for any $T_1, T_2 \in \mathcal{T}$ we have $\bar{T}_1 \cap \bar{T}_2$ is a full subsimplex of both, $\bar{T}_1$ and $\bar{T}_2$,
3. $\bigcup_{T\in\mathcal{T}} \bar{T} = \bar{\Omega}$.

The *meshsize* h is defined as

$$h := \max_{T \in \mathcal{T}} h_T,$$

where h_T denotes the diameter of T.

Definition 3.1 (Interface, boundary face)**:** *Let $\mathcal{T}$ be a mesh of the domain Ω. We call a subset e of $\bar{\Omega}$ a* mesh face*, if e has positive $(d-1)$-dimensional Hausdorff measure and if one of the following conditions is fulfilled:*

1. *There are two distinct mesh elements $T_1, T_2 \in \mathcal{T}$ such that $e = T_1 \cap T_2$. In this case we call e an* interface*.*
2. *There exists $T \in \mathcal{T}$ with $e = \partial T \cap \partial\Omega$. Then we call e a* boundary face*.*

Let $\mathcal{E}$ be the set of interfaces of the triangulation $\mathcal{T}$. Given a mesh face e, we denote $e \in \mathcal{E}$ if e is in the interior of Ω and $e \in \partial\Omega$ if e is a boundary face.

Definition 3.2 (Broken Sobolev spaces, trace spaces)**:** *We define for $k \geq 0$ the broken Sobolev space*

$$H^k(\mathcal{T}) := \left\{\phi \in L^2(\Omega) : \forall T \in \mathcal{T}, \phi|_T \in H^k(T)\right\},$$

and similarly for $H_0^1(\mathcal{T})$ and $H_{\boldsymbol{n}}^1(\mathcal{T})$.
In order to use functions defined in broken spaces restricted to the skeleton $\mathcal{E}$ of the triangulation, we define the trace space

$$\mathrm{Tr}(\mathcal{E}) := \prod_{T \in \mathcal{T}} L^2(\partial T).$$

Equipped with this definition and notations we are now able to give the definition of a weak solution to the system in mixed-formulation.

Definition 3.3 (Weak solution to (3.1)–(3.6) with (3.7))**:** *The tuple*

$$(\rho, \boldsymbol{v}, \varphi) \in L^2(0,T; H^1(\mathcal{T})) \times (L^2(0,T; H_0^1(\mathcal{T})))^d \times L^2(0,T; H^1(\mathcal{T}))$$

with

$$(\partial_t\rho, \partial_t\boldsymbol{v}, \partial_t\varphi) \in L^2(0,T; L^2(\mathcal{T})) \times (L^2(0,T; L^2(\mathcal{T})))^d \times L^2(0,T; L^2(\mathcal{T}))$$

and

$$(\mu, \tau, \boldsymbol{\sigma}) \in L^2(0,T; H^1(\mathcal{T})) \times L^2(0,T; H^1(\mathcal{T})) \times L^2(0,T; H_{\boldsymbol{n}}^1(\mathcal{T}))$$

such that

$$\left(\frac{\partial\rho\tilde{f}}{\partial\rho}, \frac{\partial\rho\tilde{f}}{\partial\varphi}\right) \in L^2(0,T;L^2(\mathcal{T})) \times L^2(0,T;L^2(\mathcal{T}))$$

is called a weak solution to (3.1)–(3.6) *with* (3.7) *iff*

$$\begin{aligned}
0 &= \int_\Omega (\partial_t\rho + \operatorname{div}(\rho\boldsymbol{v}))\psi \ \mathrm{d}\boldsymbol{x} + \int_{\mathcal{E}\cup\partial\Omega} F_1(\rho,\boldsymbol{v},\varphi,\mu,\tau,\boldsymbol{\sigma},\psi) \ \mathrm{d}s, \qquad (3.8)\\
0 &= \int_\Omega \Big(\rho\partial_t\boldsymbol{v} + \operatorname{div}(\rho\boldsymbol{v}\otimes\boldsymbol{v}) - \operatorname{div}(\rho\boldsymbol{v})\boldsymbol{v}\\
&\qquad + \rho\nabla\tau - \mu\nabla\varphi - \frac{1}{2}\rho\nabla|\boldsymbol{v}|^2\Big)\cdot\boldsymbol{X} \ \mathrm{d}\boldsymbol{x}\\
&\quad + \int_{\mathcal{E}\cup\partial\Omega} F_2(\rho,\boldsymbol{v},\varphi,\mu,\tau,\boldsymbol{\sigma},\boldsymbol{X}) \ \mathrm{d}s + B(\boldsymbol{v},\boldsymbol{X};\varphi),\\
0 &= \int_\Omega \left(\partial_t\varphi + \boldsymbol{v}\cdot\nabla\varphi + \eta\frac{\mu}{\rho}\right)\Theta \ \mathrm{d}\boldsymbol{x} + \int_{\mathcal{E}\cup\partial\Omega} F_3(\rho,\boldsymbol{v},\varphi,\mu,\tau,\boldsymbol{\sigma},\Theta) \ \mathrm{d}s,\\
0 &= \int_\Omega \left(\mu - \frac{\partial\rho\tilde{f}}{\partial\varphi}(\rho,\varphi) + \gamma\operatorname{div}(\boldsymbol{\sigma})\right)\chi \ \mathrm{d}\boldsymbol{x} + \int_{\mathcal{E}\cup\partial\Omega} F_4(\rho,\boldsymbol{v},\varphi,\mu,\tau,\boldsymbol{\sigma},\chi) \ \mathrm{d}s,\\
0 &= \int_\Omega \left(\tau - \frac{\partial\rho\tilde{f}}{\partial\rho}(\rho,\varphi) - \frac{1}{2}|\boldsymbol{v}|^2\right)\zeta \ \mathrm{d}\boldsymbol{x} + \int_{\mathcal{E}\cup\partial\Omega} F_5(\rho,\boldsymbol{v},\varphi,\mu,\tau,\boldsymbol{\sigma},\zeta) \ \mathrm{d}s,\\
0 &= \int_\Omega (\boldsymbol{\sigma} - \nabla\varphi)\cdot\boldsymbol{Z} \ \mathrm{d}\boldsymbol{x} + \int_{\mathcal{E}\cup\partial\Omega} F_6(\rho,\boldsymbol{v},\varphi,\mu,\tau,\boldsymbol{\sigma},\boldsymbol{Z}) \ \mathrm{d}s, \qquad (3.9)\\
&\forall(\psi,\boldsymbol{X},\Theta,\chi,\zeta,\boldsymbol{Z}) \in H^1(\mathcal{T}) \times (H_0^1(\mathcal{T}))^d \times H^1(\mathcal{T}) \times H^1(\mathcal{T}) \times H^1(\mathcal{T}) \times H_{\boldsymbol{n}}^1(\mathcal{T}).
\end{aligned}$$

Here,

$$\begin{aligned}
F_1, F_3, F_4, F_5 &: H^1(\mathcal{T}) \times (H_0^1(\mathcal{T}))^d \times H^1(\mathcal{T}) \times H^1(\mathcal{T}) \times H^1(\mathcal{T}) \times H_{\boldsymbol{n}}^1(\mathcal{T}) \times H^1(\mathcal{T})\\
&\qquad \to L^2(\mathcal{E}),\\
F_2 &: H^1(\mathcal{T}) \times (H_0^1(\mathcal{T}))^d \times H^1(\mathcal{T}) \times H^1(\mathcal{T}) \times H^1(\mathcal{T}) \times H_{\boldsymbol{n}}^1(\mathcal{T}) \times (H_0^1(\mathcal{T}))^d\\
&\qquad \to L^2(\mathcal{E}),\\
F_6 &: H^1(\mathcal{T}) \times (H_0^1(\mathcal{T}))^d \times H^1(\mathcal{T}) \times H^1(\mathcal{T}) \times H^1(\mathcal{T}) \times H_{\boldsymbol{n}}^1(\mathcal{T}) \times H_{\boldsymbol{n}}^1(\mathcal{T})\\
&\qquad \to L^2(\mathcal{E})
\end{aligned}$$

are elementwise fluxes, which are chosen in the sequel to fulfill our requirements. The bilinear form $B : (H_0^1(\mathcal{T}))^d \times (H_0^1(\mathcal{T}))^d \times H^1(\mathcal{T}) \to \mathbb{R}$ *corresponds to the weak formulation of the divergence of the viscous stress tensor* $\boldsymbol{S}$*. The notation* $\int_\Omega \bullet \ \mathrm{d}\boldsymbol{x}$ *means* $\sum_{T\in\mathcal{T}} \int_T \bullet \ \mathrm{d}\boldsymbol{x}$.

Remark 3.4: *1. The spaces for the variational formulation are chosen in a way that all occurring integrals are well-defined. However, we assume the existence of weak solutions. There is no well-posedness analysis for this system up to our knowledge. We use Definition 3.3 solely to derive the dG scheme Algorithm 3.11.*

2. We have used a non-conservative formulation for the momentum balance equation in (3.2)*. However, it is too restrictive to have mass conservation, energy consistency* and *conservation of momentum. We drop the momentum conservation property in favor of the others.*

3.2 Spatial Semi-Discretization

In the following, we develop the energy-consistent dG scheme. For convenience, we split the derivation in two parts. The first one is the spatial semi-discretization, presented in this section. The second part is the temporal semi-discretization, derived in the next section. In order to obtain the full scheme, both parts need to be combined.
In this section, we derive conditions for the fluxes $F_1, \dots, F_6$ of a generic scheme applied to the mixed variational formulation (3.8)–(3.9). The desired properties of this generic system are the conservation of mass and energy consistency.
We now define the discontinuous Galerkin space by

$$\begin{aligned} V_h &\coloneqq \left\{u \in L^2(\Omega) : \ \forall T \in \mathcal{T}, u|_T \in \mathbb{P}^k\right\}, \\ \overset{\circ}{V}_h &\coloneqq V_h \cap H_0^1(\mathcal{T}), \\ \overset{\boldsymbol{n}}{V}_h &\coloneqq V_h \cap H_{\boldsymbol{n}}^1(\mathcal{T}), \end{aligned}$$

where $\mathbb{P}^k$ is the space of polynomials up to degree k.
Further, let $\mathcal{V}_h = V_h \times (\overset{\circ}{V}_h)^d \times V_h \times V_h \times V_h \times \overset{\boldsymbol{n}}{V}_h$.

Definition 3.5 (Jump and average operators)**:** *We define the jump and average operators as follows: Let T_1 and T_2 be two mesh elements with a common facet e, Φ a scalar-valued and $\boldsymbol{u}$ a vector-valued function on Ω. In addition, let T be a mesh element with boundary facet $e_b = \partial T \cap \partial\Omega$. Then,*

$$\begin{aligned} \{\Phi\}_e &\coloneqq \frac{1}{2}(\Phi|_{T_1} + \Phi|_{T_2}), & \{\Phi\}_{e_b} &\coloneqq \Phi|_T, \\ \{\boldsymbol{u}\}_e &\coloneqq \frac{1}{2}(\boldsymbol{u}|_{T_1} + \boldsymbol{u}|_{T_2}), & \{\boldsymbol{u}\}_{e_b} &\coloneqq \boldsymbol{u}|_T, \\ [\![\Phi]\!]_e &\coloneqq \Phi|_{T_1}\boldsymbol{n}_{T_1} + \Phi|_{T_2}\boldsymbol{n}_{T_2}, & [\![\Phi]\!]_{e_b} &\coloneqq \Phi|_T\boldsymbol{n}_T, \\ [\![\boldsymbol{u}]\!]_e &\coloneqq \boldsymbol{u}|_{T_1} \cdot \boldsymbol{n}_{T_1} + \boldsymbol{u}|_{T_2} \cdot \boldsymbol{n}_{T_2}, & [\![\boldsymbol{u}]\!]_{e_b} &\coloneqq \boldsymbol{u}|_T \cdot \boldsymbol{n}_T, \end{aligned}$$

$$[\![\boldsymbol{u}]\!]_{\otimes,e} \coloneqq \boldsymbol{u}|_{T_1} \otimes \boldsymbol{n}_{T_1} + \boldsymbol{u}|_{T_2} \otimes \boldsymbol{n}_{T_2}, \qquad [\![\boldsymbol{u}]\!]_{\otimes,e_b} \coloneqq \boldsymbol{u}|_T \otimes \boldsymbol{n}_T.$$

We omit the subscripts e, e_b whenever no confusion can arise.

Equipped with the definitions above, we introduce the spatially discrete dG formulation of the problem (3.1)–(3.6).
To discretize the viscous stress tensor, we use a coercive discrete bilinear form $B_h : (\mathring{V}_h)^d \times (\mathring{V}_h)^d \times V_h) \longrightarrow \mathbb{R}$.
The generic spatially discrete problem reads

Algorithm 3.6 (Generic spatially semi-discrete scheme)**:**
Find $(\rho_h, \boldsymbol{v}_h, \varphi_h, \mu_h, \tau_h, \boldsymbol{\sigma}_h) : [0, T] \longrightarrow \mathcal{V}_h$ *such that*

$$0 = \int_\Omega (\partial_t \rho_h + \operatorname{div}(\rho_h \boldsymbol{v}_h))\psi \ \mathrm{d}\boldsymbol{x} + \int_{\mathcal{E}\cup\partial\Omega} F_1(\rho_h, \boldsymbol{v}_h, \varphi_h, \mu_h, \tau_h, \boldsymbol{\sigma}_h, \psi) \ \mathrm{d}s \tag{3.10}$$

$$\begin{aligned} 0 = \int_\Omega \Big(& \rho_h \partial_t \boldsymbol{v}_h + \operatorname{div}(\rho_h \boldsymbol{v}_h \otimes \boldsymbol{v}_h) - \operatorname{div}(\rho_h \boldsymbol{v}_h)\boldsymbol{v}_h \\ & + \rho_h \nabla \tau_h - \mu_h \nabla \varphi_h - \frac{1}{2}\rho_h \nabla |\boldsymbol{v}_h|^2 \Big) \cdot \boldsymbol{X} \ \mathrm{d}\boldsymbol{x} \\ & + \int_{\mathcal{E}\cup\partial\Omega} F_2(\rho_h, \boldsymbol{v}_h, \varphi_h, \mu_h, \tau_h, \boldsymbol{\sigma}_h, \boldsymbol{X}) \ \mathrm{d}s + B_h(\boldsymbol{v}_h, \boldsymbol{X}; \varphi_h) \end{aligned} \tag{3.11}$$

$$\begin{aligned} 0 = & \int_\Omega \left(\partial_t \varphi_h + \boldsymbol{v}_h \cdot \nabla \varphi_h + \eta \frac{\mu_h}{\rho_h} \right) \Theta \ \mathrm{d}\boldsymbol{x} \\ & + \int_{\mathcal{E}\cup\partial\Omega} F_3(\rho_h, \boldsymbol{v}_h, \varphi_h, \mu_h, \tau_h, \boldsymbol{\sigma}_h, \Theta) \ \mathrm{d}s \end{aligned} \tag{3.12}$$

$$\begin{aligned} 0 = & \int_\Omega \left(\mu_h - \frac{\partial \rho \tilde{f}}{\partial \varphi}(\rho_h, \varphi_h) + \gamma \operatorname{div}(\boldsymbol{\sigma}_h) \right) \chi \ \mathrm{d}\boldsymbol{x} \\ & + \int_{\mathcal{E}\cup\partial\Omega} F_4(\rho_h, \boldsymbol{v}_h, \varphi_h, \mu_h, \tau_h, \boldsymbol{\sigma}_h, \chi) \ \mathrm{d}s \end{aligned} \tag{3.13}$$

$$\begin{aligned} 0 = & \int_\Omega \left(\tau_h - \frac{\partial \rho \tilde{f}}{\partial \rho}(\rho_h, \varphi_h) - \frac{1}{2}|\boldsymbol{v}_h|^2 \right) \zeta \ \mathrm{d}\boldsymbol{x} \\ & + \int_{\mathcal{E}\cup\partial\Omega} F_5(\rho_h, \boldsymbol{v}_h, \varphi_h, \mu_h, \tau_h, \boldsymbol{\sigma}_h, \zeta) \ \mathrm{d}s \end{aligned} \tag{3.14}$$

$$0 = \int_\Omega (\boldsymbol{\sigma}_h - \nabla \varphi_h) \cdot \boldsymbol{Z} \ \mathrm{d}\boldsymbol{x} + \int_{\mathcal{E}\cup\partial\Omega} F_6(\rho_h, \boldsymbol{v}_h, \varphi_h, \mu_h, \tau_h, \boldsymbol{\sigma}_h, \boldsymbol{Z}) \ \mathrm{d}s \tag{3.15}$$

$$\forall\, (\psi, \boldsymbol{X}, \Theta, \chi, \zeta, \boldsymbol{Z}) \in \mathcal{V}_h.$$

In order to complete the spatial semi-disrete scheme, we need to specify the discrete bilinear form B_h. For the sake of maintaining the symmetry of the exact bilinear form and to obtain a discrete coercivity property, we rely on a symmetric interior penalty discretization [6]:

$$\begin{aligned} B_h(\boldsymbol{v}, \boldsymbol{X}; \varphi_h) = &\int_\Omega \boldsymbol{S}(\nabla \boldsymbol{v}, \varphi) : \nabla \boldsymbol{X} \, \mathrm{d}\boldsymbol{x} \\ &- \sum_{e \in \mathcal{E} \cup \partial\Omega} \int_e \{\boldsymbol{S}(\nabla \boldsymbol{v}, \varphi)\} : [\![\boldsymbol{X}]\!]_\otimes + \{\boldsymbol{S}(\nabla \boldsymbol{X}, \varphi)\} : [\![\boldsymbol{v}]\!]_\otimes \, \mathrm{d}s \\ &+ \sum_{e \in \mathcal{E} \cup \partial\Omega} \int_e \frac{\alpha_B}{|e|} [\![\boldsymbol{v}]\!]_\otimes : [\![\boldsymbol{X}]\!]_\otimes \, \mathrm{d}s. \end{aligned} \tag{3.16}$$

If α_B is chosen sufficiently large, we ensure coercivity of $B_h(\bullet, \bullet; \varphi)$.

To prove the mass conservation and energy consistency of (3.10)–(3.36) in Theorem 3.8, we make use of the following proposition:

Proposition 3.7 (Elementwise integration)**:** *Let*

$$H^{\mathrm{div}}(\mathcal{T}) \coloneqq \{\boldsymbol{u} \in (L^2(\mathcal{T}))^d : \ \mathrm{div}(\boldsymbol{u}) \in L^2(\mathcal{T})\}.$$

If $\boldsymbol{u} \in H^{\mathrm{div}}(\mathcal{T})$ and $\varphi \in H^1(\mathcal{T})$, then

$$\begin{aligned} \sum_{T \in \mathcal{T}} \int_T \mathrm{div}(\boldsymbol{u}) \varphi \, \mathrm{d}\boldsymbol{x} &= \sum_{T \in \mathcal{T}} \left(- \int_T \boldsymbol{u} \cdot \nabla \varphi \, \mathrm{d}\boldsymbol{x} + \int_{\partial T} \varphi \boldsymbol{u} \cdot \boldsymbol{n}_T \, \mathrm{d}s \right) \\ &= \sum_{T \in \mathcal{T}} - \int_T \boldsymbol{u} \cdot \nabla \varphi \, \mathrm{d}\boldsymbol{x} + \int_{\mathcal{E} \cup \partial\Omega} [\![\boldsymbol{u}]\!] \{\varphi\} \, \mathrm{d}s + \int_{\mathcal{E} \cup \partial\Omega} [\![\varphi]\!] \{\boldsymbol{u}\} \, \mathrm{d}s \\ &= - \int_\Omega \boldsymbol{u} \cdot \nabla \varphi \, \mathrm{d}\boldsymbol{x} + \int_{\mathcal{E} \cup \partial\Omega} [\![\varphi \boldsymbol{u}]\!] \, \mathrm{d}s. \end{aligned}$$

Proof. The identities follow by elementwise partial integration and the definition of the jump and average operators, see Definition 3.5. ∎

We present the theorem

Theorem 3.8: *A generic scheme of the form* (3.10)–(3.15)

1. *conserves mass iff*

$$\int_{\mathcal{E} \cup \partial\Omega} F_1(\rho_h, \boldsymbol{v}_h, \varphi_h, \mu_h, \tau_h, \boldsymbol{\sigma}_h, 1) \, \mathrm{d}s = - \int_{\mathcal{E} \cup \partial\Omega} [\![\rho_h \boldsymbol{v}_h]\!] \, \mathrm{d}s \qquad \forall (\rho_h, \boldsymbol{v}_h, \varphi_h, \mu_h, \tau_h, \boldsymbol{\sigma}_h) \in \mathcal{V}_h.$$

Here, 1 *is the constant function with value* 1 *everywhere on* Ω*,*

2. *satisfies the energy dissipation equality*

$$\begin{aligned}\frac{\mathrm{d}}{\mathrm{d}\,t}\left(\int_\Omega \rho\tilde{f}(\rho_h,\varphi_h)+\frac{\gamma}{2}|\boldsymbol{\sigma}_h|^2+\frac{\rho_h}{2}|\boldsymbol{v}_h|^2\ \mathrm{d}\boldsymbol{x}\right)\\ =-\int_\Omega \frac{\eta}{\rho_h}\mu_h^2\ \mathrm{d}\boldsymbol{x}-\int_\Omega B_h(\boldsymbol{v}_h,\boldsymbol{v}_h;\varphi_h)\ \mathrm{d}\boldsymbol{x}\\ \leq 0\end{aligned} \tag{3.17}$$

iff

$$\begin{aligned}0=&-\int_{\mathcal{E}\cup\partial\Omega}\gamma D_t F_6(\rho_h,\boldsymbol{v}_h,\varphi_h,\mu_h,\tau_h,\boldsymbol{\sigma}_h,\boldsymbol{\sigma}_h)-\gamma[\![\partial_t\varphi_h\boldsymbol{\sigma}_h]\!]\ \mathrm{d}s\\ &-\int_{\mathcal{E}\cup\partial\Omega}F_4(\rho_h,\boldsymbol{v}_h,\varphi_h,\mu_h,\tau_h,\boldsymbol{\sigma}_h,\partial_t\varphi_h)\ \mathrm{d}s\end{aligned} \tag{3.18}$$

$$\begin{aligned}0=&\int_{\mathcal{E}\cup\partial\Omega}F_1(\rho_h,\boldsymbol{v}_h,\varphi_h,\mu_h,\tau_h,\boldsymbol{\sigma}_h,\tau_h)\ \mathrm{d}s\\ &+\int_{\mathcal{E}\cup\partial\Omega}F_2(\rho_h,\boldsymbol{v}_h,\varphi_h,\mu_h,\tau_h,\boldsymbol{\sigma}_h,\boldsymbol{v}_h)\ \mathrm{d}s\\ &+\int_{\mathcal{E}\cup\partial\Omega}F_3(\rho_h,\boldsymbol{v}_h,\varphi_h,\mu_h,\tau_h,\boldsymbol{\sigma}_h,\mu_h)+[\![\rho_h\boldsymbol{v}_h\tau_h]\!]\ \mathrm{d}s.\end{aligned} \tag{3.19}$$

for all $(\rho_h,\boldsymbol{v}_h,\varphi_h,\mu_h,\tau_h,\boldsymbol{\sigma}_h):\ [0,T]\longrightarrow\mathcal{V}_h$.

Proof. 1. We use $\psi\equiv 1$ in (3.10) and obtain

$$\begin{aligned}0=&\partial_t\left(\int_\Omega\rho_h\ \mathrm{d}\boldsymbol{x}\right)=\int_\Omega\partial_t\rho_h\ \mathrm{d}\boldsymbol{x}=-\int_\Omega\operatorname{div}(\rho_h\boldsymbol{v}_h)\ \mathrm{d}\boldsymbol{x}\\ &-\int_{\mathcal{E}\cup\partial\Omega}F_1(\rho_h,\boldsymbol{v}_h,\varphi_h,\mu_h,\tau_h,\boldsymbol{\sigma}_h,1)\ \mathrm{d}s.\end{aligned}$$

We infer with Proposition 3.7 and $\boldsymbol{v}=\boldsymbol{0}$ on $\partial\Omega$

$$=-\int_{\mathcal{E}\cup\partial\Omega}[\![\rho_h\boldsymbol{v}_h]\!]\{1\}\ \mathrm{d}s-\int_{\mathcal{E}\cup\partial\Omega}F_1(\rho_h,\boldsymbol{v}_h,\varphi_h,\mu_h,\tau_h,\boldsymbol{\sigma}_h,1)\ \mathrm{d}s.$$

2. With

$$E(\rho_h,\boldsymbol{v}_h,\varphi_h,\boldsymbol{\sigma}_h)=\int_\Omega\rho\tilde{f}(\rho_h,\varphi_h)+\frac{\gamma}{2}|\boldsymbol{\sigma}_h|^2+\frac{\rho_h}{2}|\boldsymbol{v}_h|^2\ \mathrm{d}\boldsymbol{x}$$

we want to show (3.17).

Hence, we explicitly compute the time derivative

$$\partial_t E = \int_\Omega \frac{\partial \rho \tilde{f}}{\partial \rho}(\rho_h, \varphi_h)\partial_t \rho_h + \frac{\partial \rho \tilde{f}}{\partial \varphi}(\rho_h, \varphi_h)\partial_t \varphi_h + \frac{1}{2}\partial_t \rho_h |\boldsymbol{v}_h|^2 + \rho_h \boldsymbol{v}_h \cdot \partial_t \boldsymbol{v}_h + \gamma \boldsymbol{\sigma}_h : \partial_t \boldsymbol{\sigma}_h \, \mathrm{d}\boldsymbol{x}.$$

With (3.15) we obtain

$$\begin{aligned}\partial_t E = \int_\Omega & \frac{\partial \rho \tilde{f}}{\partial \rho}(\rho_h, \varphi_h)\partial_t \rho_h + \frac{\partial \rho \tilde{f}}{\partial \varphi}(\rho_h, \varphi_h)\partial_t \varphi_h + \frac{1}{2}\partial_t \rho_h |\boldsymbol{v}_h|^2 \\ & + \rho_h \boldsymbol{v}_h \cdot \partial_t \boldsymbol{v}_h + \gamma \boldsymbol{\sigma}_h : \nabla(\partial_t \varphi_h) \, \mathrm{d}\boldsymbol{x} \\ & - \gamma \int_{\mathcal{E}} D_t F_6(\rho_h, \boldsymbol{v}_h, \varphi_h, \mu_h, \tau_h, \boldsymbol{\sigma}_h, \boldsymbol{\sigma}_h) \, \mathrm{d}s.\end{aligned}$$

Applying Proposition 3.7 yields

$$\begin{aligned}\partial_t E = \int_\Omega & \frac{\partial \rho \tilde{f}}{\partial \rho}(\rho_h, \varphi_h)\partial_t \rho_h + \frac{\partial \rho \tilde{f}}{\partial \varphi}(\rho_h, \varphi_h)\partial_t \varphi_h + \frac{1}{2}\partial_t \rho_h |\boldsymbol{v}_h|^2 \\ & + \rho_h \boldsymbol{v}_h \cdot \partial_t \boldsymbol{v}_h - \gamma \partial_t \varphi_h \cdot \operatorname{div}(\boldsymbol{\sigma}_h) \, \mathrm{d}\boldsymbol{x} \\ & - \gamma \int_{\mathcal{E}} D_t F_6(\rho_h, \boldsymbol{v}_h, \varphi_h, \mu_h, \tau_h, \boldsymbol{\sigma}_h, \boldsymbol{\sigma}_h) - [\![(\partial_t \varphi_h)\boldsymbol{\sigma}_h]\!] \, \mathrm{d}s \\ & + \int_{\partial\Omega} \gamma \partial_t \varphi_h \boldsymbol{\sigma}_h \boldsymbol{n} \, \mathrm{d}s.\end{aligned}$$

Using (3.11) and (3.13) we obtain

$$\begin{aligned}\partial_t E = \int_\Omega & \tau_h \partial_t \rho_h + \mu_h \partial_t \varphi_h - \operatorname{div}(\rho_h \boldsymbol{v}_h \otimes \boldsymbol{v}_h)\boldsymbol{v}_h + \operatorname{div}(\rho_h \boldsymbol{v}_h)|\boldsymbol{v}_h|^2 \\ & - \rho_h \boldsymbol{v}_h \nabla \tau_h + \mu_h \boldsymbol{v}_h \nabla \varphi_h + \frac{1}{2}\rho_h \boldsymbol{v}_h \nabla |\boldsymbol{v}_h|^2 \, \mathrm{d}\boldsymbol{x} \\ & - \int_{\mathcal{E}} F_4(\rho_h, \boldsymbol{v}_h, \varphi_h, \mu_h, \tau_h, \boldsymbol{\sigma}_h, \partial_t \varphi_h) \, \mathrm{d}s \\ & - \gamma \int_{\mathcal{E}} D_t F_6(\rho_h, \boldsymbol{v}_h, \varphi_h, \mu_h, \tau_h, \boldsymbol{\sigma}_h, \boldsymbol{\sigma}_h) - [\![(\partial_t \varphi_h)\boldsymbol{\sigma}_h]\!] \, \mathrm{d}s \\ & + \int_{\partial\Omega} \gamma \partial_t \varphi_h \boldsymbol{\sigma}_h \boldsymbol{n} \, \mathrm{d}s - \int_{\mathcal{E}} F_2(\rho_h, \boldsymbol{v}_h, \varphi_h, \mu_h, \tau_h, \boldsymbol{\sigma}_h, \boldsymbol{v}_h) \, \mathrm{d}s\end{aligned}$$

$$- B_h(\boldsymbol{v}_h, \boldsymbol{v}_h; \varphi_h).$$

We eliminate the time derivatives of ρ and φ with (3.10) and (3.12) which results in

$$\begin{aligned}
\partial_t E = \int_\Omega & -\tau_h \operatorname{div}(\rho_h \boldsymbol{v}_h) - \mu_h \nabla \varphi_h \cdot \boldsymbol{v}_h - \eta \frac{|\mu_h|^2}{\rho_h} \\
& - \operatorname{div}(\rho_h \boldsymbol{v}_h \otimes \boldsymbol{v}_h)\boldsymbol{v}_h + \operatorname{div}(\rho_h \boldsymbol{v}_h)|\boldsymbol{v}_h|^2 - \rho_h \boldsymbol{v}_h \nabla \tau_h \\
& + \mu_h \boldsymbol{v}_h \cdot \nabla \varphi_h + \frac{1}{2} \rho_h \boldsymbol{v}_h \nabla |\boldsymbol{v}_h|^2 \, \mathrm{d}\boldsymbol{x} \\
& - \int_{\mathcal{E}} F_4(\rho_h, \boldsymbol{v}_h, \varphi_h, \mu_h, \tau_h, \boldsymbol{\sigma}_h, \partial_t \varphi_h) \, \mathrm{d}s \\
& - \gamma \int_{\mathcal{E}} D_t F_6(\rho_h, \boldsymbol{v}_h, \varphi_h, \mu_h, \tau_h, \boldsymbol{\sigma}_h, \boldsymbol{\sigma}_h) - [\![(\partial_t \varphi_h) \boldsymbol{\sigma}_h]\!] \, \mathrm{d}s \\
& + \int_{\partial\Omega} \gamma \partial_t \varphi_h \boldsymbol{\sigma}_h \boldsymbol{n} \, \mathrm{d}s \\
& - \int_{\mathcal{E}} F_2(\rho_h, \boldsymbol{v}_h, \varphi_h, \mu_h, \tau_h, \boldsymbol{\sigma}_h, \boldsymbol{v}_h) \, \mathrm{d}s - B_h(\boldsymbol{v}_h, \boldsymbol{v}_h; \varphi_h) \\
& - \int_{\mathcal{E}} F_3(\rho_h, \boldsymbol{v}_h, \varphi_h, \mu_h, \tau_h, \boldsymbol{\sigma}_h, \mu_h) \, \mathrm{d}s - \int_{\mathcal{E}} F_1(\rho_h, \boldsymbol{v}_h, \varphi_h, \mu_h, \tau_h, \boldsymbol{\sigma}_h, \tau_h) \, \mathrm{d}s.
\end{aligned}$$

Finally, we obtain

$$\begin{aligned}
\partial_t E = & - \int_{\mathcal{E}} F_4(\rho_h, \boldsymbol{v}_h, \varphi_h, \mu_h, \tau_h, \boldsymbol{\sigma}_h, \partial_t \varphi_h) \, \mathrm{d}s \\
& - \gamma \int_{\mathcal{E}} D_t F_6(\rho_h, \boldsymbol{v}_h, \varphi_h, \mu_h, \tau_h, \boldsymbol{\sigma}_h, \boldsymbol{\sigma}_h) - [\![\partial_t \varphi_h \boldsymbol{\sigma}_h]\!] \, \mathrm{d}s \\
& + \int_{\partial\Omega} \gamma \partial_t \varphi_h \boldsymbol{\sigma}_h \cdot \boldsymbol{n} \, \mathrm{d}s \\
& - \int_{\mathcal{E} \cup \partial\Omega} [\![\rho_h \boldsymbol{v}_h \tau_h]\!] \, \mathrm{d}s - \int_{\mathcal{E}} F_1(\rho_h, \boldsymbol{v}_h, \varphi_h, \mu_h, \tau_h, \boldsymbol{\sigma}_h, \tau_h) \, \mathrm{d}s \\
& - \int_{\mathcal{E}} F_2(\rho_h, \boldsymbol{v}_h, \varphi_h, \mu_h, \tau_h, \boldsymbol{\sigma}_h, \boldsymbol{v}_h) \, \mathrm{d}s - \int_{\mathcal{E}} F_3(\rho_h, \boldsymbol{v}_h, \varphi_h, \mu_h, \tau_h, \boldsymbol{\sigma}_h, \mu_h) \, \mathrm{d}s \\
& - B_h(\boldsymbol{v}_h, \boldsymbol{v}_h; \varphi_h) - \int_\Omega \eta \frac{\mu_h^2}{\rho_h} \, \mathrm{d}\boldsymbol{x}.
\end{aligned}$$

To fulfill the discrete energy dissipation equation (3.17), we need

$$\begin{aligned}
0 = &- \int_{\mathcal{E}} F_4(\rho_h, \boldsymbol{v}_h, \varphi_h, \mu_h, \tau_h, \boldsymbol{\sigma}_h, \partial_t \varphi_h) \, \mathrm{d}s \\
&- \gamma \int_{\mathcal{E}} D_t F_6(\rho_h, \boldsymbol{v}_h, \varphi_h, \mu_h, \tau_h, \boldsymbol{\sigma}_h, \boldsymbol{\sigma}_h) - [\![\partial_t \varphi_h \boldsymbol{\sigma}_h]\!] \, \mathrm{d}s \\
&+ \int_{\partial\Omega} \gamma \partial_t \varphi_h \boldsymbol{\sigma}_h \cdot \boldsymbol{n} \, \mathrm{d}s \\
&- \int_{\mathcal{E}\cup\partial\Omega} [\![\rho_h \boldsymbol{v}_h \tau_h]\!] \, \mathrm{d}s - \int_{\mathcal{E}} F_1(\rho_h, \boldsymbol{v}_h, \varphi_h, \mu_h, \tau_h, \boldsymbol{\sigma}_h, \tau_h) \, \mathrm{d}s \\
&- \int_{\mathcal{E}} F_2(\rho_h, \boldsymbol{v}_h, \varphi_h, \mu_h, \tau_h, \boldsymbol{\sigma}_h, \boldsymbol{v}_h) \, \mathrm{d}s \\
&- \int_{\mathcal{E}} F_3(\rho_h, \boldsymbol{v}_h, \varphi_h, \mu_h, \tau_h, \boldsymbol{\sigma}_h, \mu_h) \, \mathrm{d}s.
\end{aligned}$$

Note that when this equality holds, F_6 cannot depend on $\rho_h, \boldsymbol{v}_h, \tau_h, \mu_h, \boldsymbol{\sigma}_h$. Additionally, every summand in $D_t F_6$ and F_4 has to depend on $\partial_t \varphi_h$. Since the trace of $\partial_t \varphi_h$ is independent of the traces of the other quantities, the terms containing $\partial_t \varphi_h$ and the ones without $\partial_t \varphi_h$ need to cancel each other. This yields the two conditions (3.18) and (3.19). ■

The following (non-unique) choice of fluxes fulfills the condition of the theorem:

$$\begin{aligned}
F_1 &= -[\![\rho_h \boldsymbol{v}_h]\!] \{\psi\}, \\
F_2 &= -[\![\tau_h]\!] \{\rho_h \boldsymbol{X}\} + [\![\varphi_h]\!] \{\mu_h \boldsymbol{X}\}, \\
F_3 &= -[\![\varphi_h]\!] \{\Theta \boldsymbol{v}_h\}, \\
F_4 &= -\gamma [\![\boldsymbol{\sigma}_h]\!] \{\chi\}, \\
F_6 &= [\![\varphi_h]\!] \{\boldsymbol{Z}\}.
\end{aligned}$$

For stabilization reasons we might allow to dissipate a small additional amount of energy. Then the conditions of Theorem 3.8 relax to

$$\begin{aligned}
0 \geq &- \int_{\mathcal{E}\cup\partial\Omega} \gamma D_t F_6(\rho_h, \boldsymbol{v}_h, \varphi_h, \mu_h, \tau_h, \boldsymbol{\sigma}_h, \boldsymbol{\sigma}_h) - \gamma [\![\partial_t \varphi_h \boldsymbol{\sigma}_h]\!] \, \mathrm{d}s \\
&- \int_{\mathcal{E}\cup\partial\Omega} F_4(\rho_h, \boldsymbol{v}_h, \varphi_h, \mu_h, \tau_h, \boldsymbol{\sigma}_h, \partial_t \varphi_h) \, \mathrm{d}s, \\
0 \leq &\int_{\mathcal{E}\cup\partial\Omega} F_1(\rho_h, \boldsymbol{v}_h, \varphi_h, \mu_h, \tau_h, \boldsymbol{\sigma}_h, \tau_h) \, \mathrm{d}s + \int_{\mathcal{E}\cup\partial\Omega} F_2(\rho_h, \boldsymbol{v}_h, \varphi_h, \mu_h, \tau_h, \boldsymbol{\sigma}_h, \boldsymbol{v}_h) \, \mathrm{d}s
\end{aligned}$$

$$+ \int_{\mathcal{E}\cup\partial\Omega} F_3(\rho_h, \boldsymbol{v}_h, \varphi_h, \mu_h, \tau_h, \boldsymbol{\sigma}_h, \mu_h) + [\![\rho_h \boldsymbol{v}_h \tau_h]\!] \, \mathrm{d}s.$$

This allows the following choice of fluxes ($\alpha_1, \alpha_2, \alpha_3 \geq 0$):

$$F_1 = -[\![\rho_h \boldsymbol{v}_h]\!]\{\psi\} + \alpha_1 [\![\tau_h]\!][\![\psi]\!], \tag{3.20}$$

$$F_2 = -[\![\tau_h]\!]\{\rho_h \boldsymbol{X}\} + [\![\varphi_h]\!]\{\mu_h \boldsymbol{X}\} + \alpha_2 [\![\boldsymbol{v}_h]\!][\![\boldsymbol{X}]\!], \tag{3.21}$$

$$F_3 = -[\![\varphi_h]\!]\{\Theta \boldsymbol{v}_h\} + \alpha_3 [\![\mu_h]\!][\![\Theta]\!], \tag{3.22}$$

$$F_4 = -\gamma [\![\boldsymbol{\sigma}_h]\!]\{\chi\}, \tag{3.23}$$

$$F_6 = [\![\varphi_h]\!]\{\boldsymbol{Z}\}. \tag{3.24}$$

3.3 Temporal Semi-Discretization

Let $0 = t_0 < t_1 < \ldots < t_N = T$ be a temporal decomposition of $[0, T]$. We set $\Delta t_n = t_{n+1} - t_n$. Moreover, we denote $\Phi^n(\cdot) = \Phi(\cdot, t_n)$ and $\Phi^{n+1/2} = \frac{\Phi^{n+1}+\Phi^n}{2}$. The temporal discretisation is of Crank–Nicholson type and chosen in a way that the discrete energy inequality holds. The resulting scheme is of second order accuracy.

Algorithm 3.9 (Temporal semi-discrete energy-consistent scheme)**:** *With initial conditions $\rho^0, \boldsymbol{v}^0, \varphi^0, \mu^0, \tau^0, \boldsymbol{\sigma}^0$ the temporal semi-discrete scheme reads as:*
For $n \in \mathbb{N}_0$ find $\rho^{n+1}, \boldsymbol{v}^{n+1}, \varphi^{n+1}, \mu^{n+1}, \tau^{n+1}, \boldsymbol{\sigma}^{n+1}$ such that $\boldsymbol{v}^{n+1} = 0$ and $\boldsymbol{\sigma}^{n+1} \cdot \boldsymbol{n} = 0$ on $\partial\Omega$ and

$$0 = \frac{\rho^{n+1} - \rho^n}{\Delta t_n} + \operatorname{div}(\rho^{n+1/2} \boldsymbol{v}^{n+1/2}) \tag{3.25}$$

$$\begin{aligned} \boldsymbol{0} =& \rho^{n+1/2} \left(\frac{\boldsymbol{v}^{n+1} - \boldsymbol{v}^n}{\Delta t_n} \right) + \operatorname{div}(\rho^{n+1/2} \boldsymbol{v}^{n+1/2} \otimes \boldsymbol{v}^{n+1/2}) - \operatorname{div}(\rho^{n+1/2} \boldsymbol{v}^{n+1/2}) \boldsymbol{v}^{n+1/2} \\ & - \frac{1}{2} \rho^{n+1/2} \nabla |\boldsymbol{v}^{n+1/2}|^2 + \rho^{n+1/2} \nabla \tau^{n+1/2} - \mu^{n+1/2} \nabla \varphi^{n+1/2} - \operatorname{div}(\boldsymbol{S}(\varphi^{n+1/2}, \nabla \boldsymbol{v}^{n+1/2})) \end{aligned} \tag{3.26}$$

$$0 = \frac{\varphi^{n+1} - \varphi^n}{\Delta t_n} + \nabla \varphi^{n+1/2} \cdot \boldsymbol{v}^{n+1/2} + \eta \frac{\mu^{n+1/2}}{\rho^{n+1/2}} \tag{3.27}$$

$$0 = \mu^{n+1/2} - \frac{\rho^{n+1} \tilde{f}(\rho^{n+1}, \varphi^{n+1}) - \rho^{n+1} \tilde{f}(\rho^{n+1}, \varphi^n) + \rho^n \tilde{f}(\rho^n, \varphi^{n+1}) - \rho^n \tilde{f}(\rho^n, \varphi^n)}{2(\varphi^{n+1} - \varphi^n)}$$

$$+ \gamma \operatorname{div}(\boldsymbol{\sigma}^{n+1/2}) \tag{3.28}$$

$$0 = \tau^{n+1/2} - \frac{\rho^{n+1}\tilde{f}(\rho^{n+1},\varphi^{n+1}) - \rho^{n}\tilde{f}(\rho^{n},\varphi^{n+1}) + \rho^{n+1}\tilde{f}(\rho^{n+1},\varphi^{n}) - \rho^{n}\tilde{f}(\rho^{n},\varphi^{n})}{2(\rho^{n+1}-\rho^{n})} - \frac{1}{4}\left(|\boldsymbol{v}^{n+1}|^2 + |\boldsymbol{v}^{n}|^2\right) \tag{3.29}$$

$$\mathbf{0} = \boldsymbol{\sigma}^{n+1} - \nabla\varphi^{n+1}. \tag{3.30}$$

The following theorem states that this temporal semi-discretization is energy-consistent.

Theorem 3.10 (Discrete Energy Inequality)**:**
The scheme specified by Algorithm 3.9 satisfies the following energy dissipation property for all $0 \le n \le N$*:*

$$\int_\Omega \rho^n \tilde{f}(\rho^n,\varphi^n) + \frac{1}{2}\rho^n|\boldsymbol{v}^n|^2 + \frac{\gamma}{2}|\boldsymbol{\sigma}^n|^2 \,\mathrm{d}\boldsymbol{x} = \int_\Omega \rho^0 \tilde{f}(\rho^0,\varphi^0) + \frac{1}{2}\rho^0|\boldsymbol{v}^0|^2 + \frac{\gamma}{2}|\boldsymbol{\sigma}^0|^2 \,\mathrm{d}\boldsymbol{x} - \sum_{j=0}^{n-1}\Delta t_j \int_\Omega \boldsymbol{S}(\varphi^{j+1/2},\nabla\boldsymbol{v}^{j+1/2}) : \nabla\boldsymbol{v}^{j+1/2} + \eta\frac{|\mu^{j+1/2}|^2}{\rho^{j+1/2}} \,\mathrm{d}\boldsymbol{x}.$$

Proof. By multiplying (3.25) with $\tau^{n+1/2}$, (3.26) with $\boldsymbol{v}^{n+1/2}$ and (3.27) with $\mu^{n+1/2}$ we obtain after integrating over Ω

$$\begin{aligned} 0 = \int_\Omega & \frac{\rho^{n+1}\tilde{f}(\rho^{n+1},\varphi^{n+1}) - \rho^{n+1}\tilde{f}(\rho^{n+1},\varphi^{n}) + \rho^{n}\tilde{f}(\rho^{n},\varphi^{n+1}) - \rho^{n}\tilde{f}(\rho^{n},\varphi^{n})}{2\Delta t_n} \\ & + \frac{\rho^{n+1}-\rho^{n}}{4\Delta t_n}\left(|\boldsymbol{v}^{n+1}|^2 + |\boldsymbol{v}^{n}|^2\right) \\ & + \operatorname{div}(\rho^{n+1/2}\boldsymbol{v}^{n+1/2})\tau^{n+1/2} \,\mathrm{d}\boldsymbol{x}, \end{aligned}$$

$$\begin{aligned} 0 = \int_\Omega & \frac{\rho^{n+1/2}}{2\Delta t_n}\left(|\boldsymbol{v}^{n+1}|^2 - |\boldsymbol{v}^{n}|^2\right) + \boldsymbol{v}^{n+1/2}\operatorname{div}(\rho^{n+1/2}\boldsymbol{v}^{n+1/2}\otimes\boldsymbol{v}^{n+1/2}) \\ & - \operatorname{div}(\rho^{n+1/2}\boldsymbol{v}^{n+1/2})|\boldsymbol{v}^{n+1/2}|^2 - \frac{1}{2}\rho^{n+1/2}\nabla|\boldsymbol{v}^{n+1/2}|^2\boldsymbol{v}^{n+1/2} + \rho^{n+1/2}\boldsymbol{v}^{n+1/2}\nabla\tau^{n+1/2} \\ & - \mu^{n+1/2}\nabla\varphi^{n+1/2}\boldsymbol{v}^{n+1/2} - \operatorname{div}(\boldsymbol{S}(\varphi^{n+1/2},\nabla\boldsymbol{v}^{n+1/2}))\cdot\boldsymbol{v}^{n+1/2} \,\mathrm{d}\boldsymbol{x}, \end{aligned}$$

$$0 = \int_\Omega \frac{\rho^{n+1}\tilde{f}(\rho^{n+1},\varphi^{n+1}) - \rho^{n}\tilde{f}(\rho^{n},\varphi^{n+1}) + \rho^{n+1}\tilde{f}(\rho^{n+1},\varphi^{n}) - \rho^{n}\tilde{f}(\rho^{n},\varphi^{n})}{2\Delta t_n}$$

$$- \frac{\varphi^{n+1} - \varphi^n}{\Delta t_n} \gamma \operatorname{div}(\boldsymbol{\sigma}^{n+1/2}) + \nabla \varphi^{n+1/2} \cdot \boldsymbol{v}^{n+1/2} \mu^{n+1/2} + \eta \frac{|\mu^{n+1/2}|^2}{\rho^{n+1/2}} \, \mathrm{d}\boldsymbol{x}.$$

We define

$$\begin{aligned}
I_1 =& \frac{\rho^{n+1} - \rho^n}{\Delta t_n} \left(\frac{\rho^{n+1} \tilde{f}(\rho^{n+1}, \varphi^{n+1}) - \rho^{n+1} \tilde{f}(\rho^{n+1}, \varphi^n) + \rho^n \tilde{f}(\rho^n, \varphi^{n+1}) - \rho^n \tilde{f}(\rho^n, \varphi^n)}{2(\rho^{n+1} - \rho^n)} \right. \\
&\left. + \frac{1}{4} \left(|\boldsymbol{v}^{n+1}|^2 + |\boldsymbol{v}^n|^2 \right) \right) + \frac{1}{\Delta t_n} \rho^{n+1/2} \boldsymbol{v}^{n+1/2} \cdot (\boldsymbol{v}^{n+1} - \boldsymbol{v}^n) \\
&+ \frac{\varphi^{n+1} - \varphi^n}{\Delta t_n} \left(\frac{\rho^{n+1} \tilde{f}(\rho^{n+1}, \varphi^{n+1}) - \rho^n \tilde{f}(\rho^n, \varphi^{n+1}) + \rho^{n+1} \tilde{f}(\rho^{n+1}, \varphi^n) - \rho^n \tilde{f}(\rho^n, \varphi^n)}{2(\varphi^{n+1} - \varphi^n)} \right. \\
&\left. - \gamma \operatorname{div}(\boldsymbol{\sigma}^{n+1/2}) \right), \\
I_2 =& \operatorname{div}(\rho^{n+1/2} \boldsymbol{v}^{n+1/2}) \tau^{n+1/2} + \rho^{n+1/2} \boldsymbol{v}^{n+1/2} \nabla \tau^{n+1/2} \\
=& \operatorname{div}(\rho^{n+1/2} \boldsymbol{v}^{n+1/2} \tau^{n+1/2}), \\
I_3 =& \boldsymbol{v}^{n+1/2} \operatorname{div}(\rho^{n+1/2} \boldsymbol{v}^{n+1/2} \otimes \boldsymbol{v}^{n+1/2}) - \operatorname{div}(\rho^{n+1/2} \boldsymbol{v}^{n+1/2}) |\boldsymbol{v}^{n+1/2}|^2 - \frac{1}{2} \rho^{n+1/2} \nabla |\boldsymbol{v}^{n+1/2}|^2 \boldsymbol{v}^{n+1/2} \\
=& 0, \\
I_4 =& - \operatorname{div}(\boldsymbol{S}(\varphi^{n+1/2}, \boldsymbol{v}^{n+1/2}) \cdot \boldsymbol{v}^{n+1/2} + \eta \frac{|\mu^{n+1/2}|^2}{\rho^{n+1/2}}.
\end{aligned}$$

Now

$$\begin{aligned}
\Delta t_n \int_\Omega I_1 \, \mathrm{d}\boldsymbol{x} =& \int_\Omega \rho^{n+1} \tilde{f}(\rho^{n+1}, \varphi^{n+1}) + \frac{1}{2} \rho^{n+1} |\boldsymbol{v}^{n+1}|^2 + \frac{\gamma}{2} |\boldsymbol{\sigma}^{n+1}|^2 \, \mathrm{d}\boldsymbol{x} \\
&- \int_\Omega \rho^n \tilde{f}(\rho^n, \varphi^n) + \frac{1}{2} \rho^n |\boldsymbol{v}^n|^2 + \frac{\gamma}{2} |\boldsymbol{\sigma}^n|^2 \, \mathrm{d}\boldsymbol{x}
\end{aligned}$$

and

$$\int_\Omega I_2 \, \mathrm{d}\boldsymbol{x} = 0,$$

since $\boldsymbol{v} \cdot \boldsymbol{n} = 0$ on $\partial\Omega$.
Additionally,

$$\int_\Omega I_4 \, \mathrm{d}\boldsymbol{x} = \int_\Omega \boldsymbol{S}(\varphi^{n+1/2}, \boldsymbol{v}^{n+1/2}) : \nabla \boldsymbol{v}^{n+1/2} + \eta \frac{|\mu^{n+1/2}|^2}{\rho^{n+1/2}} \, \mathrm{d}\boldsymbol{x}.$$

Because of $0 = \int_\Omega I_1 + I_2 + I_3 + I_4 \, \mathrm{d}\boldsymbol{x}$ the assertion is shown. ■

3.4 The Fully Discrete Scheme

Finally, in this section we present the fully discrete scheme of (3.1)–(3.6). This is a combination of the two previous sections. The arguments of these sections can be combined to obtain the fully discrete scheme with the desired properties. With (2.1) the fully discrete scheme reads as follows:

Algorithm 3.11: *Let a temporal decomposition $0 = t_0 < t_1 < \ldots < t_N = T$, with $\Delta t_n = t_{n+1} - t_n$, and a triangulation $\mathcal{T}$ of Ω be given. With initial data $(\rho_h^0, \boldsymbol{v}_h^0, \varphi_h^0, \mu_h^0, \tau_h^0, \boldsymbol{\sigma}_h^0) \in \mathcal{V}_h$, for $n = 0, \ldots, N-1$ find $(\rho_h^{n+1}, \boldsymbol{v}_h^{n+1}, \varphi_h^{n+1}, \mu_h^{n+1}, \tau_h^{n+1}, \boldsymbol{\sigma}_h^{n+1}) \in \mathcal{V}_h$ such that*

$$0 = \int_\Omega \left(\frac{\rho_h^{n+1} - \rho_h^n}{\Delta t} + \operatorname{div}(\rho_h^{n+1/2} \boldsymbol{v}_h^{n+1/2}) \right) \psi \, \mathrm{d}\boldsymbol{x} - \int_\mathcal{E} [\![\rho_h^{n+1/2} \boldsymbol{v}_h^{n+1/2}]\!] \{\psi\} \, \mathrm{d}s, \tag{3.31}$$

$$\begin{aligned} 0 = \int_\Omega \Bigg(& \rho_h^{n+1/2} \left(\frac{\boldsymbol{v}_h^{n+1} - \boldsymbol{v}_h^n}{\Delta t} \right) + \operatorname{div}(\rho_h^{n+1/2} \boldsymbol{v}_h^{n+1/2} \otimes \boldsymbol{v}_h^{n+1/2}) - \operatorname{div}(\rho_h^{n+1/2} \boldsymbol{v}_h^{n+1/2}) \boldsymbol{v}_h^{n+1/2} \\ & - \frac{1}{2} \rho_h^{n+1/2} \nabla |\boldsymbol{v}_h^{n+1/2}|^2 + \rho_h^{n+1/2} \nabla \tau_h^{n+1/2} - \mu_h^{n+1/2} \nabla \varphi_h^{n+1/2} \Bigg) \cdot \boldsymbol{X} \, \mathrm{d}\boldsymbol{x} \\ & - \int_\mathcal{E} [\![\tau_h^{n+1/2}]\!] \cdot \{\rho_h^{n+1/2} \boldsymbol{X}\} - [\![\varphi_h^{n+1/2}]\!] \cdot \{\mu_h^{n+1/2} \boldsymbol{X}\} \, \mathrm{d}s + B_h(\boldsymbol{v}_h^{n+1/2}, \boldsymbol{X}; \varphi_h^{n+1/2}), \end{aligned} \tag{3.32}$$

$$0 = \int_\Omega \left(\frac{\varphi_h^{n+1} - \varphi_h^n}{\Delta t} + \nabla \varphi_h^{n+1/2} \cdot \boldsymbol{v}_h^{n+1/2} + \eta \frac{\mu_h^{n+1/2}}{\rho_h^{n+1/2}} \right) \Theta \, \mathrm{d}\boldsymbol{x} - \int_\mathcal{E} [\![\varphi_h^{n+1/2}]\!] \cdot \{\Theta \boldsymbol{v}_h^{n+1/2}\} \, \mathrm{d}s, \tag{3.33}$$

$$\begin{aligned} 0 = \int_\Omega \Bigg(& \mu_h^{n+1/2} - \frac{\rho^{n+1} \tilde{f}(\rho^{n+1}, \varphi^{n+1}) - \rho^{n+1} \tilde{f}(\rho^{n+1}, \varphi^n) + \rho^n \tilde{f}(\rho^n, \varphi^{n+1}) - \rho^n \tilde{f}(\rho^n, \varphi^n)}{2(\varphi^{n+1} - \varphi^n)} \\ & + \gamma \operatorname{div}(\boldsymbol{\sigma}_h^{n+1/2}) \Bigg) \chi \, \mathrm{d}\boldsymbol{x} - \int_\mathcal{E} \gamma [\![\boldsymbol{\sigma}_h^{n+1/2}]\!] \{\chi\} \, \mathrm{d}s, \end{aligned} \tag{3.34}$$

$$\begin{aligned} 0 = \int_\Omega \Bigg(& \tau_h^{n+1/2} - \frac{\rho^{n+1} \tilde{f}(\rho^{n+1}, \varphi^{n+1}) - \rho^n \tilde{f}(\rho^n, \varphi^{n+1}) + \rho^{n+1} \tilde{f}(\rho^{n+1}, \varphi^n) - \rho^n \tilde{f}(\rho^n, \varphi^n)}{2(\rho^{n+1} - \rho^n)} \\ & - \frac{1}{4} (|\boldsymbol{v}_h^{n+1}|^2 + |\boldsymbol{v}_h^n|^2) \Bigg) \zeta \, \mathrm{d}\boldsymbol{x}, \end{aligned} \tag{3.35}$$

$$0 = \int_\Omega \left(\boldsymbol{\sigma}_h^{n+1} - \nabla \varphi_h^{n+1} \right) \cdot \boldsymbol{Z} \, \mathrm{d}\boldsymbol{x} + \int_\mathcal{E} [\![\varphi_h^{n+1}]\!] \cdot \{\boldsymbol{Z}\} \, \mathrm{d}s, \tag{3.36}$$

holds for all $(\psi, \boldsymbol{X}, \Theta, \chi, \zeta, \boldsymbol{Z}) \in \mathcal{V}_h$.

The discretization is chosen such that the discrete counterpart 3.12 of the energy inequality is satisfied.

Theorem 3.12 (Fully discrete energy inequality)**:** *The discrete solution of the scheme* (3.31)–(3.36) *conserves mass and satisfies the energy dissipation equality, i.e.*

$$\begin{aligned}\int_\Omega \rho_h^{n+1}\tilde{f}(\rho_h^{n+1},\varphi_h^{n+1}) + \frac{\gamma}{2}|\boldsymbol{\sigma}_h^{n+1}|^2 + \frac{\rho_h^{n+1}}{2}|\boldsymbol{v}_h^{n+1}|^2\,\mathrm{d}\boldsymbol{x}\\ - \int_\Omega \rho_h^{n}\tilde{f}(\rho_h^{n},\varphi_h^{n}) + \frac{\gamma}{2}|\boldsymbol{\sigma}_h^{n}|^2 + \frac{\rho_h^{n}}{2}|\boldsymbol{v}_h^{n}|^2\,\mathrm{d}\boldsymbol{x}\\ = -\Delta t\int_\Omega \eta\frac{|\mu_h^{n+1/2}|^2}{\rho_h^{n+1/2}}\,\mathrm{d}\boldsymbol{x} - \Delta t B_h(\boldsymbol{v}_h^{n+1/2},\boldsymbol{v}_h^{n+1/2};\varphi_h^{n+1/2}).\end{aligned}$$

Proof. The proof is simply combining Theorem 3.8 and 3.10. ∎

Remark 3.13 (Quotients of the free energy density)**:** *In the implementation we do not use the difference quotients*

$$\frac{\rho^{n+1}\tilde{f}(\rho^{n+1},\varphi^{n+1}) - \rho^{n+1}\tilde{f}(\rho^{n+1},\varphi^{n}) + \rho^{n}\tilde{f}(\rho^{n},\varphi^{n+1}) - \rho^{n}\tilde{f}(\rho^{n},\varphi^{n})}{2(\varphi^{n+1}-\varphi^{n})} \tag{3.37}$$

and

$$\frac{\rho^{n+1}\tilde{f}(\rho^{n+1},\varphi^{n+1}) - \rho^{n}\tilde{f}(\rho^{n},\varphi^{n+1}) + \rho^{n+1}\tilde{f}(\rho^{n+1},\varphi^{n}) - \rho^{n}\tilde{f}(\rho^{n},\varphi^{n})}{2(\rho^{n+1}-\rho^{n})}. \tag{3.38}$$

We make two simplifications instead. First, we replace (3.37) *and* (3.38) *with*

$$\frac{\rho^{n+1/2}\tilde{f}(\rho^{n+1/2},\varphi^{n+1}) - \rho^{n+1/2}\tilde{f}(\rho^{n+1/2},\varphi^{n})}{\varphi^{n+1}-\varphi^{n}} \tag{3.39}$$

and

$$\frac{\rho^{n+1}\tilde{f}(\rho^{n+1},\varphi^{n+1/2}) - \rho^{n}\tilde{f}(\rho^{n},\varphi^{n+1/2})}{\rho^{n+1}-\rho^{n}}. \tag{3.40}$$

It can be shown by means of Taylor expansions that these difference quotients are an approximation of the original ones with error $O((\rho^{n+1}-\rho^n)^2)$, $O((\varphi^{n+1}-\varphi^n)^2)$, *respectively.*
Secondly, since (3.39)–(3.40) *might be badly conditioned (ill-defined) for small (vanishing) difference* $|\varphi^{n+1}-\varphi^n|$ *and* $|\rho^{n+1}-\rho^n|$, *we replace them by the representation*

$$\frac{\rho^{n+1/2}\tilde{f}(\rho^{n+1/2},\varphi^{n+1}) - \rho^{n+1/2}\tilde{f}(\rho^{n+1/2},\varphi^{n})}{\varphi^{n+1}-\varphi^{n}}$$

$$= \rho^{n+1/2}\tilde{f}(\rho^{n+1/2}, \varphi^{n+1/2}) + \frac{1}{24}\frac{\partial^3}{\partial\varphi^3}\left(\rho^{n+1/2} f(\rho^{n+1/2}, \varphi^{n+1/2})\right)(\varphi^{n+1} - \varphi^n)^2$$

and

$$\begin{aligned}
&\frac{\rho^{n+1}\tilde{f}(\rho^{n+1}, \varphi^{n+1/2}) - \rho^n \tilde{f}(\rho^n, \varphi^{n+1/2})}{\rho^{n+1} - \rho^n} \\
&= \rho^{n+1/2}\tilde{f}(\rho^{n+1/2}, \varphi^{n+1/2}) + \frac{1}{24}\frac{\partial^3}{\partial\rho^3}\left(\rho^{n+1/2} f(\rho^{n+1/2}, \varphi^{n+1/2})\right)(\rho^{n+1} - \rho^n)^2 \\
&\quad + \frac{1}{1920}\frac{\partial^5}{\partial\rho^5}(\rho^{n+1/2}\tilde{f}(\rho^{n+1/2}, \varphi^{n+1/2}))(\rho^{n+1} - \rho^n)^4
\end{aligned}$$

The representation for the quotient with respect to φ is exact, since the double well is a polynomial of degree 4. However, the representation for the quotient with respect to ρ is an approximation with error $O((\rho^{n+1} - \rho^n)^6)$.

3.5 Numerical Experiments

3.5.1 Convergence Studies

In this section we perform numerical experiments in order to verify the rate of convergence of the Algorithm 3.11 with respect to space and time.
We implemented the energy-consistent dG solver 3.11 with the finite element toolbox FEniCS, which is based on the C++ library DOLFIN [73]. In each time step the nonlinear system is solved by an inexact Newton method. The linear subsystems are approximated by a biconjugate gradient stabilized method (bicgstab) with an incomplete LU preconditioner. The absolute tolerance of both solvers is set to 10^{-10}.
We test the convergence properties in one space dimension on $\Omega = [0, 1]$. For that reason we employ a manufactured solution

$$\begin{aligned}
\rho_{\text{exact}}(x, t) &= \frac{1}{2}\cos(5\pi t)\cos(2\pi x) + \frac{3}{2}, \\
v_{\text{exact}}(x, t) &= \cos(5\pi t)\cos(4\pi x), \\
\varphi_{\text{exact}}(x, t) &= \frac{1}{2}\cos(5\pi t)\cos(2\pi x) + \frac{1}{2}.
\end{aligned} \tag{3.41}$$

We compute source terms $S_\rho(x,t), S_v(x,t)$, and $S_\varphi(x,t)$ for (2.4)–(2.6) such that $(\rho_{\text{exact}}, v_{\text{exact}}, \varphi_{\text{exact}})$ solves the system with source terms exactly. We use the Sympy python library [82] for the symbolical calculations leading to the source terms. For the equations of state in the bulk phases, we choose stiffened gas equations

$$\rho f_{\text{L/V}} = \alpha_{\text{L/V}} \rho \ln(\rho) + (\beta_{\text{L/V}} - \alpha_{\text{L/V}})\rho + \gamma_{\text{L/V}},$$

with parameters

$$\begin{aligned} \alpha_{\text{L}} &= 1.5, \quad \alpha_{\text{V}} = 1, \\ \beta_{\text{L}} &= \ln(2), \beta_{\text{V}} = 0, \\ \gamma_{\text{L}} &= 0, \quad \gamma_{\text{V}} = 0.5. \end{aligned}$$

For the bulk viscosities we set $\mu_{\text{L}} = \mu_{\text{V}} = 0.001$. The capillary parameter is taken $\gamma = 0.001$ and the mobility $\eta = 1$. The double well is chosen as $W(\varphi) = 0.1\varphi^2(1-\varphi)^2$.

3.5.1.1 Convergence in Space

For the computations we use a time step size depending on the dG polynomial degree. For $k = 0, 1$ we choose $\Delta t = 10^{\lfloor \log_{10}(1/N) \rfloor}$, where N denotes the number of cells. For $k \geq 2$ we choose $\Delta t = 10^{\lfloor \log_{10}(1/N^2) \rfloor}$.
We run the simulation up to $T = 0.03$ on grids with different number N of cells. We found that the convergence rate depends on the choice of stabilization parameters α_B and α_1, cf. (3.16),(3.20). This is especially true for $k = 1$. We list the parameters we used in Table 3.1. The other parameters α_2, α_3 (3.21),(3.22) are chosen to be 0.

k	α_B	α_1
0	1e-03	0
1	1.7e-03	6e-03
2	7e-03	1e-03
3	2e-02	1e-01

Table 3.1: Stabilization parameters used in the numerical experiments, depending on polynomial degree k.

We investigate the errors of the discrete solution (ρ_h, v_h, φ_h) and the exact solution $(\rho_{\text{exact}}, v_{\text{exact}}, \varphi_{\text{exact}})$ (3.41) in $L^\infty(0, T; L^2(\Omega))$. The results in Tables 3.2–3.5 indicate that the scheme converges with order $k + 1$ in space and order 2 in time.

N	$\|\rho - \rho_h\|_{L^\infty(L^2)}$	EOC_ρ	$\|v - v_h\|_{L^\infty(L^2)}$	EOC_v	$\|\varphi - \varphi_h\|_{L^\infty(L^2)}$	EOC_φ
16	5.3927e-02	–	1.6099e-01	–	3.9793e-02	–
32	2.3266e-02	1.21	7.9256e-02	1.02	1.9836e-02	1.00
64	1.0400e-02	1.16	3.9587e-02	1.00	9.9282e-03	1.00
128	5.0357e-03	1.05	2.0036e-02	0.98	5.0093e-03	0.99
256	2.5047e-03	1.01	1.0019e-02	1.00	2.5047e-03	1.00
512	1.2523e-03	1.00	5.0093e-03	1.00	1.2523e-03	1.00
1024	6.2624e-04	1.00	2.5050e-03	1.00	6.2624e-04	1.00
2048	3.1312e-04	1.00	1.2525e-03	1.00	3.1312e-04	1.00
4096	1.5656e-04	1.00	6.2624e-04	1.00	1.5656e-04	1.00
8192	7.8281e-05	1.00	3.1312e-04	1.00	7.8281e-05	1.00

Table 3.2: Numerical error in the $L^\infty(0, T; L^2(\Omega))$ norm for dG polynomial degree $k = 0$.

N	$\|\rho - \rho_h\|_{L^\infty(L^2)}$	EOC_ρ	$\|v - v_h\|_{L^\infty(L^2)}$	EOC_v	$\|\varphi - \varphi_h\|_{L^\infty(L^2)}$	EOC_φ
16	7.0177e-02	0.00	8.4485e-02	0.00	1.4141e-02	0.00
32	3.4156e-02	1.04	3.5802e-02	1.24	4.8521e-03	1.54
64	1.7161e-02	0.99	1.4091e-02	1.35	2.5639e-03	0.92
128	8.9180e-03	0.94	3.6522e-03	1.95	5.0880e-04	2.33
256	4.1448e-03	1.11	6.8157e-04	2.42	2.3976e-04	1.09
512	1.6387e-03	1.34	1.9353e-04	1.82	1.0784e-04	1.15
1024	5.8990e-04	1.47	2.5084e-05	2.95	3.5755e-05	1.59
2048	1.7574e-04	1.75	3.4145e-06	2.88	1.0780e-05	1.73

Table 3.3: Numerical error in the $L^\infty(0, T; L^2(\Omega))$ norm for dG polynomial degree $k = 1$.

N	$\|\rho - \rho_h\|_{L^\infty(L^2)}$	EOC_ρ	$\|v - v_h\|_{L^\infty(L^2)}$	EOC_v	$\|\varphi - \varphi_h\|_{L^\infty(L^2)}$	EOC_φ
16	9.4031e-03	–	5.0512e-03	–	1.0466e-03	–
32	1.3901e-03	2.76	5.2801e-04	3.26	1.3235e-04	2.98
64	3.4729e-05	5.32	3.0377e-05	4.12	2.6400e-06	5.65
128	3.3313e-06	3.38	3.8284e-06	2.99	2.3993e-07	3.46
256	3.2122e-07	3.37	4.7174e-07	3.02	2.9784e-08	3.01
512	2.9897e-08	3.43	5.9655e-08	2.98	3.7434e-09	2.99

Table 3.4: Numerical error in the $L^\infty(0, T; L^2(\Omega))$ norm for dG polynomial degree $k = 2$.

N	$\|\rho - \rho_h\|_{L^\infty(L^2)}$	EOC_ρ	$\|v - v_h\|_{L^\infty(L^2)}$	EOC_v	$\|\varphi - \varphi_h\|_{L^\infty(L^2)}$	EOC_φ
16	1.1536e-03	–	6.7507e-04	–	7.9957e-05	–
32	5.2932e-05	4.45	1.6833e-05	5.33	3.7722e-06	4.41
64	2.5162e-06	4.39	8.9823e-07	4.23	2.3245e-07	4.02
128	1.4674e-07	4.10	3.3460e-08	4.75	1.3706e-08	4.08

Table 3.5: Numerical error in the $L^\infty(0, T; L^2(\Omega))$ norm for dG polynomial degree $k = 3$.

3.5.1.2 Convergence in Time

Since the convergence order for $k = 1$ is not completely clear, we conduct an additional experiment in this section to investigate the convergence order with respect to time. In order to ensure a low spatial discretization error we use dG polynomials with degree $k = 5$ for different Δt on a grid with 64 cells. For the simulation we use $\alpha_B = \alpha_1 = 1.5$. We investigate the errors of the discrete solution (ρ_h, v_h, φ_h) and the exact solution $(\rho_{\text{exact}}, v_{\text{exact}}, \varphi_{\text{exact}})$ (3.41) in $L^2(\Omega)$ at final time $T = 0.03$. The results in Table 3.6 shows that the scheme converges with order 2 in time.

Δt	$\|\rho - \rho_h\|_{L^2}$	EOC_ρ	$\|v - v_h\|_{L^2}$	EOC_v	$\|\varphi - \varphi_h\|_{L^2}$	EOC_φ
1.00e-02	2.6833e-03	-	3.8994e-03	-	1.6787e-03	-
5.00e-03	6.4094e-04	2.07	9.3611e-04	2.06	3.9728e-04	2.08
1.00e-03	2.5357e-05	2.01	3.7026e-05	2.01	1.5626e-05	2.01
5.00e-04	6.3372e-06	2.00	9.2533e-06	2.00	3.9046e-06	2.00
1.00e-04	2.5348e-07	2.00	3.7009e-07	2.00	1.5616e-07	2.00
5.00e-05	6.3383e-08	2.00	9.2525e-08	2.00	3.9041e-08	2.00
1.00e-05	2.5908e-09	1.99	3.8099e-09	1.98	1.5698e-09	2.00

Table 3.6: Numerical error in the $L^2(\Omega)$ norm at time $T = 0.03$ for dG polynomial degree $k = 5$.

3.5.2 Energy Consistency

In this section we consider an example of two merging droplets in 2D. This illustrates on one hand that phase-field models are able to handle topological changes, and on the other hand we investigate the discrete energy in order to illustrate the discrete energy consistency from Theorem 3.10.

For the bulk viscosities we set $\mu_{\mathrm{L}} = 0.0125$ and $\mu_{\mathrm{V}} = 0.00125$. The capillary parameter is taken $\gamma = 5 \cdot 10^{-4}$ and the mobility $\eta = 10$. The polynomial order of the dG polynomials is $k = 2$.

For the EOS, we choose stiffened gas equations

$$\rho f_{\mathrm{L/V}} = \alpha_{\mathrm{L/V}} \rho \ln(\rho) + (\beta_{\mathrm{L/V}} - \alpha_{\mathrm{L/V}})\rho + \gamma_{\mathrm{L/V}}, \tag{3.42}$$

with parameters

$$\begin{aligned} \alpha_{\mathrm{L}} &= 5, \quad \alpha_{\mathrm{V}} = 1.5, \\ \beta_{\mathrm{L}} &= -4, \quad \beta_{\mathrm{V}} = 1.8, \\ \gamma_{\mathrm{L}} &= 11, \quad \gamma_{\mathrm{V}} = 0.324. \end{aligned}$$

Initially we have no velocity field, $\boldsymbol{v}_0 = \mathbf{0}$ and look at two kissing droplets. The computational domain is $\Omega = [0,1] \times [0,1]$. The droplets are located at $(0.39, 0.5)$ and $(0.6, 0.5)$ with radii 0.08 and 0.12. The initial density profile is smeared out with value $\rho_{\mathrm{L}} = 2.23$ inside and $\rho_{\mathrm{V}} = 0.3$ outside the droplet. As expected the droplets merge into one larger droplet. This evolution with $\eta = 10$ is depicted in Figure 3.1.

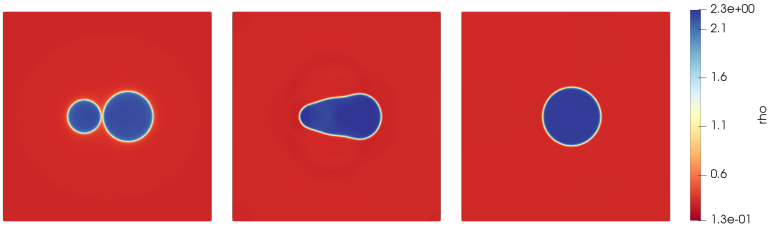

Figure 3.1: Merging droplets. Density ρ at times $t = 0$, $t = 0.2$, and $t = 2$ for $\eta = 10$.

We can observe that the model handles topological changes easily. However, the dynamics of the phase-field relaxation are determined by the mobility η which needs to be chosen according to the problem. This is illustrated in Figure 3.2, where the energy over time for different values of the mobility η is plotted.
From Figure 3.2 we observe that the discrete energy decreases, as expected from Theorem 3.10. Moreover, we see that the higher the value of η, the faster the energy dissipation.

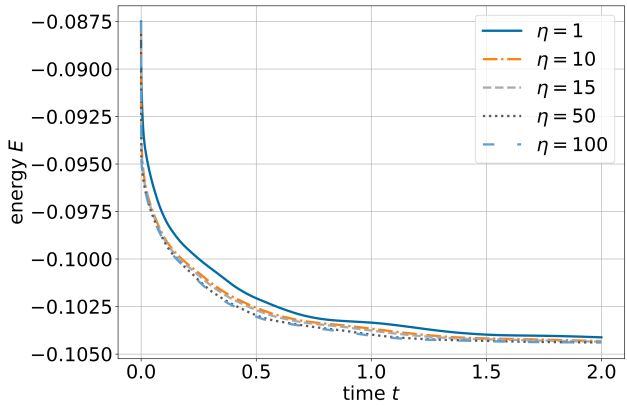

Figure 3.2: Energy E over time for droplet merging simulation with different values for the mobility η.

4 Droplet–Wall Interactions

In this chapter we consider droplet–wall interactions as example to employ the NSAC model introduced in Chapter 2.
In the context of droplet impingement incompressibility is only justified for small impact speeds. High impact speeds trigger compressibility effects of the liquid droplet, which can determine the flow dynamics significantly. Examples for high speed droplet impact scenarios can be found in many industrial applications such as liquid-fueled engines, spray cooling or spray cleaning. In [55] it has been shown that incompressible models are not adequate to describe high speed impacts, especially due to the fact that the jetting dynamics are influenced by a developing shock wave in the liquid phase [54]. The time after the impact of the droplet until jetting is actually smaller than the predicted time of incompressible models due to the shock wave pattern. In [55] a compressible sharp-interface model is used for the simulations. However, sharp-interface models become intricate in the presence of changes in droplet topology and contact line motion.
For this reason, we employ the compressible NSAC model (2.4)–(2.6), which allows for complex interface morphologies and dynamic contact angles. To do so, first we have to reconsider the boundary conditions we prescribe. Droplet–wall interactions are characterized by a moving contact line (MCL) . The boundary conditions (2.9)–(2.10) do not suffice to capture the MCL. Therefore, in the following section we derive a complete set of boundary conditions that allow for MCL.

4.1 Boundary Conditions

The system (2.4)–(2.6) needs to be complemented with appropriate initial and boundary conditions. We are now interested in MCL problems. With a sharp-interface point of view, the contact line is the intersection of the liquid–vapor interface with the solid wall. The requirement of a contact line moving along the wall renders the derivation of boundary conditions nontrivial. Figure 4.1 depicts a sketch of a compressible droplet impact scenario with the rebound shock wave dynamics and a moving contact line. We derive boundary conditions to handle

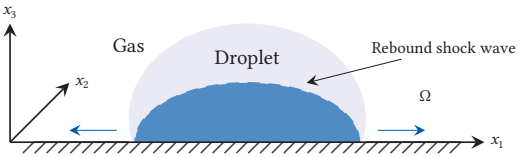

Figure 4.1: Sketch of a compressible droplet impingement on a flat wall with moving contact line.

MCL problems with the NSAC system (2.4)–(2.6) in this section.
For the incompressible case, so called *general Navier boundary conditions* (GNBC) have been derived [93, 94]. Motivated by these works we extend the GNBC to the compressible case.
Because phase-field modeling goes well with energy principles, cf. Chapter 2, we add a wall free energy term $\int_{\partial\Omega} g(\varphi)\ \mathrm{d}s$ to the energy E from (2.8) and obtain (with a slight abuse of notation)

$$E(t) = \int_\Omega \rho(\boldsymbol{x},t) f(\rho(\boldsymbol{x},t), \varphi(\boldsymbol{x},t), \nabla\varphi(\boldsymbol{x},t)) + \frac{1}{2}\rho(\boldsymbol{x},t)|\boldsymbol{v}(\boldsymbol{x},t)|^2\ \mathrm{d}\boldsymbol{x} + \int_{\partial\Omega} g(\varphi(\boldsymbol{x},t))\ \mathrm{d}s. \tag{4.1}$$

Here $g(\varphi)$ is the interfacial free energy per unit area at the fluid-solid boundary depending only on the local composition [94]. The specific choice for g is motivated by Young's equation. With a sharp-interface point of view we have

$$\sigma\cos(\theta_s) = \sigma_S - \sigma_{LS}, \tag{4.2}$$

with the surface free energy σ of the liquid, the static contact angle θ_s, surface free energy σ_S of the solid, and interfacial free energy σ_{LS} between liquid and solid, see Figure 4.2. We prescribe the difference in energy for g, i.e.

$$\sigma_S - \sigma_{LS} = g(0) - g(1).$$

Then, we choose a smooth interpolation between the values $\pm\frac{\Delta g}{2} = \pm\frac{g(1)-g(0)}{2}$. However, it was shown in [93] that the choice of the kind interpolation has no large impact. Hence, for reasons of consistency, we use h as interpolation function, see (2.2). With (4.2) we obtain

$$g(\varphi) \coloneqq -\sigma\cos(\theta_s)\left(h(\varphi) - \frac{1}{2}\right).$$

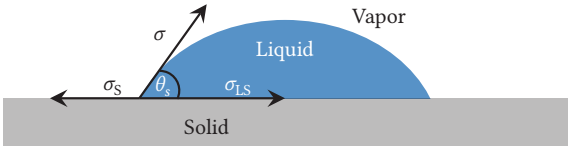

Figure 4.2: Illustration of Young's equation $\sigma\cos(\theta_s) = \sigma_S - \sigma_{LS}$.

A variation $\delta\varphi$ of φ leads to a variation δE of the energy (4.1), that is

$$\delta E = \int_\Omega \mu\delta\varphi \ \mathrm{d}\boldsymbol{x} - \int_{\partial\Omega} L(\varphi)\frac{\partial\varphi}{\partial_{\boldsymbol{\tau}}}\delta\varphi_{\boldsymbol{\tau}} \ \mathrm{d}s.$$

Here,

$$L(\varphi) \coloneqq \gamma\frac{\partial\varphi}{\partial\boldsymbol{n}} + g'(\varphi)$$

can be interpreted as uncompensated Young stress [93]. The boundary tangential vector is denoted by $\boldsymbol{\tau}$ and $\boldsymbol{n}$ denotes the outer normal. Thus, $L(\varphi) = 0$ is the Euler–Lagrange equation at the fluid-solid boundary for minimizing the energy (4.1) with respect to the phase-field variable. We assume a boundary relaxation dynamics for φ given by

$$\partial_t\varphi + \boldsymbol{v}\cdot\nabla_{\boldsymbol{\tau}}\varphi = -\frac{\alpha}{\rho}L(\varphi),$$

with a relaxation parameter $\alpha > 0$. Here $\nabla_{\boldsymbol{\tau}} \coloneqq \nabla - (\boldsymbol{n}\cdot\nabla)\boldsymbol{n}$ is the gradient along the tangential direction. Since $\boldsymbol{v}\cdot\boldsymbol{n} = 0$, we have $\boldsymbol{v}\cdot\nabla_{\boldsymbol{\tau}}\varphi = v_{\boldsymbol{\tau}}\frac{\partial\varphi}{\partial\boldsymbol{\tau}}$, and finally we obtain

$$\partial_t\varphi + v_{\boldsymbol{\tau}}\frac{\partial\varphi}{\partial\boldsymbol{\tau}} = -\frac{\alpha}{\rho}L(\varphi) \quad \text{on } \partial\Omega.$$

In order to complete the derivation of the GNBC, we incorporate a slip velocity boundary condition. In single-phase models, the slip velocity is often taken proportional to the tangential viscous stress. However, in our case we also have to take the uncompensated Young stress into account. In [93] it is shown from molecular dynamic simulations that the slip velocity should be taken proportional to the sum of the tangential viscous stress and the uncompensated Young stress. Hence, with the slip length $\beta > 0$ we prescribe the boundary condition

$$\beta v_{\boldsymbol{\tau}} + \nu(\varphi)\frac{\partial v_{\boldsymbol{\tau}}}{\partial\boldsymbol{n}} - L(\varphi)\frac{\partial\varphi}{\partial\boldsymbol{\tau}} = 0 \quad \text{on } \partial\Omega. \tag{4.3}$$

The last term in (4.3) drops out away from the interface and we have the classical Navier-slip condition. On the other hand, in the interface region the additional term acts and allows for correct contact line movement.
In summary we obtain the following GNBC for the MCL problem

$$\boldsymbol{v} \cdot \boldsymbol{n} = 0, \tag{4.4}$$

$$\beta v_{\boldsymbol{\tau}} + \nu(\varphi)\frac{\partial v_{\boldsymbol{\tau}}}{\partial \boldsymbol{n}} - L(\varphi)\frac{\partial \varphi}{\partial \boldsymbol{\tau}} = 0, \qquad \text{on } \partial\Omega \tag{4.5}$$

$$\partial_t \varphi + v_{\boldsymbol{\tau}}\frac{\partial \varphi}{\partial \boldsymbol{\tau}} = -\frac{\alpha}{\rho}L(\varphi). \tag{4.6}$$

Remark 4.1 (Special cases)**:** *The boundary conditions* (4.4)–(4.6) *contain several special cases. If we let the relaxation parameter* α *tend to infinity, we end up with*

$$\begin{aligned} \boldsymbol{v} \cdot \boldsymbol{n} &= 0, \\ \beta v_{\boldsymbol{\tau}} + \nu(\varphi)\frac{\partial v_{\boldsymbol{\tau}}}{\partial \boldsymbol{n}} &= 0, \\ L(\varphi) &= 0. \end{aligned}$$

If additionally $\theta_s = \pi/2$ *we have*

$$\begin{aligned} \boldsymbol{v} \cdot \boldsymbol{n} &= 0, \\ \beta v_{\boldsymbol{\tau}} + \nu(\varphi)\frac{\partial v_{\boldsymbol{\tau}}}{\partial \boldsymbol{n}} &= 0, \\ \nabla\varphi \cdot \boldsymbol{n} &= 0. \end{aligned}$$

Finally, by sending the slip length β *to infinity we obtain the no-slip condition*

$$\begin{aligned} \boldsymbol{v} &= \boldsymbol{0}, \\ \nabla\varphi \cdot \boldsymbol{n} &= 0. \end{aligned}$$

4.1.1 Energy Inequality

The energy introduced in (4.1) consists of the bulk and wall free energies and the kinetic energy. The addition of the wall free energy in comparison to (2.8) changes slightly the corresponding energy inequality in Theorem 2.3.

Theorem 4.2 (Energy inequality with GNBC)**:** *Let* $(\rho, \boldsymbol{v}, \varphi)$ *with values in* $(0, \infty) \times \mathbb{R}^d \times [0, 1]$ *be a classical solution to* (2.4)–(2.6) *in* $(0, T) \times \Omega$ *satisfying the boundary conditions* (4.4)–(4.6) *on* $(0, T) \times \partial\Omega$*. Then for all* $t \in (0, T)$ *the following energy*

inequality holds:

$$\begin{aligned}\frac{\mathrm{d}}{\mathrm{d}t}E(t) &= \frac{\mathrm{d}}{\mathrm{d}t}(E_{\text{free}}(t) + E_{\text{kin}}(t) + E_{\text{wall}}(t)) \\ &= \frac{\mathrm{d}}{\mathrm{d}t}\left(\int_\Omega \rho f(\rho, \varphi, \nabla\varphi) + \frac{1}{2}\rho|\boldsymbol{v}|^2 \,\mathrm{d}\boldsymbol{x} + \int_{\partial\Omega} g(\varphi) \,\mathrm{d}s\right) \\ &= -\int_\Omega \frac{\eta}{\rho}\mu^2 \,\mathrm{d}\boldsymbol{x} - \int_\Omega \boldsymbol{S} : \nabla\boldsymbol{v} \,\mathrm{d}\boldsymbol{x} - \int_{\partial\Omega} \beta|v_{\boldsymbol{\tau}}|^2 \,\mathrm{d}s - \int_{\partial\Omega} \frac{\alpha}{\rho}|L(\varphi)|^2 \,\mathrm{d}s \leq 0.\end{aligned}$$

Proof. The proof is completely analog to the proof of Theorem 2.3. The extra terms appear by using the boundary conditions (4.4)–(4.6) in the occurring boundary integrals. ∎

We now have entropy production due to phase transition, viscosity, wall slip, and composition relaxation at the solid interface.

4.2 Numerical Experiments

In the following we present numerical simulations using the energy-consistent discontinuous Galerkin scheme derived in Chapter 3, described by Algorithm 3.11. We note that we present academic examples, i.e. chosen densities, velocity, and regimes of physical parameters do not match realistic fluids. The reason behind this is that for realistic EOS and density values for current numerical schemes there is a slight mismatch between the density and phase-field profile. This leads to a slightly too high percentage of liquid at very low density in the mixing zone and thus large negative pressures.

4.2.1 Choice of Parameters

For the EOS in the bulk phases, we choose stiffened gas type EOS (3.42).
In order to avoid to prefer one of the phases, we choose the minima of the two free energies $\rho f_{\text{L/V}}$ to be at the same height.
Due to surface tension, the density inside a liquid droplet is slightly higher than the value which minimizes ρf_{L}. The value of the surrounding vapor is slightly lower than the minimizer of ρf_{V}. We choose the initial density profile accordingly. For the bulk viscosities we set $\mu_{\text{L}} = 0.0125$ and $\mu_{\text{V}} = 0.00125$. If not stated otherwise the mobility is taken $\eta = 10$. The polynomial order of the dG polynomials is $k = 2$.

4.2.2 Contact Angle

In this example we address droplet–wall interactions. We consider the case of static contact angle. This means we let the relaxation parameter α in (4.6) tend to infinity. In the limit we obtain the static contact angle boundary conditions.
We set the static contact angle $\theta_s = 0.1\pi \approx 18^\circ$. The computational domain is $\Omega = [0,1] \times [0,1]$. The parameters for the equations of states are

$$\begin{aligned} \alpha_L &= 5, \quad \alpha_V = 1.5, \\ \beta_L &= -4, \quad \beta_V = 1.8, \\ \gamma_L &= 11, \quad \gamma_V = 0.324. \end{aligned}$$

The initial density profile is smeared out with value $\rho_L = 2.23$ inside and $\rho_V = 0.3$ outside the droplet. As initial condition we use a droplet sitting on a flat surface with a contact angle of 90°. The droplet position is $(0.5, 0)$ with radius 0.2. Since the initial condition is far away from equilibrium, we have dynamics on the wall-boundary towards the equilibrium configuration. Thus, we can observe a wetting dynamic, see Figure 4.3.

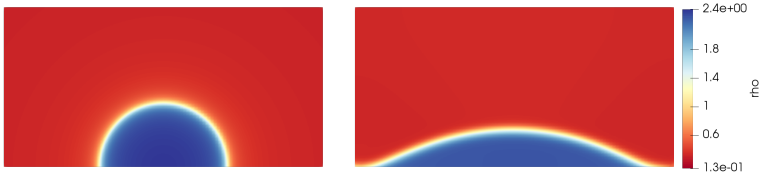

Figure 4.3: Wetting of smooth wall with GNBC boundary conditions for the static limit $\alpha \longrightarrow \infty$ and contact angle $\theta_s = 0.1\pi$. Density ρ at $t = 0$ and $t = 0.9$.

The wall contribution leads to a large force on the boundary, which renders the system stiff. Although we have an implicit scheme we increased the interface width to be able to handle the boundary terms. Hence, we chose in this simulation $\gamma = 10^{-2}$.

4.2.3 Droplet Impingement

With this example we consider droplet impingement. The computational domain is the same as in Section 4.2.2. As initial condition we use a droplet at $(0.5, 0.2)$ with radius 0.1. The parameters for the equations of states are

$$\alpha_L = 5, \qquad \alpha_V = 1.5,$$

$$\beta_L = -0.8, \quad \beta_V = 1.8,$$
$$\gamma_L = 5.5, \quad \gamma_V = 0.084.$$

For the capillary parameter, we choose $\gamma = 5 \cdot 10^{-4}$. The initial density profile is smeared out with value $\rho_L = 1.2$ inside and $\rho_V = 0.3$ outside the droplet. The initial velocity inside the droplet is $v_y = -1$.
Sharp-interface models based on the Navier–Stokes equations in the bulk become ill-posed if no-slip conditions are imposed. However, solutions of phase-field models come with contact line movement even if no-slip conditions are used.
This is due to the fact that the contact line is regularized and the dynamics are driven by evolution in the phase-field variable rather than advective transport. This can be seen in Figure 4.4 where a droplet impact with no-slip conditions is simulated. This is a special case of the GNBC, with $\alpha \longrightarrow \infty$ and $\beta \longrightarrow \infty$.

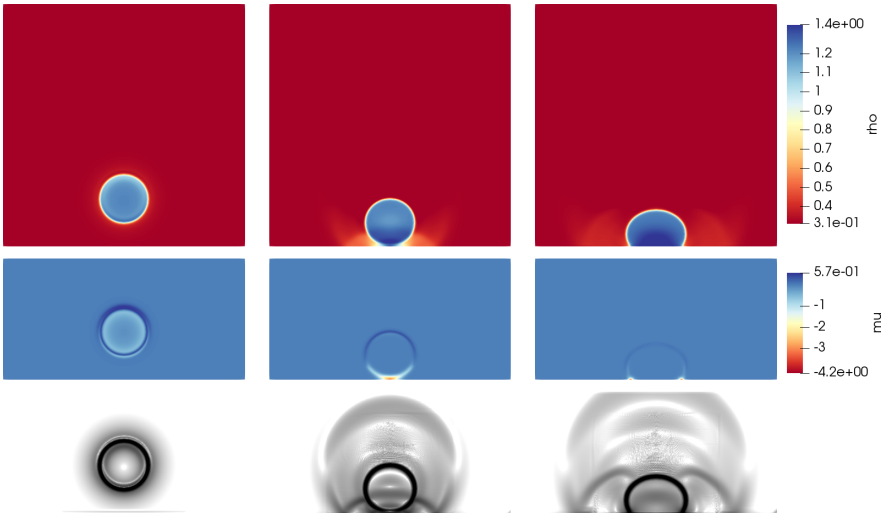

Figure 4.4: Droplet impact simulation. Density ρ, chemical potential μ and Schlieren picture at times $t = 0.005$, $t = 0.13$, $t = 0.21$.

It can be seen that the generalized chemical potential μ is low at the contact line which leads to fast dynamics in the phase-field. This leads to a moving contact line. Additionally, especially in the Schlieren picture, we can see the (smeared out) shock waves in the vapor phase and also in the liquid phase where the shocks move faster due to a higher speed of sound in the liquid phase.

In order to verify the compressibility of the droplet we plot the maximum of the local Mach number $M_{\rho f} = \bar{v}\sqrt{\frac{\bar{\rho}}{\rho f}}$ in Figure 4.5. We can observe a peak right after the impact.

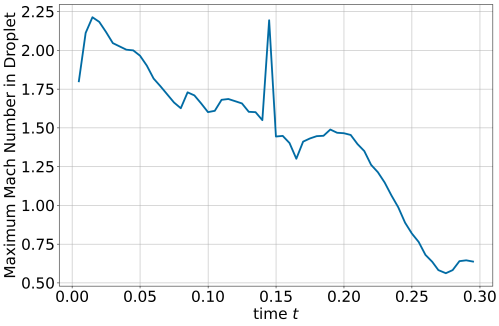

Figure 4.5: Droplet impact simulation. Maximum of the local Mach number inside the liquid phase.

The NSAC Model Within a Multi-Scale Framework

5

In this chapter we study the NSAC model (2.4)–(2.6) embedded in a multi-scale framework to model coupled free-flow/porous-medium-flow (FF/PM) situations. Coupled FF/PM systems occur in numerous natural and technical applications. We are interested in two-phase liquid–vapor flows such that the porous medium can be considered hydrophobic. The liquid wetting phase might emerge from the porous-medium domain forming drops on the interface. In this context an important aspect is the influence of the drops' accumulation on the exchange processes at the interface between the porous medium and its surrounding. Quantifying these transfer fluxes of mass, momentum and energy is crucial for applications like evaporation from soil, water management in fuel cells, the transport of therapeutic agents in the human body, or turbine heat exchange processes.

An approach to include drop-related processes in a macroscopic model concept is presented in [7]. A simple homogenization technique is applied to take the drops' influence on the macroscopic flow processes into account. The outcome of the model are the drop volume evolution as well as the influence of the drops on the coupling fluxes between free-flow and porous medium. A modified multi-scale approach is introduced in [3], where the drops are considered in additional balance equations for the interface region. Again, the coupling fluxes are scaled depending on the total drop volume at the interface between free-flow and porous medium. While both approaches yield computationally efficient models, micro-scale information is lost.

To overcome some of the disadvantages of a macroscopic ansatz, we develop in this chapter a multi-scale coupling concept that governs the exchange of information between the micro- and the macro-scale. In this new approach, drops are resolved and computed with the help of a compressible phase-field model on the micro-scale. Both, the free-flow and the flow in the porous medium are modeled on the macro-scale. Instead of coupling these two flow regimes directly, information is exchanged across the scales with the phase-field model to include the drops' influence on the complete flow field. The coupling is bidirectional. On one hand information from the porous medium is handed over to the phase-field model to

compute drop formation and growth. On the other hand, information about the drop behavior is given to the macro-scale model, which is then able to take the drop's influence into account.
The aim of this chapter is to obtain a conceptual model for the exchange of information between the micro-scale and the macro-scale in the context of drops in a FF/PM system. In addition, we demonstrate the applicability of our model by means of a basic show case. The show case is simplified in the sense that the density difference between the two phases is quite small excluding typical vapor–liquid density ratios. We conjecture that our multi-scale approach remains effective for such fluids but we are not aware of a numerical method that ensures the robust approximation of diffuse-interface models used for the micro-scale domains.
The chapter is structured as follows. In the next Section 5.1 we specify the problem description. In Section 5.2, the macro-scale models for free-flow and flow in porous media are explained. In addition, a simple coupling concept which does not take drops into account as well as its numerical implementation are presented. Section 5.3 recaps the NSAC model used on the micro-scale. The multi-scale coupling concept is presented in Section 5.4. The simplified fluid system is introduced in Section 5.5, where some numerical results illustrate the coupling concept.

5.1 Problem Description

Our goal is to develop a model for coupling free flow with porous-medium flow by using a micro-scale model at the interface between the two domains which comprises the effect of liquid phases leaving the porous-medium domain and forming drops at the interface. This concept is depicted in Figure 5.1.
We consider a viscous compressible Newtonian fluid at isothermal conditions. The fluid occupies a domain $\Omega^{\text{macro}} \subset \mathbb{R}^3$. The domain consists of a free-flow part $\Omega_{\text{ff}}^{\text{macro}}$ and a porous-medium part $\Omega_{\text{pm}}^{\text{macro}}$ which share the interface $\Gamma_{\text{ff–pm}}$. In order to derive conditions on the interface $\Gamma_{\text{ff–pm}}$ between the two domains, which incorporate the description of drops forming and detaching at this interface, for some $N \in \mathbb{N}$ we introduce micro-domains Ω_i^{micro}, $i = 1, \dots, N$.
The number N of micro-domains Ω_i^{micro} will depend on the pore distribution within $\Omega_{\text{pm}}^{\text{macro}}$. In fact, the precise choice of N is constrained by the mesh resolution in the discretization used for Ω^{macro}, see Section 5.4.3. We assume that all the pores within one computational cell are of the same size. This allows to consider only one micro-domain per cell. For more complicated structures it would be necessary to connect to each cell multiple micro-domains with different radii for the cuboid pores. However, the number N_{pores} of pores inside one macro-cell needs to

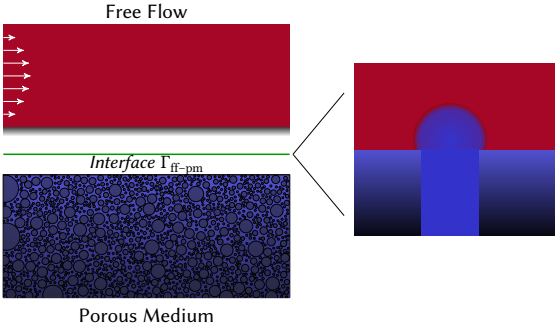

Figure 5.1: Multi-scale approach for coupled free-flow/porous-mediums systems using a micro-scale model for liquid drops forming at and detaching from the interface.

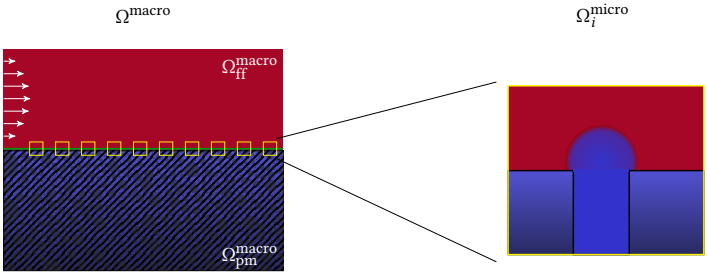

Figure 5.2: Sketch of the modeling concept with macro- and micro-domains Ω^{macro} and Ω_i^{micro}.

be taken into account when information gathered on the macro-domain is used to prescribe inflow condition for the micro-domain Ω_i^{micro}. This will be specified in Section 5.5.

We consider a pseudo 3D problem in the sense that we fix the elongation in x_3-direction, i.e. the direction normal to the prevailing flow-direction, to unity. We assume no flow in x_3-direction. The shape of the drops is therefore cylindrical. In the micro-domains Ω_i^{micro} we mean by drop the liquid in the upper part of the domain, sitting on the pore throat. Corresponding quantities are denoted with the subscript *drop*.

Recap the following notations and definitions. We denote the fluid density by $\rho > 0$, the velocity with $\boldsymbol{v} \in \mathbb{R}^3$. For simplicity we assume single-component two-phase flow, i.e. liquid–vapor flow and neglect gravity effects. The two phases

of the fluid are denoted by the subscript $\alpha \in \{\mathrm{L}, \mathrm{V}\}$. In each phase α the fluid is thermodynamically described by the corresponding specific Helmholtz free energies per unit mass, denoted by $f_\alpha = f_\alpha(\rho)$. From them we can compute the partial pressures with the relationship

$$p_\alpha = p_\alpha(\rho) = -\rho f_\alpha(\rho) + \rho \frac{\partial(\rho f_\alpha)}{\partial \rho}(\rho). \tag{5.1}$$

This is the EOS which relates the pressure and the density of the fluid.
We may add superscripts *macro* and *micro* to indicate if we consider the corresponding quantity on the macro- or on the micro-scale.
In the following two sections we specify the precise models used on the macro-scale and on the micro-scale domain.

5.2 The Macro-Scale Model

In the following, neglecting drop-related processes, the macro-scale model and the macro-scale coupling conditions are explained. The flow processes in the coupled system are described by two sets of (macro-scale) evolution equations. The equations to model the flow in the porous-medium domain $\Omega_{\mathrm{pm}}^{\mathrm{macro}}$ are given in Section 5.2.1, whereas the free-flow model for $\Omega_{\mathrm{ff}}^{\mathrm{macro}}$ is presented in Section 5.2.2. The coupling conditions for the exchange of mass and momentum are detailed in Section 5.2.3. In Section 5.2.4 we conclude with an overview of the macro-scale discretization.
As explained in Section 5.1, the domain $\Omega^{\mathrm{macro}} \subset \mathbb{R}^3$ is supposed to split into $\Omega_{\mathrm{ff}}^{\mathrm{macro}}$ and $\Omega_{\mathrm{pm}}^{\mathrm{macro}}$. The flat interface $\Gamma_{\mathrm{ff-pm}}$ separates the subdomains such that

$$\overline{\Omega^{\mathrm{macro}}} = \overline{\Omega_{\mathrm{ff}}^{\mathrm{macro}}} \cup \overline{\Omega_{\mathrm{pm}}^{\mathrm{macro}}} \quad \text{and} \quad \overline{\Omega_{\mathrm{ff}}^{\mathrm{macro}}} \cap \overline{\Omega_{\mathrm{pm}}^{\mathrm{macro}}} = \Gamma_{\mathrm{ff-pm}}.$$

5.2.1 Flow Model in the Porous-Medium Domain $\Omega_{\mathrm{pm}}^{\mathrm{macro}}$

In the subdomain $\Omega_{\mathrm{pm}}^{\mathrm{macro}}$, we assume a two-phase flow in a rigid, non-deformable porous medium. For $\alpha \in \{\mathrm{L}, \mathrm{V}\}$ we consider the two fluids in the liquid phase ($\alpha = \mathrm{L}$) and in the vapor phase ($\alpha = \mathrm{V}$), where the former is assumed to be the non-wetting phase. Instead of resolving the porous structure, all quantities are averaged over representative elementary volumes. Therefore, the flow processes are described using the volume-averaged quantities porosity Φ, phase saturations S_α, intrinsic permeability $\boldsymbol{K}$ and relative permeabilities $k_{r,\alpha}$. The porosity Φ describes the ratio of void space volume and total volume. Each phase saturation S_α is defined as the phase volume per total volume. Hence, the saturations add up to one:

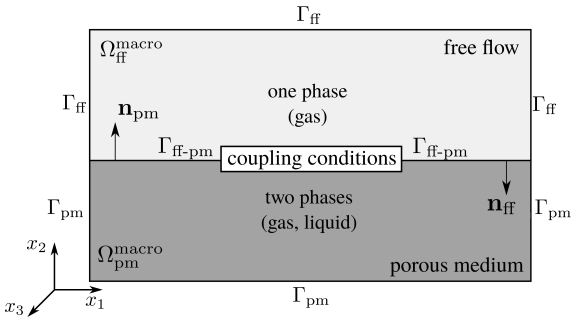

Figure 5.3: Detailed geometry of the macro-scale model domains.

$S_{\text{L}} + S_{\text{V}} = 1$. The intrinsic permeability $\boldsymbol{K} = (K_{ij})$ is a material parameter which takes the effect of the porous structure on the micro-scale flow paths into account. The relative permeabilities $k_{r,\alpha} = k_{r,\alpha}(S_\alpha)$ depend on the phase saturations and account for the permeability reduction due to the presence of the other phase. For $\alpha \in \{\text{L}, \text{V}\}$, the mass balance in $\Omega_{\text{pm}}^{\text{macro}}$ is given by

$$\Phi \partial_t(\rho_\alpha(p_\alpha) S_\alpha) + \operatorname{div}\left(\rho_\alpha(p_\alpha)\boldsymbol{v}_\alpha\right) = q_\alpha, \tag{5.2}$$

with q_α accounting for a possible balance term.
For the momentum balance, Darcy's law can be applied and rearranged to an equation for the phase velocity [15]. Since gravity is neglected, this results for $\alpha \in \{\text{L}, \text{V}\}$ in

$$\boldsymbol{v}_\alpha = -\boldsymbol{K}\frac{k_{r,\alpha}}{\mu_\alpha}\nabla p_\alpha. \tag{5.3}$$

Here μ_α denotes the dynamic viscosity of the corresponding phase. With (5.3), the phase velocity $\boldsymbol{v}_\alpha$ in Equation (5.2) can be replaced, which reduces the number of equations to be solved. We choose the vapor pressure p_{V} and the liquid saturation S_{L} as primary unknowns in Ω^{pm} and solve the mass balance equations (5.2) for each phase separately. The pressures are linked by the capillary pressure

$$p_c(S_{\text{V}}) = p_{\text{L}}(S_{\text{V}}) - p_{\text{V}}, \tag{5.4}$$

where the function p_c needs to be prescribed depending on the application. Hence, we can reconstruct the liquid pressure from (5.4) with p_{V}. Both phases are assumed to be compressible and the viscosities μ_α to be constant. More details on modeling flow in porous media can be found in e.g. [15, 57].

5.2.2 The Flow Model in the Free-Flow Domain $\Omega_{\mathrm{ff}}^{\mathrm{macro}}$

In $\Omega_{\mathrm{ff}}^{\mathrm{macro}}$ we assume to have a single-phase compressible gaseous free-flow. The total mass balance is given as

$$\partial_t \rho_{\mathrm{V}} + \operatorname{div}(\rho_{\mathrm{V}} \boldsymbol{v}_{\mathrm{V}}) = 0, \tag{5.5}$$

with the density $\rho_{\mathrm{V}} = \rho_{\mathrm{V}}(p_{\mathrm{V}})$ and the velocity $\boldsymbol{v}_{\mathrm{V}}$.
For the momentum balance, we employ the Navier–Stokes equations as

$$\partial_t(\rho_{\mathrm{V}} \boldsymbol{v}_{\mathrm{V}}) + \operatorname{div}\left(\rho_{\mathrm{V}} \boldsymbol{v}_{\mathrm{V}} \otimes \boldsymbol{v}_{\mathrm{V}} + p_{\mathrm{V}} \boldsymbol{I}\right) = \operatorname{div}\left(\mu_{\mathrm{V}} \left(\nabla \boldsymbol{v}_{\mathrm{V}} + \nabla \boldsymbol{v}_{\mathrm{V}}^{\top}\right)\right), \tag{5.6}$$

where p_{V} is the pressure, $\boldsymbol{I}$ the identity tensor and μ_{V} the dynamic viscosity as in Section 5.2.1.
As primary variables in $\Omega_{\mathrm{ff}}^{\mathrm{macro}}$ we choose the pressure p_{V} and the velocity $\boldsymbol{v}_{\mathrm{V}}$. Due to the fluid's compressibility, the density depends on the pressure. This dependency is characterized by the EOS (5.1), which will be specified later, see (5.30) below.

5.2.3 The Macro-Scale Coupling Concept

The exchange of mass and momentum between free-flow and porous-medium domains is modeled with the help of appropriate coupling conditions. These conditions are prescribed at the interface $\Gamma_{\mathrm{ff-pm}}$ as an interior boundary condition. Additionally, on Γ_{ff} and Γ_{pm}, (external) boundary conditions have to be set. The interface $\Gamma_{\mathrm{ff-pm}}$ is assumed to be devoid of thermodynamic properties, i.e. it cannot store mass or momentum. Consequently, the continuity of fluxes across the interface has to be guaranteed. The following coupling concept is taken from [83], where the previously existing coupling concepts for single-phase systems are extended such that a two-phase flow in the porous medium can be considered. It is based on the assumption of local thermodynamic equilibrium at the interface. For an isothermal, immiscible system, only mechanical equilibrium at the interface has to be taken into account for the coupling.
The stress balance in normal direction is given by

$$\left[\boldsymbol{n} \cdot \left(p_{\mathrm{V}} \boldsymbol{I} - \mu_{\mathrm{V}}(\nabla \boldsymbol{v}_{\mathrm{V}} + \nabla \boldsymbol{v}_{\mathrm{V}}^{\top}) + \rho_{\mathrm{V}} \boldsymbol{v}_{\mathrm{V}} \otimes \boldsymbol{v}_{\mathrm{V}}\right) \boldsymbol{n}\right]^{\mathrm{ff}} = \left[p_{\mathrm{V}}\right]^{\mathrm{pm}},$$

with the respective unit outer normal vectors $\boldsymbol{n}$. The square brackets indicate that all variables are either taken from $\Omega_{\mathrm{ff}}^{\mathrm{macro}}$ or $\Omega_{\mathrm{pm}}^{\mathrm{macro}}$, i.e. for some quantity u and $\boldsymbol{x} \in \Gamma_{\mathrm{ff-pm}}$ we define

$$[u]^{\mathrm{ff}} = \lim_{\varepsilon \to 0, \varepsilon > 0} u(\boldsymbol{x} - \varepsilon \boldsymbol{n}_{\mathrm{ff}}), \qquad [u]^{\mathrm{pm}} = \lim_{\varepsilon \to 0, \varepsilon > 0} u(\boldsymbol{x} + \varepsilon \boldsymbol{n}_{\mathrm{ff}}).$$

The viscous forces in the porous medium are already accounted for in the Darcy velocity (5.3). Therefore, the pressure p_V on the porous medium side has to balance the complete stress tensor from the free-flow side.
For the tangential forces at the interface, a condition for the tangential free-flow velocity has to be formulated. An appropriate choice is the Beavers–Joseph–Saffman condition [98]:

$$\left[\left(\boldsymbol{v}_V + \frac{\sqrt{K_{ii}}}{\alpha_{BJ}}(\nabla \boldsymbol{v}_V + \nabla \boldsymbol{v}_V^\top)\boldsymbol{n}\right) \cdot \boldsymbol{t}_i\right]^{ff} = 0, \quad i = 2, 3. \tag{5.7}$$

In (5.7) we denote the tangential vector for dimension i by $\boldsymbol{t}_i$, the i-th diagonal entry of the permeability tensor $\boldsymbol{K}$ with K_{ii} and the Beavers–Joseph coefficient by α_{BJ}. By using (5.7) we neglect the small tangential velocity in the porous medium near the interface.
Assuming that all liquid that reaches the interface immediately evaporates into the free-flow, the continuity of mass fluxes across Γ_{ff-pm} is given as

$$\left[\left(\rho_V \boldsymbol{v}_V\right) \cdot \boldsymbol{n}\right]^{ff} = \left[\left(\rho_V \boldsymbol{v}_V + \rho_L \boldsymbol{v}_L\right) \cdot \boldsymbol{n}\right]^{pm}.$$

As mentioned in the before, this assumption should be reconsidered since it does not take into account the influence of drops at the interface.
In order to include drop-related effects in the model, we have to omit the assumption of immediate evaporation. Then, only the gaseous fluxes are balanced, which yields

$$\left[\left(\rho_V \boldsymbol{v}_V\right) \cdot \boldsymbol{n}\right]^{ff} = \left[\left(\rho_V \boldsymbol{v}_V\right) \cdot \boldsymbol{n}\right]^{pm}. \tag{5.8}$$

The conditions above lead to a well-posed model, however the corresponding model cannot capture drops forming at the interface Γ_{ff-pm}. To capture them, we introduce in the following the phase-field model on the micro-scale to include these effects.
Concerning the condition for the liquid phase at the upper boundary, we use an outflow condition, based on the velocity

$$\boldsymbol{v}_L = -\boldsymbol{K}\frac{k_{r,L}}{\mu_L}\nabla p_L. \tag{5.9}$$

To compute ∇p_L, we use information from the micro-scale domain. This will be specified later, see (5.23).

5.2.4 Numerical Discretization

We use the open-source simulator DuMu^x [47] to solve the equations in the coupled FF/PM flow system.
The spatial discretization is based on the finite-volume method. In the free-flow domain, we apply a staggered grid, where the velocity components are shifted by half a cell away from the cell centers, see [56]. For the porous medium, a cell-centered two-point flux approximation scheme is used [1]. A fully-implicit Euler method is used for the temporal discretization.
The global system is solved monolithically. The solution of the non-linear system is based on Newton's method. The linear subsystems are solved using the UMFPack library.

5.3 The Micro-Scale Model

In this section we briefly recap the NSAC model. We utilize this model on the micro-scale domains Ω_i^{micro}. Boundary and initial conditions appropriate to the problem setting are discussed in Section 5.3.2.

5.3.1 The Phase-Field Model in Ω_i^{micro}

On the micro-scale we employ the isothermal compressible Navier–Stokes–Allen–Cahn model introduced in Chapter 2. The two-phase fluid occupies a domain $\Omega_i^{\text{micro}} \subset \mathbb{R}^3$, see Figure 5.4.
For the sake of readability we skip the indices i of the state variables for the remainder of this section. Recall the isothermal compressible Navier–Stokes–Allen–Cahn system (2.4)–(2.6):

$$\begin{aligned} \partial_t \rho + \operatorname{div}(\rho \boldsymbol{v}) &= 0, \\ \partial_t(\rho \boldsymbol{v}) + \operatorname{div}(\rho \boldsymbol{v} \otimes \boldsymbol{v} + p\boldsymbol{I}) &= \operatorname{div}(\boldsymbol{S}) - \gamma \operatorname{div}(\nabla\varphi \otimes \nabla\varphi) \quad \text{in } \Omega_i^{\text{micro}} \times (0, T), \\ \rho \partial_t \varphi + \rho \nabla\varphi \cdot \boldsymbol{v} &= -\eta\mu. \end{aligned}$$

5.3.2 Boundary and Initial Conditions

The computational domain Ω_i^{micro} is depicted in Figure 5.4.
The boundary $\partial\Omega_i^{\text{micro}}$ can be divided into an inflow boundary $\Gamma_{i,\text{inflow}}$, slip boundary $\Gamma_{i,\text{slip}}$, no-slip boundary $\Gamma_{i,\text{no-slip}}$ and symmetry boundary $\Gamma_{i,\text{symmetry}}$ (see Figure 5.4) such that

$$\partial\Omega_i^{\text{micro}} = \Gamma_{i,\text{inflow}} \cup \Gamma_{i,\text{slip}} \cup \Gamma_{i,\text{no-slip}} \cup \Gamma_{i,\text{symmetry}}.$$

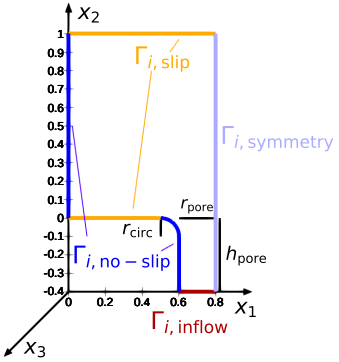

Figure 5.4: Sketch of the computational domain Ω_i^{micro} with the different boundary types.

Assuming an impermeable wall at $\Gamma_{i,\text{slip}} \cup \Gamma_{i,\text{no-slip}}$, the velocity must satisfy the boundary condition

$$\boldsymbol{v} \cdot \boldsymbol{n} = 0, \tag{5.10}$$

$$\nabla\varphi \cdot \boldsymbol{n} = 0, \qquad \text{on } \Gamma_{i,\text{slip}}. \tag{5.11}$$

$$\boldsymbol{v} = \boldsymbol{0}, \tag{5.12}$$

$$\nabla\varphi \cdot \boldsymbol{n} = 0, \qquad \text{on } \Gamma_{i,\text{no-slip}} \tag{5.13}$$

Note that the conditions (5.11), (5.13) realize static contact angle boundary conditions with $\theta_s = 90^\circ$.
To couple to the porous-medium macro-scale domain we prescribe at the inflow $\Gamma_{i,\text{inflow}}$ on the bottom

$$v_{x_1}(\boldsymbol{x}, t) = 0, \tag{5.14}$$

$$v_{x_2}(\boldsymbol{x}, t) = \frac{3}{4r_{\text{pore}}} v_{\text{inflow}} \left(1 - \left(\frac{x_1 - l/2}{r_{\text{pore}}}\right)^2\right), \tag{5.15}$$

$$v_{x_3}(\boldsymbol{x}, t) = 0, \qquad (\boldsymbol{x}, t) \in \Gamma_{i,\text{inflow}} \times [0, T_{\text{final}}), \tag{5.16}$$

$$\varphi(\boldsymbol{x}, t) = 1, \tag{5.17}$$

$$\rho(\boldsymbol{x}, t) = \rho_{\text{L}}(p), \tag{5.18}$$

where $l/2 = 0.8$ is the length of domain. The quantities v_{inflow} and $\rho_{\text{L}}(p)$ are obtained from the solution in the porous-medium domain $\Omega_{\text{pm}}^{\text{macro}}$.
Equation (5.15) realizes a parabolic velocity profile which is coupled to the scaled velocity v_{inflow} obtained from the macro-scale computation (cf. (5.33) below). In fact, (5.15) implies

$$\int_{\Gamma_{i,\text{inflow}}} v_{x_2}(\boldsymbol{x}) \, \mathrm{d}\boldsymbol{x} = 2 \int_0^1 \int_{l/2 - r_{\text{pore}}}^{l/2} v_{x_2}(x_1) \, \mathrm{d}x_1 \, \mathrm{d}x_3 = v_{\text{inflow}}.$$

Since there is no inflow in tangential direction, we can assume symmetry and prescribe symmetrical boundary conditions on Γ_{symmetry}.
It remains to endow the system with initial conditions. We assume that initially the pore throat is filled with liquid, but no drop is formed. For $\boldsymbol{x} \in \Omega^{\text{micro}}$, this means

$$\tilde{\rho}_0(\boldsymbol{x}) = \begin{cases} \rho_{\text{L}} & : x_2 \leq 0, \\ \rho_{\text{V}} & : x_2 > 0, \end{cases} \tag{5.19}$$

$$\tilde{\varphi}_0(\boldsymbol{x}) = \begin{cases} 1 & : x_2 \leq 0, \\ 0 & : x_2 > 0, \end{cases} \tag{5.20}$$

$$\tilde{\boldsymbol{v}}_0(\boldsymbol{x}) = \boldsymbol{0}. \tag{5.21}$$

The function $\tilde{u}_0 = (\tilde{\rho}_0, \tilde{\varphi}_0, \tilde{\boldsymbol{v}}_0)$ is discontinuous. However, such data can trigger instabilities for the (numerical) solution of a diffuse-interface model. In order to avoid a large initial layer in time, we replace $\tilde{u}_0$ by a regularization. We set the discontinuous initial data from (5.19)–(5.21) and solve the diffusion problem

$$-\lambda \Delta u_0 + u_0 = \tilde{u}_0 \quad \text{on } \Omega_i^{\text{micro}},$$

in order to obtain the final initial data u_0. The diffusion coefficient λ is chosen according to the thickness of the diffuse interface, which in turn is determined by γ. In our example the choice $\lambda = \frac{\gamma^2}{2}$ lead to a good approximation of the interface width.

5.3.3 Numerical Discretization

For the numerical discretization of the NSAC model on the micro-scale we employ the energy-consistent dG scheme from Chapter 3, given by Algorithm 3.11.

5.4 Coupling the Different Scales

The new coupling concept presented in this chapter combines two models, acting on different length scales, to a multi-scale model for the simulation of processes with interaction between micro-scale drops and macroscopic FF/PM systems. Other than for instance in homogenization model concepts, the liquid drops are resolved individually with help of the NSAC model presented in Section 5.3. The drops grow due to outflow of liquid from the porous-medium domain and detach at some point.
However, we cannot combine the two models presented in Sections 5.2 and 5.3 in a straightforward way. The consideration to provide compatible quantities is described in Section 5.4.1. The main multi-scale coupling strategy and data exchange procedure are explained in Section 5.4.2. Notably, we formulate it directly at the time-discrete level.

5.4.1 Compatibility of the Two Models

Fluid Parameters and Primary Variables

We need to be careful about consistent assumptions on the separate scales to use in the respective models. The viscosity parameters μ_α used in the macro-domain model need to be scaled according to (6.1). The same is true for the velocity $\boldsymbol{v}_{\mathrm{pm}}$ from the macro-scale porous-medium model. The scaling of the velocity is described below in detail and results in (5.33).
In order to couple the models of the macro- and micro-domains Ω^{macro} and $\Omega_i^{\mathrm{micro}}$, we need to find a way to reconstruct the primary variables of each model from the ones of the respective other domain. Due to the different balance equations used in the two models, we have the primary variables p^{macro}, $\boldsymbol{v}^{\mathrm{macro}}$, $S_{\mathrm{l}}^{\mathrm{macro}}$ in Ω^{macro} and ρ_i^{micro}, $\boldsymbol{v}_i^{\mathrm{micro}}$, $\varphi_i^{\mathrm{micro}}$ in $\Omega_i^{\mathrm{micro}}$. For the precise exchange of information between the two scales, the primary variables have to be linked to each other. The (common) EOS of stiffened gas type enables us to compute the macro-scale pressure p^{macro} from the micro-scale density ρ_i^{micro}, and vice versa. The macro-scale velocity $\boldsymbol{v}^{\mathrm{macro}}$ in the porous medium is scaled with the porosity to obtain the micro-scale velocity, which then corresponds to the velocity $\boldsymbol{v}_i^{\mathrm{micro}}$ in the micro-scale model on $\Omega_i^{\mathrm{micro}}$. The phase-field variable $\varphi_i^{\mathrm{micro}}$ is related to the volume-based liquid saturation S_l^{macro}. However, we do not interchange information based on these quantities directly. Thus, we do not need to specify the exact relation.

Assumptions on the Pore Distribution in the Porous-Medium Domain

Since we have different length scales on the two model domains it is natural that in one computational cell (macro-cell) on the macro-domain several pores can be found. This depends on the spatial resolution used on the macro-domain Ω^{macro} and the material characteristics of the porous medium. We assume for simplicity that all pores within one macro-cell have the same size. This allows us to solve only one micro-problem in the micro-domain Ω_i^{micro} per macro-cell. Note that with this choice we restrict ourselves to homogeneous porous media. However, it is possible to extend this approach to a heterogeneous pore-size distribution, which leads us to solve multiple cell problems and combine their outputs.

5.4.2 The Coupling Strategy

The coupling strategy is based on the iterative exchange of data between the numerical solvers of the two models. Given a time mesh $t_0 = 0 < t_1 < t_2 < \ldots$, let

$$u_n^{\text{macro}} := (p^{\text{macro}}, \boldsymbol{v}^{\text{macro}}, S_{\text{L}}^{\text{macro}})^\top(\cdot, t_n)$$

and

$$u_{i,n}^{\text{micro}} := (\rho_i^{\text{micro}}, \boldsymbol{v}_i^{\text{micro}}, \varphi_i^{\text{micro}})^\top(\cdot, t_n).$$

For the sake of readability, the macro-scale solver is referred to as $\text{MacroSolver} = \text{MacroSolver}(u^{\text{micro}})$ and the micro-scale solvers as $\text{MicroSolver}_i = \text{MicroSolver}_i(u^{\text{macro}})$ in the following.
The general multi-scale procedure to advance the solution from the discrete time t_n to $t_{n+1} = t_n + \Delta t_n$ is the following:

Algorithm 5.1 (Multi-Scale Procedure)**:**

1. *MicroSolver*$_i(u_n^{\text{macro}})$ *provides the solution of problem* (2.4)–(2.6) *with boundary conditions* (5.10)–(5.18)*, for all domains* Ω_i^{micro} *in time-step* $(t_n, t_{n+1}]$*. If* $t_n = 0$ *or a drop has detached in* t_{n-1}*, we prescribe the condition* (5.19)–(5.21)*, else we use* $u_{i,n-1}^{\text{micro}}$*.*

2. *MicroSolver*$_i$ *transfers solution* $u_{i,n+1}^{\text{micro}}$ *to MacroSolver.*

3. *MacroSolver*$(u_{1,n+1}^{\text{micro}}, \ldots u_{N,n+1}^{\text{micro}})$ *provides the solution to problem* (5.2)–(5.3),(5.5)–(5.9) *in* Ω^{macro} *in time-step* $(t_n, t_{n+1}]$*.*

4. *MacroSolver hands back* u_{n+1}^{macro} *to MicroSolver*$_i$*.*

For the detachment criterium used in step 1, we refer to Section 5.4.3. Note that transferring the solution from one solver to the other seems trivial but can be cumbersome in practice. Since we use the C++ based solver DuMu^x to obtain the macro-scale solution and a FEniCS based solver using Python for the micro-scale problems, this step is actually not straightforward.
We observe, that the coupling is done explicitly in time, with both solvers using the same time-step size. The time-step size in the micro-scale simulation is most of the time more restrictive such that we could compute several (micro-) time-steps and update afterwards. However, this leads to problems for the macro-scale Newton iteration, which would need time-resolved initial guesses. Since the macro solver is computationally less expensive anyway, we simply run both solvers with the same time-step size.

5.4.3 Data Exchange in the Multi-Scale Algorithm

As shown in Figure 5.5, different data is exchanged between the scales.

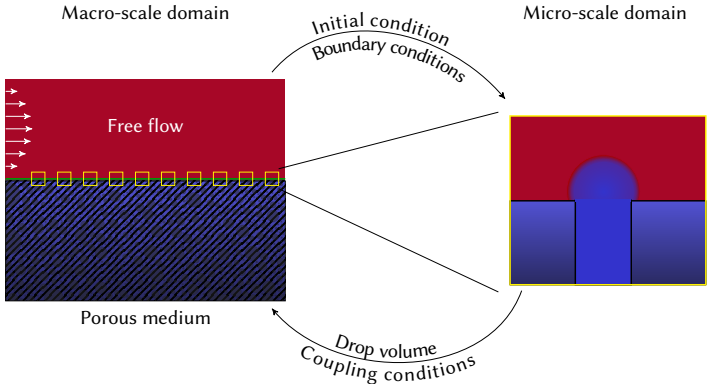

Figure 5.5: Visualization of the coupling concept. Data exchange between macro- and micro-scale domains.

This exchange procedure can vary in complexity, depending on which data is exchanged across the scales. In this paper we use to following version.

5.4.3.1 Data Exchange Between Ω_{pm} and Ω_i^{micro}

The number N of micro-domains Ω_i^{micro} is now fixed to the number of macro-cells at the boundary Γ_{ff-pm} in the domain Ω_{pm}^{macro} in x_1-direction. For each such cell we communicate the flux $\rho_L \boldsymbol{v}_{pm} = \rho_{i,L} \boldsymbol{v}_{i,pm}$. This is used for the boundary condition on Ω_i^{micro}. From the micro-scale we hand the drop volume $V_{i,drop}$, surface tension σ_i, and mean pressure $\langle p_i^{micro} \rangle$ to the macro-scale.
The mean pressure $\langle p_i^{micro} \rangle$ is computed as

$$\langle p_i^{micro} \rangle = \int_{\Omega_i^{micro}} p(\rho^{micro}(\boldsymbol{x})) \mathbf{1}|_{\{x_2=-0.3\}}(\boldsymbol{x}) \, \mathrm{d}\boldsymbol{x}, \tag{5.22}$$

where $\mathbf{1}|_{\{x_2=-0.3\}}$ denotes the indicator function, i.e. for a set A

$$\mathbf{1}|_A(\boldsymbol{x}) = \begin{cases} 1, & \boldsymbol{x} \in A, \\ 0, & \boldsymbol{x} \notin A. \end{cases} \tag{5.23}$$

With this pressure, for the porous-medium domain, a flux across the upper boundary can be computed by means of

$$v_{i,x_3,L} = -\boldsymbol{K} \frac{k_{r,L}}{\mu_L} \frac{\Delta p_{L,i}}{\Delta x_2},$$

where $\Delta p_{L,i}$ denotes the difference of the pressure inside the i-th uppermost computational cell of the porous-medium domain and the corresponding mean pressure, and Δx_2 denotes the difference of the cell center of this cell and the boundary Γ_{ff-pm}.
The drop volume and surface tension are computed from u_i^{micro} according to (5.28) and (5.29). They are used to check the detachment criterion, see (5.27) below.
Therefore, all boundary conditions for the free-flow balance equations at the interface depend directly on the processes happening in the porous medium as given in Section 5.2.3.

Remark 5.2 (Mean pressure)**:** *Note that we compute the mean pressure* (5.22) *slightly above the lower boundary of the micro-domain. This due to the fact, that we prescribe the density (and therefore the pressure) on the lower boundary. Hence, the mean pressure is taken above the boundary layer, where it changes rapidly.*

5.4.3.2 Data Exchange Between Ω_{ff} and Ω_i^{micro}

The macro-scale solver evaluates the solution from the micro-scale domains Ω_i^{micro} to determine whether a drop detaches. The detachment decision is done by balancing the forces acting on the drop. To do so, we balance forces for an artificially

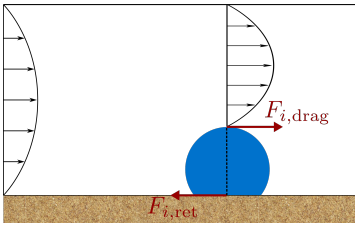

Figure 5.6: Force balance on a spherical drop.

designed macro-scale drop with the corresponding volume $V_{i,\text{drop}}$: The drag force $F_{i,\text{drag}}$ is the force exerted by the macro-scale flow field, while the retention force $F_{i,\text{ret}}$ is the force which holds the drop on the solid surface, as illustrated in Figure 5.6. The drag force can be computed as e.g. given in [111] by

$$F_{i,\text{drag}}(\boldsymbol{x}, t) = \frac{1}{2}\rho_V(\boldsymbol{x}, t)v_{\text{V},x_1}(\boldsymbol{x}, t)^2 c_\text{d}(\text{Re})A_{i,\text{proj}}(t), \tag{5.24}$$

with the drag coefficient $c_\text{d}(\text{Re}) = \frac{30}{\sqrt{\text{Re}}}$ ([28]), the Reynolds number $\text{Re} = \frac{Lv_V\rho_V}{\mu_V}$, the horizontal velocity component v_{V,x_1} and the projected area of the drop normal to the flow direction $A_{i,\text{proj}}(t) = r_{i,\text{drop}}(t)(1 - \cos(\theta))|\boldsymbol{e}_{x_3}|$, where $\boldsymbol{e}_{x_3}$ denotes the three-dimensional unit vector in x_3 direction, $r_{i,\text{drop}}$ is the drop radius on Ω_i^{micro}, and θ is the given equilibrium contact angle between the liquid–vapor interface and the solid surface.
The retention force can be computed in our setting as given in [27] by

$$F_{i,\text{ret}}(t) = \sigma_i(t)(\cos(\pi - \theta_a) + \cos(\theta_r))|\boldsymbol{e}_{x_3}|. \tag{5.25}$$

Here, θ_a is the advancing and θ_r is the receding contact angle. Therefore, the drop deformation cannot be neglected for the computation of the retention force and the assumption of a spherical drop has to be omitted here. Let the surface tension coefficient computed in the micro-scale simulation be denoted by σ_i.
We evaluate the drag force at the phase interface $\boldsymbol{x}_i$ above the center of the drop. As soon as this drag force exceeds the retention force at some point in time, i.e.

$$F_{i,\text{drag}}(\boldsymbol{x}_i, t) > F_{i,\text{ret}}(t) \tag{5.26}$$

holds, a drop detaches from the solid surface, and is not considered anymore in the (macro-scale) free-flow domain.

Since the drop radius $r_{i,\text{drop}}$ occurs in the drag force, we can obtain a condition to determine the critical drop volume $V_{i,\text{drop}}$ (5.28), for which a drop detaches, using (5.26). Inserting Equations (5.24) and (5.25), and rearranging the terms leads to

$$V_{i,\text{drop}}(t) > V_{i,\text{critical}}(t), \tag{5.27}$$

with

$$V_{i,\text{critical}}(t) := \frac{\pi}{2}\left(\frac{2\sigma_i(\cos(\pi-\theta_a)+\cos(\theta_r))}{(1-\cos(\theta))}\frac{\sqrt{\text{Re}}}{30\rho_V(\boldsymbol{x}_i,t)v_{\text{V},x_1}(\boldsymbol{x}_i,t)^2}\right)^2|\boldsymbol{e}_{x_3}|.$$

Inequality (5.27) gives us a condition on the drop volume to determine whether a drop detaches. If a drop detaches, the micro-solver is newly initiated according to conditions (5.19)–(5.21).

The micro-scale model on the other hand uses the flux $\rho_{\text{pm}}\boldsymbol{v}_{\text{pm}}$ from the macro-scale solution in $\Omega_{\text{pm}}^{\text{macro}}$ as boundary condition at the lower inflow boundary Γ_{inflow}. The drop volume is computed by

$$V_{i,\text{drop}}(t) = 2\int_{\Omega_{\text{micro}}}\varphi(\boldsymbol{x},t)\ \mathrm{d}\boldsymbol{x} - \left(d_{i,\text{pore}}h_{i,\text{pore}} + 2r_{i,\text{circ}}^2\left(1-\frac{\pi}{4}\right)\right)|\boldsymbol{e}_{x_3}|, \tag{5.28}$$

where $h_{i,\text{pore}}$ denotes the height of the pore and $r_{i,\text{circ}}$ is the radius of the rounded corner, see Figure 5.4.

The surface tension σ_i is calculated via

$$\sigma_i(t) = 2\gamma\int_{\Gamma_{i,1}}|T\nabla\varphi(S,t)|^2\ \mathrm{d}S, \tag{5.29}$$

where T denotes the trace operator.

Here $\Gamma_{i,1}$ denotes the boundary which consists of the left boundary of the pore, the curved boundary and the lower boundary of the free-flow part, cf. Figure 5.4. Considering (5.29), we note that the surface tension σ_i can be interpreted as the energy in the interface region.

The exchange procedure as described above allows to obtain a qualitative understanding on the influence of both scales on each other. Of course, more data should be exchanged to capture more aspects of the coupled system. A possible extension is to take also into account information of the free-flow in the micro-scale simulation. In this fashion we can directly simulate the deformation of the drop due to free-flow velocity. First results in this direction are depicted in Figure 5.7.

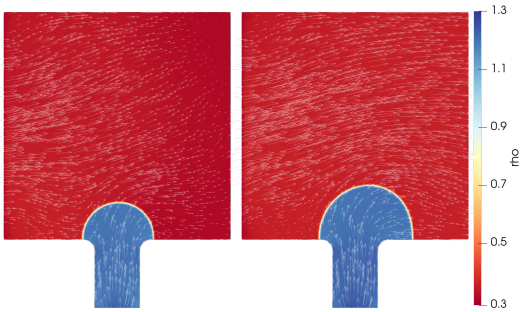

Figure 5.7: Micro-scale simulation of a deforming drop due stress by the free-flow velocity field. Density ρ with velocity glyph at two different times.

5.5 Numerical Experiments

In this section we present numerical experiments and results to illustrate the usage of our multi-scale model.

5.5.1 Fluid Properties

To illustrate the new multi-scale approach a somewhat artificial fluid system is used. The fluid consists of a single component which occurs in its gaseous as well as its liquid state. We use a stiffened-gas type EOS to relate the density to the pressure of the compressible fluid, i.e.,

$$\begin{aligned} p_{\mathrm{L}}(\rho) &= 5\rho - 5.5, \\ p_{\mathrm{V}}(\rho) &= 1.5\rho - 0.084. \end{aligned} \tag{5.30}$$

Here $p_\alpha(\rho), \alpha \in \{\mathrm{L}, \mathrm{V}\}$, denotes the partial pressure of the liquid (vapor) phase. Using (5.1) this translates into the following free energy densities for the phase-field model:

$$\rho f_{\mathrm{L}}(\rho) = 5\rho \ln(\rho/\rho_0) - 5.8\rho + 5.5, \tag{5.31}$$

$$\rho f_{\mathrm{V}}(\rho) = 1.5\rho \ln(\rho/\rho_0) + 0.3\rho + 0.084, \tag{5.32}$$

with ρ_0 normalized to 1.
The parameters in (5.31), (5.32) are chosen in a way that the minima of the free energy densities have the same height, i.e. no phase is energetically more favorable. Additionally, we shift the location of the minima to the single-phase equilibrium

values

$$\rho_{\mathrm{L,EQ}} \coloneqq \operatorname*{argmin}_{\rho} \rho f_{\mathrm{L}}(\rho) \approx 1.2,$$

$$\rho_{\mathrm{V,EQ}} \coloneqq \operatorname*{argmin}_{\rho} \rho f_{\mathrm{V}}(\rho) \approx 0.3.$$

For the viscosities in (5.3), (5.6), (2.7), we use $\mu_{\mathrm{L}} = 0.1025$ and $\mu_{\mathrm{V}} = 0.01025$.
As capillary pressure relation (5.4) we use the simple constant relation

$$p_c(S_{\mathrm{V}}) = p_c \coloneqq 0.134.$$

This value is chosen such that the difference between the liquid pressure and the vapor pressure is constant equal to the value in the single-phase equilibria, i.e. $p_{\mathrm{L}}(\rho_{\mathrm{L,eq}}) - p_{\mathrm{V}}(\rho_{\mathrm{V,eq}}) = 0.134$.

5.5.2 Setup of the Numerical Example

We choose the macroscopic domain as $\Omega^{\mathrm{macro}} = [0, 0.25] \times [0, 0.35]$. The free-flow part is $\Omega^{\mathrm{macro}}_{\mathrm{ff}} = [0, 0.25] \times [0.25, 0.35]$ and the porous-medium part $\Omega^{\mathrm{macro}}_{\mathrm{pm}} = [0, 0.25] \times [0, 0.25]$. To save computational effort, we use only one cell in x_1-direction, i.e. $\Delta x_1 = 0.25$. In each subdomain we have three cells in x_2-direction, i.e. $\Delta x_{2,\mathrm{ff}} = {}^{0.1}/_{3}$ and $\Delta x_{2,\mathrm{pm}} = {}^{0.25}/_{3}$, as shown in Figure 5.8.
The initial data are chosen as follows. In $\Omega^{\mathrm{macro}}_{\mathrm{ff}}$, the pressure is initially set to $p_{\mathrm{V}} = 0.366$. For the horizontal velocity, a parabolic profile with a maximum velocity of $v_{\mathrm{V},x_1} = 5$ is assumed. The vertical velocity is $v_{\mathrm{V},x_2} = 0$. The initial pressure in $\Omega^{\mathrm{macro}}_{\mathrm{pm}}$ is set to $p_{\mathrm{V}} = 0.366$ and the initial saturation is given as $S_{\mathrm{L}} = 0.5$.
For boundary and coupling conditions we set the following. On the left and upper boundaries of $\Omega^{\mathrm{macro}}_{\mathrm{ff}}$, the velocity components are set according to the initial values. The Dirichlet values on the right boundary are equal to the initial values. On the left boundary, a no-flow condition is set for the mass balance. At the coupling interface $\Gamma_{\mathrm{ff-pm}}$, the coupling conditions (5.7) and (5.8) are set as Neumann boundary conditions for p_{V} and $\boldsymbol{v}_{\mathrm{V}}$. For the $\boldsymbol{v}_{\mathrm{L}}$ we use (5.9). No-flow boundary conditions are prescribed at the left and right boundary. On the lower boundary, inflow rates of $q_{\mathrm{L}} = 0.5$, $q_{\mathrm{V}} = 0.3$ are chosen. At $\Gamma_{\mathrm{ff-pm}}$, equation (5.8) is evaluated for the mass balance of the vapor phase.
The porosity is set to $\Phi = 0.41$ and the intrinsic permeability is $\boldsymbol{K} = 0.9\boldsymbol{I}$. For the relative permeabilities we use a linear material law, i.e. $k_{r,\alpha}(S_\alpha) = S_\alpha$.

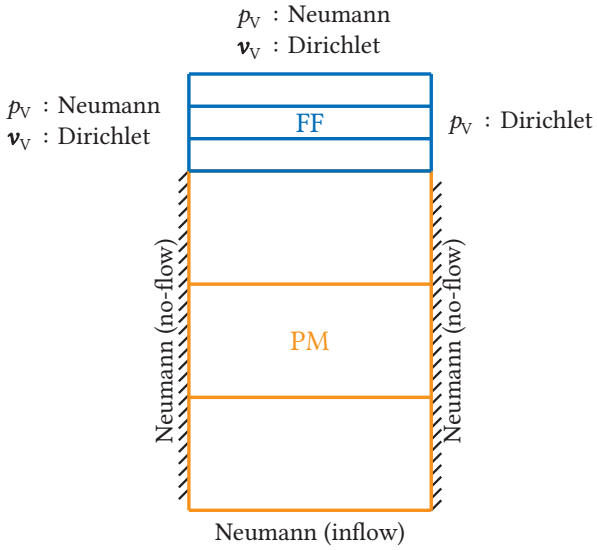

Figure 5.8: Sketch of computational domain Ω^{macro} and macro-cells for the macro-scale problem.

The microscopic domain is depicted in Figure 5.4. We have 2324 unstructured triangle cells in the computational domain and dG polynomial degree $k = 1$. As initial values we employ (5.19)–(5.21), with $r_{1,\text{pore}} = 0.2$ and $h_{1,\text{pore}} = 0.4$. Note that we use $h_{1,\text{pore}} = 2r_{1,\text{pore}}$. This is an additional degree of freedom whose influence should be investigate in future work by means of comparison to experimental data.
We assume $N_{\text{pore}} = 23$ pores with diameter $d_{1,\text{pore}} = 4.4 \cdot 10^{-3}$ for computational cell in the macroscopic domain.
To ensure mass conservation, the flux through the boundary of one macro cell needs to be equal to the sum of the micro fluxes through N_{pore} pores, i.e.,

$$l\rho v_{\text{pm}} = \rho v_{\text{inflow}} d_{\text{pore}} N_{\text{pore}} \implies v_{\text{inflow}} = \frac{l}{N_{\text{pore}} d_{\text{pore}}} v_{\text{pm}} \approx 2.47 v_{\text{pm}}. \tag{5.33}$$

Here, $l = 0.25$ denotes the length of the macro cell.
Note that we get v_{pm} from the macro-scale solution in $\Omega^{\text{macro}}_{\text{pm}}$ with the help of Darcy's law (5.3).
We run the simulation until the final time $T_{\text{end}} = 3$.

5.5.3 Results

We are first interested in the microscopic results, especially in the drop volume and surface tension values over time. These quantities are depicted in Figure 5.9. After some initial time a periodic behavior is reached. After detachment of a drop we have a small initial layer since the phase-field simulation is newly initialized after detachment. This can be seen in the rapid behavior of the surface tension coefficient σ. The drop volume increases over time until a critical value of approximately 0.03 is reached. This value depends on the surface tension. We see a periodic behavior which is expected due to the constant inflow and free-flow velocities.

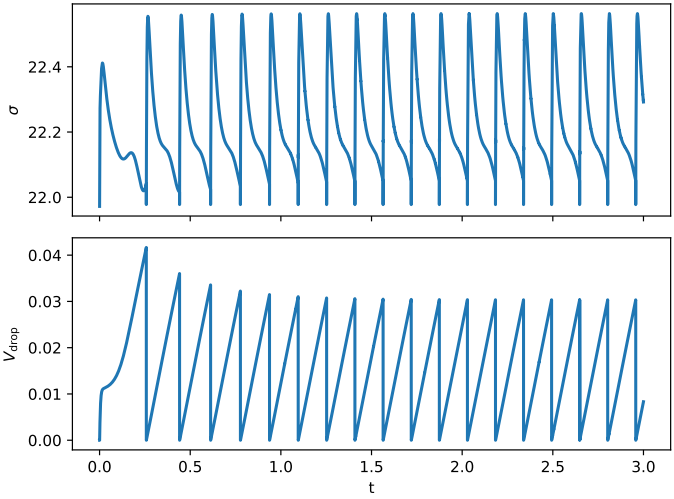

Figure 5.9: Top: Surface tension value σ over time t. Bottom: Drop volume V_{drop} over time t.

In Figure 5.10 the phase-field variable of one micro-scale simulation is shown. On the left we have the initial configuration at time $t = 0$ and on the right the final state before detachment at $t = 0.25$. Close to the interface we have slightly negative values for the phase-field variable which are unphysical. The problem of values for the phase-field variable outside $[0, 1]$ is common in numerical simulations of phase-field models in multiple space dimensions [110]. The choice of the nonlinear interpolation function h (see (2.2)) is used to deal with that issue. It limits the contribution of phase-field values outside $[0, 1]$.

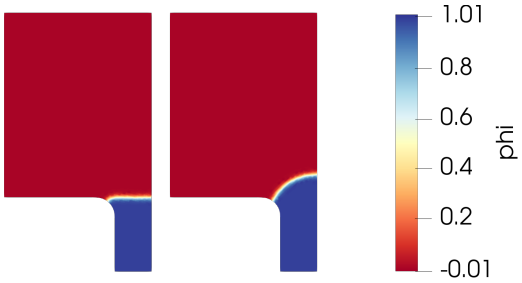

Figure 5.10: Result of micro-scale scale simulation. phase-field variable. Left: Initial configuration at time $t = 0$. Right: Configuration before detachment at $t = 0.25$.

To investigate the influence of the micro-scale on the macro-scale behavior, we compare the simulation with the case of no inflow at the porous medium, i.e. $q_\alpha = 0$. The drop volume and surface tension are depicted in Figure 5.11.

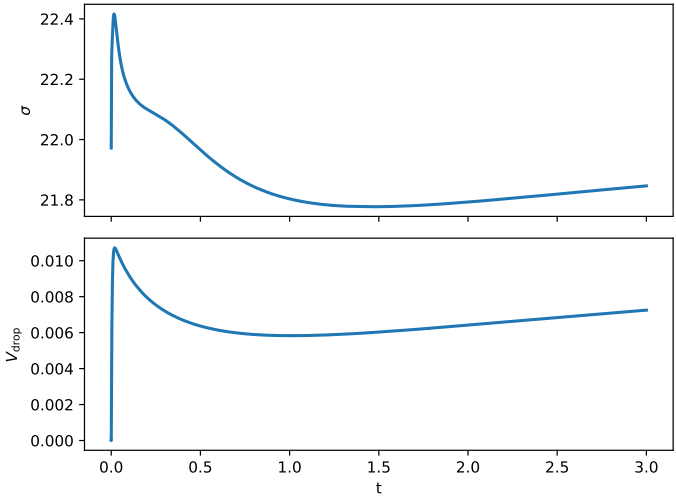

Figure 5.11: Simulation without inflow. Top: Surface tension value σ over time t. Bottom: Drop volume V_{drop} over time t.Drop volume V_{drop} over time t.

We can see that no drop is formed.

From the macro-scale solution, we plot the values for liquid saturation, liquid pressure, and liquid and vapor velocity magnitude for the uppermost cell in the porous-medium domain over time. The results are depicted in Figure 5.12.

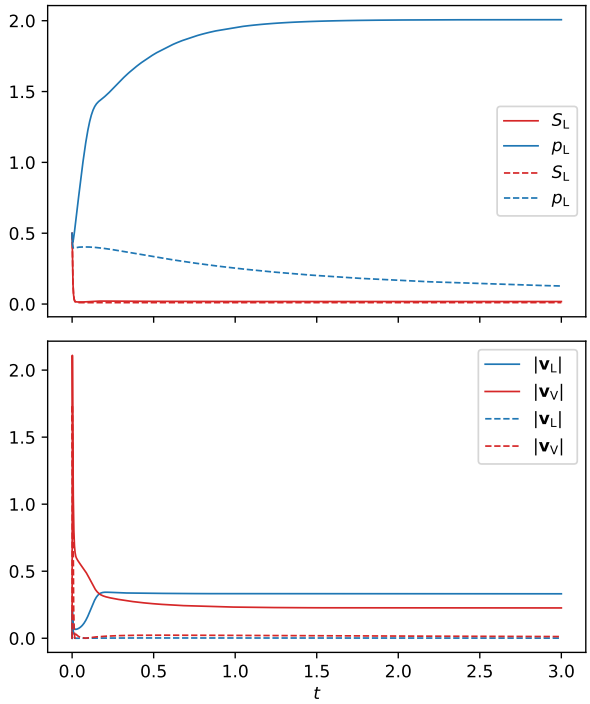

Figure 5.12: Comparison of liquid saturation, liquid pressure, and liquid and vapor velocity magnitude of multi-scale simulation with and without inflow. The values of the uppermost cell in the porous-medium domain are plotted over time. The dashed lines depict the result of the simulation without inflow, while the solid lines show the result of the simulation with inflow.

It can be observed, that in both cases at $t = 3$ we are already close to an equilibrium situation. The liquid saturation is quite low in both cases. However, due to the inflow the liquid pressure is higher resulting in an outflow and the growth of drops.

6 Conclusion and Outlook

In this second part we studied a phase-field model for the description of compressible two-phase flows. We introduced the NSAC model based on energy principles. Further, we proved an energy inequality and therefore thermodynamic consistency. We mentioned the topic of sharp-interface limits. We referred to works which show that the NSAC model yields physically meaningful SI limit systems. In order to discretize the system, we derived an energy-consistent dG scheme, which is a higher order scheme which satisfies an energy inequality on the discrete level. We then showed with two examples the applicability of the NSAC model and our scheme.

First, we presented a phase-field approach to model and simulate compressible droplet impingement scenarios. For this, we derived generalized Navier boundary conditions, which allows to describe moving contact line. They have been implemented for static contact angles, which we illustrated with a boundary wetting example. However, for future studies dynamic contact angle can be implemented in order to observe jetting phenomena in the impact case.

As second example we presented a novel multi-scale approach to model coupled porous-medium and free flow. The advantage of the approach is that it is capable to describe droplet related processes at the interface between the porous-medium and free-flow domain. This is achieved by introducing the micro-scale phase-field model for the description of a single drop. A numerical example demonstrated the advantage of the new model concept. In future work comparison studies with experiments are interesting to discuss the areas of application for the multi-scale approach.

Appendix

A Domain Enlargement

In the numerical example from Section 5.5, the pore diameter d_{pore} in the micro domain should be $4.4 \cdot 10^{-3}$. However, we rescale the micro-domain such that the pore diameter is $\bar{d} = 0.4$. That means we scale the length x_1, and also x_2 with

$$\frac{\bar{d}}{d} = 90.$$

We need to adapt the system in order to correct the scaling. The nondimensional form of the system (2.4)–(2.6) reads as

$$\begin{aligned}
\partial_t \rho + \operatorname{div}(\rho \boldsymbol{v}) &= 0, \\
\partial_t(\rho \boldsymbol{v}) + \operatorname{div}\cdot(\rho \boldsymbol{v}\boldsymbol{v}^\top) + \frac{1}{M_{\rho\psi}^2}\nabla\left(\rho^2 \frac{\partial \psi}{\partial \rho}\right) &= \frac{1}{Re}\operatorname{div}(\boldsymbol{S}) + \frac{1}{M_W^2}\frac{1}{\gamma}\nabla W(\varphi) \\
&\quad - \frac{\varepsilon^2}{M_W^2}\gamma \operatorname{div}(\nabla\varphi\nabla\varphi^\top - \frac{1}{2}|\nabla\varphi|^2 \boldsymbol{I}), \\
\partial_t(\rho\varphi) + \operatorname{div}(\rho\varphi\boldsymbol{v}) &= -M_p {M_W}^2 \eta\left(\frac{1}{{M_W}^2}\frac{W'(\varphi)}{\gamma} + \right. \\
&\quad \left. \frac{1}{M_{\rho\psi}^2}\frac{\partial(\rho\psi)}{\partial\varphi} - \frac{\varepsilon^2}{{M_W}^2}\gamma\Delta\varphi\right),
\end{aligned}$$

with the Mach and Reynolds numbers

$$M_W = v^c\sqrt{\frac{\rho^c \gamma^c}{W^c}}, \quad M_{\rho\psi} = v^c\sqrt{\frac{\rho^c}{(\rho\psi)^c}} \quad M_p = \frac{\eta^c t^c W^c}{\rho^c \gamma^c}, \quad Re = \frac{\rho^c v^c x^c}{\mu_{\text{LV}}^c}.$$

Moreover, the following small parameter is proportional to the interface thickness

$$\varepsilon = \sqrt{\frac{(\gamma^c)^2}{(x^c)^2 W^c}}.$$

Here c denotes the characteristic scale of the corresponding quantity.
In order to maintain the characteristic numbers we need to adapt μ_{LV}:

$$\bar{\mu}_{\mathrm{LV}} = 90\mu_{\mathrm{LV}}, \tag{6.1}$$

which means that we have to scale the viscosity parameter in the micro-scale simulation by factor 90.

Part III
Incompressible–Compressible Phase-Field Flow

1 Introduction

In Chapter 4 of Part II we discussed compressible effects in droplet impingement scenarios utilizing the compressible NSAC model. Compressible effects of the liquid phase are negligible for smaller impact velocities and therefore small Mach numbers. In such cases the fluid can be considered incompressible. In [8] a volume-of-fluid method is used to simulate incompressible droplet impacts. However, the liquid and the vapor phase are both assumed to be incompressible. For the vapor phase the assumption of incompressibility is often infeasible.

Aiming to quantify compressible effects, we consider an incompressible–compressible phase-field model, based on [96]. This model is able to handle two phases, a compressible vapor phase and an incompressible liquid phase. Up to now, very little is known about this novel system. In [96] only an energy inequality for a mixed-formulation of the ICNSCH system is proven. Hence, we investigate some properties of this model. Namely, for our version of the ICNSCH model, we prove an energy inequality which ensures thermodynamic consistency. Further, as novelty, we investigate the surface tension in the system and the limit for small Mach numbers. For the effective surface tension we derive the expression (2.36). For the low Mach limit, we show formally, the convergence to a meaningful limit system, the (quasi-)incompressible Lowengrub–Truskinovsky system. In [96] an energy-consistent dG scheme similar to Algorithm 3.11 in Part II has been introduced, but not implemented. In order to overcome the drawbacks of energy-consistent dG schemes, like the restrictive time discretization and stabilization problems in advection-dominated regimes, we present an idea towards a high-order dG scheme based on Godunov fluxes to discretize the incompressible–compressible system.

This part is structured as follows. In the following Chapter 2 we introduce the incompressible–compressible–Navier–Stokes–Cahn–Hilliard (ICNSCH) system and discuss the above-mentioned properties. In Chapter 3 we present an approach towards a dG scheme to solve the system numerically. We show some preliminary results in Chapter 4, where the applicability of our idea is shown in a single-phase situation. Finally, we conclude in Chapter 5.

2 The ICNSCH Model

In this chapter we present the incompressible–compressible–Navier–Stokes–Cahn–Hilliard model. This model was originally derived in [96] with the motivation to model the expansion of a metal foam inside a hollow mold. In contrast to the Allen–Cahn-type models, like the one used in Part II, here the phases are conserved. In particular, no phase transition can occur. Since, especially in isothermal conditions, phase transition phenomena are often not of primary interest, the choice of a Cahn–Hilliard-type model stands to reason. In this ICNSCH phase-field model the vapor phase is considered compressible while the liquid phase is assumed to be incompressible. The main difference in the derivation of this system, in contrast to the one in Part II, is that one has to rely on the specific Gibbs free energy g, rather than the specific Helmholtz free energy f used in the fully compressible case. This is due to the fact, that the Helmholtz free energy degenerates in the incompressible case and no relation between the pressure p and density ρ can be found. Hence, the Gibbs free energy $g = g(p, \varphi, \nabla\varphi)$ is used, which allows to define the following relation between pressure and density:

$$\frac{1}{\rho} = \frac{\partial g}{\partial p}. \tag{2.1}$$

Note that the Gibbs free energy g depends on the pressure p and not on the density ρ like the Helmholtz free energy. This leads to the fact that the corresponding system has the pressure p as unknown rather than the density ρ.
Let the fluid occupy a domain $\Omega \subset \mathbb{R}^d, d \in \mathbb{N}$. The isothermal Navier–Stokes–Cahn–Hilliard (NSCH) system for the pressure $p \in \mathbb{R}$, velocity $\boldsymbol{v} \in \mathbb{R}^d$ and phase-field variable $\varphi \in [0, 1]$ reads in non-conservative form as

$$\partial_t \rho + \operatorname{div}(\rho \boldsymbol{v}) = 0, \tag{2.2}$$

$$\partial_t(\rho \boldsymbol{v}) + \operatorname{div}(\rho \boldsymbol{v} \otimes \boldsymbol{v}) = \operatorname{div}\left(\boldsymbol{S} - p\boldsymbol{I} + \boldsymbol{C}\right) \quad \text{in } \Omega \times (0, T), \tag{2.3}$$

$$\rho \partial_t \varphi + \rho \nabla\varphi \cdot \boldsymbol{v} = \operatorname{div}\left(\eta \nabla\mu\right), \tag{2.4}$$

with

$$\frac{1}{\rho} = \frac{\varphi}{\rho_{\mathrm{L}}(p)} + \frac{1-\varphi}{\rho_{\mathrm{V}}(p)}, \tag{2.5}$$

$$g = g(p, \varphi, \nabla\varphi) = g_0(p, \varphi) + \frac{\gamma}{2}|\nabla\varphi|^2, \tag{2.6}$$

$$\boldsymbol{C} = -\rho\gamma\nabla\varphi \otimes \nabla\varphi,$$

$$\boldsymbol{S} = \tilde{\mu}\left(\nabla\boldsymbol{v} + \nabla\boldsymbol{v}^{\top} - \frac{2}{3}\operatorname{div}(\boldsymbol{v})\boldsymbol{I}\right),$$

$$\mu = \frac{\partial g_0}{\partial\varphi} - \frac{1}{\rho}\operatorname{div}\left(\gamma\rho\nabla\varphi\right). \tag{2.7}$$

Here $(\dot{\ })$ denotes the material derivative, i.e. $\dot{x} = x_t + \nabla x \cdot \boldsymbol{v}$. The constant parameters η, γ and $\tilde{\mu}$ are the mobility, the capillary parameter and the viscosity. The system (2.2)–(2.4) holds for both, compressible and incompressible fluids. In the following we specify this property by fixing the density pressure relation $\rho_{\mathrm{L/V}}(p)$ for both phases.

The liquid phase is modeled as an incompressible liquid with constant density, i.e.

$$\rho_L(p) = \rho_L = \text{const.} \tag{2.8}$$

The vapor phase is assumed to be a perfect gas, i.e.

$$p(\rho_{\mathrm{V}}) = \alpha\rho_{\mathrm{V}}, \tag{2.9}$$

for some parameter $\alpha > 0$. Accordingly, with (2.5) follows

$$\frac{1}{\rho} = \frac{\varphi}{\rho_L} + \alpha\frac{1-\varphi}{p}. \tag{2.10}$$

We integrate (2.1) from p_0 to p and combine it with (2.6) and (2.10) to obtain the specific Gibbs free energy

$$g(p, \varphi, \nabla\varphi) = \varphi\frac{p - p_0}{\rho_L} + \left(1-\varphi\right)\alpha\ln\frac{p}{p_0} + \frac{\gamma}{2}|\nabla\varphi|^2 + g_1(\varphi).$$

A standard choice for the function $g_1(\varphi)$ is the double well potential

$$g_1(\varphi) = W(\varphi) = \beta\varphi^2\left(1-\varphi\right)^2, \tag{2.11}$$

with $\beta > 0$, cf. Chapter 2 in Part II.

Then, the chemical potential μ in (2.7) becomes

$$\mu = \frac{p - p_0}{\rho_L} - \alpha \ln \frac{p}{p_0} + W'(\varphi) - \frac{1}{\rho} \operatorname{div}\left(\rho\gamma\nabla\varphi\right).$$

With the assumption on the pressure-density relationship for both phases (2.8)–(2.9), we now call the NSCH model (2.2)–(2.4) *Incompressible–Compressible–NSCH system.*

In order to recast the ICNSCH system in the dimensionless form, we introduce the generic nondimensional quantity $\vartheta^* = \vartheta/\vartheta^c$ where ϑ^c is denotes the characteristic scale of the corresponding quantity. Consider the relations

$$t^c = l^c/u^c, \qquad \text{and} \qquad p^c = \rho^c\mu^c,$$

with t^c and l^c the characteristic time and length scale respectively, and the dimensionless numbers

$$\begin{aligned}
\mathrm{Ca} &= \frac{\gamma}{\mu^c (l^c)^2}, \\
\mathrm{Ma} &= \sqrt{\frac{(u^c)^2}{\mu^c}}, \\
\mathrm{Re} &= \frac{\rho^c u^c l^c}{\tilde{\mu}^c}, \\
\mathrm{Pe} &= \frac{\rho^c u^c l^c}{\eta_T \mu^c}, \\
a &= \frac{\alpha}{\mu^c}, \\
b &= \frac{\beta}{\mu^c},
\end{aligned}$$

with $\eta_T = \eta/T$.

Omitting the $(^c)$ notation, the nondimensional ICNSCH system reads

$$\partial_t \rho + \operatorname{div}(\rho \boldsymbol{v}) = 0, \tag{2.12}$$

$$\partial_t(\rho \boldsymbol{v}) + \operatorname{div}(\rho \boldsymbol{v} \otimes \boldsymbol{v}) = \operatorname{div}\left(\frac{1}{\mathrm{Re}}\boldsymbol{S} - \frac{1}{\mathrm{Ma}^2} p\boldsymbol{I} + \frac{\mathrm{Ca}}{\mathrm{Ma}^2}\boldsymbol{C}\right), \quad \text{in } \Omega \times (0, T) \tag{2.13}$$

$$\rho\partial_t\varphi + \rho\nabla\varphi \cdot \boldsymbol{v} = \operatorname{div}\left(\frac{1}{\mathrm{Pe}}\nabla\mu\right), \tag{2.14}$$

where

$$\begin{aligned}
\frac{1}{\rho} &= \frac{\varphi}{\rho_L} + a\frac{1-\varphi}{p},\\
g(p,\varphi,\nabla\varphi) &= \varphi\frac{p-p_0}{\rho_L} + \left(1-\varphi\right) a\ln\frac{p}{p_0} + \frac{\mathrm{Ca}}{2}|\nabla\varphi|^2 + bW(\varphi) \qquad (2.15)\\
\boldsymbol{S} &= \nabla\boldsymbol{v} + \nabla\boldsymbol{v}^\top - \frac{2}{3}\left(\operatorname{div}\boldsymbol{v}\right)\boldsymbol{I},\\
\boldsymbol{C} &= -\rho\nabla\varphi\otimes\nabla\varphi,\\
\mu &= \frac{p-p_0}{\rho_L} - a\ln\frac{p}{p_0} + bW'(\varphi) - \mathrm{Ca}\frac{1}{\rho}\operatorname{div}\left(\rho\nabla\varphi\right),\\
W(\varphi) &= \varphi^2\left(1-\varphi\right)^2.
\end{aligned}$$

Notice that the chemical potential contribution in (2.14) is given by its gradients only. Therefore, the choice of p_0 is free.
Assuming an impermeable no-slip wall and 90° static contact angle, we have the boundary conditions

$$\boldsymbol{v} = \boldsymbol{0}, \qquad (2.16)$$

$$\nabla\varphi\cdot\boldsymbol{n} = 0, \qquad \text{on } \partial\Omega\times(0,T). \qquad (2.17)$$

Further, we assume no diffusion through the boundary, i.e.

$$\nabla\mu\cdot\boldsymbol{n} = 0. \qquad (2.18)$$

Additionally, the system is endowed with initial conditions

$$p = p_0, \quad \boldsymbol{v} = \boldsymbol{v}_0, \quad \varphi = \varphi_0 \quad \text{on } \Omega\times\{0\},$$

using suitable functions $(p_0, \boldsymbol{v}_0, \varphi_0) : \Omega \longrightarrow \mathbb{R}\times\mathbb{R}^d\times[0,1]$.
The energy corresponding to (2.12)–(2.14) reads as

$$E(t) \coloneqq \int_\Omega \left(\frac{1}{2}\rho|\boldsymbol{v}|^2 + \frac{1}{\mathrm{Ma}^2}\rho g(p,\varphi,\nabla\varphi) - \frac{1}{\mathrm{Ma}^2}p\right)\mathrm{d}\boldsymbol{x}. \qquad (2.19)$$

Note that we subtract the pressure in the energy. This is due to the following relation between the specific Gibbs free energy g, specific Helmholtz free energy f and specific energy e:

$$f = e - Ts$$

$$g = e - Ts + \frac{p}{\rho} = f + \frac{p}{\rho}.$$

Here T denotes the temperature and s the specific entropy. From this relation it is clear that

$$-\frac{\mathrm{d}}{\mathrm{d}t}E(t) = \frac{\mathrm{d}}{\mathrm{d}t}\int_\Omega T\rho s \ \mathrm{d}\boldsymbol{x}$$

is exactly the entropy production.

Remark 2.1 (Viscosity)**:** *In the original version of the ICNSCH system [96], the vapor phase is inviscid. We drop this assumption, hence in our system* (2.12)–(2.14) *the vapor phase has viscosity. However, for the readers convenience we assume the same viscosity parameter $\tilde{\mu}$ for both phases. All our results generalize to the case of different viscosity parameter interpolated by the phase-field variable.*

2.1 Properties of the ICNSCH System

In this section we study some properties of the ICNSCH system. In the next section we provide an energy inequality, which renders the ICNSCH system (2.12)–(2.14) thermodynamically consistent. In the subsequent Section 2.1.2, we investigate the surface tension in the system. Section 2.1.3 investigates the limit of the ICNSCH system for low Mach numbers. In this limit we show formally that the solutions to the ICNSCH system converge to solutions of the quasi-incompressible Lowengrub–Truskinovsky (LT) system [74]. The latter system is a phase-field model, where both phases are assumed to be incompressible with different densities. Hence the addition *quasi-incompressible*.

2.1.1 Energy Inequality

Similar to the NSAC system in Part II, we can show that the ICNSCH system satisfies an energy inequality. For isothermal models thermodynamical consistency means to verify that solutions of the problem at hand admit an energy inequality. The entropy production of the system is exactly $-\frac{\mathrm{d}E}{\mathrm{d}t}(t)$. Hence, by assuring that the energy E decreases over time, we show increasing entropy and therefore thermodynamical consistency.
We formulate the following result:

Theorem 2.2 (Energy Inequality)**:** *Let $(p, \boldsymbol{v}, \varphi)$ with values in $\mathbb{R} \times \mathbb{R}^d \times [0,1]$ be a classical solution to* (2.12)–(2.14) *in $\Omega \times (0,T)$ satisfying the boundary conditions* (2.16)–(2.18) *on $\partial\Omega \times (0,T)$.*

Then, for all $t \in (0, T)$ the following energy inequality holds:

$$\begin{aligned}\frac{\mathrm{d}}{\mathrm{d}\,t}E(t) &= \frac{\mathrm{d}}{\mathrm{d}\,t}\left(E_{\mathrm{kin}}(t) + E_{\mathrm{free}}(t)\right)\\ &= \frac{\mathrm{d}}{\mathrm{d}\,t}\left(\int_\Omega \frac{1}{2}\rho|\boldsymbol{v}|^2 + \frac{1}{\mathrm{Ma}^2}\rho g(p,\varphi,\nabla\varphi) - \frac{1}{\mathrm{Ma}^2}p \;\mathrm{d}\boldsymbol{x}\right)\\ &= -\int_\Omega \frac{1}{\mathrm{Ma}^2\mathrm{Pe}}|\nabla\mu|^2 \;\mathrm{d}\boldsymbol{x} - \int_\Omega \frac{1}{\mathrm{Re}}\boldsymbol{S} : \nabla\boldsymbol{v} \;\mathrm{d}\boldsymbol{x} \le 0. \end{aligned} \tag{2.20}$$

Proof. We directly compute:

$$\begin{aligned}\frac{\mathrm{d}}{\mathrm{d}\,t}E(t) &= \frac{\mathrm{d}}{\mathrm{d}\,t}\left(\int_\Omega \frac{1}{2}\rho|\boldsymbol{v}|^2 + \frac{1}{\mathrm{Ma}^2}\rho g(p,\varphi,\nabla\varphi) - \frac{1}{\mathrm{Ma}^2}p \;\mathrm{d}\boldsymbol{x}\right)\\ &= \int_\Omega \boldsymbol{v}(\rho\boldsymbol{v})_t - \frac{1}{2}\rho_t|\boldsymbol{v}|^2 + \frac{1}{\mathrm{Ma}^2}\rho_t g + \frac{1}{\mathrm{Ma}^2}\rho g_t - \frac{1}{\mathrm{Ma}^2}p_t \;\mathrm{d}\boldsymbol{x}\\ &= \int_\Omega \boldsymbol{v}(\rho\boldsymbol{v})_t - \frac{1}{2}\rho_t|\boldsymbol{v}|^2 + \frac{1}{\mathrm{Ma}^2}\rho_t g + \frac{1}{\mathrm{Ma}^2}\rho\left(\frac{\partial g}{\partial\varphi}\varphi_t + \frac{\partial g}{\partial p}p_t + \frac{\partial g}{\partial\nabla\varphi}\nabla\varphi_t\right)\\ &\quad - \frac{1}{\mathrm{Ma}^2}p_t \;\mathrm{d}\boldsymbol{x}.\end{aligned}$$

With (2.1) and (2.15) we obtain

$$\frac{\mathrm{d}}{\mathrm{d}\,t}E(t) = \int_\Omega \boldsymbol{v}(\rho\boldsymbol{v})_t - \frac{1}{2}\rho_t|\boldsymbol{v}|^2 + \frac{1}{\mathrm{Ma}^2}\rho_t g + \frac{1}{\mathrm{Ma}^2}\rho\frac{\partial g}{\partial\varphi}\varphi_t + \frac{\mathrm{Ca}}{\mathrm{Ma}^2}\rho\nabla\varphi\nabla\varphi_t \;\mathrm{d}\boldsymbol{x}$$

Using integration by parts and the boundary condition (2.17) results in

$$= \int_\Omega \boldsymbol{v}(\rho\boldsymbol{v})_t - \frac{1}{2}\rho_t|\boldsymbol{v}|^2 + \frac{1}{\mathrm{Ma}^2}\rho_t g + \frac{1}{\mathrm{Ma}^2}\rho\frac{\partial g}{\partial\varphi}\varphi_t - \frac{\mathrm{Ca}}{\mathrm{Ma}^2}\operatorname{div}(\rho\nabla\varphi)\varphi_t \;\mathrm{d}\boldsymbol{x}.$$

Replacing the time derivatives in the volume integrals using (2.12)–(2.14) yields

$$\begin{aligned}\frac{\mathrm{d}}{\mathrm{d}\,t}E(t) &= \int_\Omega \boldsymbol{v}\left(-\operatorname{div}(\rho\boldsymbol{v}\otimes\boldsymbol{v}) - \frac{1}{\mathrm{Ma}^2}\nabla p - \frac{\mathrm{Ca}}{\mathrm{Ma}^2}\operatorname{div}(\rho\nabla\varphi\otimes\nabla\varphi) + \frac{1}{\mathrm{Re}}\operatorname{div}(\boldsymbol{S})\right)\\ &\quad - \operatorname{div}(\rho\boldsymbol{v})\left(\frac{1}{\mathrm{Ma}^2}g - \frac{1}{2}|\boldsymbol{v}|^2\right) + \frac{1}{\mathrm{Ma}^2}\frac{\partial g}{\partial\varphi}\left(\frac{1}{\mathrm{Pe}}\Delta\mu - \rho\boldsymbol{v}\cdot\nabla\varphi\right)\\ &\quad - \frac{\mathrm{Ca}}{\mathrm{Ma}^2}\operatorname{div}(\rho\nabla\varphi)\left(\frac{1}{\mathrm{Pe}}\frac{1}{\rho}\Delta\mu - \boldsymbol{v}\cdot\nabla\varphi\right)\mathrm{d}\boldsymbol{x}\\ &= \int_\Omega -\operatorname{div}(\rho\boldsymbol{v}\otimes\boldsymbol{v})\cdot\boldsymbol{v} + \frac{1}{\mathrm{Re}}\operatorname{div}(\boldsymbol{S})\cdot\boldsymbol{v} + \frac{1}{2}\operatorname{div}(\rho\boldsymbol{v})|\boldsymbol{v}|^2\end{aligned}$$

$$
\begin{aligned}
&- \frac{1}{\mathrm{Ma}^2}\nabla p \cdot \boldsymbol{v} - \frac{1}{2}\frac{\mathrm{Ca}}{\mathrm{Ma}^2}\rho\boldsymbol{v}\nabla(|\nabla\varphi|^2) - \frac{1}{\mathrm{Ma}^2}\operatorname{div}(\rho\boldsymbol{v})g \\
&+ \frac{1}{\mathrm{Ma}^2\mathrm{Pe}}\Delta\mu\left(\frac{\partial g}{\partial\varphi} - \mathrm{Ca}\frac{1}{\rho}\operatorname{div}(\rho\nabla\varphi)\right) - \frac{1}{\mathrm{Ma}^2}\frac{\partial g}{\partial\varphi}\rho\boldsymbol{v}\cdot\nabla\varphi \;\mathrm{d}\boldsymbol{x}.
\end{aligned}
$$

Using the definition of μ (2.7) leads to

$$
\begin{aligned}
\frac{\mathrm{d}}{\mathrm{d}\,t}E(t) = \int_\Omega &- \operatorname{div}(\rho\boldsymbol{v}\otimes\boldsymbol{v})\cdot\boldsymbol{v} + \frac{1}{\mathrm{Re}}\operatorname{div}(\boldsymbol{S})\cdot\boldsymbol{v} + \frac{1}{2}\operatorname{div}(\rho\boldsymbol{v})|\boldsymbol{v}|^2 \\
&- \frac{1}{\mathrm{Ma}^2}\nabla p\cdot\boldsymbol{v} - \frac{1}{2}\frac{\mathrm{Ca}}{\mathrm{Ma}^2}\rho\boldsymbol{v}\nabla(|\nabla\varphi|^2) - \frac{1}{\mathrm{Ma}^2}\operatorname{div}(\rho\boldsymbol{v})g \\
&+ \frac{1}{\mathrm{Ma}^2\mathrm{Pe}}\mu\Delta\mu - \frac{1}{\mathrm{Ma}^2}\frac{\partial g}{\partial\varphi}\rho\boldsymbol{v}\cdot\nabla\varphi \;\mathrm{d}\boldsymbol{x}.
\end{aligned}
$$

With the definition of g (2.15) it holds

$$
\begin{aligned}
\frac{\mathrm{d}}{\mathrm{d}\,t}E(t) &= \int_\Omega - \operatorname{div}(\rho\boldsymbol{v}\otimes\boldsymbol{v})\cdot\boldsymbol{v} + \frac{1}{\mathrm{Re}}\operatorname{div}(\boldsymbol{S})\cdot\boldsymbol{v} + \frac{1}{2}\operatorname{div}(\rho\boldsymbol{v})|\boldsymbol{v}|^2 \\
&\quad - \frac{1}{\mathrm{Ma}^2}\operatorname{div}(\rho\boldsymbol{v})g - \frac{1}{\mathrm{Ma}^2}\rho\boldsymbol{v}\nabla g + \frac{1}{\mathrm{Ma}^2\mathrm{Pe}}\mu\Delta\mu \;\mathrm{d}\boldsymbol{x} \\
&= \int_\Omega - \operatorname{div}(\rho\boldsymbol{v}\otimes\boldsymbol{v})\cdot\boldsymbol{v} + \frac{1}{\mathrm{Re}}\operatorname{div}(\boldsymbol{S})\cdot\boldsymbol{v} + \frac{1}{2}\operatorname{div}(\rho\boldsymbol{v})|\boldsymbol{v}|^2 \\
&\quad - \frac{1}{\mathrm{Ma}^2}\operatorname{div}(\rho\boldsymbol{v}g) + \frac{1}{\mathrm{Ma}^2\mathrm{Pe}}\mu\Delta\mu \;\mathrm{d}\boldsymbol{x}.
\end{aligned}
$$

Finally, Gauss's theorem, integration by parts and using the boundary conditions (2.16)–(2.18) results in

$$
\frac{\mathrm{d}}{\mathrm{d}\,t}E(t) = -\int_\Omega \frac{1}{\mathrm{Re}}\boldsymbol{S} : \nabla\boldsymbol{v} \;\mathrm{d}\boldsymbol{x} - \int_\Omega \frac{1}{\mathrm{Ma}^2\mathrm{Pe}}|\nabla\mu|^2 \;\mathrm{d}\boldsymbol{x}. \qquad \blacksquare
$$

2.1.2 Surface Tension

In this section, we investigate the effective surface tension similarly to Section 2.1.3 in Part II. We consider the dimensionless ICNSCH system (2.12)–(2.14). Recall the energy (2.19).

In order to derive the surface tension, we consider a planar equilibrium profile and integrate the excess free energy density over this profile. The excess free energy is the difference of the free energy in the considered system and in a (sharp-interface) reference system where the bulk values are maintained up to a dividing interface. We assume that static equilibrium conditions hold, i.e. $\boldsymbol{v} = \boldsymbol{0}$. The planar profile

assumed to be parallel to the x_1-axis while everything is independent from t and the other space dimensions x_i, $i \neq 1$. For the sake of readability we omit the subscript in x_1 in the following . Then the equilibrium is governed by the solution of the following boundary value problem on the real line. Find $p = p(x), \varphi = \varphi(x)$ such that

$$p_x = -\mathrm{Ca}(\rho\varphi_x^2)_x, \tag{2.21}$$

$$\mu_{xx} = 0 \tag{2.22}$$

and

$$p(\pm\infty) = p_{\mathrm{L/V}}, \qquad \varphi(\pm\infty) = \varphi_{\mathrm{L/V}}, \qquad \varphi_x(\pm\infty) = 0. \tag{2.23}$$

We assume that there exists a solution to (2.21)–(2.23). Integrating the reduced momentum equation (2.21) from $-\infty$ to some $x \in \mathbb{R}$ leads to the pressure

$$p(x) = p_{\mathrm{V}} - \mathrm{Ca}\rho(x)\varphi_x^2(x). \tag{2.24}$$

Equation (2.24) immediately yields for $x \longrightarrow \infty$

$$p_{\mathrm{L}} = p_{\mathrm{V}}. \tag{2.25}$$

Even more, the pressure p is constant equal to $p_{\mathrm{L/V}}$ whenever φ_x vanishes, i.e. outside the interface region.

Remark 2.3: *Note that* (2.24) *yields that the hydrostatic pressure p is not constant in a planar equilibrium situation (i.e. without surface tension effects). This raises some confusion due to the definition of (mechanical) thermodynamic equilibrium. However, the pressure defined as* $\frac{1}{d}\,\mathrm{trace}(\boldsymbol{T})$, *with stress tensor* $\boldsymbol{T} = \boldsymbol{S} - p\boldsymbol{I} + \boldsymbol{C}$ *is constant in this case.*

We write

$$\mu = \frac{\partial g_0(\varphi, p)}{\partial \varphi} - \frac{\mathrm{Ca}}{\rho}(\rho\varphi_x)_x. \tag{2.26}$$

From (2.22) we have $\mu = c_0 x + c_1$, with some constants $c_0, c_1 \in \mathbb{R}$. If we consider the asymptotic behavior for $x \longrightarrow \pm\infty$ it becomes clear that $c_0 = 0$ and hence

$$\mu = c_1, \tag{2.27}$$

with

$$c_1 = g_{0,\varphi}(\varphi_{\mathrm{V}}, p_{\mathrm{V}}) = g_{0,\varphi}(\varphi_{\mathrm{L}}, p_{\mathrm{L}}).$$

Consider now (2.27) with the definition of μ (2.26):

$$g_{0,\varphi} - \frac{\mathrm{Ca}}{\rho}(\rho\varphi_x)_x = c_1. \tag{2.28}$$

We multiply (2.28) by φ_x and obtain

$$g_{0,x} - g_{0,p}p_x - \frac{\mathrm{Ca}}{2}(\varphi_x^2)_x - \mathrm{Ca}\frac{\rho_x}{\rho}\varphi_x^2 = c_1\varphi_x.$$

Using the relation between Gibbs free energy and pressure (2.1) yields

$$g_{0,x} - \frac{p_x}{\rho} - \frac{\mathrm{Ca}}{2}(\varphi_x^2)_x - \mathrm{Ca}\frac{\rho_x}{\rho}\varphi_x^2 = c_1\varphi_x.$$

Equation (2.21) leads to

$$g_{0,x} + \frac{\mathrm{Ca}}{2}(\varphi_x^2)_x = c_1\varphi_x$$

Finally, we integrate from $-\infty$ to some $x \in \mathbb{R}$ and obtain

$$g_0(p(x), \varphi(x)) - g_0(p_\mathrm{V}, \varphi_\mathrm{V}) + \frac{\mathrm{Ca}}{2}\varphi_x^2(x) = c_1(\varphi(x) - \varphi_\mathrm{V}). \tag{2.29}$$

By sending $x \longrightarrow \infty$ we have from (2.29)

$$g_0(p_\mathrm{V}, \varphi_\mathrm{V}) - c_1\varphi_\mathrm{V} = g_0(p_\mathrm{L}, \varphi_\mathrm{L}) - c_1\varphi_\mathrm{L}.$$

We will use this relation later with the short notation

$$g_\mathrm{V} - c_1\varphi_\mathrm{V} = g_\mathrm{L} - c_1\varphi_\mathrm{L} = g_{\mathrm{L/V}} - c_1\varphi_{\mathrm{L/V}}. \tag{2.30}$$

As mentioned before, surface tension can be defined by means of the excess free energy. We specify the interface position x_0 by vanishing excess density, i.e. the balance of mass of the two phases. Hence, we fix the position of the interface by demanding

$$\int_{-\infty}^{x_0} (\rho\varphi - \rho_\mathrm{V}\varphi_\mathrm{V})\ \mathrm{d}x = \int_{x_0}^{\infty} (\rho_\mathrm{L}\varphi_\mathrm{L} - \rho\varphi)\ \mathrm{d}x. \tag{2.31}$$

To obtain the surface tension, i.e. the excess free energy, we integrate the free energy over the equilibrium profile and subtract the energy of a sharp-interface reference system:

$$\sigma = \int_{-\infty}^{x_0} \frac{1}{\mathrm{Ma}^2}(\rho g(p,\varphi,\varphi_x) - \rho_\mathrm{V} g_\mathrm{V}) - \frac{1}{\mathrm{Ma}^2}(p - p_\mathrm{V})\ \mathrm{d}x + \int_{x_0}^{\infty} \frac{1}{\mathrm{Ma}^2}(\rho g(p,\varphi,\varphi_x) - \rho_\mathrm{L} g_\mathrm{L}) - \frac{1}{\mathrm{Ma}^2}(p - p_\mathrm{L})\ \mathrm{d}x.$$

With (2.24) and (2.25) it follows

$$\sigma = \int_{-\infty}^{x_0} \frac{1}{\mathrm{Ma}^2}(\rho g(p,\varphi,\varphi_x) - \rho_\mathrm{V} g_\mathrm{V}) + \frac{\mathrm{Ca}}{\mathrm{Ma}^2}\rho\varphi_x^2\ \mathrm{d}x + \int_{x_0}^{\infty} \frac{1}{\mathrm{Ma}^2}(\rho g(p,\varphi,\varphi_x) - \rho_\mathrm{L} g_\mathrm{L}) + \frac{\mathrm{Ca}}{\mathrm{Ma}^2}\rho\varphi_x^2\ \mathrm{d}x.$$

Due to the form of g, see (2.6), we get

$$\sigma = \frac{3\mathrm{Ca}}{2\mathrm{Ma}^2}\int_{-\infty}^{\infty} \rho\varphi_x^2\ \mathrm{d}x + \frac{1}{\mathrm{Ma}^2}\int_{-\infty}^{x_0} \rho g_0(p,\varphi) - \rho_\mathrm{V} g_\mathrm{V}\ \mathrm{d}x + \frac{1}{\mathrm{Ma}^2}\int_{x_0}^{\infty} \rho g_0(p,\varphi) - \rho_\mathrm{L} g_\mathrm{L}\ \mathrm{d}x.$$

Then, with (2.29) it holds

$$\sigma = \frac{\mathrm{Ca}}{\mathrm{Ma}^2}\int_{-\infty}^{\infty} \rho\varphi_x^2\ \mathrm{d}x + \frac{1}{\mathrm{Ma}^2}\int_{-\infty}^{x_0} \rho g_\mathrm{V} - \rho_\mathrm{V} g_\mathrm{V} + c_1\rho(\varphi - \varphi_\mathrm{V})\ \mathrm{d}x + \frac{1}{\mathrm{Ma}^2}\int_{x_0}^{\infty} \rho g_\mathrm{L} - \rho_\mathrm{L} g_\mathrm{L} + c_1\rho(\varphi - \varphi_\mathrm{L})\ \mathrm{d}x.$$

We use the notation (2.30) to obtain

$$\sigma = \frac{\mathrm{Ca}}{\mathrm{Ma}^2}\int_{-\infty}^{\infty} \rho\varphi_x^2\ \mathrm{d}x + \frac{1}{\mathrm{Ma}^2}\left(\int_{-\infty}^{x_0} (g_{\mathrm{L/V}} - c_1\varphi_{\mathrm{L/V}})\rho + c_1\rho\varphi - \rho_\mathrm{V} g_\mathrm{V}\ \mathrm{d}x + \int_{x_0}^{\infty} (g_{\mathrm{L/V}} - c_1\varphi_{\mathrm{L/V}})\rho + c_1\rho\varphi - \rho_\mathrm{L} g_\mathrm{L}\ \mathrm{d}x\right).$$

With the vanishing excess density condition (2.31) we have

$$\sigma = \frac{\mathrm{Ca}}{\mathrm{Ma}^2}\int_{-\infty}^{\infty}\rho\varphi_x^2\ \mathrm{d}x + \frac{1}{\mathrm{Ma}^2}(g_{\mathrm{L/V}} - c_1\varphi_{\mathrm{L/V}})\left(\int_{-\infty}^{x_0}\rho - \rho_{\mathrm{V}}\ \mathrm{d}x + \int_{x_0}^{\infty}\rho - \rho_{\mathrm{L}}\ \mathrm{d}x\right).$$

We assume that the second term drops out, see Remark 2.4, and finally obtain

$$\sigma = \frac{\mathrm{Ca}}{\mathrm{Ma}^2}\int_{-\infty}^{\infty}\rho\varphi_x^2\ \mathrm{d}x. \tag{2.32}$$

We want to find a better form of the surface tension coefficient, which ideally does not require knowledge of the equilibrium profile. Hence, we have a closer look at (2.29) and plug in the specific terms for the ICNSCH system:

$$g_0(p,\varphi) = \frac{\varphi}{\rho_{\mathrm{L}}}(p - p_0) + a(1-\varphi)\ln\frac{p}{p_0} + bW(\varphi), \tag{2.33}$$

$$c_1 = \frac{\partial g_0}{\partial\varphi}(p_{\mathrm{V}},\varphi_{\mathrm{V}}) = \frac{p_{\mathrm{V}} - p_0}{\rho_{\mathrm{L}}} - a\ln\frac{p_{\mathrm{V}}}{p_0}, \tag{2.34}$$

$$W(\varphi_{\mathrm{L/V}}) = W'(\varphi_{\mathrm{L/V}}) = 0.$$

Thus, (2.29) reads:

$$c_1(\varphi - \varphi_{\mathrm{V}}) = g_0(p,\varphi) - g_{\mathrm{V}} + \frac{\mathrm{Ca}}{2}\varphi_x^2.$$

With (2.33) and (2.24) we infer

$$\begin{aligned} c_1(\varphi - \varphi_{\mathrm{V}}) = {} & \frac{\varphi}{\rho_{\mathrm{L}}}(p_{\mathrm{V}} - p_0) - \frac{\mathrm{Ca}}{\rho_{\mathrm{L}}}\rho\varphi\varphi_x^2 + a(1-\varphi)\ln\frac{p}{p_0} + bW(\varphi) \\ & - \frac{\varphi_{\mathrm{V}}}{\rho_{\mathrm{L}}}(p_{\mathrm{V}} - p_0) - a(1-\varphi_{\mathrm{V}})\ln\frac{p_{\mathrm{V}}}{p_0} + \frac{\mathrm{Ca}}{2}\varphi_x^2. \end{aligned}$$

Substituting (2.34) yields

$$\begin{aligned} \left(\frac{p_{\mathrm{V}} - p_0}{\rho_{\mathrm{L}}} - a\ln\frac{p_{\mathrm{V}}}{p_0}\right)(\varphi - \varphi_{\mathrm{V}}) = {} & bW(\varphi) + (\varphi - \varphi_{\mathrm{V}})\frac{p_{\mathrm{V}} - p_0}{\rho_{\mathrm{L}}} + a(1-\varphi)\ln\frac{p}{p_0} \\ & - a(1-\varphi_{\mathrm{V}})\ln\frac{p_{\mathrm{V}}}{p_0} + \frac{\mathrm{Ca}}{2}\varphi_x^2 - \frac{\mathrm{Ca}}{\rho_{\mathrm{L}}}\rho\varphi\varphi_x^2. \end{aligned}$$

Hence,

$$\begin{aligned} 0 =& bW(\varphi) + a(1-\varphi)\left(\ln\frac{p}{p_0} - \ln\frac{p_\mathrm{V}}{p_0}\right) \\ &+ \frac{\mathrm{Ca}}{2}\varphi_x^2 - \frac{\mathrm{Ca}}{\rho_\mathrm{L}}\rho\varphi\varphi_x^2. \end{aligned}$$

For the logarithm terms we use a Taylor expansion:

$$\begin{aligned} 0 =& bW(\varphi) \\ &+ a(1-\varphi)\left(\ln\frac{p}{p_0} - \left(\ln\frac{p}{p_0} + \frac{1}{p}(p_\mathrm{V}-p) + O(|p-p_\mathrm{V}|^2)\right)\right) \\ &+ \frac{\mathrm{Ca}}{2}\varphi_x^2 - \frac{\mathrm{Ca}}{\rho_\mathrm{L}}\rho\varphi\varphi_x^2. \end{aligned}$$

Using (2.24) and neglecting the higher order terms of the Taylor expansion, we have

$$\begin{aligned} 0 \approx& bW(\varphi) - \frac{a(1-\varphi)}{p}\mathrm{Ca}\rho\varphi_x^2 + \frac{\mathrm{Ca}}{2}\varphi_x^2 - \frac{\mathrm{Ca}}{\rho_\mathrm{L}}\varphi\rho\varphi_x^2 \\ 0 \approx& bW(\varphi) - \mathrm{Ca}\rho\varphi_x^2\left(\frac{\varphi}{\rho_\mathrm{L}} + \frac{a(1-\varphi)}{p}\right) + \frac{\mathrm{Ca}}{2}\varphi_x^2 \\ 0 \approx& bW(\varphi) - \frac{\mathrm{Ca}}{2}\varphi_x^2. \end{aligned}$$

Thus, we obtain

$$\frac{\mathrm{Ca}}{2}\varphi_x^2 \approx bW(\varphi). \tag{2.35}$$

Finally, we plug (2.35) into (2.32) and obtain using the substitution $\phi = \varphi(x)$

$$\begin{aligned} \sigma =& \frac{\mathrm{Ca}}{\mathrm{Ma}^2}\int_{-\infty}^{\infty}\rho\varphi_x^2\ \mathrm{d}x \\ \approx& \frac{\sqrt{2\mathrm{Ca}}}{\mathrm{Ma}^2}\int_{\varphi_\mathrm{V}}^{\varphi_\mathrm{L}}\rho(\phi,p(\phi))\sqrt{bW(\phi)}\ \mathrm{d}\phi. \end{aligned} \tag{2.36}$$

In the last step we used the transformation from x to ϕ integration. Note that $p = p(\varphi, \varphi_x)$ due to (2.10) and (2.24). Because of (2.35) we have $p = p(\varphi)$.

We can see that the surface tension σ is computable. The capillary number Ca determines the width of the interface. Hence, in practice, an interface width, which can be realized by the numerical scheme can be prescribed and desired values of effective surface tension can be obtained by tuning the Mach number Ma and double-well parameter b. Of course this procedure might exclude some flow regimes.

Remark 2.4: *The assumption*

$$\left(\int_{-\infty}^{x_0} \rho - \rho_V \, \mathrm{d}x + \int_{x_0}^{\infty} \rho - \rho_L \, \mathrm{d}x \right) = 0$$

can be achieved together with (2.31) *in the following way. The total mass should be constant independent of the interface width. This can be obtained by choosing the double-well potential W in a way that the corresponding equilibrium profile of φ is point symmetric. This is especially true for the standard double-well potential* (2.11)*, if the EOS related terms in* (2.36) *can be neglected.*
Outside the interface the pressure is constant (2.24) *and due to the equation of state also the density is constant equal ρ_L in the gas phase. That means in a sharp interface limit, the assumption is true and since a positive interface width does not change the total mass, it is also true in this case.*

2.1.3 Low Mach Limit

In this section we investigate the consistency of the ICNSCH system with respect to low Mach numbers. We formally show that the solutions to the ICNSCH system converge to the solutions of the quasi-incompressible Lowengrub–Truskinovsky system [74]. For the reader's convenience we will drop p_0 in the following, since it has no impact on the result.
Recap the ICNSCH system in nondimensional form (2.12)–(2.14):

$$\partial_t \rho + \boldsymbol{v} \cdot \nabla \rho + \rho \operatorname{div}(\boldsymbol{v}) = 0, \tag{2.37}$$

$$\rho \partial_t \boldsymbol{v} + \rho(\boldsymbol{v} \cdot \nabla)\boldsymbol{v} + \frac{1}{\mathrm{Ma}^2} \nabla p = \frac{1}{\mathrm{Re}} \operatorname{div}(\boldsymbol{S}) - \frac{\mathrm{Ca}}{\mathrm{Ma}^2} \operatorname{div}(\rho \nabla \varphi \otimes \nabla \varphi), \tag{2.38}$$

$$\rho \partial_t \varphi + \rho \boldsymbol{v} \cdot \nabla \varphi = \frac{1}{\mathrm{Pe}} \Delta \mu. \tag{2.39}$$

Here,

$$\begin{aligned} \mu &= \frac{p}{\rho_L} - a \ln(p) + b W'(\varphi) - \frac{\mathrm{Ca}}{\rho} \operatorname{div}(\rho \nabla \varphi), \\ \rho^{-1} &= \frac{\varphi}{\rho_L} + (1 - \varphi) \frac{a}{p}. \end{aligned} \tag{2.40}$$

The Lowengrub–Truskinovsky system reads as

$$\operatorname{div}(\boldsymbol{v}) = -\frac{1}{\rho}\frac{\partial \rho}{\partial \varphi}(\partial_t \varphi + \boldsymbol{v}\cdot\nabla\varphi), \tag{2.41}$$

$$\rho\partial_t \boldsymbol{v} + \rho(\boldsymbol{v}\cdot\nabla)\boldsymbol{v} + \nabla p = \operatorname{div}(\boldsymbol{S}) - \operatorname{div}(\rho\nabla\varphi\otimes\varphi), \tag{2.42}$$

$$\rho\partial_t\varphi + \rho\boldsymbol{v}\cdot\nabla\varphi = \Delta\mu. \tag{2.43}$$

Here,

$$\mu = W'(\varphi) - \frac{p}{\rho^2}\frac{\partial\rho}{\partial\varphi} - \frac{1}{\rho}\operatorname{div}(\rho\nabla\varphi),$$
$$\rho^{-1} = \frac{\varphi}{\rho_{\mathrm{L}}} + \frac{(1-\varphi)}{\rho_{\mathrm{V}}},$$

with the constant (but possibly different) densities ρ_{L} and ρ_{V}.
We consider the following regime:

$$\mathrm{Ma} = \varepsilon, \quad \mathrm{Ca} = \varepsilon^2, \quad \mathrm{Re} = 1, \quad \mathrm{Pe} = \varepsilon^2, \quad b = \varepsilon^2, \quad a = 1.$$

The regime is chosen in a way that we retain the viscous stress tensor and capillary stress tensor in the limit.
First, we formulate (2.37) in terms of the pressure. Let us note

$$\frac{1}{\rho} = g_p, \quad \rho = \frac{1}{g_p}, \tag{2.44}$$
$$g = g(p,\varphi,\nabla\varphi), \quad g_p = g_p(p,\varphi),$$
$$\partial_t\rho = -\frac{1}{g_p^2}(g_{pp}\partial_t p + g_{p\varphi}\partial_t\varphi),$$
$$\nabla\rho = -\frac{1}{g_p^2}(g_{pp}\nabla p + g_{p\varphi}\nabla\varphi).$$

Then, from (2.37) we have

$$\frac{1}{g_p^2}(g_{pp}\partial_t p + g_{p\varphi}\partial_t\varphi) + \frac{1}{g_p^2}\boldsymbol{v}\cdot(g_{pp}\nabla p + g_{p\varphi}\nabla\varphi) - \frac{1}{g_p}\operatorname{div}(\boldsymbol{v}) = 0$$
$$\frac{g_{pp}}{g_p}(\partial_t p + \boldsymbol{v}\cdot\nabla p) + \frac{g_{p\varphi}}{g_p}(\partial_t\varphi + \boldsymbol{v}\cdot\nabla\varphi) - \operatorname{div}(\boldsymbol{v}) = 0. \tag{2.45}$$

Note that $-\dfrac{g_{pp}}{g_p}$ is the (isothermal) compressibility.

We assume the asymptotic expansions:

$$\begin{aligned}\rho &= \rho^{(0)} + \varepsilon\rho^{(1)} + \varepsilon^2\rho^{(2)} + \dots,\\ p &= p^{(0)} + \varepsilon p^{(1)} + \varepsilon^2 p^{(2)} + \dots,\\ \boldsymbol{v} &= \boldsymbol{v}^{(0)} + \varepsilon\boldsymbol{v}^{(1)} + \varepsilon^2\boldsymbol{v}^{(2)} + \dots,\\ \varphi &= \varphi^{(0)} + \varepsilon\varphi^{(1)} + \varepsilon^2\varphi^{(2)} + \dots.\end{aligned}$$

In the following we will use the superscripts $^{(i)}$, $i \in \mathbb{N}_0$ for other quantities as well to denote the i-th order part of the corresponding quantity.
Inserting the expansions above into (2.38), we infer

$$\begin{aligned}&\rho^{(0)}\partial_t\boldsymbol{v}^{(0)} + \rho^{(0)}(\boldsymbol{v}^{(0)}\cdot\nabla)\boldsymbol{v}^{(0)} + \frac{1}{\varepsilon^2}\nabla p^{(0)} + \frac{1}{\varepsilon}\nabla p^{(1)} + \nabla p^{(2)}\\ &\quad = \operatorname{div}(\boldsymbol{S}^{(0)}) - \operatorname{div}(\rho^{(0)}\nabla\varphi^{(0)}\otimes\nabla\varphi^{(0)}) + O(\varepsilon).\end{aligned} \tag{2.46}$$

Comparing the powers of ε we obtain immediately

$$\nabla p^{(0)} = 0 \Longrightarrow p^{(0)} = p^{(0)}(t), \tag{2.47}$$

$$\nabla p^{(1)} = 0 \Longrightarrow p^{(1)} = p^{(1)}(t), \tag{2.48}$$

$$\rho^{(0)}\partial_t\boldsymbol{v}^{(0)} + \rho^{(0)}(\boldsymbol{v}^{(0)}\cdot\nabla)\boldsymbol{v}^{(0)} + \nabla p^{(2)} = \operatorname{div}(\boldsymbol{S}^{(0)}) - \operatorname{div}(\rho^{(0)}\nabla\varphi^{(0)}\otimes\nabla\varphi^{(0)}).$$

The last equation yields the momentum equation (2.42) of the LT system for $\rho^{(0)}$, $\boldsymbol{v}^{(0)}$ and $p^{(2)}$.
Hence, we have with (2.44), (2.47), and (2.48) for the zeroth-order in (2.45)

$$\frac{g_{pp}^{(0)}}{g_p^{(0)}}\partial_t p^{(0)} = \operatorname{div}(\boldsymbol{v}^{(0)}) + \frac{1}{\rho^{(0)}}\frac{\partial\rho^{(0)}}{\partial\varphi^{(0)}}(\partial_t\varphi^{(0)} + \boldsymbol{v}^{(0)}\cdot\nabla\varphi^{(0)}).$$

With (2.39) we infer

$$\begin{aligned}\frac{g_{pp}^{(0)}}{g_p^{(0)}}\partial_t p^{(0)} &= \operatorname{div}(\boldsymbol{v}^{(0)}) + \frac{1}{\rho^{(0)}}\frac{\partial\rho^{(0)}}{\partial\varphi^{(0)}}\frac{1}{\rho^{(0)}}\Delta\mu^{(2)}\\ &= \operatorname{div}(\boldsymbol{v}^{(0)}) + (g_p^{(0)})^2\frac{\partial\rho^{(0)}}{\partial\varphi^{(0)}}\Delta\mu^{(2)}\\ &= \operatorname{div}(\boldsymbol{v}^{(0)}) - g_{p\varphi}^{(0)}(t)\Delta\mu^{(2)}.\end{aligned} \tag{2.49}$$

Note that due to (2.44), (2.40), and (2.47) we have $g_{p\varphi}^{(0)} = g_{p\varphi}^{(0)}(t)$.

Thus,

$$\begin{aligned}\partial_t p^{(0)} \int_\Omega \frac{g_{pp}^{(0)}}{g_p^{(0)}}\,\mathrm{d}\boldsymbol{x} &= \int_\Omega \operatorname{div}(\boldsymbol{v}^{(0)})\,\mathrm{d}\boldsymbol{x} - g_{p\varphi}^{(0)} \int_\Omega \Delta\mu^{(2)}\,\mathrm{d}\boldsymbol{x} \\ &= \int_{\partial\Omega} \boldsymbol{v}^{(0)} \cdot \boldsymbol{n}\,\mathrm{d}s - g_{p\varphi}^{(0)} \int_{\partial\Omega} \nabla\mu^{(2)} \cdot \boldsymbol{n}\,\mathrm{d}s \\ &= 0.\end{aligned}$$

In the last step we used the boundary conditions (2.16)–(2.18).
Therefore,

$$\partial_t p^{(0)} = 0 \Longrightarrow p^{(0)} = \text{const.} =: \rho_{\mathrm{V}}. \tag{2.50}$$

Then, with (2.49) we obtain

$$\operatorname{div}(\boldsymbol{v}^{(0)}) = -\frac{1}{\rho^{(0)}} \frac{\partial\rho^{(0)}}{\partial\varphi^{(0)}} (\partial_t \varphi^{(0)} + \boldsymbol{v}^{(0)} \cdot \nabla\varphi^{(0)}),$$

which is the first equation (2.41) of the LT system for $\boldsymbol{v}^{(0)}, \rho^{(0)}, \varphi^{(0)}$ and $p^{(0)}$.
With (2.50) we have

$$\frac{1}{\rho} = \frac{\varphi^{(0)}}{\rho_{\mathrm{L}}} + \frac{1-\varphi^{(0)}}{p^{(0)}} + O(\varepsilon).$$

Before we take a look at the phase-field equation (2.39), exploiting Taylor expansions, we note the following identities:

$$\begin{aligned}\ln(p) &= \ln(p^{(0)} + \varepsilon p^{(1)} + \varepsilon^2 p^{(2)}) + O(\varepsilon^3) \\ &= \ln(p^{(0)} + \varepsilon p^{(1)}) + \frac{1}{p^{(0)} + \varepsilon p^{(1)}} \varepsilon^2 p^{(2)} + O(\varepsilon^3) \\ &= \ln(p^{(0)}) + \frac{1}{p^{(0)}} \varepsilon p^{(1)} + \left(\frac{1}{p^{(0)}} - \frac{1}{(p^{(0)})^2} \varepsilon p^{(1)} + O(\varepsilon^2) \right) \varepsilon^2 p^{(2)} + O(\varepsilon^3) \\ &= \ln(p^{(0)}) + \frac{1}{p^{(0)}} \varepsilon p^{(1)} + \left(\frac{1}{p^{(0)}} - \frac{1}{(p^{(0)})^2} \varepsilon p^{(1)} \right) \varepsilon^2 p^{(2)} + O(\varepsilon^3).\end{aligned}$$

We are interested in the $O(1)$-part of equation (2.39) given by

$$\rho^{(0)} \partial_t \varphi^{(0)} + \rho^{(0)} \boldsymbol{v}^{(0)} \cdot \nabla\varphi^{(0)} + O(\varepsilon) = \frac{1}{\varepsilon^2} \Delta\mu,$$

with

$$\mu = \varepsilon^2 W'(\varphi^0) + \frac{p^{(0)}}{\rho_{\mathrm{L}}} + \varepsilon \frac{p^{(1)}}{\rho_{\mathrm{L}}} + \varepsilon^2 \frac{p^{(2)}}{\rho_{\mathrm{L}}} - \ln(p^{(0)}) - \frac{1}{p^{(0)}} \varepsilon p^{(1)} - \left(\frac{1}{p^{(0)}}\right) \varepsilon^2 p^{(2)} - \frac{\varepsilon^2}{\rho} \operatorname{div}(\rho^{(0)} \nabla \varphi^{(0)}) + O(\varepsilon^3).$$

Next, we look at the $O(\varepsilon^2)$-part of μ:

$$\mu^{(2)} = W'(\varphi^0) + \frac{p^{(2)}}{\rho_{\mathrm{L}}} - \frac{p^{(2)}}{p^{(0)}} - \frac{1}{\rho^{(0)}} \operatorname{div}(\rho^{(0)} \nabla \varphi^{(0)}).$$

Since $p^{(0)} = p_{\mathrm{V}}$, we have

$$\begin{aligned} \mu^{(2)} &= W'(\varphi^0) + p^{(2)} \left(\frac{1}{\rho_{\mathrm{L}}} - \frac{1}{\rho_{\mathrm{V}}}\right) - \frac{1}{\rho^{(0)}} \operatorname{div}(\rho^{(0)} \nabla \varphi^{(0)}) \\ &= W'(\varphi^0) + p^{(2)} \left(\frac{1}{(\rho^{(0)})^2} \frac{\partial \rho^{(0)}}{\partial \varphi^{(0)}}\right) - \frac{1}{\rho^{(0)}} \operatorname{div}(\rho^{(0)} \nabla \varphi^{(0)}). \end{aligned}$$

The Laplacian of $\mu^{(0)}$ and $\mu^{(1)}$ vanish since $p^{(0)}$ and $p^{(1)}$ do not depend on $\boldsymbol{x}$.
With this result we obtain the last remaining equation (2.43).
In summary, we showed formally the convergence of solutions $p^{(2)}, \boldsymbol{v}^{(0)}, \varphi^{(0)}$ to the ICNSCH system (2.37)–(2.39) in the regime (2.46) to solutions to the quasi-incompressible LT system (2.41)–(2.43).

Towards a DG Discretization for the ICNSCH System

3

A popular class of solvers for phase-field systems are energy-consistent dG schemes [51, 69, 86, 96]. They are based on the idea that the energy inequality (2.20) of the phase-field system should be recovered on the discrete level without introducing numerical dissipation. This prevents parasitic currents in a near equilibrium situation [61]. In [96] such a solver was proposed for the ICNSCH system (2.12)–(2.14) but not implemented by the authors.

As main drawback, these schemes show restrictions with respect to the step-size of the time integration. Indeed, at best a second order convergence in time can be achieved. Additionally, the solver is sensitive with respect to larger variations in energy. Because of the above-mentioned drawbacks and our interest in simulations away from equilibrium, where parasitic currents are negligible, we want to design a novel solver which can achieve higher order in time and circumvent the time step restriction by means of implicit discretizations.

The idea is to develop a fully-implicit dG scheme based on Godunov fluxes. The idea of Godunov fluxes is to obtain the numerical inter-element fluxes $f_{i+1/2}$ through the solution of Riemann problems at the inter-element boundaries. The Godunov fluxes are hence expressed as

$$f^{\text{god}}_{i+1/2}(u^n_i, u^n_{i+1}) = f(u_{i+1/2}(0)),$$

where f is the flux function of the underlying PDE and $u_{i+1/2}(0)$ denotes the exact solution $u_{i+1/2}(x/t)$ to the corresponding Riemann problem with initial values (u^n_i, u^n_{i+1}), evaluated at $x/t = 0$.

In order to compute the numerical fluxes, we exploit the exact solution of local Riemann problems at inter-element boundaries. However, due to the incompressible nature of the liquid phase, the time derivative of the continuity equation vanishes. Hence, it is impossible to find a Riemann problem solution. In order to overcome this issue we adopt an artificial compressibility approach. Following the work of [11] an artificial compressibility is added for the liquid phase only at the inter-element level thus ensuring the hyperbolic nature of local problems.

A natural approach is to add artificial compressibility with parameter $a_0 > 0$, only for the incompressible phase. This will be described in detail in the next section. However, then the speed of sound is

$$c^2 := \frac{\mathrm{d}\,p}{\mathrm{d}\,\rho} = v^2 + \hat{a}^2 \left(1 - \frac{1-\varphi}{p^2}\alpha(\rho v)^2\right).$$

Hence, this approach cannot be applied since hyperbolicity is not guaranteed and the sound speed depends both on the velocity and pressure. This results in the fact that we cannot explicitly compute a Riemann solution. Therefore, we introduce an artificial equation of state, namely

$$\frac{1}{\rho} = \varphi \frac{a_0^2}{p - p_0 + \rho_{\mathrm{L}} a_0^2} + (1-\varphi)\frac{\alpha}{p}. \tag{3.1}$$

With (3.1) the speed of sound is

$$c^2 = \frac{(\varphi p a_0^2 + (1-\varphi)(p - p_0 + \rho_{\mathrm{L}} a_0^2)\alpha)^2}{\varphi p^2 a_0^2 + (1-\varphi)(p - p_0 + \rho_{\mathrm{L}} a_0^2)^2 \alpha} > 0$$

and the corresponding system hyperbolic. Note that for $\varphi = 0$ we obtain $c^2 = \alpha$ and for $\varphi = 1$ we obtain $c^2 = a_0^2$.
This approach is described in detail in the following Sections 3.1–3.3.
In the next Chapter 4 we apply this novel approach to the simpler case of a single-phase incompressible Navier–Stokes system with the artificial equation of state

$$\rho = \frac{p - p_0}{a_0^2} + \rho_{\mathrm{L}}.$$

We implement the artificial EOS-based Riemann solver in a dG framework and conduct numerical experiments in Section 4.3.

3.1 The ICNSCH System at Inter-Element Boundaries

In order to derive a dG scheme based on Godunov fluxes, one major task is the solution of local Riemann problems at inter-element boundaries. These problems are formulated for the following first-order part of the monodimensional ICNSCH

system

$$\partial_t \rho + \partial_x(\rho v) = 0, \tag{3.2}$$

$$\partial_t(\rho v) + \partial_x(\rho v^2 + p) = 0, \tag{3.3}$$

$$\partial_t(\rho \varphi) + \partial_x(\rho \varphi v) = 0, \tag{3.4}$$

with the EOS

$$\frac{1}{\rho} = \frac{\varphi}{\rho_l} + \left(1 - \varphi\right)\frac{\alpha}{p}.$$

We seek the solution to the 1D Riemann problem

$$\boldsymbol{U}(x, t_0) = \begin{pmatrix} p \\ v \\ \varphi \end{pmatrix}(x, t_0) = \begin{cases} \boldsymbol{U}_L = (p_L, v_{nL}, \varphi_L)^\top & x < x_0, \\ \boldsymbol{U}_R = (p_R, v_{nR}, \varphi_R)^\top & x > x_0, \end{cases}$$

for (3.2)–(3.4). Here, x_0 is the position of the jump at initial time t_0 and L and R the subscripts denoting the initial states on the left and on the right of the discontinuity, respectively.

For $\varphi = 1$, the time derivative of the first equation (3.2) vanishes. In this case it is not possible to find a solution to the corresponding Riemann problem.

Hence, we modify the system of equation to find a solution to the modified system. This can be done in two ways. Either, we take the full system and make modifications or we reduce it first due to the following observation and modify afterwards. From the first and third equation of (3.2)–(3.4) it follows that the phase-field variable φ is purely advected. Hence, the φ can only change across the contact discontinuity, i.e.

$$\varphi_{\star L} = \varphi_L \quad \text{and} \quad \varphi_{\star R} = \varphi_R.$$

Consequently, the star region solution for pressure and velocity are decoupled from the phase-field. Thus, we can modify the first two equations only, and use the solution of φ from the original system.

However, in order to test the applicability of different modifications of the original system, the corresponding Riemann solvers have to be implemented in a dG framework and approved by numerical experiments.

3.2 Artificial Compressibility Modification

In the single-phase incompressible case, the artificial compressibility modification is used by adding the time derivative $\frac{1}{a_0^2}\partial_t p$ for the first equation $\partial_x v = 0$. In the following we discuss why this idea cannot be straightforwardly applied to the phase-field situation.
We modify (3.2) and (3.3) in the following way using pressure and momentum as unknowns

$$\begin{aligned} \partial_t p + \partial_x(\rho \hat{a}^2 v) &= 0, \\ \partial_t(\rho v) + \partial_x(\rho v^2 + p) &= 0, \end{aligned} \tag{3.5}$$

with

$$\begin{aligned} \frac{1}{\rho} &= \frac{\hat{\varphi}}{\rho_l} + \left(1 - \hat{\varphi}\right)\frac{\alpha}{p}, \\ \hat{a}^2 &= \hat{\varphi} a_0^2 + \left(1 - \hat{\varphi}\right)\alpha. \end{aligned} \tag{3.6}$$

Here, $\hat{\varphi}$ is the phase field variable value given by the initial conditions, i.e. $\hat{\varphi}$ takes the left/right initial value $\varphi_{L/R}$ on the left/right of the contact discontinuity. Further, a_0 the artificial speed of sound needed to recover the hyperbolic nature of the problem when dealing with incompressible fluids ($\hat{\varphi} = 1$). Notice that for $\hat{\varphi} = 0$ (perfect gas) we have $p = \rho\alpha$ and the correct continuity equation is regained. However, for values $0 < \hat{\varphi} < 1$ we obtain a different speed of sound than in the original system. Note that (3.6) is inconsistent in the sense that with the second equation and the definition $\hat{a}^2 = \frac{\mathrm{d}p}{\mathrm{d}\rho}$ the first equation contradicts for $\varphi \in (0, 1)$. Hence, the introduction of artificial compressibility might be infeasible. However, in the following we show that even the choice (3.6) does not suffice to ensure hyperbolicity of the corresponding system.
The system (3.5) can be written in the matrix form

$$\partial_t \boldsymbol{w} + \partial_x(\boldsymbol{F}(\boldsymbol{w})) = \boldsymbol{0},$$

with

$$\boldsymbol{w} = \begin{pmatrix} p \\ \rho v \end{pmatrix}, \qquad \boldsymbol{F}(\boldsymbol{w}) = \begin{pmatrix} \rho \hat{a}^2 v \\ \rho v^2 + p \end{pmatrix}.$$

The flux Jacobian matrix is given by

$$\boldsymbol{A} = \frac{\partial \boldsymbol{F}(\boldsymbol{w})}{\partial \boldsymbol{w}} = \begin{pmatrix} 0 & \hat{a}^2 \\ 1 - \dfrac{1 - \hat{\varphi}}{p^2}\alpha\left(\rho v\right)^2 & 2v \end{pmatrix},$$

while the eigenvalues $\boldsymbol{\lambda} = (\lambda_-, \lambda_+)^\top$ and left eigenvector matrix $\boldsymbol{L}$ are

$$\boldsymbol{\lambda} = \begin{pmatrix} \lambda_- \\ \lambda_+ \end{pmatrix} = \begin{pmatrix} v - c \\ v + c \end{pmatrix},$$
$$\boldsymbol{L} = \begin{pmatrix} 1 & -\dfrac{\hat{a}^2}{\lambda_+} \\ -1 & \dfrac{\hat{a}^2}{\lambda_-} \end{pmatrix},$$

respectively, where

$$c^2 = v^2 + \hat{a}^2 \left(1 - \frac{1-\hat{\varphi}}{p^2} \alpha \left(\rho v\right)^2\right).$$

It cannot be guaranteed that $c^2 \geq 0$. It can attain negative values if $\dfrac{1-\hat{\varphi}}{p^2} \alpha \left(\rho v\right)^2$ dominates, e.g. for large α.

3.3 Artificial EOS Modification

To overcome the problem of possibly non-positive speed of sound, we modify the system (3.2)–(3.4) by means of the artificial EOS, i.e. we consider

$$\begin{aligned} \partial_t \rho + \partial_x(\rho v) &= 0, \\ \partial_t(\rho v) + \partial_x(\rho v^2 + p) &= 0, \\ \partial_t(\rho \varphi) + \partial_x(\rho \varphi v) &= 0, \end{aligned}$$

with

$$\frac{1}{\rho} = \varphi \frac{a_0^2}{p - p_0 + \rho_L a_0^2} + (1-\varphi)\frac{\alpha}{p}. \tag{3.7}$$

Again, by combining the first and last equation it is clear that

$$\varphi_{\star L} = \varphi_L \quad \text{and} \quad \varphi_{\star R} = \varphi_R,$$

so in the following we consider the first two equations only and replace φ by $\hat{\varphi}$, which is equal to $\varphi_{L/R}$ on the left and right side of the contact discontinuity, respectively. The corresponding reduced system can be written in the matrix form

$$\partial_t \boldsymbol{w} + \partial_x(\boldsymbol{F}(\boldsymbol{w})) = \boldsymbol{0},$$

with

$$\boldsymbol{w} = \begin{pmatrix} \rho \\ \rho v \end{pmatrix}, \qquad \boldsymbol{F}(\boldsymbol{w}) = \begin{pmatrix} \rho v \\ \rho v^2 + p \end{pmatrix}.$$

Then, the flux Jacobian matrix is

$$\boldsymbol{A} = \frac{\partial \boldsymbol{F}(\boldsymbol{w})}{\partial \boldsymbol{w}} = \begin{pmatrix} 0 & 1 \\ -v^2 + \frac{\partial p}{\partial \rho} & 2v \end{pmatrix}.$$

In this case the eigenvalues $\boldsymbol{\lambda} = (\lambda_-, \lambda_+)^\top$ and left eigenvector matrix $\boldsymbol{L}$ are given by

$$\boldsymbol{\lambda} = \begin{pmatrix} \lambda_- \\ \lambda_+ \end{pmatrix} = \begin{pmatrix} v - c \\ v + c \end{pmatrix},$$
$$\boldsymbol{L} = \begin{pmatrix} \lambda^+ & -1 \\ \lambda^- & -1 \end{pmatrix},$$

where now

$$c^2 = \frac{(\hat{\varphi} p a_0^2 + (1 - \hat{\varphi})(p - p_0 + \rho_\mathrm{L} a_0^2)\alpha)^2}{\hat{\varphi} p^2 a_0^2 + (1 - \hat{\varphi})(p - p_0 + \rho_\mathrm{L} a_0^2)^2 \alpha}.$$

It is clear that $c^2 \geq 0$ and thus $\lambda_- < 0$, $\lambda_+ > 0$, $\lambda_- < v < \lambda_+$.
Hence, the modification of (3.5) by means of the artificial EOS (3.7) is more promising than the modification with the artificial compressibility (3.6). In order to test the applicability of the artificial EOS approach for dG schemes, we apply it in the following chapter for the simpler incompressible single-phase situation.

An Artificial EOS-Based Riemann Solver for a DG Discretization of Incompressible Flows

4

In this chapter we study the applicability of the artificial EOS approach in a simpler setting. Namely, we consider inviscid incompressible single-phase flow. A crucial point for all dG schemes based on Godunov fluxes is the solution of Riemann problems at the inter-element boundaries. Hence, in the following section we introduce the corresponding Riemann problem and the artificial EOS approach. In Section 4.3 we conduct numerical test, where we implemented the artificial EOS Riemann solver in a dG framework, which we briefly describe in Section 4.2.

4.1 The Riemann Problem

Let us consider the d-dimensional incompressible Euler equations split in the n-direction:

$$\begin{aligned} \frac{\partial q_n}{\partial x_n} &= 0, \\ \frac{\partial q_n}{\partial t} + \frac{\partial (q_n^2 + p/\rho_0)}{\partial x_n} &= 0, \\ \frac{\partial \boldsymbol{\theta}}{\partial t} + \frac{\partial (\boldsymbol{\theta} q_n)}{\partial x_n} &= 0. \end{aligned} \tag{4.1}$$

This corresponds to the first-order part for the case $\varphi = 1$ in the ICNSCH system. The primary unknowns are the pressure $p \in \mathbb{R}$, the normal velocity $q_n \in \mathbb{R}$, and the tangential velocity $\boldsymbol{\theta} \in \mathbb{R}^d$. The constant reference density is denoted by $\rho_0 \in (0, \infty)$. The normal unitary vector $\boldsymbol{n}$ has to be understood as the direction normal to the mesh element boundary and it gives the direction of splitting, i.e., $q_n = \boldsymbol{v} \cdot \boldsymbol{n}$, $x_n = \boldsymbol{x} \cdot \boldsymbol{n}$, with $\boldsymbol{v}$ and $\boldsymbol{x}$ the velocity and the position vectors, respectively. The quantity $\boldsymbol{\theta} \in \mathbb{R}^d$ is the velocity component tangential to $\boldsymbol{n}$. Accordingly, the velocity vector can be written as $\boldsymbol{v} = q_n \boldsymbol{n} + \boldsymbol{\theta}$.

The system (4.1) does not fit into the framework of hyperbolic PDE. Moreover, it lacks of a velocity-pressure coupling. As a consequence, a solution to the Riemann problem by means of hyperbolic wave patterns cannot be found. By Riemann prob-

lem we mean the initial value problem with the piece-wise constant data

$$\boldsymbol{U}(x_n, t_0) = \begin{pmatrix} p \\ q_n \\ \boldsymbol{\theta} \end{pmatrix}(x_n, t_0) = \begin{cases} \boldsymbol{U}_L = (p_L, q_{nL}, \boldsymbol{\theta}_L)^\top & x_n < x_{n_0}, \\ \boldsymbol{U}_R = (p_R, q_{nR}, \boldsymbol{\theta}_R)^\top & x_n > x_{n_0}. \end{cases} \tag{4.2}$$

Here, x_{n_0} is the position of the jump at initial time t_0 and L and R the subscripts denoting the initial states on the left and on the right of the discontinuity, respectively. Solving Riemann problems like (4.1)–(4.2) is an important issue for all numerical methods which rely on Godunov fluxes.

4.1.1 The Artificial Compressibility Approach

In order to find a solution to the Riemann problem (4.1)–(4.2), Elsworth and Toro [42] proposed to use the artificial compressibility approach devised by Chorin [29]. The approach uses an approximation for the split set of incompressible Euler equations given by

$$\begin{aligned} \frac{\partial p}{\partial t} + \frac{\partial(\rho_0 a_0^2 q_n)}{\partial x_n} &= 0, \\ \frac{\partial q_n}{\partial t} + \frac{\partial(q_n^2 + p/\rho_0)}{\partial x_n} &= 0, \\ \frac{\partial \boldsymbol{\theta}}{\partial t} + \frac{\partial(\boldsymbol{\theta} q_n)}{\partial x_n} &= 0. \end{aligned} \tag{4.3}$$

Here, the primary variables are p, q_n, and $\boldsymbol{\theta}$. Further, the parameter $a_0 \in (0, \infty)$ is the constant artificial compressibility coefficient. Formally, (4.1) is recovered for $a_0 \longrightarrow \infty$.
Note, that (4.3) is strictly hyperbolic with eigenvalues

$$\lambda_1 = q_n - \sqrt{a_0^2 + q_n^2}, \quad \lambda_2 = q_n, \quad \lambda_3 = q_n + \sqrt{a_0^2 + q_n^2}.$$

The solution to (4.3) with initial data (4.2) consists of four states separated by two external acoustic waves and a central contact discontinuity, see Figure 4.1.
The acoustic waves can be either rarefactions or shocks, depending on the choice of $\boldsymbol{U}_{L/R}$. Across these waves all the properties can change. The star region between them is divided into the left ($\star L$) and the right ($\star R$) part by the contact discontinuity. Across the contact discontinuity only $\boldsymbol{\theta}$ can vary. The complete derivation of the solution to the Riemann problem for the system (4.3) can be found in [11, 42]. However, the wave pattern described above can be violated for certain combination of initial values and artificial compressibility parameters. As pointed out in [13], depending on the Riemann problem left and right states, there could exist a

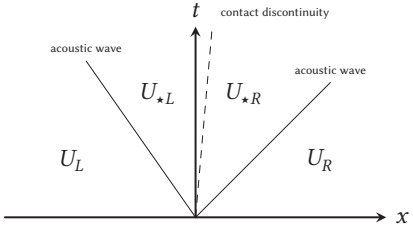

Figure 4.1: The structure of the solution to the Riemann problem (4.2) *for the split multi-dimensional case.*

critical value of the artificial compressibility $\overline{a}_0$ for which the contact discontinuity is as fast as the left or the right shock. In this case, for $a_0 < \overline{a}_0$ the Riemann solver predicts a contact wave overtaking the shock (see Appendix A).
A way to avoid this unphysical behavior is to choose a_0 higher than the critical value $\overline{a}_0$. However, since $\overline{a}_0$ depends upon the initial data, there is no way to ensure a priori that the chosen a_0 will prevent the issue.

4.1.2 The Artificial EOS Approach

With the aim to find the solution to the Riemann problem avoiding the wave pattern violation, we propose a new approximation to the incompressible Euler equations based on the definition of an artificial equation of state. In particular, as a modification of the original incompressible system, we consider the set of n-split isothermal compressible Euler equations

$$\begin{aligned} \frac{\partial \rho}{\partial t} + \frac{\partial (\rho q_n)}{\partial x_n} &= 0 \\ \frac{\partial (\rho q_n)}{\partial t} + \frac{\partial (\rho q_n^2 + p)}{\partial x_n} &= 0 \\ \frac{\partial (\rho \boldsymbol{\theta})}{\partial t} + \frac{\partial (\rho \boldsymbol{\theta} q_n)}{\partial x_n} &= 0, \end{aligned} \tag{4.4}$$

with primary variables ρ, (ρq_n), and $(\rho \boldsymbol{\theta})$.
In order to derive the artificial EOS, we exploit the generic definition of the sound speed with isothermal conditions

$$a_0^2 = \frac{\mathrm{d}\, p}{\mathrm{d}\, \rho}, \tag{4.5}$$

where now a_0 has to be considered as the artificial speed of sound. We keep a_0 constant and integrate (4.5) to derive the artificial EOS

$$\rho(p) = \frac{p - p_0}{a_0^2} + \rho_0 \iff p(\rho) = a_0^2(\rho - \rho_0) + p_0. \tag{4.6}$$

Here, $p_0 \in \mathbb{R}$ is the reference pressure, whose value must be carefully defined to avoid negative densities, and $\rho_0 \in (0, \infty)$ is the constant density of the incompressible regime. Notice that with this artificial EOS (4.6) for (4.4) the set of the incompressible Euler equations (4.1) is formally recovered in the limit $a_0 \longrightarrow \infty$.
The solution to the system of isothermal compressible Euler equations with initial value (4.2) is well known in the literature, e.g. [72]. It consists again of four states separated by two external acoustic waves and a central contact discontinuity, see Figure 4.1. However, to the authors knowledge, this is the first time that an exact Riemann solver for (4.4)–(4.6) is presented.
As a first remark, it must be pointed out that the artificial EOS does not destroy the strictly hyperbolic nature of the system (4.4). In fact, we have three distinct real eigenvalues

$$\lambda_1 = q_n - a_0, \quad \lambda_2 = q_n, \quad \lambda_3 = q_n + a_0.$$

As a second remark, from the analysis of (4.4) it is interesting to note that, combining the first and the last equation, the following advection equation is obtained

$$\frac{\partial \theta}{\partial t} + q_n \frac{\partial \theta}{\partial x_n} = 0. \tag{4.7}$$

Accordingly, the last equation of (4.4) describes the evolution of the θ variable only and the pressure-velocity solution is decoupled from θ.
Taking inspiration from [72] for isothermal compressible flows, we derive the exact Riemann solver for (4.2),(4.4),(4.6).
For the sake of comprehension, the solutions for pressure and velocity are reported in Appendix B. There, in addition we show that the choice of the reference pressure

$$p_0 = \min(p_L, p_R) \tag{4.8}$$

is effective in ensuring the positivity of the density.
As next step, we simply note from (4.7) that θ is purely advected and thus it cannot change across acoustic waves. Accordingly, the Riemann problem solution for θ simply reads as

$$\theta_{\star L} = \theta_L \qquad \text{and} \qquad \theta_{\star R} = \theta_R, \tag{4.9}$$

cf. Figure 4.1.

As stated before, the n-split multi-dimensional Riemann problem solution entails the presence of the contact discontinuity. The peculiar feature of this type of wave is that the mass flow vanishes across the interface. Therefore, the contact wave speed is equal to the star region velocity $q_{n\star}$. However, from the Riemann solution derivation in Appendix B it is known that the shock wave speed is

$$s^{\pm} = q_{n1} \pm a_0 \sqrt{\frac{\rho_2}{\rho_1}} = q_{n2} \pm a_0 \sqrt{\frac{\rho_1}{\rho_2}}, \tag{4.10}$$

where the negative sign (−) is for a left shock while the positive sign (+) is for a right shock. The subscripts 1 and 2 denote the two states which are on either side of the shock. From (4.10) it is clear that

$$s^- < q_{ni} \qquad \text{and} \qquad s^+ > q_{ni} \qquad i = 1, 2.$$

Since one of q_{n1} and q_{n2} is necessarily the star region velocity $q_{n\star}$ (see Appendix B.3), it follows that the contact wave cannot be as fast as a shock wave. As a consequence, in contrast to the Chorin's approach of the artificial compressibility, the artificial EOS approach is not affected by the wave pattern violation issue.

4.2 The DG Scheme

In this section we introduce the basic concept of the dG scheme, which is used in the next section to illustrate our EOS-based Riemann solver. Details can be found in [10]. We repeat the essentials of [10] in the following.

4.2.1 The Governing Equations

We consider as governing equations the isothermal incompressible Navier–Stokes equations, namely

$$\begin{aligned} \operatorname{div}(\boldsymbol{v}) &= 0, \\ \partial_t \boldsymbol{v} + \operatorname{div}(\boldsymbol{v} \otimes \boldsymbol{v} + p/\rho_0 \boldsymbol{I}) &= \frac{1}{\rho_0} \operatorname{div}(\boldsymbol{S}), \end{aligned} \tag{4.11}$$

with $\boldsymbol{S} = 2\mu \left(\nabla \boldsymbol{v} + \nabla \boldsymbol{v}^\top) - \frac{1}{3} \operatorname{div}(\boldsymbol{v}) \boldsymbol{I} \right)$, constant viscosity μ, and the constant density $\rho_0 > 0$.

4.2.2 The DG Setting

We recall some notation of Chapter 3 from Part II.

Let $\mathcal{T} = \{T\}$ denote a mesh of the domain $\Omega \subset \mathbb{R}^d, d \in \{1, 2, 3\}$, consisting of disjoint polyhedra T with

$$\bar{\Omega} = \bigcup_{T \in \mathcal{T}} \bar{T}.$$

Following [12], we consider the broken polynomial space

$$\mathbb{P}_d^k := \left\{ u_h \in L^2(\Omega) | u_h|_T \in \mathbb{P}_d^k(T), \forall T \in \mathcal{T} \right\}. \tag{4.12}$$

Here, $k > 0$ and $\mathbb{P}_d^k(T)$ denotes the restriction to T of polynomials in $\mathbb{P}_d^k$.
The basis for the space (4.12) is built with a modified Gram–Schmidt algorithm according to [21]. This leads to orthonormal hierarchical basis functions.
Further, we introduce the set of mesh faces $\mathcal{F}_h := \mathcal{F}_h^i \cup \mathcal{F}_h^b$, where $\mathcal{F}_h^b$ contains the boundary faces and $\mathcal{F}_h^i$ the (inner) interfaces, see Definition 3.1 in Part II. For all boundary faces $F \in \mathcal{F}_h^b$, we denote by $\boldsymbol{n}_F$ the unit outer normal to Ω. On the other hand, for interfaces $F \in \mathcal{F}_h^i$ with $F = T^+ \cap T^-$, we denote by $\boldsymbol{n}_F^+$ and $\boldsymbol{n}_F^-$ the unit normals pointing to T^+ and T^-, respectively.
We define the jump and average operators for $u_h \in \mathbb{P}_d^k(\mathcal{T})$ by

$$[\![u_h]\!] := u_h|_{T^+} \boldsymbol{n}_F^+ + u_h|_{T^-} \boldsymbol{n}_F^-, \quad \{u_h\} := \frac{1}{2}(u_h|_{T^+} + u_h|_{T^-}).$$

The second-order viscous terms are discretized using the lifting operators $\boldsymbol{r}_F$ and $\boldsymbol{r}$. For any $F \in \mathcal{F}_h$, we define the local lifting operator $\boldsymbol{r}_F : (L^2(F))^d \longrightarrow (\mathbb{P}_d^k(\mathcal{T}))^d$ such that for all $\boldsymbol{u} \in (L^2(F))^d$

$$\int_\Omega \boldsymbol{r}_F(\boldsymbol{u}) \cdot \boldsymbol{\tau}_h \, \mathrm{d}\boldsymbol{x} = -\int_F \{\boldsymbol{\tau}_h\} \cdot \boldsymbol{u} \, \mathrm{d}F \quad \forall \boldsymbol{\tau}_h \in (\mathbb{P}_d^k(\mathcal{T}))^d.$$

Then, the global lifting operator $\boldsymbol{r}$ is defined as

$$\boldsymbol{r}(\boldsymbol{u}) := \sum_{F \in \mathcal{F}_h} \boldsymbol{r}_F(\boldsymbol{u}).$$

4.2.3 DG Discretization of the Navier–Stokes Equations

We can write the incompressible Navier–Stokes equations (4.11) in the following compact form

$$\boldsymbol{P}(\boldsymbol{w}) \frac{\partial \boldsymbol{w}}{\partial t} + \mathrm{div}(\boldsymbol{F}_c(\boldsymbol{w})) + \mathrm{div}(\boldsymbol{F}_v(\boldsymbol{w}, \nabla \boldsymbol{w})) = 0, \tag{4.13}$$

where $\boldsymbol{w} \in \mathbb{R}^m$ is the vector of unknowns, $\boldsymbol{F}_c, \boldsymbol{F}_v \in \mathbb{R}^{m\times d}$ are the convective and viscous flux functions, and $\boldsymbol{P}(\boldsymbol{w}) \in \mathbb{R}^{m\times m}$ is a transformation matrix.
We have the primitive variables $\boldsymbol{w} = (p, \boldsymbol{v}^\top)^\top$, which lead to $\boldsymbol{P} = \boldsymbol{I} - \boldsymbol{e}_1^\top \boldsymbol{e}_1$, with the first unit vector $\boldsymbol{e}_1 \in \mathbb{R}^m$.
Multiplying (4.13) with a smooth test function $\boldsymbol{u}$ and integration by parts leads to the weak formulation

$$\int_\Omega \boldsymbol{u} \cdot \left(\boldsymbol{P}(\boldsymbol{w})\frac{\partial \boldsymbol{w}}{\partial t}\right) \,\mathrm{d}\boldsymbol{x} - \int_\Omega \nabla \boldsymbol{u} \,:\, \boldsymbol{F}(\boldsymbol{w}, \nabla \boldsymbol{w}) \,\mathrm{d}\boldsymbol{x} + \int_{\partial\Omega} \boldsymbol{u} \otimes \boldsymbol{n} \,:\, \boldsymbol{F}(\boldsymbol{w}, \nabla \boldsymbol{w}) \,\mathrm{d}s = \boldsymbol{0}, \tag{4.14}$$

where $\boldsymbol{F} = \boldsymbol{F}_c + \boldsymbol{F}_v$ and $\boldsymbol{n}$ is the unit outer normal vector to $\partial\Omega$.
In order to discretize (4.14), we replace the solution $\boldsymbol{w}$ and the test function $\boldsymbol{u}$ by a finite element approximation $\boldsymbol{w}_h$ and a discrete test function $\boldsymbol{u}_h$, respectively. Here, $\boldsymbol{w}_h, \boldsymbol{u}_h \in \boldsymbol{V}_h$, with $\boldsymbol{V}_h := (\mathbb{P}_d^k(\mathcal{T}))^m$.
For each of the m equations in (4.14), we choose the set of test and shape functions in any element T as the set $\{\phi\}$ of N_{dof}^K orthogonal and hierarchical basis functions in that element. With this choice each component of $\boldsymbol{w}_h \in \boldsymbol{V}_h$ can be expressed in terms of the elements of the global vector $\boldsymbol{W}$ of unknown degrees of freedom (DOF) , i.e. $w_{h,j} = \phi_l W_{j,l},\ l = 1, \dots, N_{\text{dof}}^K\ \forall T \in \mathcal{T}$.
Then, the dG discretization of the Navier–Stokes equations means finding the elements of $\boldsymbol{W}$ such that for $j = 1, \dots, m$

$$\begin{aligned}\sum_{T\in\mathcal{T}} \int_T \phi_i P_{j,k}(\boldsymbol{w}_h)\phi_l \frac{\mathrm{d}\, W_{k,l}}{\mathrm{d}\, t} \,\mathrm{d}\boldsymbol{x} - \sum_{T\in\mathcal{T}} \int_T \frac{\partial \phi_i}{\partial x_n} F_{j,n}(\boldsymbol{w}_h, \nabla_h \boldsymbol{w}_h + \boldsymbol{r}([\![\boldsymbol{w}_h]\!])) \,\mathrm{d}\boldsymbol{x} \\ + \sum_{F\in\mathcal{F}_h} \int_F [\![\phi_i]\!]_n \hat{F}_{j,n}(\boldsymbol{w}^\pm, (\nabla_h \boldsymbol{w}_h + \eta_F \boldsymbol{r}_F([\![\boldsymbol{w}_h]\!]))^\pm) \,\mathrm{d}s,\end{aligned} \tag{4.15}$$

for all $i = 1, \dots, N_{\text{dof}}^K$.
Note that we used the Einstein summation convention in (4.15), i.e. repeated indices imply summation over $k = 1, \dots, m,\ l = 1, \dots, N_{\text{dof}}^K$, and $n = 1, \dots, d$.
In order to discretize the viscous fluxes, we use the BR2 scheme [14]. Subsequently, the viscous numerical flux is given by

$$\hat{\boldsymbol{F}}_v(\boldsymbol{w}_h^\pm, (\nabla_h \boldsymbol{w}_h + \eta_F \boldsymbol{r}_F([\![\boldsymbol{w}_h]\!]))^\pm) := \{\boldsymbol{F}_v(\boldsymbol{w}_h, \nabla_h \boldsymbol{w}_h + \eta_F \boldsymbol{r}_F([\![\boldsymbol{w}_h]\!]))\},$$

where the stability parameter η_F is chosen as described in [6].
The convective numerical flux is computed with the solution of local Riemann problems in the normal direction at each integration point on element faces. We employ the artificial EOS approach for the Riemann problems as described in the previous Section 4.1.2. The solution of these problems is specified in Appendix B.

Boundary conditions are weakly enforced by defining at each integration point on boundaries the state $\boldsymbol{w}^b$ and its gradient $\nabla \boldsymbol{w}^b$. These are used to compute numerical convective and viscous fluxes and the lifting operators for all $F \in \mathcal{F}_h^b$.

4.2.4 Time Integration

The numerical integration of (4.15) with suitable Gauss quadrature rules leads to a system of differential-algebraic equations. These can be written as

$$\boldsymbol{M_P}(\boldsymbol{W})\frac{\mathrm{d}\,\boldsymbol{W}}{\mathrm{d}\,t} + \boldsymbol{R}(\boldsymbol{W}) = 0, \tag{4.16}$$

where $\boldsymbol{R}(\boldsymbol{W})$ is the vector of residuals and $\boldsymbol{M_P}(\boldsymbol{W})$ is a global block diagonal matrix arising from the discretization of the first term in (4.15). Since we use orthonormal basis functions, the matrix $\boldsymbol{M_P}$ reduces to a modified identity matrix with zeros in the diagonal positions which correspond to the degrees of freedom of the pressure. For the solution of (4.16) we employ different time integration schemes, which are specified for each test case in Section 4.3.

4.3 Numerical Tests

In this section the proposed artificial EOS-based Riemann solver is at first assessed on two Riemann problems in Section 4.3.1. The goal is to evaluate the behavior of the artificial EOS Riemann solver when implemented in a first order discontinuous Galerkin (dG $\mathbb{P}^0$) method for the numerical solution of the system (4.4), (4.6), (4.8). Besides, a comparison of two strategies in defining the reference pressure p_0 employed within the local Riemann problem arising at each mesh element face is given.

Then, the space (Section 4.3.2) and time (Section 4.3.3) convergence analysis of a high-order dG solver for the incompressible Navier–Stokes (INS) system is performed for two 2D test cases with known analytical solution. In particular, the dG solver employs the artificial EOS-based Riemann solver to compute the convective numerical fluxes responsible for the velocity-pressure coupling at the inter-element boundaries. We remark that the INS solver does not couple the artificial EOS with the discretized governing equations and, thus, does not consider any time derivative in the divergence constraint.

Finally in Section 4.3.4, the above-mentioned dG solver is used to perform the implicit large eddy simulation (ILES) of the incompressible turbulent flow over periodic hills. The Reynolds number $\mathrm{Re}_h = 10595$ in this test case is based on the hill

height h. Numerical solutions obtained with second and fourth polynomial degree approximations are compared with numerical and experimental results available in the literature.

4.3.1 Riemann Problems

The piece-wise constant initial data for the test Riemann problems are listed in Table 4.1. The first test case (T1) has a jump in pressure while the velocity is constant

Test	p_L	q_{nL}	p_R	q_{nR}
T1	1	0	0.1	0
T2	0.4	−2	0.4	2

Table 4.1: Riemann data for the two test problems T1, T2.

and the second test case (T2) has a jump in velocity with constant pressure. The variable θ is not considered in this analysis since its solution is trivial (4.9).
The exact self-similar solutions of (4.4), (4.6), (4.8) with initial values given by T1 and T2 are computed by means of the artificial EOS Riemann solver developed in this work and reported in Appendix B. The T1-solution consists of a left rarefaction wave and a right shock wave, while the T2-solution consists of two rarefaction waves. The exact solutions are compared with the numerical solutions computed with a first order discontinuous Galerkin (dG $\mathbb{P}^0$) method applied again to (4.4), (4.6), (4.8). Being a Riemann problem-based numerical scheme, the dG method requires to define the Godunov fluxes at the inter-element boundaries, where local Riemann problems arise from the discontinuous nature of the numerical solution. These numerical fluxes are here computed exploiting the artificial EOS Riemann solver. In addition, for each local Riemann problem two strategies for the choice of p_L and p_R within the reference pressure relation (4.8) are investigated. The first one, named *fixed* p_0, considers the initial pressure values defined in the global Riemann problem, i.e., the ones used for the global system of equations. This means that all the inter-element boundaries share the same reference pressure. The second one, denoted as *adaptive* p_0, takes instead the local Riemann problem left and right pressures. Accordingly, each inter-element boundary has its own reference pressure which differs from the global one and can change in time. Although the *fixed* p_0 strategy is the most consistent with respect to the discretized global system, the *adaptive* p_0 strategy has the advantage of not requiring any a priori knowledge of the minimum pressure value within the domain during the whole simulation. Thus it is more general than the *fixed* p_0 approach.

The first numerical computations use a fixed mesh with 100 grid cells on the unit interval $\Omega = [0, 1]$. The initial discontinuity is placed at $x_0 = 0.5$. For the time discretization the BDF2 temporal scheme [31] is employed. Table 4.2 reports the choice made for the artificial compressibility coefficient a_0, the time step size Δt, and the simulation end time T together with the exact pressure $p_\star$ and velocity $q_{n\star}$ solutions within the star region.

Test	a_0	Δt	T	$p_\star$	$q_{n\star}$
T1	1	1.0E − 06	0.2	4.7746086E − 01	3.2161203E − 01
T2	3	1.0E − 06	0.0333	−3.9792459E + 00	0.0000000E + 00

Table 4.2: Artificial sound speed a_0, time step width Δt, simulation end time T, exact star region pressure $p_\star$ and exact star region velocity $q_{n\star}$ for the test Riemann problems from Table 4.1.

Figure 4.2 shows the numerical solutions to the two Riemann problems for the *fixed* p_0 and the *adaptive* p_0 strategies as well as the exact solution. The difference between the numerical solutions obtained with the two strategies is negligible.

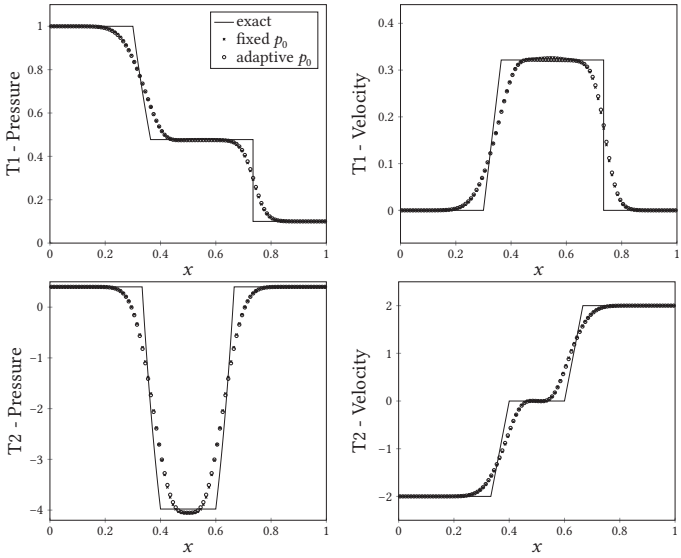

Figure 4.2: Test Riemann problems — Pressure and velocity solutions (left and right) for T1 and T2 Riemann problems (top and bottom).

In additional numerical computations we investigate the qualitative behavior regarding the grid convergence to the exact solution. For this purpose Figure 4.3 depicts the exact solution and the numerical solution obtained on three different grids: grid A with 100 cells, grid B with 1000 cells and grid C with 10000 cells. All results have been obtained with the *adaptive* p_0 strategy. As expected, the accuracy of the exact solution approximation increases with finer grids.

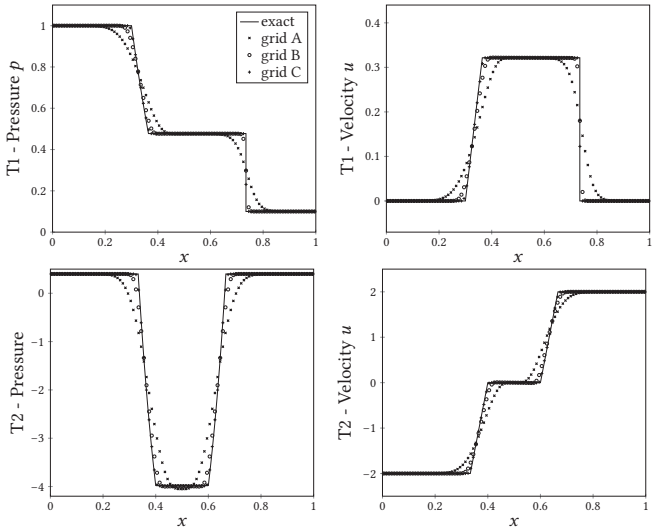

Figure 4.3: Test Riemann problems — Comparison between numerical and exact solutions for three grids with 100 (grid A), 1000 (grid B), and 10000 (grid C) elements.

4.3.2 Kovasznay Test Case

The convergence properties study and the artificial sound speed a_0 sensitivity of our dG solver are performed on the two-dimensional Kovasznay steady flow problem [68]. This test case is an exact solution of the incompressible Navier–Stokes equations and describes the motion behind a grid, consisting of equally-spaced parallel rods or strips. The governing set of equations is thus

$$\begin{aligned} \operatorname{div}(\boldsymbol{v}) &= 0, \\ \partial_t \boldsymbol{v} + \operatorname{div}(\boldsymbol{v} \otimes \boldsymbol{v} + p/\rho_0 \boldsymbol{I}) &= \operatorname{div}(\boldsymbol{S}), \end{aligned} \tag{4.17}$$

where

$$\boldsymbol{S} = 2\nu\left[\frac{1}{2}\left(\nabla\boldsymbol{v} + \nabla\boldsymbol{v}^{\top}\right) - \frac{1}{3}\,\mathrm{div}(\boldsymbol{v})\boldsymbol{I}\right]$$

is the stress tensor and ν the kinematic viscosity. The numerical convective and diffusive fluxes arising from the dG discretization of (4.17) are computed with the exact solution of the proposed artificial EOS-based Riemann solver and the BR2 method of [14], respectively. However, since the minimum pressure value within the domain during the whole simulation is unknown a priori, the *fixed* p_0 strategy cannot be applied.

Numerical solutions have been obtained for $\mathrm{Re} = 40$ and compared with the exact solution

$$\begin{aligned} v_1(x_1, x_2) &= 1 - \mathrm{e}^{\kappa x_1}\cos(2\pi x_2), \\ v_2(x_1, x_2) &= \frac{\kappa \mathrm{e}^{\kappa x_1}}{2\pi}\sin(2\pi x_2), \\ p(x_1, x_2) &= C - \frac{1}{2}\mathrm{e}^{2\kappa x_1}, \end{aligned}$$

where $C \in \mathbb{R}$ is an arbitrary constant and the parameter κ is Reynolds number dependent

$$\kappa = \frac{\mathrm{Re}}{2} - \sqrt{\frac{\mathrm{Re}^2}{4} + 4\pi^2}.$$

The square computational domain is $\Omega = [-0.5, 1.5]\times[0, 2]$ with Dirichlet boundary conditions. The dG space discretization is applied up the the fourth polynomial degree on a sequence of h-refined grids made of 2^{2i}, $i = 3, \ldots, 8$, quadrilateral elements.

Table 4.3 lists the errors computed in L^2-norm and the order of convergence for the pressure, the velocity components and the divergence constraint.

Except for the dG polynomial degree $k = 1$, where the same order of convergence is shared by all the analyzed quantities, the numerical results show a convergence rate of k for the pressure error and $k+1$ for the velocity components error. Besides, it is interesting to note that the divergence constraint is not verified up to the machine error limit, but converges with a rate of k. The same behavior occurs if the numerical convective fluxes are computed with the artificial compressibility based Riemann solver (see [11]).

All the results reported in Table 4.3 have been obtained setting $a_0 = 1$. An analysis of the influence of $a_0 \in [10^{-3}, 10^3]$ is reported in Figure 4.4 for a grid made of 32×32 quadrilateral elements.

The velocity and the divergence constraint errors are in general independent from the choice of a_0. An exception is the dG $\mathbb{P}^1$ solution where for high values of the artificial sound speed the divergence constraint error decreases, while the velocity

Table 4.3: Kovasznay test case — Errors and orders of convergence for pressure, velocity components and divergence constraint. Errors are computed in the L^2-norm on a set of grids of 2^{2i} quadrilateral elements.

	i	$\|err_p\|_{L^2}$	order	$\|err_{v_1}\|_{L^2}$	order	$\|err_{v_2}\|_{L^2}$	order	$\|\text{div } \boldsymbol{v}\|_{L^2}$	order
dG $\mathbb{P}^1$	3	3.35E−2	–	7.86E−2	–	1.09E−2	–	7.42E−2	–
	4	7.34E−3	2.19	1.79E−2	2.14	3.13E−3	1.80	2.62E−2	1.50
	5	1.90E−3	1.95	4.23E−3	2.08	8.55E−4	1.87	8.10E−3	1.69
	6	5.31E−4	1.84	1.03E−3	2.04	2.30E−4	1.89	2.30E−3	1.82
	7	1.50E−4	1.83	2.53E−4	2.02	6.15E−5	1.90	6.18E−4	1.89
	8	4.18E−5	1.84	6.31E−5	2.00	1.62E−5	1.92	1.62E−4	1.93
dG $\mathbb{P}^2$	3	3.07E−3	–	1.06E−2	–	1.55E−3	–	3.12E−2	–
	4	1.02E−3	1.59	1.38E−3	2.95	1.95E−4	2.99	9.66E−3	1.69
	5	3.48E−4	1.56	1.74E−4	2.98	2.72E−5	2.84	2.36E−3	2.03
	6	1.01E−4	1.79	2.20E−5	2.99	3.92E−6	2.80	5.28E−4	2.16
	7	2.67E−5	1.91	2.76E−6	2.99	5.42E−7	2.86	1.21E−4	2.13
	8	6.87E−6	1.96	3.46E−7	3.00	7.17E−8	2.92	2.89E−5	2.06
dG $\mathbb{P}^3$	3	5.84E−4	–	1.21E−3	–	1.87E−4	–	8.61E−3	–
	4	4.82E−5	3.60	8.08E−5	3.91	1.15E−5	4.02	1.22E−3	2.82
	5	4.41E−6	3.45	5.18E−6	3.96	6.37E−7	4.17	1.52E−4	3.01
	6	4.65E−7	3.25	3.27E−7	3.98	3.57E−8	4.16	1.89E−5	3.00
	7	5.45E−8	3.09	2.06E−8	3.99	2.09E−9	4.09	2.38E−6	2.99
	8	6.69E−9	3.03	1.29E−9	4.00	1.25E−10	4.07	2.99E−7	2.99
dG $\mathbb{P}^4$	3	6.35E−5	–	1.00E−4	–	2.21E−5	–	1.05E−3	–
	4	6.70E−6	3.24	3.09E−6	5.02	6.63E−7	5.06	7.02E−5	3.90
	5	5.92E−7	3.50	9.65E−8	5.00	2.32E−8	4.84	4.35E−6	4.01
	6	4.27E−8	3.79	3.03E−9	4.99	7.81E−10	4.89	2.62E−7	4.05
	7	2.83E−9	3.92	9.48E−11	5.00	2.46E−11	4.99	1.61E−8	4.02
	8	1.82E−10	3.96	2.93E−12	5.02	6.21E−13	5.31	1.01E−9	4.00

error increases. The pressure error, instead, always increases linearly for $a_0 \gg 1$. However, it can be seen that such pressure error increase moves towards higher values of a_0 for higher dG polynomial degrees. As a final remark, the numerical results show that it is safe to choose a_0 close to 1 if smooth solutions are expected.

4.3.3 Time Accuracy

In this section an incompressible damped travelling waves test case is used to assess the time integration accuracy of the dG solver used for the previous test case. The time integration schemes considered are the classic implicit second order one stage two steps BDF scheme (BDF2 [31]), the implicit fifth-order eight stages single step ESDIRK scheme (ESDIRK-5(8) [66]), the linearly implicit fifth-order eight stages single step Rosenbrock scheme (ROD5_1 [36, 97]) and the linearly implicit sixth-order six stages two steps Peer scheme (Peer6 [91]). Implementation details of these high order implicit temporal schemes within the current dG framework

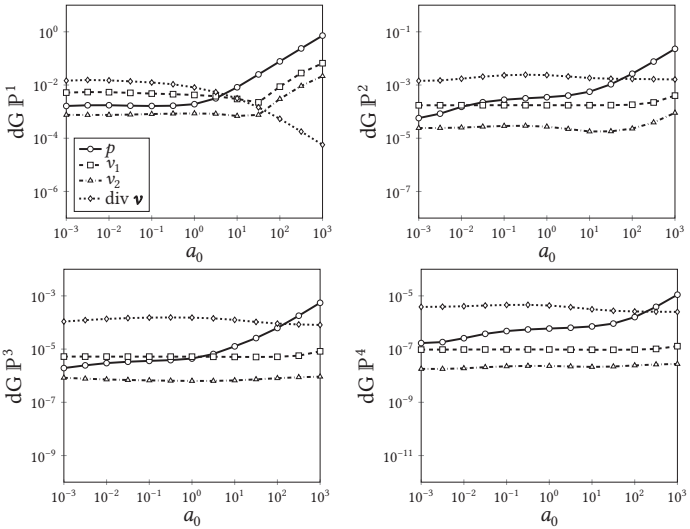

Figure 4.4: Kovasznay test case — Numerical errors on pressure (p), velocity components (v_1, v_2) and divergence constraint (div $\boldsymbol{v}$) with dG $\mathbb{P}^{1\to4}$ solutions on the 32×32 mesh for different artificial speed of sound (a_0) values.

can be found in [10, 79]. The exact solution of traveling damped waves to the incompressible Navier–Stokes equations on the square $\Omega = [0.25, 1.25] \times [0.5, 1.5]$ with periodic boundary reads as:

$$
\begin{aligned}
v_1(x_1, x_2, t) &= 1 + 2\cos(2\pi(x_1 - t))\sin(2\pi(x_2 - t))e^{-8\pi^2 \nu t},\\
v_2(x_1, x_2, t) &= 1 - 2\sin(2\pi(x_1 - t))\cos(2\pi(x_2 - t))e^{-8\pi^2 \nu t},\\
p(x_1, x_2, t) &= 3 - (\cos(4\pi(x_1 - t)) + \cos(4\pi(x_2 - t)))e^{-16\pi^2 \nu t},
\end{aligned}
$$

with $\nu = \mathrm{Re}^{-1} = 1\mathrm{e} - 2$. The initial velocity magnitude and pressure distribution are shown in Figure 4.5.

We compute the solution on the time interval $t \in [0, 1]$ with a fixed time step width Δt.

For the spatial discretization we use a dG $\mathbb{P}^{13}$ approximation on a cartesian mesh with (4×4) square elements. This combination of polynomial degree and mesh might appear unusual. However, we found that this combination for the spatial discretization is the most efficient in order to keep the space discretization error near the double precision machine error, i.e., below the time integration error.

The results are shown in Table 4.4 and illustrated in Figure 4.6. For all consid-

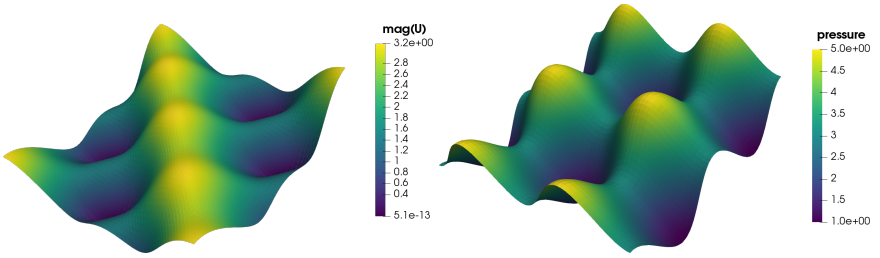

Figure 4.5: Damped travelling waves test case — Initial velocity magnitude (left) and pressure (right) distributions.

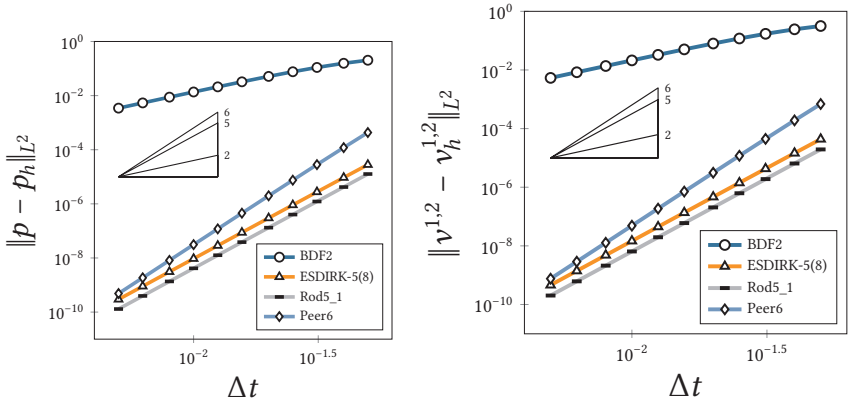

Figure 4.6: Damped travelling waves test case — $dG\,\mathbb{P}^{13}$ solutions with different time integration schemes. L2 norm of the error in pressure and velocity components with respect to the exact solution over time steps.

ered time step sizes, the ROD5_1 scheme shows the best accuracy. Moreover, the expected formal order of convergence for all schemes is verified. Hence, the artificial EOS-based Riemann solver has no effect on the convergence rates for all tested time integration schemes.

4.3.4 The Periodic Hill Test Case

In this section the dG scheme is used to perform an implicit large eddy simulation of the incompressible flow over smoothly constrictions in a plane channel with streamwise periodic boundary conditions. We call this test case therefore the *pe-*

riodic hills test case. Because it is an implicit LES, it does not require any subgrid-scale model [92]. For this class of simulations, the natural dissipation of the space discretization method acts like a subgrid viscosity.
The test case is characterized by the formation of a large re-circulation area behind the hill crest followed by a post-reattachment-recovery region. In the literature many flow studies at different Reynolds numbers and for both compressible and incompressible flow models have been performed, see for example [24, 49, 52, 62, 81]. A full description of the test case, both from the experimental and the numerical point of view, is available on the ERCOFTAC database web page [43].
For hill height $h > 0$, we compute the flow using the h-based Reynolds number $\mathrm{Re}_h = 10595$. The (streamwise) channel length and height are $L_1 = 9h$ and $L_2 = 3.035h$, while and the spanwise extent is $L_3 = 4.5h$. The mesh is made of $64 \times 32 \times 32$ hexahedral elements with quadratic edges (see Figure 4.7). The computations are performed with dG $\mathbb{P}^2$ and $\mathbb{P}^4$ polynomial approximations, resulting in 655 360 and 2 293 760 DOF per equation.

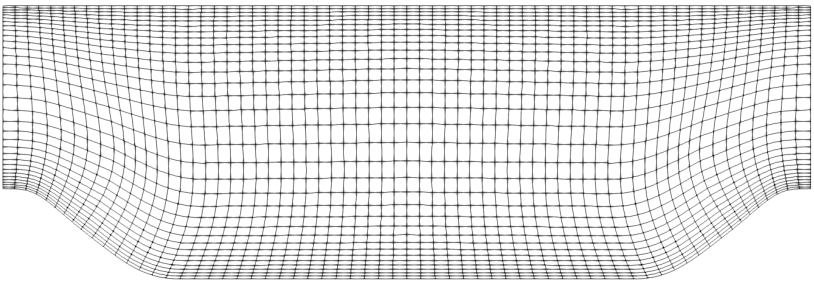

Figure 4.7: Periodic hill — Mesh section.

The domain is periodic both in streamwise and spanwise directions. At the solid upper and lower walls the no-slip boundary condition is imposed. The non-periodic behavior of the pressure distribution is handled by adding the mean pressure gradient as a source term f, imposed uniformly over the whole domain, to the momentum equation in streamwise direction.
The time integration is performed with the most accurate temporal scheme used for the travelling wave test case in Section 4.3.3, i.e., the Rosenbrock scheme Rod5_1. A global adaptive time step strategy is employed in order to increase the code robustness as shown in [85]. By global strategy we mean that every computational cell is advanced with the same time step width, which can vary over time. The resulting average time step width over the whole simulation is $1/202\ CTU$, where $CTU = L_1/v_b$ is the convective time unit. Here, v_b denotes the streamwise bulk velocity. The time averages are taken over a time window of 40 CTU.

During each time step $\Delta t^n = t^{n+1} - t^n$, the constant forcing term $f^{n+\frac{1}{2}}$ is imposed. To derive this forcing term, we modified the approach of [16] to allow for varying time step sizes. The forcing term reads as

$$f^{n+1/2} = f^{n-1/2} + \frac{\zeta}{\sigma^n} \frac{\langle \dot{m} \rangle_{L_1}^{n+1} - (1+\sigma^n)\langle \dot{m} \rangle_{L_1}^{n} + \sigma^n \langle \dot{m} \rangle_{L_1}^{n-1}}{\Delta t^{n-1} \langle A \rangle_{L_1}}, \tag{4.18}$$

where $\zeta = 0.1$ is an user-defined damping factor, $\sigma^n = \Delta t^n / \Delta t^{n-1}$ the time step ratio, $\dot{m}$ and A are the streamwise mass flow rate and the streamwise channel section, and $\langle \bullet \rangle_\Psi$ denotes the integral average operator over the generic set Ψ. Notice that the streamwise averaged mass flow rate at the next step is set according to the prescribed Reynolds number

$$\langle \dot{m} \rangle_{L_1}^{n+1} = \rho_0 v_b A_h = \frac{\rho_0 \nu A_h}{h} \mathrm{Re}_h,$$

where A_h is the streamwise channel section defined at the hill crest. The derivation of (4.18) is stated in detail in the Appendix C.
The results of the simulations are shown in Figure 4.8, where the distribution of the skin friction coefficient

$$\mathrm{C_f} = S_w / (0.5 \rho_0 v_b^2)$$

on the bottom wall is plotted. Here S_w denotes the wall stress. This quantity is usefull to describe turbulent flows, see discussion below and [92, 103].

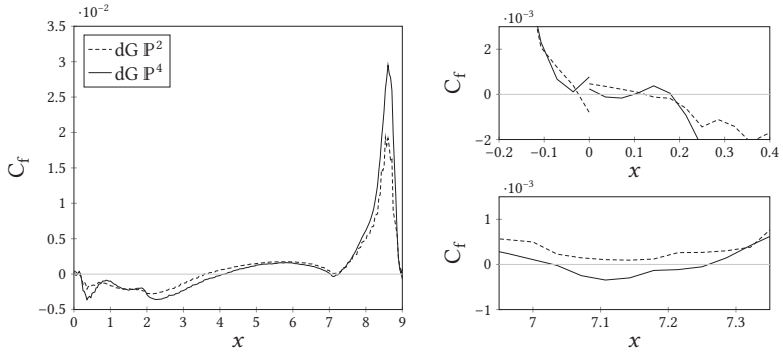

Figure 4.8: Periodic hill — Left: Skin friction coefficient at the bottom wall (a). Top right: Details at the hill crest (b). Bottom right: Details at the base of the second hill (c).

The existence of negative values clearly denotes the presence of a re-circulation bubble after the hill crest. In particular, the positions of the separation and reattachment points are reported in Table 4.5 together with references available in the literature [24, 49, 52].

Our results predict a reattachment point slightly shifted upstream if compared to the reference numerical results. Nevertheless, if compared with the experimental result, the dG $\mathbb{P}^4$ solution provides the lowest gap. The separation point position is in good agreement with all numerical references except for [52], the only case for which the separation occurs at the beginning of the hill crest. However, looking in greater detail right in front of the separation point, a tiny region of negative values of the shear stress is visible both from the dG $\mathbb{P}^2$ and $\mathbb{P}^4$ solution, see Figure 4.8 (b). This result suggests the presence of a precursory separation bubble which has also been found in [49] and [24]. In [52] similar oscillations were observed but with no positive values of the shear stress such that the mean flow remains separated. This behavior explains the upstream position of the separation point. This peculiarity has been attributed to compressibility effects. At the base of the second hill, for $x/h \in [7.03 - 7.26]$, the dG $\mathbb{P}^4$ solution detects a small re-circulation region, see Figure 4.8 (c). This has been found by all the numerical references. After that point the flow is strongly accelerated, leading to a remarkable increase of the shear stress and a peak of the skin friction coefficient $C_f = 1.93 \cdot 10^{-2}$ for dG $\mathbb{P}^2$ and $C_f = 2.95 \cdot 10^{-2}$ $\mathbb{P}^4$, at $x/h \approx 8.60$, right before the hill crest. Eventually, at the hill crest, due to the change of the pressure gradient, the shear stress rapidly drops.

Figure 4.9 and Figure 4.10 show the mean velocity $\langle v_1 \rangle / v_b$, $\langle v_2 \rangle / v_b$, the Reynolds stresses $\langle v_1' v_1' \rangle / v_b^2$, $\langle v_2' v_2' \rangle / v_b^2$, $\langle v_1' v_2' \rangle / v_b^2$, and the turbulent kinetic energy k / v_b^2 profiles obtained with dG $\mathbb{P}^2$ and $\mathbb{P}^4$ at streamwise locations $x_1 = 0.05h$ and $x_1 = 5h$, respectively.

These locations are just in front of the separation point and right after the reattachment point of the re-circulation bubble. For these profiles the average operator is applied both in time and in spanwise direction. Data comparison is performed with experimental results obtained in [95] and numerical results reported in [24], which are available on the ERCOFTAC database [43]. Despite the coarse mesh and the low number of DOF, a good agreement is achieved with respect to the reference data. Notice that the vertical velocity, the Reynolds stresses and the turbulent kinetic energy profiles are about one order of magnitude smaller than the streamwise velocity. Thus, they are amplified when shown in figures for the sake of comprehension. As a consequence, also the discrepancies with respect to reference data are amplified.

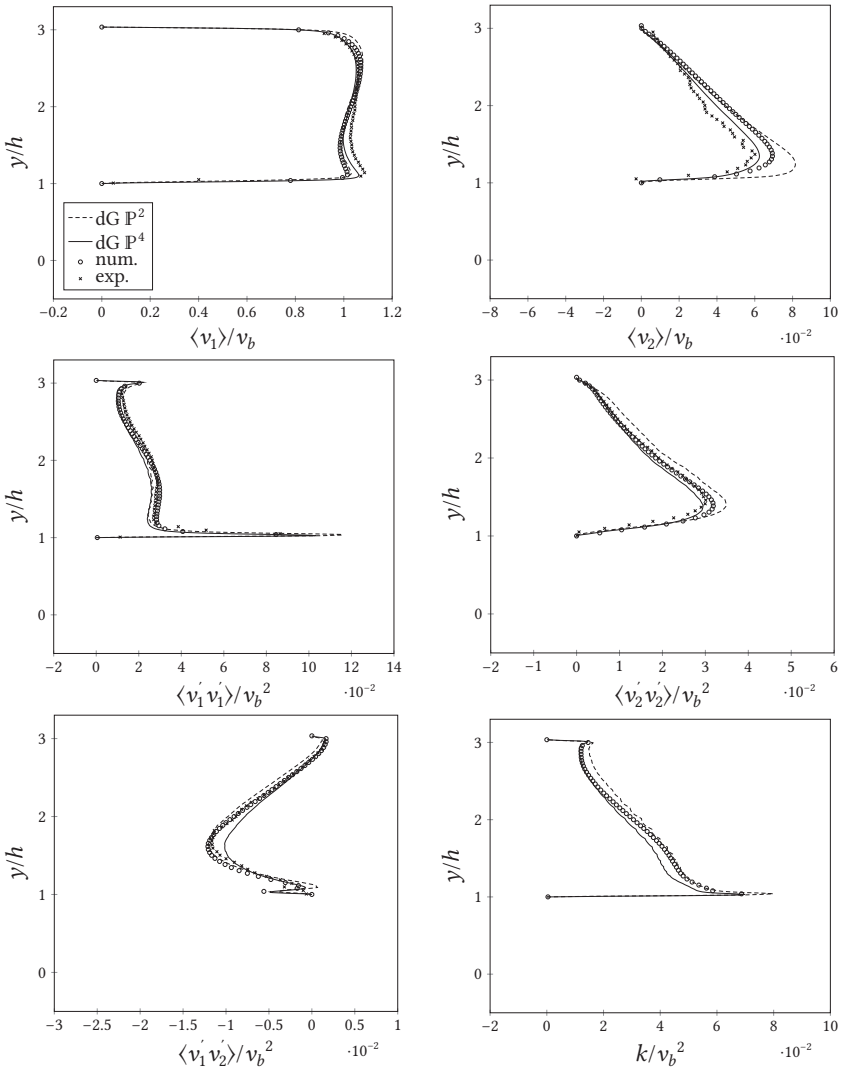

Figure 4.9: Periodic hill — Profiles at position $x/h = 0.05$.

Finally, Figure 4.11 displays the instantaneous Q-criterion both for dG $\mathbb{P}^2$ and dG $\mathbb{P}^4$ solutions. Here,

$$Q \coloneqq \frac{1}{2}\left(\left\|\frac{\nabla \boldsymbol{v} - \nabla \boldsymbol{v}^\top}{2}\right\|^2 - \left\|\frac{\nabla \boldsymbol{v} + \nabla \boldsymbol{v}^\top}{2}\right\|^2\right),$$

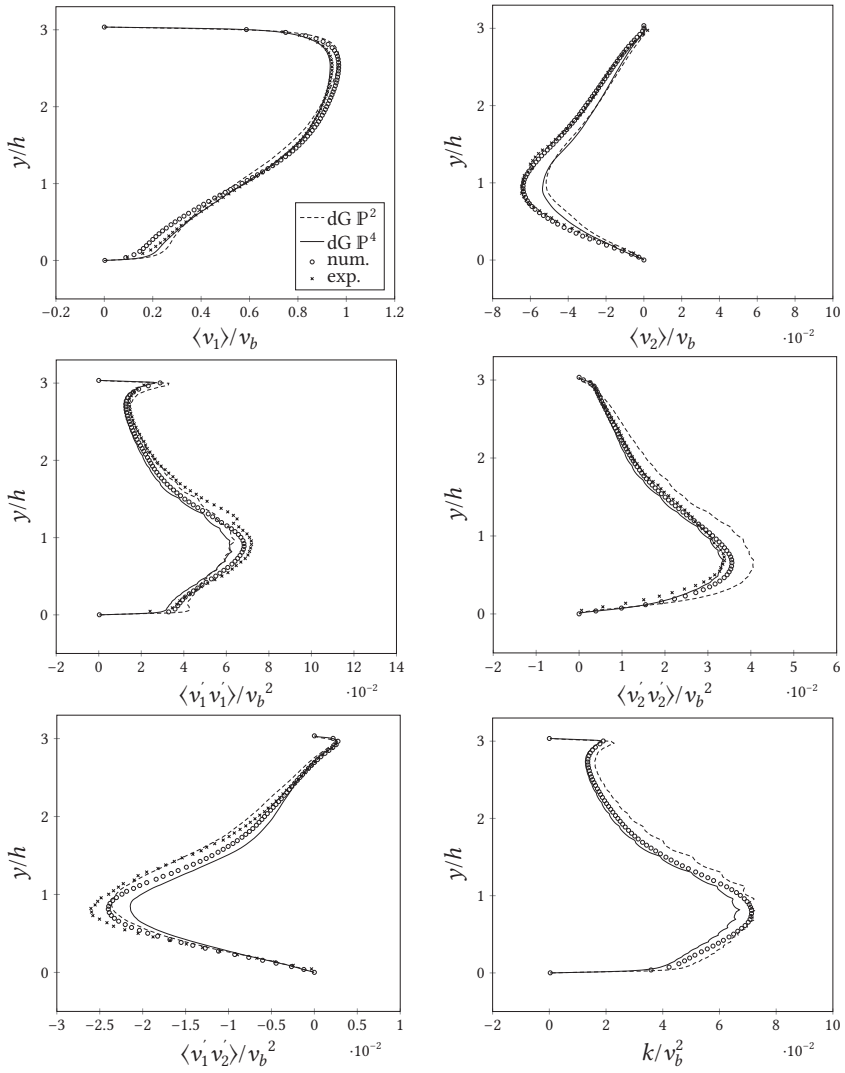

Figure 4.10: Periodic hill — Profiles at position $x/h = 5$.

where $\frac{\nabla \boldsymbol{v} - \nabla \boldsymbol{v}^\top}{2}$ is the vorticity tensor. Vortices are located where $Q > 0$, i.e. vortices are areas where the vorticity magnitude is greater than the magnitude of the rate of strain. In Figure 4.11 we color the isolines $Q = 30$ with the nondimensional

vorticity magnitude $\frac{L_1}{v_b}\|\nabla \times \boldsymbol{v}\|$. The vorticity is a measure for the local spinning motion. It is easy to see that the higher order approximation dramatically improves the resolution of the vortical structures above the hill crest.

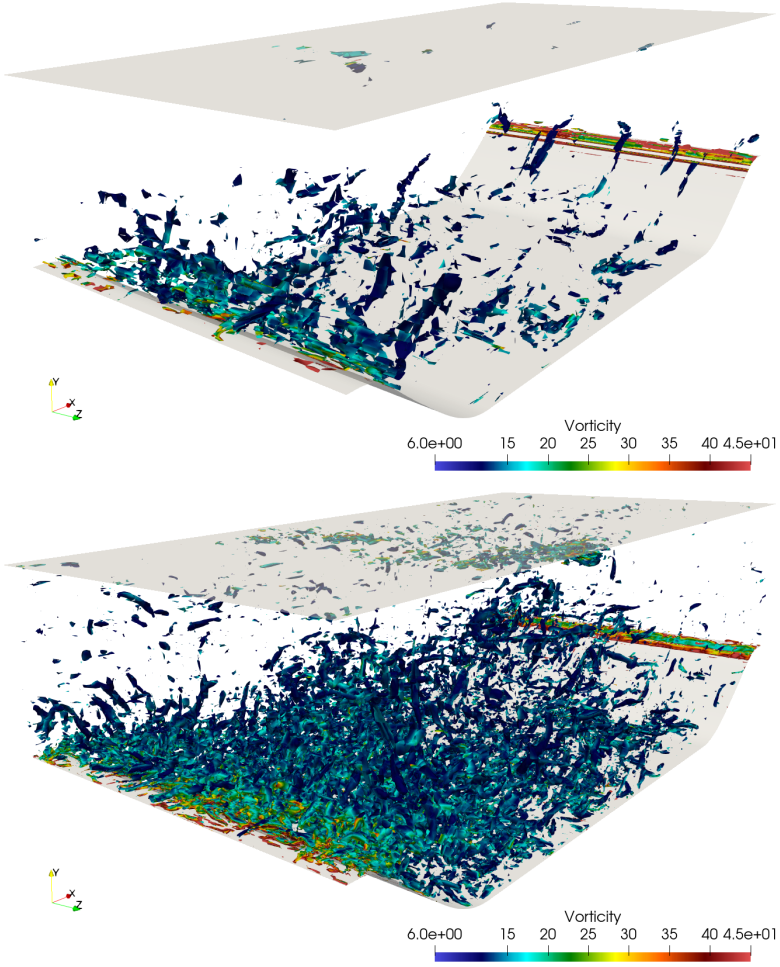

Figure 4.11: Periodic hill — Isosurface of the instantaneous nondimensional Q-criterion ($Q \cdot h^2/v_b^2 = 30$) for the dG $\mathbb{P}^2$ (top) and the dG $\mathbb{P}^4$ (bottom) solutions colored with nondimensional vorticity magnitude.

Table 4.4: Travelling waves test case, $\mathbb{P}^{13}$ solutions with different time integration schemes — L^2 norm of the error with respect to the exact solution for pressure and x_1-,x_2-component of velocity

Scheme	Δt	$\|p - p_h\|_{L^2}$	order$_p$	$\|v^{1,2} - v_h^{1,2}\|_{L^2}$	order$_{v^{1,2}}$
BDF2	T/20	2.027e-01	-	3.157e-01	-
	T/25	1.565e-01	1.160	2.437e-01	1.160
	T/32	1.098e-01	1.437	1.709e-01	1.437
	T/40	7.610e-02	1.641	1.185e-01	1.641
	T/50	5.122e-02	1.774	7.977e-02	1.774
	T/64	3.232e-02	1.865	5.034e-02	1.865
	T/80	2.105e-02	1.921	3.279e-02	1.921
	T/100	1.361e-02	1.954	2.120e-02	1.954
	T/125	8.766e-03	1.973	1.365e-02	1.973
	T/160	5.370e-03	1.985	8.363e-03	1.985
	T/200	3.443e-03	1.992	5.362e-03	1.992
ESDIRK-5(8)	T/20	2.803e-05	-	4.365e-05	-
	T/25	9.337e-06	4.927	1.454e-05	4.927
	T/32	2.750e-06	4.951	4.283e-06	4.951
	T/40	9.078e-07	4.967	1.414e-06	4.967
	T/50	2.989e-07	4.978	4.656e-07	4.978
	T/64	8.733e-08	4.985	1.360e-07	4.985
	T/80	2.868e-08	4.989	4.467e-08	4.989
	T/100	9.415e-09	4.993	1.466e-08	4.992
	T/125	3.089e-09	4.994	4.811e-09	4.995
	T/160	8.996e-10	4.998	1.401e-09	4.996
	T/200	2.951e-10	4.995	4.595e-10	4.997
ROD5_1	T/20	1.265e-05	-	1.949e-05	-
	T/25	4.174e-06	4.970	6.453e-06	4.954
	T/32	1.221e-06	4.978	1.893e-06	4.968
	T/40	4.016e-07	4.984	6.234e-07	4.977
	T/50	1.320e-07	4.988	2.050e-07	4.983
	T/64	3.849e-08	4.991	5.985e-08	4.988
	T/80	1.263e-08	4.993	1.965e-08	4.991
	T/100	4.144e-09	4.995	6.448e-09	4.993
	T/125	1.359e-09	4.996	2.115e-09	4.995
	T/160	3.958e-10	4.997	6.162e-10	4.996
	T/200	1.298e-10	4.995	2.021e-10	4.997
PEER6A	T/20	4.319e-04	-	6.905e-04	-
	T/25	1.196e-04	5.753	1.904e-04	5.773
	T/32	2.814e-05	5.863	4.459e-05	5.880
	T/40	7.497e-06	5.927	1.184e-05	5.941
	T/50	1.982e-06	5.962	3.123e-06	5.974
	T/64	4.525e-07	5.983	7.113e-07	5.993
	T/80	1.187e-07	5.995	1.864e-07	6.003
	T/100	3.112e-08	6.001	4.878e-08	6.007
	T/125	8.153e-09	6.003	1.276e-08	6.009
	T/160	1.851e-09	6.006	2.894e-09	6.011
	T/200	4.855e-10	5.997	7.593e-10	5.995

source	grid elements	model	method	x_s/h	x_r/h
MIGALE	64 × 32 × 32	I	dG $\mathbb{P}^2$ ILES	0.12	3.57
MIGALE	64 × 32 × 32	I	dG $\mathbb{P}^4$ ILES	0.18	4.13
LESOCC [24]	$12.4 \cdot 10^6$	I	FV-CD LES+DSM	0.19	4.69
LESOCC [49]	196 × 128 × 186	I	FV-CD LES+DSM	0.20	4.56
STREAMLES [49]	196 × 128 × 186	I	FV-CD LES+WALE	0.22	4.72
numerical [52]	512 × 256 × 256	C	DRP11 LES	-0.12	4.305
experimental [95]	–	–	LDA-PIV	n/a	4.21

Table 4.5: Periodic hill - Comparison between current results and different studies available in the literature in terms of the nondimensional position of the separation (x_s) and reattachment (x_r) points of the re-circulation bubble. Reference numerical solutions have been obtained for both incompressible (I) and compressible low Mach number (C) flow models. The implemented methods are Finite Volumes (FV) applied with second order central differences (CD) and Finite Differences coupled with a Dispersion-Relation-Preserving optimization procedure (DRP). Subgrid-scale models adopted are the Dynamic Smagorinsky Model (DSM) and the Wall-Adapted Local Eddy-viscosity model (WALE). Experimental studies have been performed with the Laser Doppler Anemometer (LDA) and the Particle Image Velocimetry (PIV) methods. Further details can be found in the respective reference.

5 Conclusion and Outlook

In this third part we studied a phase-field model for the description of liquid–vapor flows with one compressible and one incompressible phase. We introduced the ICNSCH system from [96] and proved an energy inequality for the same. In this way we ensured that the system is thermodynamically consistent. Further, we investigated the effective surface tension in the system, which lead to a new computable expression. In particular, parameters can be tuned to fit surface tension values given by the underlying physics of the simulation.

Moreover, we considered the low Mach limit of the system. We formally showed the convergence to a (quasi-)incompressible model, where both phases are incompressible with different constant densities. For further studies it would be interesting to examine the sharp-interface limit as well. The discretization of an incompressible–compressible SI model is cumbersome, as seen in [84], where coupling strategies in the case of inviscid fluids are derived. The use of a phase-field model could overcome this issues, provided that it has a meaningful SI limit. If such a result was established, one could also investigate the low Mach limit for the corresponding SI limit system. Ideally, this should yield the SI limit system of the LT model.

Additionally, as the main numerical contribution, we presented an idea for a dG discretization of the ICNSCH system based on Godunov fluxes. We introduced the concept of artificial EOS modification in order to derive a Riemann problem solution to define the Godunov fluxes. The approach was then implemented in a simpler setting, namely for single-phase incompressible flow. We showed that the artificial EOS modification preserves the convergence properties of the dG scheme, both in space and time. Furthermore, the approach is also suited for complex simulations, as we demonstrated in the 3D ILES periodic hill test case, where the obtained results showed good agreement with experimental results and other numerical results from the literature. However, this is merely a first step towards the dG discretization of the ICNSCH system. For future studies, it should be con-

sidered how to deal with the higher-order terms of the ICNSCH system in order to obtain the dG discretization. In particular the discretization of the capillary tensor is not straightforward.

Appendix

A The Wave Pattern Violation

The Riemann problem solution based on the split multi-dimensional artificial compressibility set of equations (4.3) predicts a shock wave speed equal to

$$s^{\pm} = \frac{q_{nX} + q_{n\star}}{2} \pm \sqrt{\left(\frac{q_{nX} + q_{n\star}}{2}\right)^2 + a_0^2},$$

where the negative sign (−) is for a left shock ($X = L$) while the positive sign (+) is for a right shock ($X = R$), see Appendix B below. The contact discontinuity speed is instead equal to the star region velocity $q_{n\star}$. If the two speeds are equated, a critical value of the artificial compressibility can be found and reads for both shocks $s^{\pm}$ as

$$\overline{a}_{0X} = \sqrt{-q_{n\star} q_{nX}}.$$

It is clear that, when $q_{n\star}$ and q_{nX} have the same sign, the critical value is imaginary and the occurrence of a contact wave as fast as the shock is impossible. However, except for the requirements of an entropy satisfying shock, i.e.

$$\begin{cases} q_{n\star} < q_{nL} & \text{for a left shock} \\ q_{n\star} > q_{nR} & \text{for a right shock} \end{cases},$$

no a-priori restrictions are imposed on the velocity signs. As a consequence, when the two velocities have opposite sign the critical artificial compressibility becomes real. If this is the case for the left or right shock, setting an artificial compressibility smaller than this critical $\overline{a}_{0X}$, leads the Riemann solver to predict a contact wave which overtakes the shock, i.e., $|q_{n\star}| \geq |s^{\pm}|$. Thus, it violates the wave pattern postulated in Figure 4.1 on which the Riemann solver itself is derived. In order to regain the correct wave pattern, the value of a_0 must be increased such that in presence of the shock it holds

$$a_0 > \overline{a}_{0X}.$$

Interestingly, increasing the artificial compressibility reduces the perturbation on the set of equations thus approaching the incompressible regime.
A simple example in which the wave pattern violation occurs is given in Table 5.1.

i	p_L	$\overline{a}_{0R}$
−2	1.01	-
−1	1.1	1.4350004E−01
0	2	2.9676758E−01
1	11	5.5068316E−01
2	101	9.9289835E−01
3	1001	1.7739369E+00

Table 5.1: Wave pattern violation - Critical artificial compressibility for different left pressure values ($p_L = p_R + 10^i$, $i = -2, -1, \dots, 3$) with given right pressure ($p_R = 1$) and velocities ($v_L = v_R = -0.1$).

Here, the initial velocities and the initial right pressure are set as follows: $q_{nL} = q_{nR} = -1$, $p_R = 1$. The initial left pressure is then modified according to the relation $p_L = p_R + 10^i$, with $i = -2, -1, \dots, 3$. The wave pattern arising from these Riemann problems predicts as external acoustic waves a left rarefaction and a right shock. Looking at the right shock, a simple numerical investigation by means of the artificial compressibility based Riemann solver (see [11, 42]) reveals that for the minimum left pressure considered ($i = -2$) no critical artificial compressibility is found while for the remaining p_L values the critical condition exists. Besides, for higher pressure jumps the $\overline{a}_{0R}$ value grows, thus making the condition more severe.

B The Artificial EOS-Based Riemann Solver

In order to derive the exact solution to (4.4)–(4.6) with initial values (4.2) we start from the work of LeVeque [72] for the isothermal compressible flows.
As pointed out in Section 4.1.2 the pressure-velocity solution within the star region can be found independently from the variable $\boldsymbol{\theta}$. Accordingly, the reduced set of equation is

$$\frac{\partial \boldsymbol{U}}{\partial t} + \frac{\partial \boldsymbol{F}(\boldsymbol{U})}{\partial x} = 0,$$

with the vector of unknowns $\boldsymbol{U}$ and the flux $\boldsymbol{F}$

$$\boldsymbol{U} = \begin{pmatrix} \rho \\ \rho q_n \end{pmatrix}, \quad \boldsymbol{F}(\boldsymbol{U}) = \begin{pmatrix} \rho q_n \\ \rho q_n^2 + p \end{pmatrix}. \tag{5.1}$$

Recalling the artificial EOS (4.6), the flux Jacobian matrix is given by

$$\boldsymbol{A} = \frac{\mathrm{d}\,\boldsymbol{F}(\boldsymbol{U})}{\mathrm{d}\,\boldsymbol{U}} = \begin{pmatrix} 0 & 1 \\ a_0^2 - q_n^2 & 2q_n \end{pmatrix},$$

with eigenvalues

$$\boldsymbol{\lambda} = \begin{pmatrix} \lambda^- \\ \lambda^+ \end{pmatrix} = \begin{pmatrix} q_n - a_0 \\ q_n + a_0 \end{pmatrix}.$$

The resulting left and right eigenvector matrices $\boldsymbol{L}, \boldsymbol{R}$ read as

$$\boldsymbol{L} = \begin{pmatrix} \lambda^+ & -1 \\ \lambda^- & -1 \end{pmatrix}, \quad \boldsymbol{R} = \frac{1}{2a_0} \begin{pmatrix} 1 & -1 \\ \lambda^- & -\lambda^+ \end{pmatrix}.$$

Since $a_0 > 0$ there are two distinct eigenvalues $\lambda^- < \lambda^+$ and the corresponding system is hyperbolic. The wave pattern predicts two waves which can be either shocks or rarefactions. Solution variations across these waves are computed by means of the Rankine–Hugoniot jump conditions and Riemann invariants, respectively.

B.1 Rarefaction Waves and Riemann Invariants

The solution variation across a rarefaction wave can be obtained with help of Riemann invariants

$$\boldsymbol{\Gamma} = \boldsymbol{\Gamma}(\boldsymbol{U}) = \begin{pmatrix} \Gamma^-(\boldsymbol{U}) \\ \Gamma^+(\boldsymbol{U}) \end{pmatrix}.$$

These quantities are related to the left eigenvector matrix by the following definition

$$\frac{\mathrm{d}\,\boldsymbol{\Gamma}}{\mathrm{d}\,\boldsymbol{U}} = \boldsymbol{L}.$$

Thus,

$$\mathrm{d}\,\boldsymbol{\Gamma} = \mathrm{d}\begin{pmatrix} \Gamma^- \\ \Gamma^+ \end{pmatrix} = \begin{pmatrix} \lambda^+\,\mathrm{d}\,\rho - \mathrm{d}(\rho q_n) \\ \lambda^-\,\mathrm{d}\,\rho - \mathrm{d}(\rho q_n) \end{pmatrix} = \begin{pmatrix} a_0\,\mathrm{d}\,\rho - \rho\,\mathrm{d}\,q_n \\ -a_0\,\mathrm{d}\,\rho - \rho\,\mathrm{d}\,q_n \end{pmatrix}.$$

As a peculiar feature, the Riemann invariants Γ^- and Γ^+ assume constant values along the *characteristic curves*

$$C^-(x,t) = x + \lambda^- t,$$

$$C^+(x,t) = x + \lambda^+ t.$$

Accordingly, it follows

$$\begin{aligned} \mathrm{d}\,\Gamma^- &= a_0\,\mathrm{d}\,\rho - \rho\,\mathrm{d}\,q_n = 0 \qquad \text{on } C^-, \\ \mathrm{d}\,\Gamma^+ &= -a_0\,\mathrm{d}\,\rho - \rho\,\mathrm{d}\,q_n = 0 \qquad \text{on } C^+. \end{aligned}$$

By integration the Riemann invariants are

$$\begin{aligned} \Gamma^- &= \rho \mathrm{e}^{-\frac{q_n}{a_0}} = \text{const.} \qquad \text{on } C^-, \\ \Gamma^+ &= \rho \mathrm{e}^{\frac{q_n}{a_0}} = \text{const.} \qquad \text{on } C^+. \end{aligned}$$

Applying the artificial EOS (4.6) we obtain

$$\Gamma^- = \left(p - p_0 + \rho_0 a_0^2\right) \mathrm{e}^{-\frac{q_n}{a_0}} = \text{const.} \qquad \text{on } C^-, \tag{5.2}$$

$$\Gamma^+ = \left(p - p_0 + \rho_0 a_0^2\right) \mathrm{e}^{\frac{q_n}{a_0}} = \text{const.} \qquad \text{on } C^+. \tag{5.3}$$

We point out that a left rarefaction wave is crossed by the C^+ characteristic, while a right rarefaction wave by C^- characteristic.

B.2 Shock Waves and Rankine–Hugoniot Jump Conditions

Riemann invariants cannot be used to find the solution variation across a shock, since they are not constant when characteristic curves cross this type of wave. Instead, we use the Rankine–Hugoniot conditions.

We denote the jump of the conservative variables and the flux jump across a shock as $\Delta \boldsymbol{U} = \boldsymbol{U}_2 - \boldsymbol{U}_1$ and $\Delta \boldsymbol{F} = \boldsymbol{F}(\boldsymbol{U}_2) - \boldsymbol{F}(\boldsymbol{U}_1)$, respectively. Here, the subscripts 1 and 2 denote the states at the left and right of the shock. Then, the Rankine–Hugoniot conditions state that

$$\Delta \boldsymbol{F} = s \Delta \boldsymbol{U}, \tag{5.4}$$

where s is the shock speed. Applying (5.4) to (5.1) yields

$$\Delta\left(\rho q_n\right) = s \Delta \rho, \tag{5.5}$$

$$\Delta\left(\rho q_n^2\right) + \Delta p = s \Delta\left(\rho q_n\right). \tag{5.6}$$

In addition, the Lax entropy condition requires

$$\begin{aligned} \lambda_1(\boldsymbol{U}_1) &= q_{n1} - a_0 > s^- > q_{n2} - a_0 = \lambda_1(\boldsymbol{U}_2), \\ \lambda_3(\boldsymbol{U}_1) &= q_{n1} + a_0 > s^+ > q_{n2} + a_0 = \lambda_3(\boldsymbol{U}_2). \end{aligned} \tag{5.7}$$

This assures that for a shock the characteristic lines are always convergent and there is only compression.
From (5.7) it follows

$$\Delta q_n < 0. \tag{5.8}$$

From the artificial EOS (4.6) we have $\Delta p = a_0^2 \Delta\rho$. Now, with (5.5) an expression for the shock speed s is obtained. By substituting it in (5.6) it follows that

$$\frac{\Delta q_n}{\Delta\rho} = \pm \frac{a_0}{\sqrt{\rho_1 \rho_2}}. \tag{5.9}$$

The shock speed is then computed from (5.5) and (5.9) as

$$s^{\pm} = q_{n1} + \rho_2 \frac{\Delta q_n}{\Delta\rho} = q_{n1} \pm a_0 \sqrt{\frac{\rho_2}{\rho_1}}, \tag{5.10}$$

or alternatively as

$$s^{\pm} = q_{n2} + \rho_1 \frac{\Delta q_n}{\Delta\rho} = q_{n2} \pm a_0 \sqrt{\frac{\rho_1}{\rho_2}}. \tag{5.11}$$

Here, due to the Lax condition (5.7), the negative sign (−) is for the left shock, while the positive sign (+) is for the right shock. Notice that $s^- < q_{ni}$ and $s^+ > q_{ni}$ for $i = 1, 2$. By substituting (5.10) and (5.11) in the entropy condition (5.7) we obtain

$$\begin{cases} q_{n1} - a_0 > q_{n1} - a_0 \sqrt{\frac{\rho_2}{\rho_1}} = q_{n2} - a_0 \sqrt{\frac{\rho_1}{\rho_2}} > q_{n2} - a_0 & \text{for a left shock,} \\ q_{n1} + a_0 > q_{n2} + a_0 \sqrt{\frac{\rho_1}{\rho_2}} = q_{n1} + a_0 \sqrt{\frac{\rho_2}{\rho_1}} > q_{n2} - a_0 & \text{for a right shock .} \end{cases}$$

This is true iff

$$\begin{cases} \Delta\rho > 0 & \text{for a left shock} \\ \Delta\rho < 0 & \text{for a right shock.} \end{cases}$$

We perform a change of variable by $z = \sqrt{\rho_2/\rho_1}$. This transforms (5.9) to the quadratic equation

$$\pm z^2 - \frac{\Delta q_n}{a_0} z \pm (-1) = 0. \tag{5.12}$$

By construction, both solutions of (5.12) for each shock are real, but only one of them is positive, i.e.

$$\sqrt{\frac{\rho_2}{\rho_1}} = z = \pm\frac{\Delta q_n}{2a_0} + \sqrt{\left(\frac{\Delta q_n}{2a_0}\right)^2 + 1}.$$

With help of (5.10) the shock speed is computed as

$$s^{\pm} = \frac{q_{n2} + q_{n1}}{2} \pm \sqrt{\left(\frac{q_{n2} - q_{n1}}{2}\right)^2 + a_0^2}. \tag{5.13}$$

The same relation can be found defining $z = \sqrt{\rho_1/\rho_2}$ within (5.9) and using (5.11). Notice that the subscripts 1 and 2 can be switched without modifying the relation. Eventually, thanks to the artificial EOS (4.6) the pressure relation can be obtained from (5.10)

$$p_2 = p_0 - \rho_0 a_0^2 + \left(p_1 - p_0 + \rho_0 a_0^2\right)\left(\frac{s^{\pm} - q_{n1}}{a_0}\right)^2, \tag{5.14}$$

or alternatively from (5.11)

$$p_1 = p_0 - \rho_0 a_0^2 + \left(p_2 - p_0 + \rho_0 a_0^2\right)\left(\frac{s^{\pm} - q_{n2}}{a_0}\right)^2. \tag{5.15}$$

Recall that (−) and (+) of the symbol (±) are referred to a left and a right shock wave, respectively. Notice that (5.14) and (5.15) are the same relation with switched subscripts.

B.3 The Star Region Solution

Finding the solution of the Riemann problem means computing the star region pressure $p_\star$ and velocity $q_{n\star}$. Starting from the initial state given by the Riemann problem, the initial density values (ρ_L,ρ_R) are defined by the artificial EOS (4.6). Then the star region solution is found by exploiting the Riemann invariants and the Rankine–Hugoniot conditions across rarefaction (superscript R) and shock (superscript S) waves, respectively.

- If the left wave is a rarefaction, then the Γ^+ Riemann invariant (5.3) is preserved and thus

$$p_\star = p_0 - \rho_0 a_0^2 + \rho_L a_0^2 f_L^R, \tag{5.16}$$

with

$$f_L^R(q_{nL}, q_{n\star}) = e^{\frac{q_{nL} - q_{n\star}}{a_0}}.$$

- If the left wave is a shock, then from (5.14) we have

$$p_\star = p_0 - \rho_0 a_0^2 + \rho_L a_0^2 f_L^S, \tag{5.17}$$

with

$$f_L^S(q_{nL}, q_{n\star}) \coloneqq \left(\frac{q_{nL} - s_L^-}{a_0}\right)^2,$$

and

$$s_L^- = \frac{q_{nL} + q_{n\star}}{2} - \sqrt{\left(\frac{q_{nL} - q_{n\star}}{2}\right)^2 + a_0^2}.$$

- If the right wave is a rarefaction, then the Γ^- Riemann invariant (5.2) is conserved, which leads to

$$p_\star = p_0 - \rho_0 a_0^2 + \rho_R a_0^2 f_R^R, \tag{5.18}$$

with

$$f_R^R(q_{nR}, q_{n\star}) \coloneqq e^{\frac{q_{n\star} - q_{nR}}{a_0}}.$$

- If the right wave is a shock, then (5.14) yields

$$p_\star = p_0 - \rho_0 a_0^2 + \rho_R a_0^2 f_R^S, \tag{5.19}$$

with

$$f_R^S(q_{nR}, q_{n\star}) \coloneqq \left(\frac{s_R^+ - q_{nR}}{a_0}\right)^2,$$

and

$$s_R^+ = \frac{q_{n\star} + q_{nR}}{2} + \sqrt{\left(\frac{q_{n\star} - q_{nR}}{2}\right)^2 + a_0^2}.$$

The cases (5.16), (5.17), (5.18) and (5.19) can be written in the compact form

$$F(p_L, q_{nL}, p_R, q_{nR}, q_{n\star}) = \rho_R a_0^2 f_R - \rho_L a_0^2 f_L = 0, \tag{5.20}$$

where f_R and f_L are set according to the type of the acoustic waves

$$\begin{aligned} f_R(q_{nR}, q_{n\star}) &\coloneqq \begin{cases} f_R^S(q_{nR}, q_{n\star}) & q_{nR} < q_{n\star} \\ f_R^R(q_{nR}, q_{n\star}) & \text{otherwise,} \end{cases} \\ f_L(q_{nL}, q_{n\star}) &\coloneqq \begin{cases} f_L^S(q_{nL}, q_{n\star}) & q_{n\star} < q_{nL} \\ f_L^R(q_{nL}, q_{n\star}) & \text{otherwise.} \end{cases} \end{aligned} \tag{5.21}$$

Here, the $q_{nR} < q_{n\star}$ and $q_{n\star} < q_{nL}$ inequalities satisfy the entropy condition (5.8) for the right and left shock, respectively.
The only unknown in the nonlinear equation (5.20) is the star region velocity $q_{n\star}$. Its value can be found using an iterative method such as Newton's method. At each solution iteration the function F of (5.20) is the one appropriate for the wave pattern defined by (5.21). As initial guess of the iterative process we suggest to use the average velocity between the initial left and right values. Interestingly, this choice is effective in presence of strong rarefactions, where it is known the iterative process may fail [101]. In particular, in case of rarefaction waves of the same strength, this initial guess corresponds to using the two-rarefaction solution. Knowing $q_{n\star}$, the star region pressure can be computed as

$$p_\star = p_0 - \rho_0 a_0^2 + \frac{\rho_R f_R + \rho_L f_L}{2} a_0^2.$$

B.3.1 Reference pressure

The only unknown parameter in the solution derivation is the reference pressure p_0. As pointed out in Section 4.1.2 its value must be defined carefully, otherwise negative values of the density may show up during the solution of the Riemann problem. Fortunately, the simple following choice proves to ensure the density positivity

$$p_0 = \min(p_L, p_R).$$

In fact, with this choice it is easy to see from the artificial EOS (4.6) that both ρ_L and ρ_R are positive. Besides, since the star region density is defined as

$$\rho_\star = \rho_L f_L = \rho_R f_R,$$

and since f_L and f_R are positive functions, then it follows that the star region density is also positive.

B.3.2 Wave speeds

As last step to define the Riemann solution completely, the wave speeds S must be determined.

- For a rarefaction wave there are two important wave speeds, namely the ones of the head and the tail of the fan. These speed values are given by the eigenvalues at the states on either side of the rarefaction, that is

$$S_L^{\text{head}} = \lambda_L^-, \qquad S_L^{\text{tail}} = \lambda_\star^-,$$
$$S_R^{\text{head}} = \lambda_R^+, \qquad S_R^{\text{tail}} = \lambda_\star^+.$$

The speed inside the expansion fan changes linearly between the head and the tail values. Knowing this speed, the solution inside the fan is obtained by the Riemann invariants associated with the crossing characteristic curves C.

- For a shock wave the wave speed is given by (5.13), i.e.

$$S_L = s_L^-, \qquad S_R = s_R^+.$$

C The Forcing Term

The periodic hill test case has only no-slip wall and periodic boundary conditions. In order to sustain the flow through the channel, an uniform forcing term f in the stream direction x_1 as an additional boundary condition is introduced. This forcing term mimics the pressure gradient between consecutive hills. The streamwise momentum equation in the integral form for the whole volume V reads

$$\int_V \frac{\partial(\rho v_1)}{\partial t} \, \mathrm{d}\boldsymbol{x} = \int_{S_w} S_{x_1} \, \mathrm{d}\boldsymbol{x} + \int_V f \, \mathrm{d}\boldsymbol{x},$$

with the component S_{x_1} in the stream direction x_1 of the stress on the wall surfaces S_w. The convective flux contribution vanishes because of the periodicity condition of all no-wall boundaries. Since V is fixed, the partial time derivative can be moved outside the integral and become a total derivative. Moreover, we define the integral average operator $\langle\cdot\rangle_\Psi$ over the generic set Ψ. Then,

$$\frac{\mathrm{d}\langle\rho v_1\rangle_V}{\mathrm{d}\, t} = \frac{S_w}{V}\langle S_{x_1}\rangle_{S_w} + f. \tag{5.22}$$

Due to the uniform nature of the forcing term it is clear that $f = \langle f\rangle_V$.
One way to define the forcing term is to exploit the fact that the flow problem is statistically stationary [92]. Indeed, by applying the time integral average over a sufficiently long time period T on (5.22) it follows

$$\langle f\rangle_T = -\frac{S_w}{V}\langle S_{x_1}\rangle_{S_w \times T}.$$

This relation is commonly used for the channel flow test case, where $S_w/V = 1/\delta$, with the channel semi-height δ. However, it has two main drawbacks:

1. It cannot be applied to test cases where the target-averaged streamwise wall stress $\langle S_{x_1}\rangle_{S_w \times T}$ is not known a-priori.

2. It can lead to inaccuracies in the averaged velocity profiles prediction when modeling errors or numerical errors occur in the calculation of the near-wall viscous stress [16].

Another way to obtain f consists of deriving (5.22) with respect to time and neglecting the stress contribute such that

$$\frac{1}{\langle A\rangle_{L_1}} \frac{\mathrm{d}^2\langle \dot{m}\rangle_{L_1}}{\mathrm{d}\,t^2} = \frac{\mathrm{d}\,f}{\mathrm{d}\,t}, \tag{5.23}$$

where

$$\langle \rho v_1\rangle_V = \frac{1}{V}\int_{L_1}\int_{A(x_1)} \rho v_1 \,\mathrm{d}A'\,\mathrm{d}x_1 = \frac{1}{\langle A\rangle_{L_1}}\langle \dot{m}\rangle_{L_1},$$

with the streamwise average $\langle \dot{m}\rangle_{L_1}$ of the mass flow rate and of the channel section $\langle A\rangle_{L_1} = V/L_1$. Here, L_1 is the streamwise channel length. Using finite differences of second order in the neighborhood of the current time t^n leads to

$$f^{n+1/2} = f^{n-1/2} + \zeta \frac{\langle \dot{m}\rangle_{L_1}^{n+1} - 2\langle \dot{m}\rangle_{L_1}^{n} + \langle \dot{m}\rangle_{L_1}^{n-1}}{\Delta t \langle A\rangle_{L_1}}. \tag{5.24}$$

This formula has been first proposed by Benocci and Pinelli [16]. Knowing the average mass flow rates $\langle \dot{m}\rangle_{L_1}^{n}, \langle \dot{m}\rangle_{L_1}^{n-1}$ at previous times and the forcing term $f^{n-1/2}$ imposed during the last step $\Delta t = t^n - t^{n-1}$, the resulting forcing term $f^{n+1/2}$, kept constant during the current time step $\Delta t = t^{n+1} - t^n$, is function of the averaged mass flow rate at the next time $\langle \dot{m}\rangle_{L_1}^{n+1}$. This rate is set according to the prescribed Reynolds number Re. In (5.24), the user-defined damping factor $\zeta \in [0.1, 1]$ has been added. It is useful to control the temporal oscillation of the forcing term when dealing with very large time steps.

The advantage of the relation of Benocci and Pinelli is that it does not require any prior knowledge of the stress. Moreover, the forcing term is no more constant in time and can adapt to ensure the desired flow properties. However, this relation cannot be used when the time integration is coupled with an adaptive time step strategy, as it has been considered in the current work. In such a case Taylor expansions allow to write the second order derivative of the averaged mass flow rate as

$$\left.\frac{\mathrm{d}^2\langle \dot{m}\rangle_{L_1}}{\mathrm{d}\,t^2}\right|^n = 2\frac{\langle \dot{m}\rangle_{L_1}^{n+1} - \langle \dot{m}\rangle_{L_1}^{n}}{(\Delta t^n)^2} - \frac{2}{\Delta t^n}\left.\frac{\mathrm{d}\langle \dot{m}\rangle_{L_1}}{\mathrm{d}\,t}\right|^n + O(\Delta t^n),$$

where the first order time derivative can be expressed with backward differences

$$\left.\frac{\mathrm{d}\langle\dot{m}\rangle_{L_1}}{\mathrm{d}\,t}\right|^n = \frac{\langle\dot{m}\rangle_{L_1}^n - \langle\dot{m}\rangle_{L_1}^{n-1}}{\Delta t^{n-1}} + \frac{\Delta t^{n-1}}{2}\left.\frac{\mathrm{d}^2\langle\dot{m}\rangle_{L_1}}{\mathrm{d}\,t^2}\right|^n + O(\Delta t^{n-1^2}),$$

such that

$$\left.\frac{\mathrm{d}^2\langle\dot{m}\rangle_{L_1}}{\mathrm{d}\,t^2}\right|^n = 2\frac{\langle\dot{m}\rangle_{L_1}^{n+1} - (1+\sigma^n)\langle\dot{m}\rangle_{L_1}^n + \sigma^n\langle\dot{m}\rangle_{L_1}^{n-1}}{\sigma^n(1+\sigma^n)(\Delta t^{n-1})^2} + O(\Delta t^n). \tag{5.25}$$

Here, $\Delta t^n = t^{n+1} - t^n$ is the time step width and $\sigma^n = \Delta t^n/\Delta t^{n-1}$ the time step ratio at time t^n. The first order time derivative of the forcing term is written as

$$\left.\frac{\mathrm{d}\,f}{\mathrm{d}\,t}\right|^n = \frac{f^{n+1/2} - f^{n-1/2}}{\Delta t^*} + O(\Delta t^*). \tag{5.26}$$

Substituting (5.25) and (5.26) in (5.23) and neglecting terms greater than first order, the forcing term relation for an adaptive time step is

$$f^{n+1/2} = f^{n-1/2} + g(\sigma^n)\frac{\langle\dot{m}\rangle_{L_1}^{n+1} - (1+\sigma^n)\langle\dot{m}\rangle_{L_1}^n + \sigma^n\langle\dot{m}\rangle_{L_1}^{n-1}}{\Delta t^{n-1}\langle A\rangle_{L_1}},$$

where the function g depends on the choice of Δt^* in (5.26)

$$g(\sigma^n) = \begin{cases} \dfrac{2\zeta}{\sigma^n(1+\sigma^n)}, & \text{if } \Delta t^* = \Delta t^{n-1}, \\ \dfrac{2\zeta}{1+\sigma^n}, & \text{if } \Delta t^* = \Delta t^n, \\ \dfrac{\zeta}{\sigma^n}, & \text{if } \Delta t^* = \dfrac{\Delta t^n + \Delta t^{n-1}}{2}. \end{cases} \tag{5.27}$$

Each choice of Δt^* is consistent with respect to the constant time step case, i.e., $g = \zeta$ for $\sigma^n = 1$ such that (5.24) is recovered. The main differences appear when limit values of the time step ratio $\sigma^n \in (0, \infty)$ are considered. However, the adaptive algorithm can be designed to avoid excessive variations of the time step (see [85]) such that the forcing terms resulting from the three choices are comparable. In this work the third definition of g in (5.27) has been implemented, since it has an intermediate behavior compared to the other two.

List of Figures

Bibliography

[1] I. Aavatsmark. An introduction to multipoint flux approximations for quadrilateral grids. *Comput. Geosci.* 6.3-4 (2002), pp. 405–432.

[2] H. Abels, H. Garcke, and G. Grün. Thermodynamically consistent, frame indifferent diffuse interface models for incompressible two-phase flows with different densities. *Math. Models Methods Appl. Sci.* 22.3 (2012), p. 1150013.

[3] S. Ackermann, C. Bringedal, and R. Helmig. Multi-scale three-domain approach for coupling free flow and flow in porous media including droplet-related interface processes. *J. Comput. Phys.* 429 (2021), p. 109993.

[4] S. Ackermann, R. Helmig, L. Ostrowski, and C. Rohde. "A multi-scale approach for drop detachment in a coupled free-flow/porous-medium-flow system". In preparation to be submitted to: Int. J.Heat Mass Transfer.

[5] D. M. Anderson, G. B. McFadden, and A. A. Wheeler. Diffuse-interface methods in fluid mechanics. *Annu. Rev. Fluid Mech.* 30.1 (1998), pp. 139–165.

[6] D. Arnold, F. Brezzi, B. Cockburn, and L. Marini. Unified analysis of discontinuous Galerkin methods for elliptic problems. *SIAM J. Numer. Anal.* 39.5 (2002), pp. 1749–1779.

[7] K. Baber, B. Flemisch, and R. Helmig. Modeling drop dynamics at the interface between free and porous-medium flow using the mortar method. *Int. J. Heat Mass Transfer* 99 (2016), pp. 660–671.

[8] M. Baggio and B. Weigand. Numerical simulation of a drop impact on a superhydrophobic surface with a wire. *Phys. Fluids* 31.11 (2019), p. 112107.

[9] A. L. Barach, M. Eckman, et al. The effects of inhalation of helium mixed with oxygen on the mechanics of respiration. *J. Clin. Invest.* 15.1 (1936), pp. 47–61.

[10] F. Bassi, L. Botti, A. Colombo, A. Ghidoni, and F. Massa. Linearly implicit Rosenbrock-type Runge–Kutta schemes applied to the discontinuous Galerkin solution of compressible and incompressible unsteady flows. *Comput. & Fluids* 118 (2015), pp. 305–320.

[11] F. Bassi, A. Crivellini, D. Di Pietro, and S. Rebay. An artificial compressibility flux for the discontinuous Galerkin solution of the incompressible Navier–Stokes equations. *J. Comput. Phys.* 218.2 (2006), pp. 794–815.

[12] F. Bassi and S. Rebay. A high-order accurate discontinuous finite element method for the numerical solution of the compressible Navier–Stokes equations. *J. Comput. Phys.* 131.2 (1997), pp. 267–279.

[13] F. Bassi, F. Massa, L. Botti, and A. Colombo. Artificial compressibility Godunov fluxes for variable density incompressible flows. *Comput. & Fluids* 169 (2018), pp. 186–200.

[14] F. Bassi, S. Rebay, G. Mariotti, S. Pedinotti, and M. Savini. *A high order accurate discontinuous finite element method for inviscid and viscous turbomachinery flows. Turbomachinery - Fluid Dynamics and Thermodynamics, European Conference, 2.* 1997, pp. 99–108.

[15] J. Bear. *Dynamics of fluids in porous media.* Courier Corporation, 2013.

[16] C. Benocci and A. Pinelli. *The role of the forcing term in the large eddy simulation of equilibrium channel flow. Engineering Turbulence Modeling and Experiments.* Elsevier, 1990, pp. 287–296.

[17] C. Berthon, M. Bessemoulin-Chatard, and H. Mathis. Numerical convergence rate for a diffusive limit of hyperbolic systems: p-system with damping. *SMAI J. Comput. Math.* 2 (2016), pp. 99–119.

[18] E. Birgersson, J. Nordlund, H. Ekström, M. Vynnycky, and G. Lindbergh. Reduced two-dimensional one-phase model for analysis of the anode of a DMFC. *J. Electrochem. Soc.* 150.10 (2003), A1368–A1376.

[19] T. Blesgen. A generalization of the Navier–Stokes equations to two-phase flows. *J. Phys. D: Appl. Phys.* 32.10 (1999), pp. 1119–1123.

[20] D. Bothe and W. Dreyer. Continuum thermodynamics of chemically reacting fluid mixtures. *Acta Mech.* 226.6 (2014), pp. 1757–1805.

[21] L. Botti. Influence of reference-to-physical frame mappings on approximation properties of discontinuous piecewise polynomial spaces. *J. Sci. Comput.* 52.3 (2012), pp. 675–703.

[22] L. Boudin, D. Götz, and B. Grec. *Diffusion models of multicomponent mixtures in the lung. CEMRACS 2009: Mathematical modelling in medicine.* Vol. 30. ESAIM Proc. EDP Sci., Les Ulis, 2010, pp. 90–103.

[23] L. Boudin, B. Grec, and F. Salvarani. A mathematical and numerical analysis of the Maxwell–Stefan diffusion equations. *Discrete Contin. Dyn. Syst. Ser. B* 17.5 (2012), pp. 1427–1440.

[24] M. Breuer, N. Peller, C. Rapp, and M. Manhart. Flow over periodic hills – Numerical and experimental study in a wide range of Reynolds numbers. *Comput. & Fluids* 38.2 (2009), pp. 433–457.

[25] S. Bulteau, C. Berthon, and M. C. Bessemoulin-Chatard. Convergence rate of an asymptotic preserving scheme for the diffusive limit of the p-system with damping. *Comm. Math. Sci.* (2018).

[26] J. W. Cahn and J. E. Hilliard. Free energy of a nonuniform system. I. Interfacial free energy. *J. Chem. Phys.* 28.2 (1958), pp. 258–267.

[27] K. S. Chen, M. A. Hickner, and D. R. Noble. Simplified models for predicting the onset of liquid water droplet instability at the gas diffusion layer/gas flow channel interface. *Int. J. Energy Res.* 29 (2005), pp. 1113–1132.

[28] S. C. Cho, Y. Wang, and K. S. Chen. Droplet dynamics in a polymer electrolyte fuel cell gas flow channel: forces, deformation and detachment. I: Theoretical and numerical analyses. *J. Power Sources* 206 (2012), pp. 119–128.

[29] A. J. Chorin. A numerical method for solving incompressible viscous flow problems. *J. Comput. Phys.* 2.1 (1967), pp. 12–26.

[30] R. Courant, K. Friedrichs, and H. Lewy. Über die partiellen Differenzengleichungen der mathematischen Physik. *Math. Ann.* 100.1 (1928), pp. 32–74.

[31] C. F. Curtiss and J. O. Hirschfelder. Integration of stiff equations. *Proc. Natl. Acad. Sci. U.S.A.* 38.3 (1952), pp. 235–243.

[32] C. Dafermos. Stability of motions of thermoeleastic fluids. *J. Thermal Stresses* 2.1 (1979), pp. 127–134.

[33] C. Dafermos. The second law of thermodynamics and stability. *Arch. Rational Mech. Anal.* 70.2 (1979), pp. 167–179.

[34] C. Dafermos. *Hyperbolic conservation laws in continuum physics*. Heidelberg: Springer, 2010.

[35] P. Degond and M. Tang. All speed scheme for the low Mach number limit of the isentropic Euler equations. *Comm. Comput. Phys.* 10.1 (2011), pp. 1–31.

[36] G. Di Marzo. *RODAS5(4) - Méthodes de Rosenbrock d'ordre 5(4) adaptées aux problemes différentiels-algébriques*. MSc Mathematics Thesis, Faculty of Science, University of Geneva, 1993.

[37] D. Diehl. *Higher order schemes for simulation of compressible liquid-vapor flows with phase change*. Universität Freiburg im Breisgau, 2007.

[38] R. DiPerna. Uniqueness of solutions to hyperbolic conservation-laws. *Indiana Univ. Math. J.* 28.1 (1979), pp. 137–188.

[39] W. Dreyer, J. Giesselmann, and C. Kraus. A compressible mixture model with phase transition. *Phys. D* 273-274 (2014), pp. 1–13.

[40] W. Dreyer, J. Giesselmann, C. Kraus, and C. Rohde. Asymptotic analysis for Korteweg models. *Interfaces Free Bound.* 14 (2012), pp. 105–143.

[41] J. Duncan and H. Toor. An experimental study of three component gas diffusion. *AlChE J.* 8.1 (1962), pp. 38–41.

[42] D. T. Elsworth and E. F. Toro. *Riemann solvers for solving the incompressible Navier–Stokes equations using the artificial compressibility method*. 9208. College of Aeronautics, Cranfield Institute of Technology, 1992.

[43] ERCOFTAC. *Periodic Hill Flow*. 2010. URL: https://kbwiki.ercoftac.org/w/index.php?title=Abstr:2D_Periodic_Hill_Flow (visited on 10/09/2020).

[44] D. Fang and J. Xu. Existence and asymptotic behavior of C^1 solutions to the multi-dimensional compressible Euler equations with damping. *Nonlinear Anal. Theory Methods Appl.* 70.1 (2009), pp. 244–261.

[45] E. Feireisl, H. Petzeltová, E. Rocca, and G. Schimperna. Analysis of a phase-field model for two-phase compressible fluids. *Math. Models Methods Appl. Sci.* 20.07 (2010), pp. 1129–1160.

[46] A. Fick. Ueber Diffusion. *Ann. Phys.* 94r.1 (1855), pp. 59–86.

[47] B. Flemisch, M. Darcis, K. Erbertseder, B. Faigle, A. Lauser, K. Mosthaf, S. Müthing, P. Nuske, A. Tatomir, M. Wolff, et al. Dumux: DUNE for multi-{phase, component, scale, physics,…} flow and transport in porous media. *Adv. Water Resour.* 34.9 (2011), pp. 1102–1112.

[48] H. Freistühler and M. Kotschote. Phase-field and Korteweg-type models for the time-dependent flow of compressible two-phase fluids. *Arch. Rational Mech. Anal.* 224.1 (2016), pp. 1–20.

[49] J. Fröhlich, P. Mellen Christopher, W. Rodi, L. Temmerman, and M. A. Leschziner. Highly resolved large-eddy simulation of separated flow in a channel with streamwise periodic constrictions. *J. Fluid Mech.* 526 (2005), pp. 19–66.

[50] J. Giesselmann, C. Makridakis, and T. Pryer. Energy consistent DG methods for the Navier–Stokes–Korteweg system. *Math. Comp.* 83 (2014), pp. 2071–2099.

[51] J. Giesselmann and T. Pryer. Energy consistent discontinuous Galerkin methods for a quasi-incompressible diffuse two phase flow model. *ESAIM Math. Model. Numer. Anal.* 49(1) (2015), pp. 275–301.

[52] X. Gloerfelt and P. Cinnella. Large Eddy Simulation Requirements for the Flow over Periodic Hills. *Flow Turbul. Combust.* 103 (2019), pp. 55–91.

[53] B. Haberman and J. Young. Three-dimensional simulation of chemically reacting gas flows in the porous support structure of an integrated-planar solid oxide fuel cell. *Int. J. Heat Mass Transfer* 47.17–18 (2004), pp. 3617–3629.

[54] K. K. Haller, Y. Ventikos, and D. Poulikakos. Wave structure in the contact line region during high speed droplet impact on a surface: solution of theRiemann problem for the stiffened gas equation of state. *J. Appl. Phys.* 93.5 (2003), pp. 3090–3097.

[55] K. K. Haller, Y. Ventikos, D. Poulikakos, and P. Monkewitz. Computational study of high-speed liquid droplet impact. *J. Appl. Phys.* 92.5 (2002), pp. 2821–2828.

[56] F. H. Harlow and J. E. Welch. Numerical calculation of time-dependent viscous incompressible flow of fluid with free surface. *Phys. Fluids* 8 (1965), pp. 2182–2189.

[57] R. Helmig. *Multiphase flow and transport processes in the subsurface: a contribution to the modeling of hydrosystems.* Springer-Verlag, 1997.

[58] C.-H. Hsu, S.-S. Lin, and C.-R. Yang. Smooth solutions of the one-dimensional compressible Euler equation with gravity. *J. Differential Equations* 260.1 (2016), pp. 708–732.

[59] F. Huang, P. Marcati, and R. Pan. Convergence to the Barenblatt solution for the compressible Euler equations with damping and vacuum. *Arch. Rational Mech. Anal.* 176.1 (2005), pp. 1–24.

[60] X. Huo, A. Jüngel, and A. Tzavaras. High-friction limits of Euler flows for multicomponent systems. *Nonlinearity* 32.8 (2019), pp. 2875–2913.

[61] D. Jamet, D. Torres, and J. Brackbill. On the theory and computation of surface tension: the elimination of parasitic currents through energy conservation in the second-gradient method. *J. Comput. Phys.* 182.1 (2002), pp. 262–276.

[62] Y. Jang, M. Leschziner, K. Abe, and L. Temmerman. Investigation of anisotropy-resolving turbulence models by reference to highly-resolved LES data for separated flow. *Flow Turbul. Combust.* 69.2 (2002), pp. 161–203.

[63] S. Jin. Efficient asymptotic-preserving (AP) schemes for some multiscale kinetic equations. *SIAM J. Sci. Comput.* 21.2 (1999), pp. 441–454.

[64] S. Jin. Asymptotic preserving (AP) schemes for multiscale kinetic and hyperbolic equations: a review. *Riv. Math. Univ. Parma (N.S.)* 3.2 (2012), pp. 177–216.

[65] A. Jüngel and I. Stelzer. Existence analysis of Maxwell–Stefan systems for multicomponent mixtures. *SIAM J. Math. Anal.* 45.4 (2013), pp. 2421–2440.

[66] C. A. Kennedy and M. H. Carpenter. Additive Runge–Kutta schemes for convection-diffusion-reaction equations. *Appl. Numer. Math.* 44.1 (2003), pp. 139–181.

[67] M. Kotschote. Strong solutions of the Navier–Stokes equations for a compressible fluid of Allen–Cahn type. *Arch. Rational Mech. Anal.* 206.2 (2012), pp. 489–514.

[68] L. I. G. Kovasznay. Laminar flow behind a two-dimensional grid. *Math. Proc. Cambridge Philos. Soc.* 44.1 (1948), pp. 58–62.

[69] M. Kränkel and D. Kröner. *A phase-field model for flows with phase transition. Theory, Numerics and Applications of Hyperbolic Problems II.* Cham: Springer International Publishing, 2018, pp. 243–254.

[70] R. Krishna. Uphill diffusion in multicomponent mixtures. *Chem. Soc. Rev.* 44 (10 2015), pp. 2812–2836.

[71] C. Lattanzio and A. Tzavaras. Relative entropy in diffusive relaxation. *SIAM J. Math. Anal.* 45.3 (2013), pp. 1563–1584.

[72] R. J. LeVeque. *Numerical methods for conservation laws*. Second. Lectures in Mathematics ETH Zürich. Birkhäuser Verlag, Basel, 1992.

[73] A. Logg and G. N. Wells. DOLFIN: automated finite element computing. *ACM Trans. Math. Software* 37.2 (2010).

[74] J. Lowengrub and L. Truskinovsky. Quasi-incompressible Cahn–Hilliard fluids and topological transitions. *Proc. R. Soc. A* 454.1978 (1998), pp. 2617–2654.

[75] T. Luo and H. Zeng. Global existence of smooth solutions and convergence to Barenblatt solutions for the physical vacuum free boundary problem of compressible Euler equations with damping. *Comm. Pure Appl. Math.* 69.7 (2016), pp. 1354–1396.

[76] P. Marcati and A. Milani. The one-dimensional Darcy's law as the limit of a compressible Euler flow. *J. Differential Equations* 84.1 (1990), pp. 129–147.

[77] E. Mason and A. Malinauskas. *Gas transport in porous media: the dusty-gas model*. Vol. 17. Elsevier Science Ltd, 1983.

[78] F. Massa, L. Ostrowski, F. Bassi, and C. Rohde. An artificial Equation of State based Riemann solver for a discontinuous Galerkin discretization of the incompressible Navier–Stokes equations. *J. Comput. Phys.* 448 (2022), p. 110705.

[79] F. C. Massa, G. Noventa, M. Lorini, F. Bassi, and A. Ghidoni. High-order linearly implicit two-step peer schemes for the discontinuous Galerkin solution of the incompressible Navier–Stokes equations. *Comput. & Fluids* 162 (2018), pp. 55–71.

[80] J. Maxwell. On the dynamical theory of gases. *Philos. Trans. Roy. Soc. London Ser. A* (1866), pp. 49–88.

[81] C. P. Mellen, J. Fröhlich, and W. Rodi. *Large eddy simulation of the flow over periodic hills. In: Proceedings. 16th IMACS World Congress, Lausanne, Switzerland.* 2000.

[82] A. Meurer et al. SymPy: symbolic computing in python. *PeerJ Comput. Sci.* 3 (2017), e103.

[83] K. Mosthaf, K. Baber, B. Flemisch, R. Helmig, A. Leijnse, I. Rybak, and B. Wohlmuth. A coupling concept for two-phase compositional porous-medium and single-phase compositional free flow. *Water Resour. Res.* 47.10 (2011).

[84] J. Neusser and V. Schleper. Numerical schemes for the coupling of compressible and incompressible fluids in several space dimensions. *Appl. Math. Comput.* 304 (2017), pp. 65–82.

[85] G. Noventa, F. Massa, S. Rebay, F. Bassi, and A. Ghidoni. Robustness and efficiency of an implicit time-adaptive discontinuous Galerkin solver for unsteady flows. *Comput. & Fluids* 204 (2020), p. 104529.

[86] L. Ostrowski, F. C. Massa, and C. Rohde. *A phase field approach to compressible droplet impingement*. *Droplet Interactions and Spray Processes*. Ed. by G. Lamanna, S. Tonini, G. E. Cossali, and B. Weigand. Cham: Springer International Publishing, 2020, pp. 113–126.

[87] L. Ostrowski and F. Massa. *An incompressible–compressible approach for droplet impact*. *Proceedings of the DIPSI Workshop 2019. Droplet Impact Phenomena & Spray Investigations*. Ed. by G. E. Cossali and S. Tonini. 2019.

[88] L. Ostrowski and C. Rohde. *Phase field modelling for compressible droplet impingement. Hyperbolic Problems: Theory, Numerics, Applications*. Ed. by A. Bressan, M. Lewicka, D. Wang, and Y. Zheng. Hyperbolic Problems: Theory, Numerics, Applications. 17th International Conference, University Park (2018). 2018, pp. 586–593.

[89] L. Ostrowski and C. Rohde. Compressible multicomponent flow in porous media with Maxwell–Stefan diffusion. *Math. Methods Appl. Sci.* 43.7 (2020), pp. 4200–4221.

[90] Y.-J. Peng and V. Wasiolek. Parabolic limit with differential constraints of first-order quasilinear hyperbolic systems. *Ann. Inst. H. Poincare Anal. Non Lineaire* 33.4 (2016), pp. 1103–1130.

[91] H. Podhaisky, R. Weiner, and B. A. Schmitt. Rosenbrock-type 'Peer' two-step methods. *Appl. Numer. Math.* 53.2 (2005), pp. 409–420.

[92] S. B. Pope. *Turbulent flows*. Cambridge University Press, 2000.

[93] T. Qian, X.-P. Wang, and P. Sheng. Molecular scale contact line hydrodynamics of immiscible flows. *Phys. Rev. E* 68 (1 2003), p. 016306.

[94] T. Qian, X.-p. Wang, and P. Sheng. A variational approach to moving contact line hydrodynamics. *J. Fluid Mech.* 564 (2006), p. 333.

[95] C. Rapp. *Experimentelle Studie der turbulenten Strömung über periodische Hügel*. Technische Universität München, 2009, pp. 1–148.

[96] E. Repossi, R. Rosso, and M. Verani. A phase-field model for liquid–gas mixtures: mathematical modelling and discontinuous Galerkin discretization. *Calcolo* 54.4 (2017), pp. 1339–1377.

[97] H. H. Rosenbrock. Some general implicit processes for the numerical solution of differential equations. *Comput. J.* 5.4 (1963), pp. 329–330.

[98] P. G. Saffman. On the boundary condition at the surface of a porous medium. *Stud. Appl. Math.* 50.2 (1971), pp. 93–101.

[99] J. Stefan. Über das Gleichgewicht und die Bewegung, insbesondere die Diffusion von Gasgemengen. *Sitzber. Akad. Wiss. Wien* 63 (1871), pp. 63–124.

[100] R. Taylor and R. Krishna. *Multicomponent mass transfer*. Wiley Series in Chemical Engineering. Wiley, 1993.

[101] E. Toro. *Riemann solvers and numerical methods for fluid dynamics: a practical introduction*. Springer Science & Business Media, 2009.

[102] C. Truesdell. The mechanical foundations of elasticity and fluid dynamics. *J. Ration. Mech. Anal.* 1 (1952), pp. 125–300.

[103] T. Von Karman. Turbulence and skin friction. *J. Aeronaut. Sci.* 1.1 (1934), pp. 1–20.

[104] E. R. Weibel and D. M. Gomez. Architecture of the human lung. *Science* 137.3530 (1962), pp. 577–585.

[105] J. Wesselingh and R. Krishna. *Mass transfer in multicomponent mixtures*. Delft University Press, 2000.

[106] G. Witterstein. Sharp interface limit of phase change flows. *Adv. Math. Sci. Appl.* 20.2 (2010), pp. 585–629.

[107] G. Witterstein. Phase change flows with mass exchange. *Adv. Math. Sci. Appl.* 21.2 (2011), pp. 559–611.

[108] W.-A. Yong. Entropy and global existence for hyperbolic balance laws. *Arch. Rational Mech. Anal.* 172.2 (2004), pp. 247–266.

[109] L. You and H. Liu. A two-phase flow and transport model for PEM fuel cells. *J. Power Sources* 155.2 (2006), pp. 219–230.

[110] P. Yue, C. Zhou, and J. J. Feng. Spontaneous shrinkage of drops and mass conservation in phase-field simulations. *J. Comput. Phys.* 223.1 (2007), pp. 1–9.

[111] F. Y. Zhang, X. G. Yang, and C. Y. Wang. Liquid water removal from a polymer electrolyte fuel cell. *J. Electrochem. Soc* 153 (2006), A225–A232.

Abstract

This thesis consists of three parts. In the first part we consider multi-component flows through porous media. We introduce a hyperbolic system of partial differential equations which describes such flows, prove the existence of solutions, the convergence in a long-time-large-friction regime to a parabolic limit system, and finally present a new numerical scheme to efficiently simulate flows in this regime.

In the second part we study two-phase flows where both phases are considered compressible. We introduce a Navier–Stokes–Allen–Cahn phase-field model and derive an energy-consistent discontinuous Galerkin scheme for this system. This scheme is used for the simulation of two complex examples, namely drop–wall interactions and multi-scale simulations of coupled porous-medium/free-flow scenarios including drop formation at the interface between the two domains.

In the third part we investigate two-phase flows where one phase is considered incompressible, while the other phase is assumed to be compressible. We introduce an incompressible–compressible Navier–Stokes–Cahn–Hilliard model to describe such flows. Further, we present some analytical results for this system, namely a computable expression for the effective surface tension in the system and a formal proof of the convergence to a (quasi-)incompressible system in the low Mach regime. As a first step towards a discontinuous Galerkin discretization of the system, which is based on Godunov fluxes, we introduce the concept of an artificial equation of state modification, which is examined for a basic single-phase incompressible setting.